

APPLICATION OF THE ONE-DIMENSIONAL TURBULENCE MODEL TO ELECTROHYDRODYNAMICALLY ENHANCED INTERNALLY FORCED CONVECTIVE FLOWS

Von der Fakultät Maschinenbau, Elektro- und Energiesysteme der Brandenburgischen Technischen Universität Cottbus-Senftenberg zur Erlangung des akademischen Grades eines

Doktors der Ingenieurwissenschaften
(Dr.-Ing.)

genehmigte Dissertation vorgelegt von

Master of Science
Juan Alí Medina Méndez

geboren am 28.09.1988 in Valencia, Venezuela

Vorsitzender	Apl. Prof. Dr. rer. nat. habil. Uwe Harlander	BTU Cottbus-Senftenberg
Gutachter	Prof. Dr.-Ing. Heiko Schmidt	BTU Cottbus-Senftenberg
Gutachter	Prof. Dr.-Ing. Ulrich Riebel	BTU Cottbus-Senftenberg
Gutachter	Prof. Dr. rer. nat. Julius Reiß	TU Berlin

Tag der mündlichen Prüfung: 27. Oktober 2020

APPLICATION OF THE ONE-DIMENSIONAL TURBULENCE
MODEL TO ELECTROHYDRODYNAMICALLY ENHANCED
INTERNALLY FORCED CONVECTIVE FLOWS

M. SC. JUAN ALÍ MEDINA MÉNDEZ

University:

Brandenburg University of Technology Cottbus-Senftenberg

Faculty:

Mechanical Engineering, Electrical and Energy Systems

Chair:

Chair of Numerical Fluid and Gas Dynamics

M. Sc. Juan Alí Medina Méndez:
Application of the One-Dimensional Turbulence model to electrohydrodynamically enhanced internally forced convective flows,
October 2020

CHAIR OF EVALUATION COMMITTEE:
Apl. Prof. Dr. rer. nat. habil. Uwe Harlander

SUPERVISOR:
Prof. Dr.-Ing. Heiko Schmidt

REVIEWERS:
Prof. Dr.-Ing. Heiko Schmidt
Prof. Dr.-Ing. Ulrich Riebel
Prof. Dr. rer. nat. Julius Reiß

LOCATION:
Cottbus

SUBMISSION DATE:
May 2020

Dedicated to the loving memory of Elsa de la Cruz Figueredo
(1929–2015†) and her beloved daughter, Doritza (1949–2019†).

En la memoria de Elsa de la Cruz Figueredo (1929–2015†) y de su
amada hija, Doritza (1949–2019†).

ABSTRACT

This thesis is an attempt to assess some of the effects that electroquasistatic body forces exert on turbulent internally forced convective flows. In order to do that, a stochastic turbulence model is employed, namely, the One-Dimensional Turbulence (ODT) model.

The reduced dimensionality of ODT demands a reduction of the Navier-Stokes equations (and in this case, also the Maxwell equations), into a 1-D system. This is done by performing an asymptotic analysis in terms of the nondimensional numbers of the flow. Also, a validation step due to the relative novel character of the cylindrical ODT formulation is done for an incompressible and constant properties flow regime and a variable density flow regime. The validation is presented for both the temporal (T-ODT) and a novel spatial (S-ODT) formulation in both planar and cylindrical geometries. Results in the constant property case show that wall normal (and radial) profiles, in both the T-ODT and S-ODT formulations, show good agreement with each other and to the data of Direct Numerical Simulations (DNSs). For the evaluated variable density heated pipe flow, gradients at the wall can be better reproduced with S-ODT.

After validating the model, ODT is applied first into a planar configuration which emulates the flow in a wire-plate Electrostatic Precipitator (ESP). For this flow, the additional input energy due to the electroquasistatic body force has an effect on the modification of the bulk velocity, and subsequently, the skin friction coefficient. Some qualitative DNS trends are confirmed with ODT, such as the localized increase of the Reynolds stress, as a consequence of increased eddy activity close to the discharge electrodes. Next, the results of ODT simulations in a cylindrical wire-tube ESP are presented. Here, ODT results are compared to experimental results. ODT results for global integral quantities such as the streamwise pressure gradient and the Nusselt number enhancement ratio are able to match in a reasonable way the experimental results. The competing relevance between the EHD contribution to turbulence by momentum, and by affecting the temperature and density due to the Joule heating effect is also analyzed, showing the leading order relevance of the former one. Specifically for the Nusselt number results, the sensitivity of the EHD flow to transition effects is shown to be very significant.

This thesis may open the door to a vast new field of phenomena which can not only serve for the further validation of the ODT model against DNSs or experiments, but also for the real use of ODT in applications which are so far inaccessible for traditional DNSs.

ZUSAMMENFASSUNG

Ziel dieser Dissertation ist die Untersuchung der Effekte von elektroquasistatischen Volumenkräften auf turbulente druckgetriebene Strömungen. Dazu wurde das stochastisch Eindimensionale Turbulenzmodell (ODT) angewendet.

Als ein Modell niedriger Ordnung benötigt ODT eine Reduktion der Navier-Stokes-Gleichungen (sowie der Maxwell-Gleichungen hier) zu einem 1-D System. Diese Reduktion erfolgte mittels einer asymptotischen Analyse, welche die Strömung als Funktion von Leading-Order-Effekten entdimensionalisierter Kennzahlen beschreibt. Zusätzlich erfolgte in der Dissertation ein Validierungsschritt aufgrund der kürzlich veröffentlichten Zylinderformulierung für ODT. Zur Validierung wurden inkompressible Strömungen konstanter Fluideigenschaften, sowie Strömungen variabler Dichte betrachtet. Die Validierung stellt Ergebnisse von zeitlich (T-ODT) und räumlich (S-ODT) entwickelnde ODT-Simulationen für planare und zylindrische Koordinatensysteme vor. Die Ergebnisse zeigen, dass wand-normale (oder radiale) Profile, sowohl in T-ODT und S-ODT, eine gute Übereinstimmung miteinander und mit Daten von Direkten Numerische Simulationen (DNS) aufzeigen. Im Fall der aufgeheizten Rohrströmungen variabler Dichte lassen sich die Gradienten an der Wand mittels S-ODT besser reproduzieren.

Nach der Validierung des Modells wurde ODT erstmals auf eine planare Konfiguration, welche die Strömung einer Plattenelektroabscheider simuliert, angewendet. Der zusätzliche Energiebeitrag, der von der elektroquasistatischen Volumenkraft geliefert wird, hat einen Effekt auf die Bulk-Geschwindigkeit, sowie auf den Reibungsbeitrag. Einige Trends der DNS lassen sich mit ODT bestätigen, z.B. der lokalisierte Anstieg der Reynolds'schen Schubspannungen, der aufgrund der erhöhten Wahrscheinlichkeit der Erzeugung turbulenter Wirbel in der Nähe der Sprühelektrode verursacht wird. Im Anschluss werden ODT-Ergebnisse eines zylindrischen Rohrelektroabscheiders vorgestellt. Diese sind in Form von integralen Größen gegen experimentellen Messungen verglichen, z.B., der Druckgradient in Strömungsrichtung, sowie das Erhöhungsverhältnis der Nusseltzahl. Die von ODT generierten integralen Größen stimmen gut mit experimentellen Messwerten überein. Die Wichtigkeit des EHD-Beitrags zur Turbulenz mittels Impulstransport, sowie dessen Einfluss auf die Temperatur und Dichte gemäß des ersten Jouleschen Gesetzes wurde ebenfalls mit ODT untersucht. Die Ergebnisse zeigen den Effekt führender Ordnung des EHD-Beitrags auf die Turbulenz. Eine große Sensitivität der Nusseltzahl-Ergebnisse bzgl. der Transitionseffekten in EHD-Strömungen konnte parallel nachgewiesen werden.

Dank dieser Arbeit lassen sich neue Phänomene mittels numerischer Simulationen untersuchen. Dies dient zur weiteren Validierung des ODT-Modells anhand DNS und Experimenten. Außerdem erlaubt die Dissertation zukünftige Anwendungen von ODT auf Phänomene und Strömungen, die bisher unzugänglich für DNS sind.

PUBLICATIONS

PUBLICATIONS OF THE AUTHOR WHICH HAVE BEEN ADAPTED TO BE PART OF THIS THESIS

Some concepts and figures from this work have been previously presented and discussed in the following publications:

Journal articles:

J. A. Medina Méndez, H. Schmidt, D. Lignell, Application of the One-Dimensional Turbulence model to incompressible channel and pipe flow. Article submitted to *Z. Angew. Math. Mech.*, 2019.

URL: https://ignite.byu.edu/public/Medina_2019.pdf

J. A. Medina Méndez, M. Klein, H. Schmidt (2019), One-Dimensional Turbulence investigation of variable density effects due to heat transfer in a low Mach number internal air flow, *Int. J. Heat Fluid Flow*, 80, 108481.

DOI: <https://doi.org/10.1016/j.ijheatfluidflow.2019.108481>

J. A. Medina Méndez, H. Schmidt, F. Mauß, Z. Jozefik (2018), Constant volume n-Heptane autoignition using One-Dimensional Turbulence, *Combust. Flame*, 190, 388–401.

DOI: <https://doi.org/10.1016/j.combustflame.2017.12.015>

Conference proceedings:

J. A. Medina Méndez, H. Schmidt, U. Riebel, Towards a One-Dimensional Turbulence Approach for Electrohydrodynamic Flows, Proc. 11th Int. Symp. Turb. Shear Flow Phen. (TSFP11), July 30 - August 2 (2019), Southampton, UK.

URL: <http://www.tsfp-conference.org/proceedings/2019/265.pdf>

J. A. Medina Méndez, H. Schmidt, One-Dimensional Turbulence investigation of incompressible and low Mach number variable density pipe-flow, Proc. Appl. Math. Mech. 18(e201800090), March 19 - 23 (2018), Munich, Germany.

DOI: <https://doi.org/10.1002/pamm.201800090>

J. A. Medina Méndez, H. Schmidt, Application of ODT to constant volume autoignition problems, Proc. Appl. Math. Mech. 17(1), 643-644, March 6 - 10 (2017), Weimar, Germany.

DOI: <https://doi.org/10.1002/pamm.201710291>

OTHER PUBLICATIONS OF THE AUTHOR

The following is a second list of publications in which the author participated either as lead or co-author. Although these publications were carried out in a similar time frame to the one of the realization of this thesis, and may possibly be cited in this work, they may not necessarily be related to the main topics discussed here.

Journal articles:

Rakhi, M. Klein, J. A. Medina Méndez, H. Schmidt (2019), One-Dimensional Turbulence modeling of incompressible developing turbulent boundary layers with comparison to DNS, *J. Turbul.*, 20(8), 506-543.

DOI: <https://doi.org/10.1080/14685248.2019.1674859>

T. Starick, J. A. Medina Méndez, H. Schmidt (2019), One-Dimensional Turbulence Simulations for Reactive Flows in Open and Closed Systems, *Tech. Mech.*, 39(1), 162-174.

DOI: <https://doi.org/10.24352/UB.0VGU-2019-015>

C. Glawe, J. A. Medina Méndez, H. Schmidt (2018), IMEX based Multi-Scale Time Advancement in ODTLES, *Z. Angew. Math. Mech.* 98, 1907-1923.

DOI: <https://doi.org/10.1002/zamm.201800098>

D. Lignell, V. Lansinger, J. A. Medina Méndez, M. Klein, A. Kerstein, H. Schmidt, M. Fistler, M. Oevermann (2018), One-dimensional turbulence modeling for cylindrical and spherical flows: model formulation and application, *Theor. Comput. Fluid Dyn.*, 32(4), 495-520.

DOI: <https://doi.org/10.1007/s00162-018-0465-1>

Conference proceedings:

J. A. Medina Méndez, C. Glawe, T. Starick, M. S. Schöps, H. Schmidt, IMEX-ODTLES: A multi-scale and stochastic approach for highly turbulent flows, *Proc. Appl. Math. Mech.* 19(e201900433), February 18 - 22 (2019), Vienna, Austria.

DOI: <https://doi.org/10.1002/pamm.201900433>

ACKNOWLEDGMENTS

This thesis is the culmination of a research journey which could not have been possible without the contributions and support of many people. It is probably not possible to cite everybody in these lines, who, in one way or another, made a direct or indirect contribution to this thesis. For everyone, mentioned or not along these lines, my sincere words of appreciation.

It is impossible for me not to mention here, in the first place, the most direct contributor to this thesis, Prof. Heiko Schmidt. Prof. Schmidt not only entrusted me with absolute freedom to perform my research, but he also had total confidence, from the very beginning, in the fact that I would succeed in the process of delivering this thesis. Considering that I was an outsider in the field when I joined as part of the research staff at the chair, I am very grateful for the confidence, the opportunity, and the technical and professional guidance that he offered me.

In a similar level of importance, I reckon the unvaluable contributions to this thesis done by Dr. Alan Kerstein and Prof. David Lignell. I had the opportunity to have very interesting and fruitful discussions with Prof. Lignell regarding the ODT model. Prof. Lignell is also the creator of the base C++ code which was used to develop this thesis. Although I have not had the chance to meet Dr. Kerstein in person so far, I do thank him for all the time and valuable quality reviews he has done for several texts and articles which are now part of this thesis. Similarly, I would like to thank Prof. Julius Reiß for the time and effort he took to voluntarily be part of the review body of this thesis.

It would also be a grave mistake not to recognize the guidance and contributions to this thesis and to other published articles done by the research project partners of the Chair of Particle Technology at the BTU Cottbus. I want to thank Prof. Ulrich Riebel, who I consider in practical terms to be my second supervisor, as well as the project colleagues, Christian Bacher and Patrick Burger. Specifically, I want to acknowledge not only Christian's direct contributions to this work, but also his detailed, and mostly passionate discussions in the topics of EHD flows.

Special thanks to my current and former colleagues, Marten Klein, Tommy Starick, Rakhi, Mark Simon Schöps, Pedro Pupo Sa da Costa and Tian-Yun Gao. In one way or another, all of them had always offered me, more than once, not only valuable technical and professional advice, but were also ready to support me in personal issues, or simply to have a nice time at the office. I also want to thank my friends Nigel and Viviane, who went through the tedious task of proofreading and correcting parts of this thesis.

To my former professors in Venezuela, Gruber Caraballo, and Carlos Pérez Silva, may he rest in peace, I want to thank you for motivating me to come to Germany and pursue postgraduate studies in the fields of energy and fluid mechanics. To all the friends I met in Cottbus, my whole Aikido training group, and my eternal high school and university friends from Venezuela now also residing in Germany, thank you for your constant support and simply for being there.

Finally, I want to thank my family. Without them I would not be here, and this journey would simply not have been possible.

RESEARCH FUNDING SUPPORT AND OTHER FORMAL ACKNOWLEDGMENTS

The financial support provided by the European Regional Development Fund (EFRE-Brandenburg) is acknowledged and greatly appreciated. Most of the publications which are now part of this thesis were carried out within the framework of the project 'Einsatz elektrohydrodynamisch getriebener Stromungen zur erweiterten Nutzung von Elektroabscheidern', grant number EFRE StaF 23035000.

The financial support provided by the DAAD for two different research exchange visits to Prof. David Lignell at the BYU University in Utah, USA, is also acknowledged and appreciated.

Finally, I would also like to thank and acknowledge the support of the Norddeutsche Verbund für Hoch- und Höchstleistungsrechnen (HLRN - Berlin, Germany) for the supply of the computational resources which was necessary in order to carry out some of the simulations in this thesis.

CONTENTS

I INTRODUCTION AND THEORY

1	INTRODUCTION	3
1.1	The study of electrohydrodynamic flow	5
1.2	State-of-the-Art research on EHD flows	8
1.2.1	Canonical pipe flow as a study case for the understanding of wall-bounded turbulence	9
1.2.2	Transition to turbulence and turbulence modification by variable density effects	12
1.2.3	Applications of EHD-enhanced turbulent pipe and channel flows	14
1.3	The fundamental question behind this thesis	15
1.4	Thesis Outline	15
2	GOVERNING EQUATIONS FOR ELECTROHYDRODYNAMIC FLOW	17
2.1	The electroquasistatic limit of the Maxwell equations	17
2.1.1	Types of electric currents in the EQS limit	18
2.1.2	Gauss's law	20
2.1.3	Faraday's law	20
2.1.4	Charge conservation	21
2.2	Electroquasistatic force, work and energy	23
2.2.1	Lorentz and Coulomb force	23
2.2.2	Electroquasistatic energy balance	23
2.3	Eulerian and Lagrangian EQS treatment	25
2.4	Hydrodynamic equations (Navier-Stokes)	28
2.4.1	Newton's generalized law of viscosity	28
2.4.2	Fourier's law of heat conduction	28
2.4.3	Equation of state	28
2.4.4	Kinetic energy equation	29
2.4.5	Enthalpy equation	30
3	MODELING OF TURBULENT ELECTROHYDRODYNAMIC FLOW	33
3.1	Fundamentals of the One-Dimensional Turbulence model	33
3.2	Sampling of eddy events	37
3.3	Adaptive ODT formulation	39
3.4	Variable density and vector ODT formulation	41
3.5	Potential energy ODT formulation	46
3.5.1	Case I: the limit of zero transfer of potential into kinetic energy	47
3.5.2	Case II: Transfer of potential into kinetic energy	48
3.6	Deterministic ODT 1-D scalar governing equations	49
3.6.1	Low Mach number EHD-asymptotics	49

3.6.2	Reduction of the deterministic low Mach system to a scalar 1-D system	56
3.6.3	Specialization to the T-ODT and S-ODT formulations	60
II VALIDATION OF THE ODT MODEL: APPLICATION TO INCOMPRESSIBLE CONSTANT PROPERTY AND VARIABLE DENSITY INTERNALLY FORCED CONVECTIVE FLOWS		
4	INCOMPRESSIBLE CONSTANT PROPERTY CHANNEL AND PIPE FLOWS WITH ODT	67
4.1	Setup of the numerical simulations	68
4.2	Calibration of the model inputs	72
4.2.1	Calibration of the ODT model parameters in T-ODT simulations	72
4.2.2	Influence of the choice of l_{max}	74
4.2.3	Influence of the choice of $A_{TimeFac}$	74
4.3	Simulation results and discussion	77
4.3.1	Mean flow statistics	78
4.3.2	Reynolds shear stress and TKE Budgets	85
5	VARIABLE DENSITY PIPE FLOWS WITH ODT	89
5.1	Setup of the numerical simulations	90
5.2	Simulation results and discussion	92
5.2.1	Bulk flow statistics	92
5.2.2	Streamwise velocity and temperature statistics	100
5.2.3	Turbulent fluctuations	101
5.2.4	Relaminarization effect and flow regimes	109
III APPLICATION OF THE ODT MODEL TO EHD INTERNALLY FORCED CONVECTIVE FLOWS		
6	EHD FLOW IN A WIRE-PLATE ELECTROSTATIC PRECIPITATOR	115
6.1	Role of the EHD body force in turbulence and ODT modeling	115
6.2	Implementation of the EHD body force in the ODT wire-plate ESP	118
6.3	Setup of the numerical simulations	120
6.4	Simulation results and discussion	123
7	EHD FLOW IN A CYLINDRICAL ELECTROSTATIC PRECIPITATOR	135
7.1	Incompressible constant property flow in a cylindrical ESP	137
7.1.1	Setup of the numerical simulations	137
7.1.2	Bulk flow results	142
7.2	Quasi-incompressible and transitional flow in the cylindrical ESP	146
7.2.1	Setup of the numerical simulations	147
7.2.2	Bulk flow results	149

7.3	Variable density flow in a cylindrical ESP	153
7.3.1	Setup of the numerical simulations	153
7.3.2	Bulk flow results	160
8	CLOSING COMMENTS	165
8.1	Conclusions	165
8.1.1	Review and conclusions	165
8.1.2	Closing comments regarding the fundamental question of this thesis	168
8.2	Recommendations and outlook on future work	169
8.2.1	Recommendations	169
8.2.2	Outlook to future work	170
IV APPENDIX		
A	NAVIER-STOKES EQUATIONS	175
A.1	Mass conservation	176
A.1.1	Lagrangian representation	176
A.1.2	Eulerian representation	176
A.2	Momentum conservation	176
A.2.1	Lagrangian representation	176
A.2.2	Eulerian representation	177
A.3	Energy conservation	178
A.3.1	Lagrangian representation	178
A.3.2	Eulerian representation	179
B	RELEVANT THERMODYNAMIC RELATIONS	181
B.1	Some additional energy definitions	182
B.1.1	Kinetic energy	182
B.1.2	Gravitational potential energy	182
B.1.3	Electrostatic potential energy	183
C	STOCHASTIC ODT IMPLEMENTATION	185
C.1	Cylindrical triplet map	185
C.2	Energy terms and kernel coefficients calculations	187
C.3	Stochastic ODT implementation algorithm	189
D	DETERMINISTIC ODT IMPLEMENTATION	197
D.1	T-ODT governing equations	198
D.1.1	Cartesian coordinates	199
D.1.2	Cylindrical coordinates	200
D.1.3	Advancement algorithm	203
D.2	S-ODT governing equations	203
D.2.1	Cartesian coordinates	204
D.2.2	Cylindrical coordinates	206
D.2.3	Advancement algorithm	208
E	AVERAGE OPERATORS	209
E.1	Time and streamwise averages	209
E.2	Ensemble average	209
E.3	Favre average	210
F	MEAN FLOW AND TKE EQUATIONS	211

F.1	Generalized incompressible constant property mean momentum and TKE equations	211
F.2	ODT incompressible constant property mean momentum and TKE equations	212
F.2.1	Planar ODT mean flow and TKE equations	212
F.2.2	Cylindrical ODT mean flow and TKE equations	215
F.3	Generalized variable density mean flow and TKE equations	217
F.4	ODT variable density mean flow and TKE equations	220
F.4.1	Planar ODT mean flow and TKE equations	220
F.4.2	Cylindrical ODT mean flow and TKE equations	223
G	SCALING IN WALL UNITS	229
G.1	Incompressible constant property flow	229
G.2	Variable density flow	231
H	CALCULATION OF ELECTROQUASISTATIC FIELDS	235
H.1	Boundary conditions required for the calculation of electroquasistatic fields	235
H.2	Wire-plate ESP: 2-D planar electroquasistatic fields	236
H.3	Cylindrical ESP: 1-D cylindrical electroquasistatic fields	239
H.3.1	Analytical solutions	240
H.3.2	Numerical solution method	242
	BIBLIOGRAPHY	247

LIST OF FIGURES

- Figure 1.1 (a) Number of publications related to 'electrohydrodynamics' in Web Of Science from 1960-2018 (<https://apps.webofknowledge.com/>). (b) Number of Floating Point Operations per Second (FLOPS) of selected Supercomputers from the years 1985 to 2018. The names of the corresponding Supercomputers are given in the plot. 7
- Figure 1.2 Development of FLOPS of selected supercomputers in comparison to achievements in turbulent channel flow simulations 11
- Figure 1.3 Achievements in incompressible constant property pipe and channel flow simulations, as well as in variable properties (variable density, VD in the plot) pipe and channel flow simulations, as in, e.g. compressible flows. 13
- Figure 3.1 Effect of a turbulent eddy of an initially unstable thermally stratified Rayleigh-Bénard configuration (the fluid parcels have been coloured according to their temperature, where red parcels have a higher temperature than the blue ones). The image on the left is the instant right before the instability and the image on the right is the instant after the appearance of the 2-D turbulent eddy. 34
- Figure 3.2 Discrete eddy event representation of a stable charge density field within a cylindrical system (wall and inner concentric electrode). The image on the left is the instant right before the appearance of an electrical convective current and the implementation of an eddy event. The image on the right is the instant after the appearance of the electrical convective current and the eddy event implementation. 35

- Figure 4.1 (a) Wall-normal ODT line in a channel flow. (b) Radial ODT line in a pipe flow. In both (a) and (b) cases, the T-ODT formulation produces a temporal representation of the scalar profiles within the line. In the S-ODT formulation, the line is advected in the streamwise direction, producing a stationary quasi-2-D scalar representation. 67
- Figure 4.2 Influence of the ODT model parameters on the normalized wall-normal pipe flow mean velocity profile for $Re_\tau = 550, 1000, 2000$. The figures are taken from [91]. DNS results from Khoury et al. [94] ($Re_\tau = 550, 1000$) and Chin et al. [41] ($Re_\tau = 2003$) are shown for reference. Results at larger Reynolds numbers have a vertical offset of 10 nondimensional units for better visualization. a) Sensitivity to C and b) Sensitivity to Z . 73
- Figure 4.3 Influence of the upper limit of the eddy size PDF l_{max} on the normalized wall-normal pipe and channel flow mean velocity profiles. Pipe flow results are shown for $Re_\tau = 550$ and compared to DNS results from Khoury et al. [94]. Channel flow results are shown for $Re_\tau = 590$ and compared to DNS results from Moser et al. [27]. Channel flow results have been shifted upwards for better visualization. The figure is taken from [91]. 75
- Figure 4.4 Influence of $A_{TimeFac}$ on the normalized wall-normal pipe and channel flow mean velocity profiles. Pipe flow results are shown for $Re_\tau = 550$ and compared to DNS results from Khoury et al. [94]. Channel flow results are shown for $Re_\tau = 590$ and compared to DNS results from Moser et al. [27]. Channel flow results have been shifted upwards for better visualization. The figure is taken from [91]. 76
- Figure 4.5 Influence of $DA_{TimeFac}$ scaling on the normalized wall-normal pipe flow mean velocity profile for $Re_\tau = 550, 1000, 2003$. DNS results from Khoury et al. [94] ($Re_\tau = 550, 1000$) and Chin et al. [41] ($Re_\tau = 2003$) are shown for reference. The results for increasing Reynolds numbers have been shifted upwards in the plot for better visualization. The figure is taken from [91]. 77

- Figure 4.6 Wall-normal profiles of mean streamwise velocity component in ODT channel and pipe flow simulations. a) The low friction Reynolds number case (Case A) is shown along with DNS results from Moser et al. [27] (channel) and Khoury et al. [94] (pipe). b) Case B results are shown along with DNS results from Hoyas and Jiménez [30] (channel) and Khoury et al. [94] (pipe). c) Case C results are shown along with DNS results from Hoyas and Jiménez [30] (channel) and Chin et al. [41] (pipe). The figures are taken from [91]. 79
- Figure 4.7 Wall-normal RMS profiles of streamwise velocity component. (a): the low friction Reynolds number case (Case A) is shown along with DNS results from Moser et al. [27] (channel) and Khoury et al. [94] (pipe). (b): Case B results are shown along with DNS results from Hoyas and Jiménez [30] (channel) and Khoury et al. [94] (pipe). (c): Case C results are shown along with DNS results from Hoyas and Jiménez [30] (channel) and Chin et al. [41] (pipe). The figures are taken from [91]. 82
- Figure 4.8 Case B results for channel crosswise and spanwise RMS velocity profiles compared to DNS results from Hoyas and Jiménez [30]. The figure is taken from [91]. 83
- Figure 4.9 Pre-multiplied mean velocity gradient obtained in Case B simulations. DNS results from Jiménez et al. [97] (channel) and Khoury et al. [94] (pipe) are shown for reference. The figure is taken from [91]. 84
- Figure 4.10 Case B nondimensional Reynolds shear stress component $\langle u'v' \rangle / u_\tau^2$. DNS results from Lee and Moser [31] (channel) and Khoury et al. [94] (pipe) are shown along for comparison. The figure is taken from [91]. 86
- Figure 4.11 TKE Production (\mathcal{P}_{TKE}^+) and Dissipation (ϵ_{TKE}^+) budgets for T-ODT and S-ODT simulations (Case B). DNS results from Lee and Moser [31] (channel) and Khoury et al. [94] (pipe) are shown for comparison. (a) Production budget. (b) Dissipation budget. The figures are taken from [91]. 87

- Figure 5.1 This figure shows two types of flows evaluated with ODT. (a) is a free shear flow, a cylindrical jet, which can be evaluated with both the T-ODT formulation, and the traditional S-ODT formulation [64, 66, 69]. (b) is an internally forced convective flow, a pipe flow, which can also be evaluated with the T-ODT formulation, but, which motivated an alternative S-ODT formulation [72, 91]. Both (a) and (b) flows are simulated by a CFR constraint, i.e., fixed mass flux per unit area ρU_b . The figures are taken from [72]. 89
- Figure 5.2 Normalized streamwise position dependence of the bulk temperature (a) and bulk velocity (b) in the T-ODT and S-ODT simulations. DNS data from [46] is shown for reference. The Figures are adapted from the original Figures published in [72]. 96
- Figure 5.3 Normalized streamwise position dependence of the wall temperature (a) and bulk Nusselt number (b) in the T-ODT and S-ODT simulations. DNS data from [46] is shown for reference. The Figures are adapted from the original Figures published in [72]. 98
- Figure 5.4 Normalized streamwise position dependence of the skin friction coefficient C_f . DNS data from [46] is shown for reference. The Figure is adapted from the original Figure published in [72]. 99
- Figure 5.5 Wall scaling of the Van Driest streamwise velocity profile at normalized streamwise positions $z/R = 6.4$, $z/R = 28.4$ and $z/R = 49.0$. (a) Results obtained for S-ODT simulations. (b) Results obtained for T-ODT simulations. Profiles at $z/R = 28.4$ and $z/R = 49.0$ have been shifted in the vertical axis for better visibility and comparison. DNS data from [46] is shown for reference. The Figures are taken from [72]. 102

- Figure 5.6 Wall scaling of the average temperature profiles at normalized streamwise positions $z/R = 6.4$, $z/R = 28.4$ and $z/R = 49.0$. (a) Results obtained for S-ODT simulations. (b) Results obtained for T-ODT simulations. Profiles at $z/R = 28.4$ and $z/R = 49.0$ have been shifted in the vertical axis for better visibility and comparison. DNS data from [46] is shown for reference. The Figures are adapted from the original Figures published in [72]. 103
- Figure 5.7 Radial RMS velocity profiles obtained via ensemble averaging for (a) Streamwise velocity and (b) Temperature. Both profiles are obtained at a normalized streamwise position $z/R = 49.0$. The Figures are adapted from the original Figures published in [72]. 105
- Figure 5.8 Radial profiles of density weighted Favre-related streamwise velocity fluctuations at different streamwise positions. (a) S-ODT simulation results, (b) T-ODT simulation results. It is noted that $\langle \rho \rangle \langle u'' \rangle = -\langle \rho' u' \rangle$. The term $\langle \rho' u' \rangle$ is associated to the buoyancy production term in [46]. DNS data from [46] is shown for reference. The Figures are adapted from the original Figures published in [72]. 107
- Figure 5.9 Average shear stress $\langle \tau \rangle$ and Reynolds shear stress component $\langle \rho u'' v'' \rangle$ in the S-ODT and T-ODT formulations at a normalized streamwise position $z/R = 49.0$. DNS data from [46] is shown for reference. The Figure is adapted from the original Figure published in [72]. 108
- Figure 5.10 Radial profiles of turbulent heat flux component $\langle \rho h'' v'' \rangle$ at different streamwise positions. (a) S-ODT simulations. (b) T-ODT simulations. DNS data from [46] is shown for reference. The Figures are adapted from the original Figures published in [72]. 110
- Figure 5.11 Natural and forced convection regime diagram presented in [106], with the change in the characteristic Grashof and Reynolds number obtained from the S-ODT simulations between the normalized positions $z/R = 0$ and $z/R = 50$ (blue line with triangular symbols). Note that $Re_{b,0} = 6000$ in the ODT simulations. See the text for a description of the diagram. 111

- Figure 6.1 Configuration of the ODT model in a channel flow undergoing the effects of EHD body forces, resembling a wire-plate ESP. The ODT line coincides in this case with the channel crosswise direction and displaces in streamwise direction, according to the S-ODT formulation. Discharge electrodes are placed in a periodic array configuration at a distance d_{elec} . The EHD body force is generated due to the electrostatic potential difference between the electrode at ϕ_{elec} and the grounded channel walls at $\phi_{plate} = 0$. The Figure is adapted from the original Figure published in [112]. 116
- Figure 6.2 Distribution of the electrostatic potential in the wire-plate ESP (Case B, $\phi_{elec} = 42000V$). The channel height is $H = 0.04m$. 121
- Figure 6.3 Normalized mean velocity profile and Reynolds shear stresses obtained in the three simulated cases of Table 6.1. Reference DNS data from [53] is shown for reference. Figures are taken from the original publication in [112]. 125
- Figure 6.4 Eddy event distribution in the S-ODT simulations of the wire-plate ESP. (a) Reference case, without EHD forcing. (b) Case B, HV case. The different colors in the plots indicate the density in the number of events according to the supplemented color scale. The intersection of the white dashed lines indicates the position of the electrodes. The Figure is adapted from the original publication in [112]. 126
- Figure 6.5 Normalized mean velocity profile and Reynolds shear stresses obtained in the three simulated cases of Table 6.1 with the scaled ODT model parameter C given by Eq. (6.12). Reference DNS data from [53] is shown for reference. The Figures are taken from the original publication in [112]. 130
- Figure 6.6 (a) Normalized mean shear stress and (b) streamwise RMS velocity profile obtained with scaled ODT C parameter values given by Eq. (6.12). $\tau^+ = \mu(\partial\bar{u}/\partial y)/\tau_w$ in (a). Reference DNS data from [53] is shown for reference. The Figures are taken from [112]. 132

- Figure 6.7 Normalized TKE production (\mathcal{P}_{TKE}^+) and dissipation (ϵ_{TKE}^+) budgets. The left figure shows the DNS data for the reference case 0 (black line) and case B (green line) [53]. The right Figure shows the S-ODT results. The organized motion EHD production term from [53] is also included for reference in the left Figure, $\mathcal{P}_{TKE,EHD}^+$. This term can not be reproduced in ODT. The Figure is adapted from the original publication in [112]. 133
- Figure 7.1 Cylindrical ESP model evaluated with ODT. The configuration is the same as that from the heated pipe in chapter 5, with the additional presence of an axial electrode wire concentric with the pipe walls, and which is responsible for the generation of the electroquasistatic variables E_2 , ρ_f and j_2 . The variables within parenthesis may be omitted in different parts in this chapter. This is clarified in the corresponding setups of the numerical simulations performed in this chapter. The flow is forced by means of a constant streamwise mass flow rate constraint \dot{m} . Both vertical and horizontal flows are evaluated in this chapter (for horizontal flows, $g = 0$. The vertical flows are evaluated in both upward and downward directions, as indicated by the thick gray arrow in the sketch. 136
- Figure 7.2 Experimental voltage-current curves measured at the different evaluated Reynolds numbers [116] (note the citation comment at the beginning of section 7.1). a) Electrode diameter $D_{elec} = 1\text{mm}$, and b) $D_{elec} = 1.5\text{mm}$. 141
- Figure 7.3 Friction Reynolds number Re_τ obtained in experiments and T-ODT simulations as a function of the electrohydrodynamic number N_{EHD} (defined based on the hydraulic radius of the pipe). The ratio N_{EHD}^2/Re^2 is shown along the results (with both numbers defined based on the radius of the pipe). a) Electrode diameter $D_{elec} = 1\text{mm}$. b) Electrode diameter $D_{elec} = 1.5\text{mm}$. 144

- Figure 7.4 Normalized streamwise pressure gradient obtained in experiments and T-ODT simulations as a function of the electrohydrodynamic number N_{EHD} (defined based on R_H). a) Electrode diameter $D_{elec} = 1\text{mm}$. b) Electrode diameter $D_{elec} = 1.5\text{mm}$. 145
- Figure 7.5 a) Streamwise profile of normalized bulk temperature. b) Streamwise profile of normalized bulk velocity. The figures show the results of downward, horizontal, and upward S-ODT simulations. The black and red colors are indicative of different bulk Reynolds numbers. 151
- Figure 7.6 Normalized contributions to the pressure gradient in the downward, horizontal and vertical S-ODT simulations. The reported case is that at $N_{EHD} = 4722.56$ and $Re_{b,0} = 2433.33$. The horizontal solid lines indicate the reported mean experimental values, while the dashed lines indicate the mean plus or minus the standard deviation (SD) of the experimental values [116] (see the citation comment at the beginning of section 7.1). The horizontal dot-dashed line indicates the reported incompressible constant property T-ODT simulation value. 153
- Figure 7.7 Normalized contributions to the pressure gradient in the downward, horizontal and vertical S-ODT simulations. The reported case is that at $N_{EHD} = 4581.55$ and $Re_{b,0} = 4866.67$. The horizontal solid lines indicate the reported mean experimental values, while the dashed lines indicate the mean plus or minus the standard deviation (SD) of the experimental values [116] (see the citation comment at the beginning of section 7.1). The horizontal dot-dashed line indicates the reported incompressible constant property T-ODT simulation value. 154
- Figure 7.8 Experimental voltage-current curves used for the different variable density cylindrical ESP S-ODT simulations according to the reported experimental values in [50] and [49]. 156
- Figure 7.9 S-ODT simulation results for Nusselt number enhancement in the variable density cylindrical ESP. The experimental results obtained by [50] and [49] are reported for comparison. 161

Figure 7.10	S-ODT simulation results for Nusselt number enhancement in the variable density cylindrical ESP after the correction for transition effects by Eq. (7.15). The experimental results obtained by [50] and [49] are reported for comparison. 163
Figure 7.11	S-ODT simulation results for Nusselt number enhancement in the variable density cylindrical ESP after the correction for transition effects by Eqs. (7.15) and (7.16). The experimental results obtained by [50] and [49] are reported for comparison. 164
Figure C.1	(a) Planar triplet map of an initially monotonic density profile with eddy size $l = 0.6$ and left edge $y_0 = 0.2$. (b) Cylindrical triplet map of an initially monotonic density profile with eddy size $l = 0.6$ and left edge $r_0 = 0.2$. 188
Figure H.1	Calculation region and boundary conditions for the electrostatic potential Poisson equation in the wire-plate ESP case. 237

LIST OF TABLES

Table 4.1	T-ODT and S-ODT model parameters used for channel flow simulations. Table adapted from [91]. 69
Table 4.2	T-ODT and S-ODT model parameters used for pipe flow simulations. Table adapted from [91]. 69
Table 4.3	Adaptive ODT and flow configuration parameters used for channel flow simulations (T-ODT and S-ODT formulation). Table adapted from [91]. 70
Table 4.4	Adaptive ODT and flow configuration parameters used for pipe flow simulations (T-ODT and S-ODT formulation). Table adapted from [91]. 71
Table 5.1	Physical, adaptive mesh, and ensemble settings of the variable density T-ODT and S-ODT simulations. Table adapted from [72]. 93
Table 5.2	ODT model parameters of the variable density T-ODT and S-ODT simulations. Table adapted from [72]. 93

Table 6.1	Electrostatic field parameters for the different cases investigated. LV and HV refer to the low voltage and high voltage cases, respectively. 122
Table 6.2	Physical and adaptive mesh settings of the S-ODT simulations. 123
Table 6.3	ODT model parameters used for the wire-plate ESP simulations. 123
Table 6.4	Obtained bulk velocities and corresponding skin friction coefficients in the nonscaled and scaled C-parameter S-ODT simulations (C_0 and C_{scal} , respectively). The DNS obtained values are also shown for reference [53]. 134
Table 7.1	Adaptive ODT and flow configuration parameters used for incompressible constant property cylindrical ESP simulations with $D_{elec} = 1\text{mm}$ (T-ODT). 138
Table 7.2	Adaptive ODT and flow configuration parameters used for constant property cylindrical ESP simulations with $D_{elec} = 1.5\text{mm}$ (T-ODT). 139
Table 7.3	T-ODT model parameters used for the constant property cylindrical ESP simulations ($D_{elec} = 1\text{mm}$ and $D_{elec} = 1.5\text{mm}$). 140
Table 7.4	S-ODT model parameters used in the cylindrical ESP simulations for the determination of the streamwise pressure gradient ($D_{elec} = 1\text{mm}$). 147
Table 7.5	Flow configuration parameters used for variable density cylindrical ESP simulations (S-ODT). 157
Table 7.6	Adaptive mesh settings and ensemble settings used for variable density cylindrical ESP simulations (S-ODT). 158
Table 7.7	S-ODT model parameters used for the variable density cylindrical ESP simulations. Parameters calibrated to obtain values of Nu_b given by Eq. (7.11). 160
Table C.1	T-ODT eddy turnover time formula and kernel coefficients 191
Table C.2	S-ODT eddy turnover length scale formula and kernel coefficients 193
Table C.3	S-ODT eddy turnover length scale formula and kernel coefficients (boundary layer S-ODT formulation from [64, 66, 69]) 195

NOMENCLATURE

Unless explicitly listed as a symbol in this nomenclature list, any combination of latin or greek characters with superindices and/or subindices can be interpreted with all of the other list entries. Explicitly listed symbols (characters with superindices or subindices) are those in which the combination given by the corresponding character and superindex or subindex item in the nomenclature list may result in a wrong interpretation of the symbol.

Acronyms

BC	Boundary Condition
BVP	Boundary Value Problem
CFD	Computational Fluid Dynamics
CFL	Courant-Friedrichs-Lewy condition number
CFR	Constant Flow Rate
DL	Darrieus-Landau
DNS	Direct Numerical Simulations
EBF	Electric Body Force
EHD	Electrohydrodynamics
EQS	Electroquasistatic
ESP	Electrostatic Precipitator
FD	Finite Difference
FDC	Fully Developed Condition
FDM	Finite Difference Method
FLOPS	Floating Point Operations per Second
FPG	Fixed Pressure Gradient
FV	Finite Volume
FVM	Finite Volume Method
HV	High Voltage
IEEE	Institute of Electrical and Electronics Engineers

JPDF	Joint Probability Density Function
LES	Large Eddy Simulation
LHS	Left Hand Side
LV	Low Voltage
ODT	One-Dimensional Turbulence
OWC	One-Way Coupling
PDE	Partial Differential Equation
PDF	Probability Density Function
RANS	Reynolds-Averaged Navier-Stokes
RB	Rayleigh-Bénard
RHS	Right Hand Side
RMS	Root-Mean-Square
RTT	Reynolds Transport Theorem
S-ODT	Spatial ODT formulation
T-ODT	Temporal ODT formulation
TDMA	Tridiagonal Matrix Algorithm
TKE	Turbulent Kinetic Energy
TMA	Triplet Map A formulation
TMB	Triplet Map B formulation

Dimensionless parameters

$$(1 - r)^+ = \frac{(R-r)\langle\rho_w\rangle u_\tau}{\langle\mu_w\rangle} \quad \text{Nondimensional distance from the pipe wall}$$

$$Bo = \frac{Ma^2}{Fr^2} \quad \text{Bulk Boussinesq number}$$

$$f_D = \frac{8\tau_w}{\rho U_b^2} \quad \text{Nondimensional Darcy friction factor}$$

$$F_E = \frac{\phi_0 \beta_b}{\mathcal{D}_f} \quad \text{Bulk ion drift number}$$

$$Fr = \frac{U_b}{\sqrt{gL}} \quad \text{Bulk Froude number. } L \text{ is either the half-width of the channel, or the (hydraulic) radius of the pipe}$$

$$M_\beta = \frac{Re}{Re_E} \quad \text{Mobility ratio}$$

$$Ma = \frac{U_b}{\sqrt{\frac{\gamma p_b}{\rho_b}}} \quad \text{Bulk Mach number}$$

$$N_{\text{EHD}} = \sqrt{\frac{IL^3\rho_b}{S\beta_b\mu_b^2}} \text{ Bulk EHD number}$$

$$Pr = \frac{c_{p,b}\mu_b}{\sigma_{T,b}} \text{ Bulk Prandtl number}$$

$$Re = \frac{\rho_b U_b L}{\mu_b} \text{ Bulk Reynolds number. } L \text{ is either the half-width of the channel or the (hydraulic) radius of the pipe}$$

$$Re_b = \frac{\rho_b U_b L}{\mu_b} \text{ Bulk Reynolds number. For pipe flow, } Re_b \text{ uses in } L \text{ the (hydraulic) diameter of the pipe}$$

$$Re_E = \frac{\rho_b \phi_0 \beta_b}{\mu_b} \text{ Bulk electric Reynolds number}$$

$$Sc_f = \frac{\mu_b}{\rho_b D_f} \text{ Bulk free charge Schmidt number (Schmidt number of the ions with respect to air)}$$

$$St = \frac{fL}{U_b} \text{ Bulk Strouhal number. } L \text{ is either the half-width of the channel or the (hydraulic) radius of the pipe}$$

$$u_k^+ = \frac{\tilde{u}_k}{u_\tau} \text{ Inner scaled nondimensional velocity}$$

$$y^+ = \frac{y\langle\rho_w\rangle u_\tau}{\langle\mu_w\rangle} \text{ Nondimensional distance from the wall}$$

$$\epsilon_{\text{TKE}}^+ = \frac{\epsilon_{\text{TKE}}^V}{\rho u_\tau^4} \text{ Nondimensional incompressible TKE dissipation}$$

$$\mathcal{P}_{\text{TKE}}^+ = \frac{\mathcal{P}_{\text{TKE}}^V}{\rho u_\tau^4} \text{ Nondimensional incompressible TKE production}$$

$$C_f = \frac{2\tau_w}{\rho_b U_b^2} \text{ Skin friction coefficient}$$

$$Gr = \frac{gq_w D_H^4 \rho_b^2}{\mu_b^2 \sigma_{T,b} T_b} \text{ Bulk Grashof number (pipe flow)}$$

$$Nu_b = \frac{2\mathcal{H}_{cf,b} R}{\sigma_{T,w}} \text{ Bulk Nusselt number in pipe flow}$$

$$Re_\tau = \frac{\langle\rho_w\rangle u_\tau L}{\langle\mu_w\rangle} \text{ Friction Reynolds number. } L \text{ is in this case half of the channel width (or height) in planar coordinates and the (hydraulic) radius of the pipe in cylindrical coordinates}$$

Greek characters

α	ODT model parameter for kinetic energy redistribution after an eddy event	[–]
β	Mobility	[m ² /(V · s)]
$\dot{\omega}$	Charge species source term	[A/m ³]
ϵ	Energy dissipation density	[W/m ³]
ϵ_0	Electrical permittivity of the vacuum $\approx 8.854188 \times 10^{-12}$	[F/m]
η	Kolmogorov length scale	[m]

Γ	(Closed) Path	[m]
γ	Heat capacity ratio	[-]
κ	Wavenumber	[m ⁻¹]
Λ	Global eddy rate	[s ⁻¹] (T-ODT), [m ⁻¹] (S-ODT)
λ	Eddy rate	[m ⁻² · s ⁻¹] (T-ODT), [m ⁻³] (S-ODT)
μ	Dynamic viscosity	[Pa · s]
$\mu_{M,0}$	Magnetic permeability of the vacuum $\approx 1.256637 \times 10^{-6}$	[s ² /F]
ν	Kinematic viscosity	[m ² /s]
Ω	Eddy event acceptance probability	[-]
ϕ	Electrostatic potential	[V]
π	π constant	≈ 3.141593 [-]
Ψ	Generic symbol for any extensive property	[unit]
ψ	Generic symbol for any mass specific property or any kind of conserved scalar	[unit/kg] or others
ρ	Mass density	[kg/m ³]
ρ_f	Free charge density	[C/m ³]
σ	Electrical conductivity	[A/(V · m)]
σ_T	Thermal conductivity	[W/(m · K)]
τ	Shear stress	[Pa]
τ_{eddy}	Eddy turnover time	[s]
θ	Cylindrical circumferential or tangential coordinate	[rad]
Ξ	Energy	[J]
ζ	Specific energy	[J/kg]

Greek characters (only vectors or matrices)

$\underline{\kappa}$	Wavenumber vector	[m ⁻¹]
$\underline{\Phi}_E$	Power flux vector	[W/m ²]
$\underline{\tau}$	Shear stress tensor	[Pa]

Latin characters

\check{j}	Imaginary unit	[-]
-------------	----------------	-----

$\mathcal{C}_{1,Peek}$	First Peek's formula constant in a wire-cylinder configuration 31×10^5 [V/m]
$\mathcal{C}_{2,Peek}$	Second Peek's formula constant in a wire-cylinder configuration 0.0308 [$\text{m}^{\frac{1}{2}}$]
\mathcal{C}_{Av}	Avogadro constant $\approx 6.0221 \times 10^{23}$ [mol^{-1}]
\mathcal{D}	Diffusion coefficient [m^2/s]
\mathcal{F}	JPDF of eddy position and size [m^{-2}]
\mathcal{G}	Approximated JPDF of eddy position and size [m^{-2}]
\mathcal{H}_{cf}	Convective heat transfer coefficient [$\text{W}/(\text{m}^2 \cdot \text{K})$]
\mathcal{P}	(Energy) Production term [W/m^3]
\mathcal{R}	Bulk mapping and transport effects of the stochastic eddy events on a momentum component due to v_ψ , or the bulk effect of the turbulent transport on the TKE due to stochastic eddies. Also used for the bulk mapping and transport effects of the stochastic eddy events on the heat flux due to v_ψ . Momentum: [m^2/s^2]; TKE or enthalpy: [$(\text{W} \cdot \text{m})/\text{kg}$]
\mathcal{S}	Stochastic pressure scrambling effects on a momentum component by ODT eddy events (momentum source), or pressure transport contribution to the TKE due to eddy events. Momentum: [m/s^2] (constant density incompressible) or [N/m^3] (variable density); constant density TKE: [W/kg]; variable density TKE or enthalpy: [W/m^3]
\mathcal{T}	Stochastic turbulent transport effects on a momentum component by ODT eddy events, or turbulent transport contribution to the TKE due to eddy events. Also used for the turbulent transport effects on enthalpy by ODT eddy events. Momentum: [m/s^2] (constant density incompressible) or [N/m^3] (variable density); constant density TKE: [W/kg]; variable density TKE or enthalpy: [W/m^3]
a	Arc length [m]
$A_{TimeFac}$	Nondimensional proportionality factor for the time interval after which a mesh adaption process takes place [–]
B	Depth of the channel or length of the electrode in the wire-plate (channel) ESP in z direction, or length of the electrode (and pipe length) in the axial z direction in a cylindrical ESP [m]
b	ODT kernel coefficient (unless otherwise specified) [s^{-1}] (T-ODT) or [$\text{kg}/(\text{m}^3\text{s})$] (S-ODT)

C	ODT model parameter controlling eddy events frequency	$[-]$
c	ODT kernel coefficient (unless otherwise specified) (T-ODT) or $[\text{kg}/(\text{m}^3\text{s})]$ (S-ODT)	$[\text{s}^{-1}]$
c_0	Speed of light in a vacuum inertial system	$299,792,458 [\text{m}/\text{s}]$
c_p	Specific heat capacity at constant pressure	$[\text{J}/(\text{kg} \cdot \text{K})]$
c_v	Specific heat capacity at constant volume	$[\text{J}/(\text{kg} \cdot \text{K})]$
D	Pipe diameter	$[\text{m}]$
E	Electric field magnitude	$[\text{V}/\text{m}]$
E_{on}	Onset electric field. Normally given by Peek's formula, Eq. (H.13)	$[\text{V}/\text{m}]$
f	Frequency	$[\text{s}^{-1}]$
g	Gravitational acceleration	$9.8 [\text{m}/\text{s}^2]$
g_{Dens}	Nondimensional grid cell number density (input parameter for adaptive ODT formulation)	$[-]$
H	Width (or height, in ODT notation) of a channel (distance between walls)	$[\text{m}]$
h	Specific enthalpy	$[\text{J}/\text{kg}]$
I	Electric current	$[\text{A}]$
j	Electric current density component	$[\text{A}/\text{m}^2]$
J_{ODT}	ODT kernel function	$[\text{m}]$
k	Incompressible or variable density TKE	$[\text{m}^2/\text{s}^2]$
K_0	Nondimensional ODT kernel identity scaling factor for eddy turnover time or turnover length scale (see Eq. (3.33))	$[-]$
k_B	Boltzmann constant	$\approx 1.38065 \times 10^{-23} [\text{J}/\text{K}]$
K_{ODT}	ODT kernel function	$[\text{m}]$
L	(Generally characteristic) Length	$[\text{m}]$
l	Length scale; in ODT, it refers to the eddy length	$[\text{m}]$
$l_{\mathcal{F}}$	Most probable eddy length scale	$[\text{m}]$
M	Stochastic mapping effects on a momentum component by v_ψ or on the TKE due to turbulent transport. Also used for the mapping effects on enthalpy by ODT eddy events. Momentum: $[\text{m}/\text{s}^2]$ (constant density incompressible) or $[\text{N}/\text{m}^3]$ (variable density); constant density TKE: $[\text{W}/\text{kg}]$; variable density TKE or enthalpy: $[\text{W}/\text{m}^3]$	

m	Mass	[kg]
N	Number density	[m ⁻³]
N_0	Air number density at standard conditions $\approx 2.5 \times 10^{25}$	[m ⁻³]
P	Thermodynamic pressure	[Pa]
p	In Chapters 1-3 until section 3.6.1, as well as appendix A, the generalized pressure is implied. From Chapter 3 section 3.6.1 onwards, unless otherwise noted, only the hydrodynamic pressure is implied	[Pa]
Q	Heat	[J]
q	Electric charge	[C]
q_e	Elementary charge	$\approx 1.602177 \times 10^{-19}$ [C]
q_w	Wall heat flux	[W/m ²]
R	Pipe radius	[m]
r	Cylindrical radial position coordinate	[m]
r_0	Left edge position of an eddy event in a cylindrical coordinate system	[m]
R_u	Universal gas constant	≈ 8314.4626 [J/(K · kmol)]
R_{air}	Specific gas constant for air	≈ 287.058 [J/(kg · K)]
R_{gas}	Specific gas constant	[J/(kg · K)]
S	Surface or area	[m ²]
s	Specific entropy	[J/kg]
T	Temperature	[K]
t	Time	[s]
U	(Generally bulk flow) Velocity	[m/s]
u	(Generally streamwise) Velocity	[m/s]
u_D	Numerically delayed streamwise velocity component in S-ODT internal flow formulation	[m/s]
v	Velocity component aligned in the ODT line direction, either the wall-normal (y) or the radial direction (r)	[m/s]
v_ψ	Deformation velocity of a (purely deforming) ODT Lagrangian volume. Equivalently, this is the irrotational contribution to the (absolute) Eulerian velocity field in ODT	

v_a	Absolute (Eulerian) velocity field in the ODT line direction [m/s]
W	Mechanical work [J]
w	Velocity component for either the spanwise (z) direction in a planar coordinate system or the circumferential or tangential direction in a cylindrical coordinate system (θ) [m/s]
x	Cartesian streamwise position coordinate [m]
y	Cartesian crosswise (vertical) position coordinate [m]
y_0	Eddy event position (left edge of the eddy) [m]
Z	ODT model parameter for energetic viscous penalty [—]
z	Cartesian spanwise position coordinate and cylindrical streamwise (vertical) position coordinate [m]
\forall	Volume [m ³]
\forall	Specific volume [m ³ /kg]

Latin characters (only vectors or matrices)

$\underline{\check{x}}$	Unit position vector [—]
\underline{I}	Identity matrix [—]
\underline{B}	Magnetic flux density [Wb/m ²] = [T]
\underline{D}	Electric displacement vector [C/m ²]
\underline{E}	Electric field vector; $\underline{E} = E_k = [E_1, E_2, E_3]^T$ [V/m]
\underline{F}	Force vector [N]
\underline{g}	Gravitational acceleration vector [m/s ²]
\underline{H}	Magnetic field intensity vector [A/m]
\underline{J}	Electric current density vector; $\underline{J} = j_k = [j_1, j_2, j_3]^T$ [A/m ²]
\underline{n}	Unit surface normal vector [—]
\underline{P}	Polarization density vector [C/m ²]
\underline{q}	Heat flux vector [W/m ²]
\underline{S}	Surface or area vector [m ²]
\underline{V}	Velocity vector field; $\underline{V} = [u, v, w]^T = u_k = [u_1, u_2, u_3]^T$ [m/s]
\underline{V}_a	Absolute (Eulerian) velocity vector field [m/s]

Mathematical operators

:	Double dot (scalar) product
·	Scalar (inner) product
◦	Dyadic (outer) product
Δ	Difference operator. Generally used to indicate discrete cell sizes or discrete time steps
δ	Dirac delta function
$\frac{\langle D \rangle}{\langle D \rangle t}$	Averaged material derivative, $\frac{\langle D \rangle}{\langle D \rangle t} = \frac{\partial}{\partial t} + (\langle \underline{V} \rangle \cdot \nabla)$.
$\frac{D}{Dt}$	Material derivative, $\frac{D}{Dt} = \frac{\partial}{\partial t} + (\underline{V} \cdot \nabla)$.
$\frac{\tilde{D}}{\tilde{D}t}$	Favre-averaged material derivative, $\frac{\tilde{D}}{\tilde{D}t} = \frac{\partial}{\partial t} + (\tilde{\underline{V}} \cdot \nabla)$.
$\hat{\delta}$	Path differential
$\langle \psi \rangle$	Ensemble average of ψ , where ψ can be any type of tensor. The ensemble average operator is defined as, $\langle \psi \rangle = \frac{1}{N} \sum_n \psi \Delta n$, where Δn may refer either to a time or streamwise step, Δt or Δx (or Δz), or to equidistant ensemble members $\Delta n = 1$ respectively, and N to an averaging period in terms of time or streamwise advancement, or a number of ensemble members
$\mathbb{F}\{\}$	Fourier Transform
d	Total differential
∇	Nabla operator
∇^2	Laplace operator
$\bar{\psi}$	Time average (T-ODT) or streamwise spatial average (S-ODT) operator applied to ψ , where ψ can be any type of tensor
∂	Partial differential
ψ''	Favre fluctuation, $\psi'' = \psi - \tilde{\psi}$
ψ'	Ensemble fluctuation, $\psi' = \psi - \langle \psi \rangle$
sgn()	Sign operator
\times	Cross (vector) product
$\hat{\psi}$	(Triplet) Mapped scalar profile of ψ
$\tilde{\psi}$	Favre average of ψ , where ψ can be any type of tensor. The Favre average is defined as $\tilde{\psi} = \frac{\langle \rho \psi \rangle}{\langle \rho \rangle}$, where ρ is the (mass) density

- $f(r)$ Triplet map indicator (cylindrical coordinate r)
 $f(y)$ Triplet map indicator (planar coordinate y)
 $int()$ Integer rounding function

Superscripts

- ψ^* Nondimensional quantity
 ψ^+ Nondimensional quantity scaled in wall units or with inner scaling
 ψ^\dagger Fourier Transform of ψ (spectral representation)
 ψ^n Property evaluated at time-step index n (T-ODT) or streamwise position index n (S-ODT)
 $\underline{\underline{\psi}}^T$ Transpose (matrix or vector)

Subscripts

- ψ_0 Initial, or reference quantity
 ψ_Δ Filtered quantity
 ψ_τ Friction quantity
 ψ_b Bulk quantity
 ψ_c Center related quantity
 ψ_E Electric or electrical related quantity, or charge relaxation scale (if ψ is energy, it implies electrostatic potential energy)
 ψ_g Gravitational related quantity (if used with energy, implies gravitational potential energy)
 ψ_H Hydraulic quantity
 ψ_h Enthalpy or heat flux related quantity
 ψ_i Discrete grid cell i value of ψ
 ψ_k Component index k of vector $\underline{\psi}$
 ψ_M Magnetic related quantity
 ψ_n Species index n of species vector array $\underline{\psi}$
 ψ_p Polarization related quantity
 ψ_S Surface related quantity
 ψ_T Thermal related quantity

ψ_w	Wall related quantity
ψ_{conv}	Convective related quantity
ψ_{cr}	Critical quantity
ψ_{diff}	Diffusion related quantity
ψ_{eddy}	Eddy related quantity
ψ_{elec}	Electrode related quantity.
ψ_{ext}	External related quantity (generally force or force density)
ψ_{int}	Internal related quantity, generally energy (or specific energy)
ψ_{irrot}	Irrotational component of ψ
ψ_{kin}	Kinetic related quantity, generally energy (or specific energy)
ψ_{max}	Maximum of ψ
ψ_{min}	Minimum of ψ
ψ_{ODT}	ODT related quantity
ψ_{pot}	Potential related quantity, generally energy (e.g., gravitational, electrostatic)
ψ_{RMS}	RMS value, $\psi_{RMS} = \sqrt{\widetilde{\psi^2} - \widetilde{\psi}^2}$
ψ_{samp}	Sampling related quantity
ψ_{sol}	Solenoidal component of ψ
ψ_{str}	Streamwise related quantity
ψ_{tot}	Total quantity
ψ_{vert}	Vertical related quantity (the vertical direction is taken as the direction in which the gravity acts)
ψ_{vp}	Viscous penalty quantity (refer to $\Xi_{vp,eddy}$; units dependent on the ODT formulation, see appendix C)

Part I

INTRODUCTION AND THEORY

INTRODUCTION

Ever since the publication of the celebrated *Hydrodynamica* by Daniel Bernoulli in 1738 [1], the phenomenon of flow inside tubes (or *vessels*, according to the terminology used by Bernoulli) has fascinated researchers across the disciplines of natural sciences. The early ideas of classical (Newtonian) mechanics regarding motion by the act of forces, were used by Bernoulli to describe the outflow from vessels, even accounting for what could be considered today as one of the first rudimentary descriptions of energy conservation, i.e., the loss of mechanical energy from the fluid macromotion to the internal motion of particles and heat [2]. However, the widespread use of the term energy, as it is understood today, only arrived almost a century after the publication of *Hydrodynamica*¹. *Hydrodynamica* also proposes a kinetic model of air as a way to estimate the air pressure on the vessel walls in terms of the collisions between particles and walls. Nowadays, this is regarded as the precursor of the kinetic theory of gases [2].

Despite the visionary treatment of the flow inside vessels made by Bernoulli, macroscopic and microscopic phenomena were generally considered unrelated. This philosophy persisted until the appearance of statistical thermodynamics as a formal branch of science, largely thanks to the derivation by James Clerk Maxwell of the distribution of molecular velocities in 1860 [3]². The description of physical phenomena by statistical principles was a revolution in classical physics. Today, it is still one of the most solid approaches in fluid mechanics for the description of turbulent flows. Maxwell is also celebrated in physics thanks to his treatise on electromagnetism [4]. The unified theory of electricity and magnetism also implied the arrival of the concepts of fields and wave physics.

In retrospective, even 300 years after *Hydrodynamica*, some aspects of our understanding regarding the flow inside vessels, or pipes, remain, at best, confusing. In the middle part of the 19th century, thanks in part to the novel statistical treatment of physics, a new rhetoric of exactitude in the natural sciences took researchers down the path of rigorous theoretical and experimental analysis. For simple pipe flows without the influence of any external force, a monolithic work by Reynolds was published in 1883 [5]. This work could very well be the cause of much of the confusion and issues in turbulent

¹ The general consensus is that the energy conservation principle was understood and recognized in its modern day form after the connection between heat and mechanical work was demonstrated by the ideas and experiments of both James Prescott Joule and Julius Robert von Mayer

² Maxwell-Boltzmann distribution

flow research that still persist nowadays. Reynolds showed a critical value above which steady motion was superseded by the appearance of eddies in laboratory pipe flows. With most of the mathematical framework of viscous flow already developed thanks to the birth of the theory of elasticity by Claude-Louis Navier back in 1821 [6], Reynolds already considers both the theoretical and the experimental methods as the two ways to proceed forward with his investigation. The theoretical method, quoting Reynolds, “was not promising” [5]. Thus, he proceeded to state six fundamental questions, which are now the thesis of the celebrated nondimensional Reynolds number. For bulk flow, the bulk Reynolds number is defined as,

$$Re = \frac{\rho_b U_b L}{\mu_b} \quad (1.1)$$

where ρ_b is the bulk density of the flow, U_b is the bulk velocity, L is the characteristic length scale of the bulk flow and μ_b is the bulk dynamic viscosity. The nondimensionalization of the governing equations for fluid flow is now a much more systematic method than it was at the times of Reynolds. Proven by Joseph Bertrand in 1878 [7], the now called Buckingham π theorem is taught nowadays in most elementary fluid mechanics courses worldwide. For viscous flow in pipes, the bulk Reynolds number is a straightforward result of the theorem for the rate of change of the velocity when evaluating flows governed by the effects of two primary dimensions (length and time)³.

There is a certain charm in the universality of the postulates done by Reynolds, and, in general, of the results that can be obtained with the Buckingham π theorem. The fact that Reynolds was able to qualitatively (and up to some extent quantitatively) describe the pipe flow, not only from his laboratory test, but of any pipe flow⁴ is, at the very least, remarkable. Perhaps this is the reason why engineers have been investigating and naming nondimensional numbers in fluid mechanics for almost two centuries. Nondimensional numbers usually indicate the ratio between two concurrent phenomena. When the flow depends on one nondimensional number only, we can simply set a number, a *critical* value, which indicates the dominant phenomena governing the flow. For the Reynolds number, this is a *critical* value indicating the dominance of either the inertial or the viscous force. Highly viscous flows with very little inertia are laminar flows with highly organized motion. Flows with high inertia, where viscous effects do not play a large role, are turbulent flows with random velocity fluctuations⁵.

*For sure there may
be no greater joy
than having a
nondimensional
number named after
you.*

³ The variables that need to be chosen for the Buckingham π theorem are in this case the flow acceleration, the diameter of the pipe, the velocity and the kinematic viscosity of the flow

⁴ without the influence of external forces, or complicated geometries, or surface roughness

⁵ The current *critical* value for the classification of a pipe flow as fully turbulent is currently $Re_{b,cr} = 2040 \pm 10$ according to Avila et al. [8]

For two or three nondimensional numbers, the *critical* value loses its meaning and we start discussing *regimes* of interest associated with the ranges of the two or three nondimensional numbers, respectively. This can be represented in a regime diagram. Having a distinctive regime of fluid flow with clearly defined boundaries is one of the most useful tools that physicists and engineers have applied in order to develop some intuition and conceptual models for physical phenomena⁶. For more than three nondimensional numbers, however, our limited perception begins to trick us. Our understanding struggles with our *intuition*, given that we can not easily visualize diagrams in more than three dimensions.

1.1 THE STUDY OF ELECTROHYDRODYNAMIC FLOW

It is clear that in most flows of practical relevance there might be more than one nondimensional parameter governing the regimes and dynamics of the flow. The specific interest of this thesis takes us back to the contributions of Maxwell. Long before Maxwell's publication of his treatise on electromagnetism, William Gilbert noticed in the early 1600's that smoke rushed towards electrically charged regions [10]. This is considered to be one of the first experiments on electricity. Gilbert himself coined the latin term *electricus*, which evolved later in the corresponding modern english words *electric* and *electricity*. For Adamiak, the work of Gilbert is also the first experiment in the area of electrostatic precipitation [11] and thus, in Electrohydrodynamics (EHD)⁷. However, in the early 1600's, nobody believed that Gilbert's discoveries would have any real application. Further *curiosities* appeared in 1709, when Hauksbee published a compilation of experiments in which he reported the phenomena of electric wind for the first time⁸ [14].

Biscombe does a very interesting review regarding the events surrounding the discovery of electrokinetics [15]. Although the discovery of electrically induced liquid atomization by Bose in the 1740's is rebutted by Biscombe as being the discovery of electrophoresis, it is, nonetheless, one of the first relevant experiments in EHD. Accord-

⁶ There will be an exhaustive use of the word Model throughout this thesis. Çengel and Cimbala define a mathematical model as an analysis identifying important variables, making reasonable assumptions and approximations, and choosing a suitable increment for the changing variables. This is in contrast to a Partial Differential Equation (PDE), where the increments in the change of the variables are infinitesimal [9]

⁷ Electrohydrodynamics is implied here in the broadest possible sense, i.e., flow motion under the influence of electric fields. Later in this thesis, EHD is only implied as the study of electrically driven mechanical motion of fluids in weakly conducting dielectrics, as opposed to electrokinetics, which would refer to motion in electrolytes and ionic liquids [12]

⁸ Robinson defines the electric wind as the "gas motion induced by repulsion of ions from the vicinity of a high voltage discharge electrode" [13]

ing to Biscombe, the discovery of electrophoresis⁹ was done by the french chemist Nicolas Gautherot [16]. This was six years before the experiments of Ferdinand Friedrich Reuss, the commonly believed discoverer of electro-osmosis and electrophoresis [17]. These events are already very close to the publication of the theory of elasticity by Navier that was already discussed, and only approximately half a century away from the publication of Maxwell's treatise on electromagnetism. With such an intense rate of discoveries, or *new physics*, happening during the 19th century, it is a wonder, as Adamiak puts it, that there is still a very large interest in the topic of electrostatic precipitation [11]. Furthermore, the interest in EHD flows in general seems to be growing at an accelerated rate. A quick online search for the number of publications shows that the number of publications related to the topic of EHD has increased exponentially in the last 20 years, see Figure 1.1a.

This is only due to the fact that, as in the case of the simple pipe flow, after almost 400 years of *De Magnete* [10], there are a number of issues that are yet to be resolved. Of course, in comparison to the simple pipe flow, the number of issues that need some *closure* in EHD flows is significantly larger. However, the fact that there are still a multitude of *open* issues in EHD flows, does not explain the trend seen in Figure 1.1a. After all, the number of *open* issues in 2019 can not be larger than the number of *open* issues in the mid of the 1800's, the dawn of the electromagnetism and fluid mechanics research. In order to understand this trend, we need to take a look at another exponential trend from the last years, i.e., the computational resources. Figure 1.1b shows the increase in the number of floating point operations per second (FLOPS) from symbolic supercomputers in the last 30 years. The exponential increase is also seen in this logarithmic plot. Not only are the barriers for publications today smaller than ever before, but also the amount of available resources for computations is larger than ever. The mandatory comment in this regard is that we have added to the purely theoretical (analytical) and experimental (laboratory) work of the 19th century, a new numerical (computational) component, as well as the implied big data management. Yet again, the question *why are there still so many open issues, not only in EHD flows, but even in simple pipe flow research?* remains elusive. If all of the advantages of today's scientific research are compared to the means available to the researchers in the 19th century, and it is tailored against the discovery of *fundamentally new* scientific principles, as it was once the publication of Maxwell's treaty on electromagnetism, we can not avoid a feeling of dissatisfaction. Thus, a discussion of the State-of-the-Art issues that

⁹ Using Biscombe's definition taken from IUPAC, "electrophoresis involves electrical migration of colloids in liquids", while electro-osmosis is the "electrically driven motion of liquid through a porous solid medium" [15]

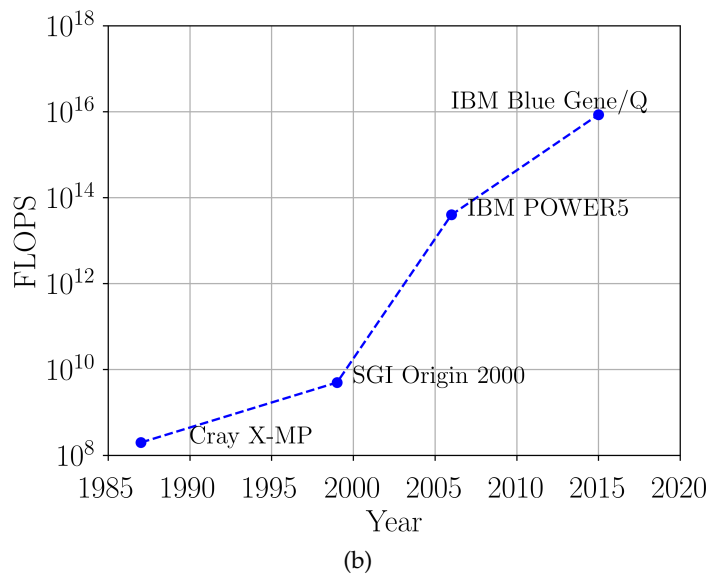
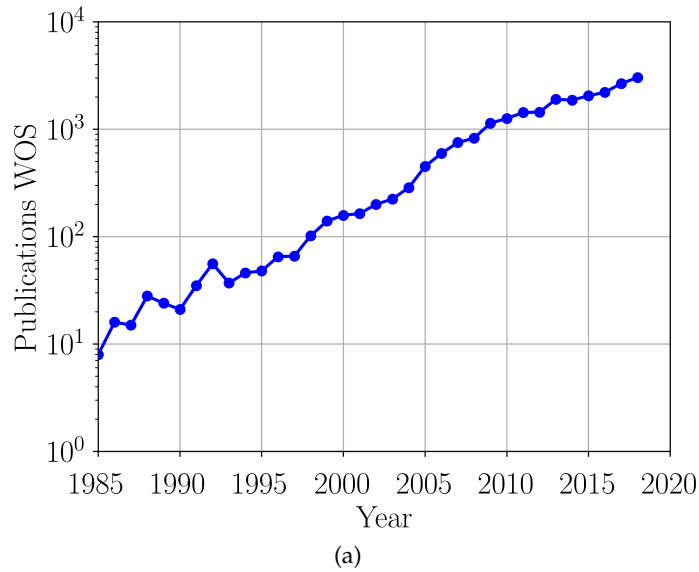


Figure 1.1: (a) Number of publications related to 'electrohydrodynamics' in Web Of Science from 1960-2018 (<https://apps.webofknowledge.com/>). (b) Number of Floating Point Operations per Second (FLOPS) of selected Supercomputers from the years 1985 to 2018. The names of the corresponding Supercomputers are given in the plot.

are faced in turbulent EHD flow research is presented next, in order to partially address this elusive question.

1.2 STATE-OF-THE-ART RESEARCH ON EHD FLOWS

Even nowadays, the solution of the Navier-Stokes equations is one of the famous Millenium Prize Problems of the Clay Institute of Mathematics [18]

Turbulent flow research is a challenge for theoretical and computational analysis due to its highly non-linear nature. Several non-successful attempts were done during the 19th century in order to find analytical solutions to the Navier-Stokes equations. Although many of these attempts were focused on finding solutions in a *heuristic* way, by comparing *educated* guessed functions against the PDEs of fluid motion, by the beginning of the 19th century, Pierre-Simon Laplace had already developed a method to transform PDEs from the temporal-spatial domain into the frequency-wavenumber domain. This was partly inspired on the work done by Joseph Fourier for decomposition of periodic functions into a superposition of harmonic sinusoidal waves. Today, that transformation function carries the name of Laplace. A special case of the bilateral Laplace Transform is the Fourier Transform, which is highly relevant in today's turbulent flow research. In order to illustrate its importance, consider the set of Navier-Stokes equations in the incompressible constant property regime, i.e., whenever ρ is a constant and total energy conservation is trivial. The reader is referred to the appendix A for a detailed derivation of the Navier-Stokes equations. Considering the incompressible constant property regime, the differential Eulerian laws for mass and momentum conservation, based on Eq. (A.6) and (A.11), are,

$$\nabla \cdot \underline{V} = 0. \quad (1.2)$$

$$\rho \frac{\partial \underline{V}}{\partial t} + \rho \nabla \cdot (\underline{V} \circ \underline{V}) = -\nabla p + \nabla \cdot \underline{\tau} + \rho \underline{g} + \rho_f \underline{E}. \quad (1.3)$$

Here, \underline{V} is the velocity vector field, p is the pressure of the Navier-Stokes momentum equation, $\underline{\tau}$ is the shear stress tensor, \underline{g} is the gravitational acceleration vector, \underline{E} is the electric field vector, and ρ_f is the charge density field. Charge density fields and electric fields are, in general, not uniform. If the Fourier Transform is applied to this set of equations, the difficulties regarding the analytical and computational analysis of the Navier-Stokes equations become clear. That is, assume the spectral representation of the velocity, pressure, shear stress, charge density and electric field, $\mathbb{F}\{\underline{V}\} = \underline{V}^\dagger$, $\mathbb{F}\{p\} = p^\dagger$, and $\mathbb{F}\{\underline{\tau}\} = \underline{\tau}^\dagger$, $\mathbb{F}\{\underline{E}\} = \underline{E}^\dagger$, $\mathbb{F}\{\rho_f\} = \rho_f^\dagger$, then,

$$\check{j}\kappa \cdot \underline{V}^\dagger = 0. \quad (1.4)$$

$$\begin{aligned}
\rho \frac{\partial \underline{V}^\dagger}{\partial t} + \check{j} \rho \underline{\kappa} \cdot \left(\iiint_{-\infty}^{\infty} \underline{V}^\dagger(\underline{k}) \underline{V}^{\dagger, T}(\underline{\kappa} - \underline{k}) d\underline{k} \right) \\
= -\check{j} p^\dagger \underline{\kappa} + \check{j} \underline{\kappa} \cdot \underline{\tau}^\dagger + \rho \delta(\underline{\kappa}) \underline{g} + \iiint_{-\infty}^{\infty} \rho_f^\dagger(\underline{k}) \underline{E}^\dagger(\underline{\kappa} - \underline{k}) d\underline{k}.
\end{aligned} \tag{1.5}$$

Here, \check{j} is the imaginary unit and $\delta(\underline{\kappa})$ is the Dirac delta function in the wavenumber domain. The attention is focused on the triple integral terms on both the LHS and RHS of Eq. (1.5). Indeed, despite having eliminated all of the other differential operators, the integral terms involving all wavenumber vectors \underline{k} have appeared. The solution for the velocity field, depends, thus, not only on one wavenumber, but on all of them. In practical terms, there are not infinite wavenumbers, since real problems have finite length and can only be measured down to a given tolerance. Nonetheless, the implications for the theoretical analysis are clear, in the sense that the integral equation is intractable. The so-called non-linearities are evident for both the advective term and the electric body force term. For the computational analysis, if a discretization of the PDE is desired, the spatial resolution should be such, that at least a wavelength equivalent to twice the maximum wavenumber can be represented¹⁰.

1.2.1 Canonical pipe flow as a study case for the understanding of wall-bounded turbulence

This work is focused on the physics of internally forced convective flows. In turbulent flow research, this area of study has the name of wall-bounded turbulence. Although there are still unresolved issues in this topic, much progress has been achieved towards the understanding of the mechanisms for turbulence generation, sustainment and decay since the experiments of Reynolds in 1883. For numerical modeling of turbulent flows, Richardson realized that the upper limit to the size of an eddy was a matter of "human convenience" [19], and that motion smaller than the numerical grid had the necessity to be ignored, yet, represented by additional terms. He also recognized two competing mechanisms for turbulence generation and decay. Turbulence generation in the wind originated near the ground and could be facilitated by instabilities in the atmospheric thermal equilibrium, thus relating it to the diffusion of eddy-heat-per-mass from places where eddies were very likely to occur, to places where eddies were seldom [20]. A large eddy could then transport air containing several smaller eddies. Concurrently, he acknowledged that (large) convectional motions were hindered by the formation of small eddies [19]. This idea of an eddy energy cascade involving different length scales was later

The famous lines by Richardson immortalizing this discovery can be found in his book from 1922: "Big whirls have little whirls that feed on their velocity, and little whirls have lesser whirls and so on to viscosity"

¹⁰ This is the Nyquist-Shannon sampling theorem

formally transformed into the most celebrated theory of turbulence by Andrei Kolmogorov [21].

In the Kolmogorov picture of turbulence¹¹, there is some inertial range of wavenumbers $[\kappa_1, \kappa_2]$ where the spectral energy density of the flow¹² is proportional to $\kappa^{-5/3}$, i.e., there is an inverse power law at some inertial range of wavenumbers [22]. Beyond this range, the decay of the spectral energy density is exponential until the length scale $\eta = 2\pi/\kappa_2$, which corresponds to the Kolmogorov length scale. Any turbulent motion with a length scale $l < \eta$ will be suppressed by the viscosity, which converts the kinetic motion of the very small eddies into heat. The Kolmogorov's hypothesis implies that there is a universal energy range, in which the characteristic length of the dissipative motion scales with η .

For wall-bounded turbulence, the Kolmogorov picture of turbulence opened the door into a heated discussion which is still going on. Unlike in the Kolmogorov isotropic turbulence picture, where the integral length scale is unique and well defined, in wall-bounded turbulence, the wall imposes a variable integral length scale for the largest eddies depending on the wall normal position [23]. Hence, the scale ratio (and thus, wavenumber range) where the spectral energy density acquires the $-5/3$ power law varies depending on the wall-normal position, making the use of a scaling based on η questionable. Nonetheless, geometrically, the energy scales are still defined based on the wall-normal position, given that there is a peak of turbulence production close to the wall, which sustains turbulence away from the wall by a diffusion mechanism. Between the region close to the wall¹³ and the region away from the wall¹⁴, there is an overlapping region at *sufficiently large* turbulence states, where turbulence generation and dissipation are in a quasi-equilibrium condition. Thus, this produces a self-similar flow [23]. Hence, the great wall-bounded turbulence flow discussion is focused on the question of *what should be the characteristic property of the flow in wall-bounded turbulence? a scaling based on viscous units, such as in the Kolmogorov's hypothesis, or some other similarity based on the geometry of the flow, i.e., the bulk flow, large scale structures or eddies?* Marusic et al. [24] give a very detailed overview of the progress and related issues regarding this discussion. A quick review of some of the theoretical aspects regarding these issues will be discussed in the Theory part of this thesis. For the current research overview, it is sufficient to say that the major push in contemporary research is on the achievement of the above mentioned *sufficiently large* turbulence state (sufficiently large Reynolds number), such that the viscous layer of the flow can overlap with the outer layer, and the self-similar picture due to geometry becomes clearer. The nondimensional number associated

¹¹ Isotropic turbulence

¹² This would be roughly equivalent to $(1/2)(\widehat{V} \cdot \widehat{V})$ in an isotropic turbulent flow

¹³ Viscous layer of the flow

¹⁴ Outer or logarithmic layer

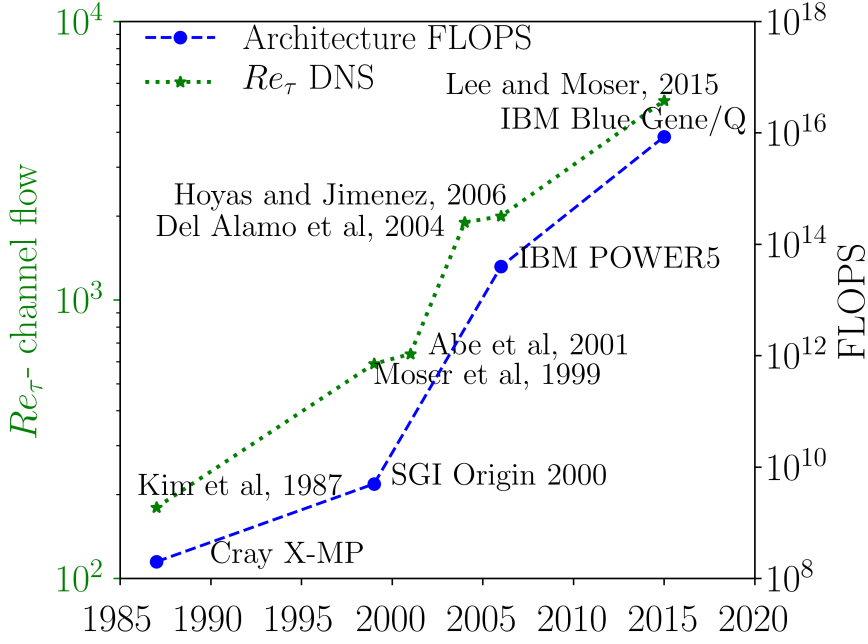


Figure 1.2: Development of FLOPS of selected supercomputers in comparison to achievements in turbulent channel flow simulations

to the magnitude of the turbulence in wall-bounded flows is the friction Reynolds number. It uses a scaling based on viscous units for all near-wall motions, partially maintaining the original idea from the Kolmogorov’s hypothesis [23],

$$Re_{\tau} = \frac{\rho_w u_{\tau} L}{\mu_w}. \tag{1.6}$$

Here, u_{τ} is the friction velocity, and the w subindex refers to the position of the wall. Depending on whether the flow is planar (channel) or cylindrical (pipe), L is equivalent to either half of the channel width or to the pipe radius. u_{τ} is defined in terms of the wall shear stress τ_w ,

$$u_{\tau} = \sqrt{\frac{\tau_w}{\rho_w}}. \tag{1.7}$$

Figure 1.2 shows again the evolution of the FLOPS for selected supercomputers in the last 30 years, this time comparing the corresponding achievements of Direct Numerical Simulations (DNS) for wall-bounded turbulence (channel flows) in terms of friction Reynolds numbers. As a comparison, for flows of interest in very large pipes, the expected friction Reynolds number is in the range of orders of magnitude $10^5 - 10^6$ [25].

1.2.2 *Transition to turbulence and turbulence modification by variable density effects*

So far, the discussion regarding the physics of wall-bounded turbulence has been done considering homogeneous (yet anisotropic) turbulent flows, i.e., incompressible constant property turbulent pipe or channel flows¹⁵. Part of the scope of this thesis considers the evaluation of turbulent flows which do not necessarily adhere to these assumptions. On top of the homogeneous turbulence picture of an incompressible constant property channel flow¹⁶, where the self-similarity due to the overlapping of the viscous and outer layers may take place at all streamwise locations in the channel, one could also account for a streamwise variation of the turbulence statistics. In the case of channel and pipe flows, the inhomogeneity in streamwise statistics is commonly known as the effect of the entrance length.

The entrance length problem is mostly interesting in the field of heat transfer, given that it determines whether the heat transfer coefficients (and therefore, the design of, e.g. the heat exchanger) are dependent or independent of the streamwise position of the internal flow. Meyer and Everts present a detailed and extensive investigation which could be considered the cornerstone of experimental research in heat transfer transitional effects [33–36]. Considering only the Nusselt number, the work of Everts and Meyer is the best evidence that can be shown concerning the distinction between the internal flows with homogeneous turbulence and non-homogeneous turbulence internal flows. For homogeneous flows, it is possible to represent the Nusselt number in terms of other nondimensional numbers (e.g. Grashof and Reynolds number) with relatively simple regression models, achieving high accuracy. For fully developed internal laminar flows with constant properties, the Nusselt number can even be obtained in an analytical way. The work of Gnielinski presents a detailed overview of several correlations used for the calculation of the Nusselt number and the heat transfer coefficient [37]. The latter ideas could be understood as a 1-D turbulence picture, given that the turbulence is only defined in this case by the characteristic Reynolds number of the flow. In the limit of transitional flow, i.e., between the fully laminar and fully turbulent flow, the correlations for the Nusselt number change. The apparent discontinuity in the behavior of the Nusselt number as a function of the Reynolds (or Grashof) number is, as of today, not accurately described by any simple regression model. For a non-homogeneous flow, this transitional limit is also achieved in the

¹⁵ In very simple terms, an homogeneous turbulent flow is one which is invariant along its translation direction, while an isotropic turbulent flow is one where turbulence propagates in the same way in all directions. A fully developed internal flow is an example of an homogeneous turbulent flow

¹⁶ see e.g. Pope for details regarding the boundary layer equations and examples for the mean and RMS velocity profiles in a canonical channel flow [32]

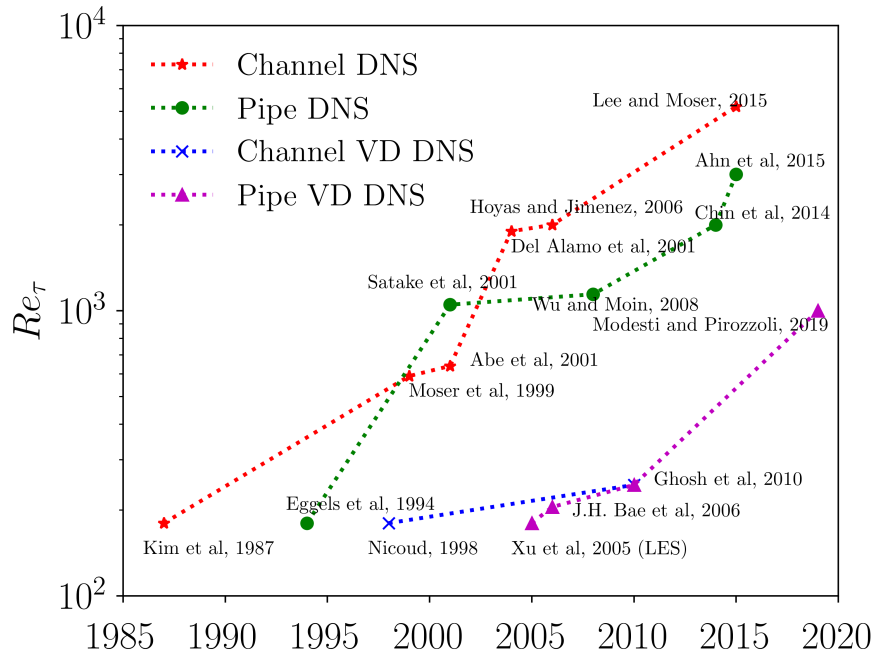


Figure 1.3: Achievements in incompressible constant property pipe and channel flow simulations, as well as in variable properties (variable density, VD in the plot) pipe and channel flow simulations, as in, e.g. compressible flows.

region between fully laminar and turbulent flow. However, this region is no longer an abstract nondimensional number space, but rather, a well defined direction of propagation of the flow. The 1-D turbulence picture may be now considered 2-D (or quasi 2-D, if a quasi-steady flow is assumed, i.e., $\partial \underline{V} / \partial t \approx 0$).

For the representation of the actual flow fields, the use of computational simulations has long superseded the little flexibility of experiments. However, due to the inherent wavenumber coupling of turbulent flows, the gap between computer simulated flows and practically relevant flows remains still significantly large for most applications, as in the pure incompressible constant property flow case. Even worse than in the constant property flow case, trying to account for variable properties in the flow, as one would expect in the study of heat transfer, results in an even larger gap, e.g. between achievements in variable property flows and constant property flows. As an example, Figure 1.3 shows the achievement in incompressible constant property channel and pipe flow simulations with respect to the friction Reynolds numbers, in comparison to variable density channel and pipe flow simulations. Variable properties such as variable density effects may also be responsible for seldom phenomena such as the relaminarization of an initially fully turbulent flow, see e.g. [38].

1.2.3 *Applications of EHD-enhanced turbulent pipe and channel flows*

The discussions regarding the nature of turbulence, transitional regimes and variable properties are also seen in the trends describing the research on EHD-enhanced internally forced convective flows. One could classify these flows into two main categories: one category comprises those flows where EHD literally enhance specific effects, and these are then considered as an optimization in the application performance (EHD is not the dominant phenomenon); a second category comprises those flows where the leading order effects are EHD effects, however, these may be affected by the flow regimes (EHD is the dominant phenomenon).

An example of flows where the EHD effects are not in leading order are the plasma assisted flames. Early experiments in this regard show flame augmentation due to the additional available energy by the electrical discharge of an electrode, as quoted by [48]. Although there may be numerous advantages for plasma assisted flames, in comparison to traditional premixed or diffusion flames, specifically regarding potential soot reduction, the main limitation for further progress in this topic is the elevated power consumption of such an application. Probably a less sophisticated example of flows in this first category is a simple heat exchanger with an incorporated array of electrodes. Experimental work from Ohadi and Nelson et al. [49, 50] show Nusselt number increases larger than 200% for transitional Reynolds number pipe flows. This could be thought of, as the effect of turbulence due to additional available energy by the generated electric field.

Probably the most salient example for this thesis of the first type of flows, is the industrial application of Electrostatic Precipitators (ESPs), or just electrostatic precipitation. In essence, an electrostatic precipitator is a device which is able to precipitate particulate matter in a flue gas (normally air). This is due to the collision-induced charging of the particulate matter with ions in air. The particulate matter is then electrically repelled from the electrode at the center of the precipitator, flying towards the collector walls of the device. One of the first numerical studies in this topic was done by Yamamoto [51]. [51] studied the behavior of the electric wind inside a wire-plate precipitator. [52] examined the characteristics of the turbulence under the influence of weak and strong Electric Body Forces (EBFs). For weak EBFs, the turbulent kinetic energy spectrum still retains features of the Kolmogorov turbulence. An electrokinetic length scale, intermediate between the integral and Kolmogorov length scale appears, marking the boundary between the inertial subrange and the EBF range in the spectrum. The EBF range ends at the dissipation range [52]. For the large EBF regime, the inertial range of the spectral energy density entirely disappears. In simpler terms, the analysis and results from [52] show that, the larger

the EBF is, the larger the importance of the ionic wind will be, until, eventually, what in principle was just a secondary flow, ends up being the primary flow, as well as the reference length and time scale of the flow.

The importance of the large structures in EHD flows certainly seem like a compelling argument for the discussion of *the characteristic property* in wall-bounded turbulence. Soldati and Banerjee performed numerical simulations in order to corroborate the influence of these large scale EHD structures on the Turbulent Kinetic Energy (TKE) budgets (e.g. production and dissipation of turbulence) [53]. The friction Reynolds number for the numerical simulation of Soldati is, not surprisingly, one order of magnitude less than the highest Re_τ achieved for variable property pipe flow. This, of course, points out to the obvious conclusion, which is that solving the Maxwell equations on top of the Navier-Stokes equations is a very expensive task.

Finally, what could be said about the transition to turbulence in EHD flows? Or more fundamentally, is the role of the characteristic nondimensional numbers in EHD flows well understood? A recommended international standard of the Institute of Electrical and Electronics Engineers (IEEE) seems to argue that there is great confusion in the use of nondimensional parameters across research studies [54]. It is, in this context, unimaginable to argue in a similar way to the studies of [33–36] regarding the Nusselt number behavior, according to whatever nondimensional number is the appropriate one for the characterization of EHD flows.

1.3 THE FUNDAMENTAL QUESTION BEHIND THIS THESIS

Can the numerical study of EHD-enhanced internally forced convective flows aid in the titanic task of bringing some light into the understanding of wall-bounded turbulence? or will this just take us further down a rabbit hole of even more sophisticated problems? If it is indeed able to bring some understanding into the topic, which alternatives are possible for the numerical simulation of slightly more realistic flows? Although this thesis will not be able to answer these questions, it is the hope of the author that this work is considered at least a summary of issues, as well as a first stepping stone towards possible solution alternatives for tackling EHD flow problems with numerical simulations.

1.4 THESIS OUTLINE

The One-Dimensional Turbulence (ODT) model will be used in this thesis to simulate EHD flows. In the next chapter of this part of the thesis, a quick review of the fundamentals of the continuum electromechanic equations will be given, i.e., an overview of the Maxwell

equations together with their coupling to the Navier-Stokes equations. Chapter 3 discusses the most important concepts required for the understanding of the One-Dimensional Turbulence model.

The Part II of this thesis is dedicated to the validation of the ODT model for non-EHD flows. The validation consists in the evaluation of the results of the model against published numerical simulation results of incompressible constant property pipe and channel flows (Chapter 4), as well as of variable density pipe flows (Chapter 5). The latter is done for the study of the relation between turbulence and heat transfer, which will be required later in the thesis.

Having a validated model is the necessary condition for the Part III of the thesis, which discusses the results of its application into a variety of EHD flows. All of the evaluated EHD flows correspond to the category of flows which can be found in ESP. First, the numerical simulation of an incompressible constant property flow inside a wire-plate electrostatic precipitator is presented (Chapter 6), followed by the results of several numerical simulations for the flows inside a wire-tube (or cylindrical) electrostatic precipitator (Chapter 7). The conclusions, recommendations, as well as an outlook for future work will be presented in Chapter 8, at the end of Part III of the thesis.

GOVERNING EQUATIONS FOR ELECTROHYDRODYNAMIC FLOW

The electrohydrodynamic phenomena are governed by the simultaneous postulates of the Maxwell and Navier-Stokes equations. A detailed presentation of the Navier-Stokes equations in Eulerian and Lagrangian representation is given in appendix A. The relevant Maxwell equations and issues regarding electrohydrodynamic flow are discussed now in this chapter. The entirety of the nomenclature used in this chapter and in subsequent chapters is described at the first time or moment of introduction of the relevant quantity, index or mathematical operator. Subsequent redundant nomenclature explanations are, thus, omitted. Nonetheless, the nomenclature is listed in a comprehensive way at the beginning of this thesis, in the Nomenclature section.

2.1 THE ELECTROQUASISTATIC LIMIT OF THE MAXWELL EQUATIONS

Probably one of Maxwell's greatest discoveries was that electricity and magnetism were just 2 manifestations of the same phenomenon. Both the electric field \underline{E} and the magnetic field intensity \underline{H} can be written in the form of the wave equation,

$$\left(\frac{\partial^2}{\partial t^2} - c_0^2 \nabla^2 \right) \underline{\Psi} = 0. \quad (2.1)$$

Here, $\underline{\Psi}$ is either \underline{E} or \underline{H} and c_0 is the speed of light in vacuum. In fact, the speed of light can be written as,

$$c_0 = \frac{1}{\sqrt{\epsilon_0 \mu_{M,0}}}. \quad (2.2)$$

ϵ_0 is the electrical permittivity of the vacuum and $\mu_{M,0}$ is the magnetic permeability of the vacuum .

Eq. (2.1) is obtained for time-dependent and dynamic electric and magnetic fields, under the assumptions of a vacuum, i.e., charge-free space. The absence of electric currents is also assumed [55]. ϵ_0 and $\mu_{M,0}$ are also assumed as constants. c_0 can, in turn, be associated to a characteristic wavelength l , and a characteristic electromagnetic wave transit time t_{EM} ,

$$c_0 = \frac{l}{t_{EM}}. \quad (2.3)$$

Alternatively to the wave philosophy, it is also possible to arrive at the definition of the electromagnetic transit time t_{EM} in a particle philosophy. This is done by means of the evaluation of the characteristic charge relaxation time scale t_E , and the characteristic magnetic diffusion time scale t_M , as in [56],

$$t_{EM} = \sqrt{t_E t_M}. \quad (2.4)$$

In order to derive appropriate scaling arguments for t_E and t_M , a reasoning based on the movement of charges, or on the presence of electric currents is required. An overview of the different types of electric currents is shown next. This thesis is focused on the phenomena associated to phenomena governed by dynamical time scales $t \gg t_{EM}$. In general, for any non-relativistic application, $t_{EM}/t \ll 1$. Melcher performs the asymptotic expansion of the complete Maxwell equations in terms of t_{EM}/t [56]. The electroquasistatic (EQS) limit of the Maxwell equations can be derived for the case where $t_E > t_{EM} > t_M$.

2.1.1.1 Types of electric currents in the EQS limit

According to [56] and [55], electric currents can be classified into the following categories.

2.1.1.1.1 True currents

These are associated to the physical transport of true (free) charges. A true or free charge is not bound to the atoms or molecules of matter. Therefore it can also be referenced as an unpaired charge [57].

1. **Conduction currents:** Free, unpaired charges can travel over relatively large distances (with respect to interatomic or intermolecular distances) under the influence of electric fields. The particle density fields are determined by such electric fields.
 - **Drift or unipolar conduction currents:** For unipolar conduction, the associated electric current density exists only in the presence of a net (free, unpaired) charge density ρ_f . For a given mobility of charges within a specific medium of propagation β , the drift current density, or unipolar conduction current density, is defined as in [57],

$$\underline{J}_{drift} = \rho_f \beta \underline{E}. \quad (2.5)$$

- **Ohmic conduction currents:** For many materials, the degree with which they can resist or facilitate this transport of charges is an inherent material property, i.e., the electrical conductivity σ [57]. The electric current density associated to a given external electric field follows in this case the Ohmic conduction model, or Ohm's law [57],

$$\underline{J}_{Ohm} = \sigma \underline{E}. \quad (2.6)$$

2. **Diffusion currents:** An analogous mechanism for molecular transport of charge is given by the transport due to non-uniform concentration of charges or charged particles, or, conversely, due to charge density gradients. The transport of charge is in this case, in contrast to conduction currents, not caused by external electric fields. If \mathcal{D} is the diffusion coefficient for the charges or charged particles, the electric current density is then given by [56] as,

$$\underline{J}_{diff} = -\mathcal{D}\nabla\rho_f. \quad (2.7)$$

Interestingly, the Einstein relation provides a way to relate drift and diffusion currents by means of the mobility and diffusion coefficient of electric charges,

$$\mathcal{D} = \frac{\beta k_B T}{q}. \quad (2.8)$$

Here, T is the temperature, q is the elementary charge and k_B is the Boltzmann constant.

2.1.1.2 Polarization currents

Unlike free charges, paired charges are bound to atoms or molecules of matter. The polarization charge density ρ_p is related to the density of electric dipoles in a medium [57]. Polarization current densities arise from the temporal rate of change of the polarization density vector \underline{P} [55],

$$\underline{J}_p = \frac{\partial \underline{P}}{\partial t}. \quad (2.9)$$

2.1.1.3 Convective currents

Additional currents can arise from convective effects, or due to the direct transport of charges by the motion of the material medium [55]. These convective currents appear naturally as a consequence of the charge flux relative to the mass-averaged velocity of the flow \underline{V} . The electric current density vector associated to a convective current is in this case,

$$\underline{J}_{conv} = \rho_f \underline{V}. \quad (2.10)$$

2.1.1.4 Electric current density vector notation in this thesis

This thesis is focused on the effects of drift currents, or unipolar conduction currents. Since fluid motion is also of interest, convective currents must also be evaluated. However, the convective current \underline{J}_{conv} is, notation-wise, not included in the electric current density vector notation used in this thesis, \underline{J} . Instead, \underline{J}_{conv} will be written directly

as a charge flux in the corresponding governing equations. Thus, notation-wise, for the scope of this thesis,

$$\underline{J} = \underline{J}_{drift} = \rho_f \beta \underline{E}. \quad (2.11)$$

2.1.2 Gauss's law

In its integral form, Gauss's law states that the flux by electric displacement of free charges through a given closed surface S is equal to the free charge q_f enclosed in the volume \mathbb{V} defined by S ,

$$\oint_S \underline{D} \cdot \underline{n} dS = \int_{\mathbb{V}} \rho_f d\mathbb{V}. \quad (2.12)$$

Here, \underline{D} is the electric displacement vector. The integral on the RHS of Eq. (2.12) is identically equal to the free charge q_f in the volume \mathbb{V} . The differential form of Gauss's law is obtained by applying the divergence theorem to Eq. (2.12) and subsequently differentiating it in terms of the volume,

$$\nabla \cdot \underline{D} = \rho_f. \quad (2.13)$$

2.1.3 Faraday's law

Faraday's law predicts how a time-varying magnetic field affects an electric field. Due to the circulation of electric field lines in a conductive loop Γ , there is a time-varying magnetic flux \underline{B} through the surface S enclosed by the conducting loop, i.e.,

$$\oint_{\Gamma} \underline{E} \cdot \check{\underline{r}} d\Gamma = - \int_S \frac{\partial \underline{B}}{\partial t} \cdot \underline{n} dS. \quad (2.14)$$

In order to obtain the differential form of Faraday's law, the LHS of Eq. (2.14) is transformed according to the Stokes' theorem and both LHS and RHS are differentiated in terms of surface elements,

$$\nabla \times \underline{E} = - \frac{\partial \underline{B}}{\partial t}. \quad (2.15)$$

Neglecting the magnetic effects, according to the assumptions in the EQS limit [56] results in,

$$\nabla \times \underline{E} = 0. \quad (2.16)$$

Given that the electric field is irrotational, it is possible to express it by means of a scalar potential. Indeed,

$$\underline{E} = -\nabla \phi, \quad (2.17)$$

where ϕ is the electrostatic potential.

2.1.4 Charge conservation

Analogous to the conservation of mass in appendix A, there is also a corresponding law for conservation of charge. Since this thesis is only focused on unipolar conduction currents, details regarding polarization currents and polarization charge densities are omitted. These details can be found in [55, 57]. In the absence of polarization effects, and due to the unipolar conduction, all the charge is associated to unpaired or free charges. Therefore, there is a simple linear relation between the electric displacement vector and the electric field, such that the electric field directly satisfies Gauss's law [55, 57],

$$\underline{D} = \epsilon_0 \underline{E}. \quad (2.18)$$

2.1.4.1 Lagrangian representation

Following appendix A, for $\Psi = q$, the postulate for charge conservation is,

$$\frac{dq}{dt} = I. \quad (2.19)$$

Here, I is the electric current, and q refers to the free charge, which is the focus of this thesis. Therefore, the integral law for a finite size system is

$$\frac{d}{dt} \int_{\mathbf{V}(t)} \rho_f d\mathbf{V} = - \oint_{S(t)} \underline{J} \cdot \underline{n} dS. \quad (2.20)$$

Here, $J = I/S$ and points, per convention, from the surface to the interior of the control volume, implying an influx of charge, or, conversely, the accumulation of charge. The vector $\underline{S} = S\underline{n}$ points outside of the control volume, hence the minus sign on the RHS of the equation, such that Eq. (2.19) holds in an absolute sense. Note that there may not necessarily be just one type of free charge. In fact, for the type of flows inside ESPs, it is very common to find, e.g., ions in air and charged dust particles. Thus, for more than one type of free charge,

$$\frac{d}{dt} \int_{\mathbf{V}(t)} \sum_n \rho_{f,n} d\mathbf{V} = - \oint_{S(t)} \underline{J} \cdot \underline{n} dS,$$

where n is in this case an index for the different types of free charges. Specifically, for the n -th *charge species*¹, after using the divergence theorem for the surface integral of the current density, the corresponding statement of charge conservation is, as in [56],

$$\frac{d}{dt} \int_{\mathbf{V}(t)} \rho_{f,n} d\mathbf{V} = \int_{\mathbf{V}(t)} \left(\dot{\omega}_{f,n} - \nabla \cdot \underline{J}_n \right) d\mathbf{V}. \quad (2.21)$$

¹ The term *charge species* is used here in analogy to the term of *chemical species* found in turbulent reactive flows

$\dot{\omega}_{f,n} = q_e dN_{f,n}/dt$ is the n -th charge species source term (rate of generation minus rate of recombination of the species), given by the product of the rate of change of the number density $N_{f,n}$ ² and the elementary charge q_e . $\dot{\omega}_{f,n}$ must satisfy,

$$\sum_n \dot{\omega}_{f,n} = 0. \quad (2.22)$$

Likewise, \underline{J}_n is the n -th current density, such that,

$$\sum_n \underline{J}_n = \underline{J}. \quad (2.23)$$

2.1.4.2 Eulerian representation

In order to obtain the differential Eulerian representation, the Reynolds Transport Theorem, Eq. (A.1), is used to transform Eq. (2.20). The surface integrals are replaced by their volume counterpart by means of the divergence theorem,

$$\int_{\mathcal{V}} \left[\frac{\partial \rho_f}{\partial t} + \nabla \cdot (\rho_f \underline{V} + \underline{J}) \right] d\mathcal{V} = 0. \quad (2.24)$$

Here, again, \underline{J} represents, physically, the surface density of any type of electric current in the system. Eq. (2.24) is the same equation for charge conservation obtained by Melcher for the reference frame measuring \underline{V} as the mass-averaged velocity [56]. For a system with an arbitrary number of types of free charges, the equivalent version of Eq. (2.24) is,

$$\int_{\mathcal{V}} \left[\frac{\partial \rho_{f,n}}{\partial t} + \nabla \cdot (\rho_{f,n} \underline{V} + \underline{J}_n) \right] d\mathcal{V} = \int_{\mathcal{V}(t)} \dot{\omega}_{f,n} d\mathcal{V}. \quad (2.25)$$

The differential Eulerian representation for charge conservation is obtained by differentiating Eq. (2.24) or (2.25) with respect to the volume,

$$\frac{\partial \rho_f}{\partial t} + \nabla \cdot (\rho_f \underline{V} + \underline{J}) = 0. \quad (2.26)$$

$$\frac{\partial \rho_{f,n}}{\partial t} + \nabla \cdot (\rho_{f,n} \underline{V} + \underline{J}_n) = \dot{\omega}_{f,n}. \quad (2.27)$$

The scope of this thesis is limited to the use of one single charge species, namely, ions in air. Nonetheless, a brief discussion concerning the effects of the presence of several types of charge species will be presented later.

² $dN_{f,n}/dt$ can be calculated, e.g., by means of the population balance equations, as in [58]

2.2 ELECTROQUASISTATIC FORCE, WORK AND ENERGY

2.2.1 Lorentz and Coulomb force

As commented by [56], it is now widely accepted that the fundamental force in electromagnetic phenomena is that one associated to a test charge. The Lorentz force acting on a charge particle in the vacuum is,

$$\underline{F}_{Lorentz} = q\underline{E} + q\underline{V}_f \times \underline{B}. \quad (2.28)$$

For a distribution of charges and in the EQS limit, Eq. (2.28) is written as,

$$\frac{d\underline{F}_E}{d\underline{V}} = \rho_f \underline{E}. \quad (2.29)$$

The latter is the general expression for the Coulomb force. Note that Eq. (2.29) can be rewritten by means of Eq. (2.13) as in [55],

$$\frac{d\underline{F}_E}{d\underline{V}} = (\nabla \cdot \underline{D}) \underline{E}. \quad (2.30)$$

This could be considered a generalized Coulomb force without the direct reference to the electric charge density field. For dielectrics or propagation media with inhomogeneous permittivity and polarization effects, the resulting force from Eq. (2.30) may not be as simple as Eq. (2.29), although both expressions would imply the same [55]. Given that polarization effects are neglected in this thesis, the appropriate version of the Coulomb force to consider for the scope of this thesis is that given by Eq. (2.29).

2.2.2 Electroquasistatic energy balance

In the presence of some external electric field, there is a work associated to the transport of charges, from one position to another, along a path Γ . Using the definition of the Coulomb force from Eq. (2.30),

$$W = - \int_{\Gamma} \underline{F}_E \cdot \delta\underline{\Gamma} = - \int_{\underline{V}} \int_{\Gamma} [(\nabla \cdot \underline{D}) \underline{E}] \cdot \delta\underline{\Gamma} d\underline{V}.$$

The minus sign is used here for the work as a consequence of the definition of work having the opposite sign to the change in the electrostatic potential energy. The electrostatic energy is recognized as a potential energy due to the fact that the Coulomb force can be expressed in terms of a scalar potential Eq. (2.17). An additional consequence of the irrotationality of the electric field is that it is possible to rewrite then the latter equation as,

$$W = \int_{\underline{V}} (\nabla \cdot \underline{D}) \phi d\underline{V}.$$

This work term is then treated as an electrostatic potential energy term Ξ_E . For a given charge increment, or an increment in the electric displacement, the increment in electrostatic potential energy is,

$$\Delta\Xi_{E,\mathcal{V}} = \int_{\mathcal{V}} (\nabla \cdot \Delta\underline{D}) \phi d\mathcal{V} = \int_{\mathcal{V}} \phi \Delta\rho_f d\mathcal{V}. \quad (2.31)$$

The latter expression on the RHS is obtained after substituting Eq. (2.13). Note that this expression considers only the field of charge within \mathcal{V} (excludes the boundaries). There may be, however, also some surface charge along the border of \mathcal{V} . For such case, the change in electrostatic potential energy would be given by,

$$\Delta\Xi_E = \int_{\mathcal{V}} \Delta\rho_f \phi d\mathcal{V} + \sum \phi_S \Delta q_S,$$

where q_S and ϕ_S are the charge and electrostatic potential at the surface (or surfaces) of the control volume. Replacing the second term on the RHS by an equivalent surface integral, i.e., Eq. (2.12), and using Eq. (2.18) while neglecting polarization effects, and finally applying the divergence theorem for that surface integral results in,

$$\Delta\Xi_E = \int_{\mathcal{V}} \Delta\rho_f \phi d\mathcal{V} - \int_{\mathcal{V}} \nabla \cdot (\epsilon_0 \phi \Delta\underline{E}) d\mathcal{V}.$$

The minus sign on the second term on the RHS results from the orientation of the normal surface vector of the boundaries, which points towards \mathcal{V} . Using a vector identity similar to the chain rule for derivatives, and Eq. (2.17), (2.18) and (2.13) results in,

$$\Delta\Xi_E = \int_{\mathcal{V}} \epsilon_0 \underline{E} \cdot \Delta\underline{E} d\mathcal{V}. \quad (2.32)$$

The energy balance in the electroquasistatic limit can be obtained based on the intuitive concept of electrical power as the multiplication of voltage and current, as in [56]. Consider the multiplication of the charge conservation equation, Eq. (2.26) with the electrostatic potential,

$$\phi \frac{\partial \rho_f}{\partial t} + \phi \nabla \cdot (\rho_f \underline{V} + \underline{J}) = 0.$$

The latter equation can be rewritten after using Eq. (2.13), (2.18) and (2.17), while neglecting polarization effects, and after applying a convenient vector calculus identity,

$$\epsilon_0 \phi \frac{\partial (\nabla \cdot \underline{E})}{\partial t} + \nabla \cdot [\phi (\rho_f \underline{V} + \underline{J})] + (\rho_f \underline{V} + \underline{J}) \cdot \underline{E} = 0.$$

Interchanging the divergence and the time derivative on the LHS of this equation, and applying again the convenient vector calculus identity results in,

$$\nabla \cdot \left(\epsilon_0 \phi \frac{\partial \underline{E}}{\partial t} \right) + \nabla \cdot [\phi (\rho_f \underline{V} + \underline{J})] + \epsilon_0 \frac{\partial \underline{E}}{\partial t} \cdot \underline{E} + (\rho_f \underline{V} + \underline{J}) \cdot \underline{E} = 0. \quad (2.33)$$

It is now possible to define the electrostatic power flux Φ_E , the electrostatic potential energy density $d\Xi_E/dV = \rho \tilde{\zeta}_E$, and the electrostatic energy dissipation density ϵ_E , as in [56],

- **Electrostatic power flux:**

$$\Phi_E = \phi \left(\epsilon_0 \frac{\partial \underline{E}}{\partial t} + \rho_f \underline{V} + \underline{J} \right). \quad (2.34)$$

- **Electrostatic potential energy density:** Similar to Eq. (2.32), the rate of change of the electrostatic potential energy density is,

$$\frac{\partial (\rho \tilde{\zeta}_E)}{\partial t} = \epsilon_0 \frac{\partial \underline{E}}{\partial t} \cdot \underline{E}. \quad (2.35)$$

Rearranging this expression by means of a convenient vector calculus identity, it is possible to write the electrostatic potential energy density as,

$$\rho \tilde{\zeta}_E = \frac{1}{2} \epsilon_0 |\underline{E}|^2. \quad (2.36)$$

- **Electrostatic energy dissipation density:**

$$\epsilon_{E,Eulerian} = -(\rho_f \underline{V} + \underline{J}) \cdot \underline{E}. \quad (2.37)$$

As it is usual in fluid mechanics, the energy dissipation density is associated to an entropy change as detailed in appendix A,

$$\epsilon_E = -\frac{d}{dV} \left(\frac{\delta Q}{dt} \right) \Big|_E = -\rho T \frac{ds}{dt} \Big|_E. \quad (2.38)$$

This electrostatic energy dissipation term is the commonly known Joule heating effect.

2.3 EULERIAN AND LAGRANGIAN EQS TREATMENT

Maxwell's treatise on electromagnetism implied the beginning of the description of physical phenomena by fields and distributions. In this sense, it is a bit odd to talk about electric fields within a Lagrangian description. Formally, calculations of electric fields need to take place within an Eulerian framework. This formalism will be partially ignored in the notation of this thesis during the discussion of the coupling between the Maxwell and Navier-Stokes equations. In such cases, the expression of the electroquasistatic force that is used is simply

$\underline{E}_E = q\underline{E}$ as in the limit of Eq. (2.28), instead of the electrostatic force given directly by Coulomb's law, i.e.,

$$\underline{E}_E = \frac{q_1 q_2}{(4\pi\epsilon_0) |\underline{r}_{21}|^2} \check{\underline{r}}_{21}. \quad (2.39)$$

Here, $q_1 = q$ and q_2 is another charge producing the electric field line, which starts at a charge q_1 and ends at another charge q_2 . \underline{r}_{21} is the position vector pointing in the direction of q_2 centered in q_1 , where $|\underline{r}_{21}|$ and $\check{\underline{r}}_{21}$ are the magnitude and unit direction of the vector, respectively. This notation and calculation dilemma will be encountered several times in the next chapter of the thesis due to the Lagrangian treatment of the turbulence model used here. In order to bridge the Eulerian and Lagrangian frameworks, an extensive use of the material derivative will be applied. Although electric field calculations will only take place within an Eulerian framework, the calculated electric field can be used in a Lagrangian framework as well. This is due to the Galilean invariance of the quasistatic formulations of electromagnetism [56], i.e., the electric field is the same in any³ reference frame.

In order to obtain another important identity relating the Eulerian and Lagrangian treatment in relevant EQS quantities used in this thesis, a discussion regarding the calculation of the rate of change of the electrostatic potential energy density follows. Indeed, there is an alternative way to calculate the rate of change of the electrostatic potential energy density. Consider the power given by the rate of change of the electrostatic potential energy,

$$\frac{\delta \Xi_E}{dt} = \underline{E}_E \cdot \underline{V}_q = q\underline{E} \cdot \underline{V}_q.$$

If $q = \rho_f \mathcal{V}$ and $\underline{V}_q = \underline{V}_f$, i.e., the velocity of the free charge continuum, then,

$$\frac{d\Xi_E}{dt} = \int_{\mathcal{V}} \rho_f \underline{E} \cdot \underline{V}_f d\mathcal{V}.$$

Thus, differentiating with respect to the volume,

$$\frac{d}{d\mathcal{V}} \left(\frac{d\Xi_E}{dt} \right) = \rho_f \underline{E} \cdot \underline{V}_f.$$

In a fixed mass system (Lagrangian system) moving with an averaged-mass velocity \underline{V} , this expression is rewritten as,

$$\rho \frac{d\check{\xi}_E}{dt} = \rho \frac{D\check{\xi}_E}{Dt} = \rho_f \underline{E} \cdot \underline{V}_f. \quad (2.40)$$

Thus, it is immediately clear that Eq. (2.40) is the Lagrangian counterpart of Eq. (2.35). This proposition is easily verifiable by considering

³ Any non-relativistic

the EQS limit of Ampere's law, as derived by Melcher. In the (fixed) Eulerian reference frame, as in [56],

$$\nabla \times \underline{H} = \underline{J} + \rho_f \underline{V} + \epsilon_0 \frac{\partial \underline{E}}{\partial t} + \frac{\partial \underline{P}}{\partial t} + \nabla \times (\underline{P} \times \underline{V}). \quad (2.41)$$

Here, \underline{H} is the magnetic field intensity vector measured at a fixed reference frame. Neglecting polarization effects and in the limit where magnetic effects are also negligible⁴, $\underline{H} \rightarrow \underline{0}$,

$$\epsilon_0 \frac{\partial \underline{E}}{\partial t} = -(\underline{J} + \rho_f \underline{V}).$$

Performing an scalar product with the electric field on both sides of the equation results in,

$$\epsilon_0 \frac{\partial \underline{E}}{\partial t} \cdot \underline{E} = -\underline{J} \cdot \underline{E} - \rho_f \underline{V} \cdot \underline{E}. \quad (2.42)$$

Substituting now \underline{J} by a relative charge flux from a system moving with the velocity of the free charges, i.e., $\underline{J} = \rho_f (\underline{V}_f - \underline{V})$,

$$\frac{\epsilon_0}{2} \frac{\partial |\underline{E}|^2}{\partial t} = -\rho_f \underline{V}_f \cdot \underline{E}.$$

The identity is then demonstrated by considering that \underline{V}_f in the Eulerian reference frame is identically equal to the same velocity but with opposite sign in the Lagrangian reference frame due to the displacement or deformation character of the Lagrangian velocity. Thus,

$$\frac{\epsilon_0}{2} \frac{D |\underline{E}|^2}{Dt} = \rho \frac{D \xi_E}{Dt} = \rho_f \underline{E} \cdot \underline{V}_f, \quad \underline{V}_{Lagrangian} = \underline{V}_f, \quad (2.43)$$

If the velocity of the Lagrangian system is just \underline{V} and not \underline{V}_f , then, it is possible to recognize that Eq. (2.42) is the same Eq. (2.33) without flux terms. This means that Eq. (2.42) is the Lagrangian power flow balance, and as such,

$$\frac{\epsilon_0}{2} \frac{\partial |\underline{E}|^2}{\partial t} \rightarrow \rho \frac{D \xi_E}{Dt} = -\underline{J} \cdot \underline{E} - \rho_f \underline{V} \cdot \underline{E}. \quad (2.44)$$

It is also possible to recognize directly from Eq. (2.44), that the electrostatic energy dissipation rate is also, in the Lagrangian framework,

$$\epsilon_{E,Lagrangian} = -\underline{J} \cdot \underline{E} - \rho_f \underline{V} \cdot \underline{E} = \epsilon_{E,Eulerian}. \quad (2.45)$$

⁴ Even in the EQS limit of the Maxwell equations, the magnetic field intensity vector is necessary for a fully consistent set of equations. It allows the consistency between the charge continuity equation, Faraday's and Gauss's law

2.4 HYDRODYNAMIC EQUATIONS (NAVIER-STOKES)

As commented at the beginning of the chapter, a detailed derivation of the Navier-Stokes equations is given in appendix A. In this section, the discussion is focused on the set of constitutive relations coupling the mass, momentum and energy conservation statements.

2.4.1 *Newton's generalized law of viscosity*

The molecular transport of momentum in Newtonian fluids can be described by the velocity gradient. This is a representation of the momentum transport between layers of fluid by means of molecular collisions. How fast the momentum can be transported between layers of fluid, depends on the viscosity⁵ of the fluid. This thesis is limited to the study of ideal gases. In such cases, the generalized statement for the relation between shear stress⁶ and velocity gradients is taken from Bird et al. [59] as,

$$\underline{\underline{\tau}} = \mu \left[\nabla \circ \underline{V} + (\nabla \circ \underline{V})^T \right] - \frac{2}{3} \mu (\nabla \cdot \underline{V}) \underline{I}. \quad (2.46)$$

2.4.2 *Fourier's law of heat conduction*

The molecular transport of energy can be represented in a very similar way to the molecular transport of momentum. The rate of heat transfer between layers of fluid, i.e., per unit area, can be related to the temperature gradient. The constant of proportionality between the heat flux and the temperature gradient is the thermal conductivity σ_T [59],

$$\underline{q} = \frac{d}{dS} \left(\frac{\delta Q}{dt} \right) = \sigma_T \nabla T \quad (2.47)$$

The corresponding energy generation density rate by heat conduction can be obtained from the previously specified heat flux, by application of the divergence theorem to Eq. (2.47). Using the notation from appendix A,

$$\nabla \cdot \underline{q} = \nabla \cdot (\sigma_T \nabla T) = \frac{d}{dV} \left(\frac{\delta Q}{dt} \right) \Big|_T = \rho T \frac{ds}{dt} \Big|_T. \quad (2.48)$$

2.4.3 *Equation of state*

The connection of the hydrodynamic equations with the actual working fluid is done via the equation of state. For ideal gases with fixed composition, this takes the form,

$$p = \rho R_{gas} T. \quad (2.49)$$

⁵ Dynamic viscosity

⁶ In this case, the force per area required for a given momentum transport

Here, p is the thermodynamic pressure and R_{gas} is the specific gas constant. For air as a working fluid, $R_{air} \approx 287.058 \text{ J}/(\text{kg} \cdot \text{K})$.

2.4.4 Kinetic energy equation

As noted in appendix B, the use of enthalpy as a state function, instead of the total energy, is preferred due to its relation with a measurable thermodynamic parameter, the temperature, see Eq. (B.5). In order to convert the total energy equation derived in appendix A into an enthalpy equation, the definition of the total energy needs to be used, Eq. (B.8). Substituting Eq. (B.8) into, e.g., Eq. (A.17) leads to,

$$\begin{aligned} & \frac{d}{dt} \int_{\mathbb{V}(t)} \rho \left(h - \frac{p}{\rho} + \zeta_{kin} \right) d\mathbb{V} \\ &= \int_{\mathbb{V}(t)} \left[-\epsilon_E + \nabla \cdot \underline{q} - \nabla \cdot (p\underline{V}) + \nabla \cdot (\underline{\tau} \cdot \underline{V}) \right] d\mathbb{V} \quad (2.50) \\ &+ \int_{\mathbb{V}(t)} \left(\rho \underline{g} \cdot \underline{V} + \rho_f \underline{E} \cdot \underline{V} \right) d\mathbb{V}. \end{aligned}$$

Here, the heat generation density rate was substituted based on the molecular heat transfer by conduction, as per Eq. (2.48), and the Joule heating per Eq. (2.38). The appropriate version of the Joule heating effect is given by Eq. (2.45). An expression for the kinetic energy density rate is required based on the LHS of the Eq. (2.50). This is presented next.

2.4.4.1 Lagrangian representation

The point Lagrangian statement for conservation of kinetic energy is obtained by doing a scalar product of Eq. (A.9) with the velocity vector \underline{V} ,

$$\underline{V} \cdot \frac{d(m\underline{V})}{dt} = -(\underline{V} \cdot \nabla p) \mathbb{V} + [\underline{V} \cdot (\nabla \cdot \underline{\tau})] \mathbb{V} + m\underline{V} \cdot \underline{g} + q\underline{V} \cdot \underline{E},$$

For a point system, $\underline{V} = \underline{V}_f$ and therefore, the only possible electrical current existing is a convective current. Applying some convenient vector identities and the specific kinetic energy definition from Eq. (B.9), this can be rewritten as,

$$\begin{aligned} \frac{d(m\zeta_{kin})}{dt} &= [-\nabla \cdot (p\underline{V}) + (p\nabla \cdot \underline{V}) + \nabla \cdot (\underline{\tau} \cdot \underline{V}) - \underline{\tau} : \nabla \circ \underline{V}] \mathbb{V} \\ &+ m\underline{V} \cdot \underline{g} + q\underline{V} \cdot \underline{E}. \end{aligned} \quad (2.51)$$

For the integral representation, substitute $m = \rho \underline{V}$ and $q = \rho_f \underline{V}$ while $\mathcal{V} \rightarrow d\mathcal{V}$, and integrate with respect to the volume,

$$\begin{aligned} & \frac{d}{dt} \int_{\mathcal{V}(t)} \rho \tilde{\zeta}_{kin} d\mathcal{V} \\ &= \int_{\mathcal{V}(t)} [-\nabla \cdot (p \underline{V}) + (p \nabla \cdot \underline{V}) + \nabla \cdot (\underline{\tau} \cdot \underline{V}) - \underline{\tau} : \nabla \circ \underline{V}] d\mathcal{V} \\ &+ \int_{\mathcal{V}(t)} (\rho \underline{V} \cdot \underline{g} + \rho_f \underline{V} \cdot \underline{E}) d\mathcal{V}. \end{aligned} \quad (2.52)$$

2.4.4.2 Eulerian representation

In order to find the differential Eulerian representation for the conservation of kinetic energy, it is sufficient to substitute $m = \rho \underline{V}$ and $q = \rho_f \underline{V}$ in Eq. (2.51). Considering a fixed control volume and applying the RTT, Eq. (A.2), to the LHS of the resulting expression leads to,

$$\begin{aligned} \frac{\partial (\rho \tilde{\zeta}_{kin})}{\partial t} + \nabla \cdot (\rho \tilde{\zeta}_{kin} \underline{V}) &= -\nabla \cdot (p \underline{V}) + (p \nabla \cdot \underline{V}) \\ &+ \nabla \cdot (\underline{\tau} \cdot \underline{V}) - \underline{\tau} : \nabla \circ \underline{V} \\ &+ \rho \underline{V} \cdot \underline{g} + \rho_f \underline{E} \cdot \underline{V}. \end{aligned} \quad (2.53)$$

The integral Eulerian representation is found by applying Eq. (A.1) to Eq. (2.52),

$$\begin{aligned} & \int_{\mathcal{V}} \left[\frac{\partial (\rho \tilde{\zeta}_{kin})}{\partial t} + \nabla \cdot (\rho \tilde{\zeta}_{kin} \underline{V}) \right] d\mathcal{V} \\ &= \int_{\mathcal{V}} [-\nabla \cdot (p \underline{V}) + (p \nabla \cdot \underline{V}) + \nabla \cdot (\underline{\tau} \cdot \underline{V}) - \underline{\tau} : \nabla \circ \underline{V}] d\mathcal{V} \\ &+ \int_{\mathcal{V}} (\rho \underline{V} \cdot \underline{g} + \rho_f \underline{E} \cdot \underline{V}) d\mathcal{V}. \end{aligned} \quad (2.54)$$

2.4.5 Enthalpy equation

2.4.5.1 Lagrangian representation

The enthalpy equation can be obtained by substituting the kinetic energy equation, e.g. Eq. (2.52) into Eq. (2.50),

$$\begin{aligned} \frac{d}{dt} \int_{\mathcal{V}(t)} \rho h d\mathcal{V} &= \int_{\mathcal{V}(t)} \left(-\epsilon_E + \nabla \cdot \underline{q} - p \nabla \cdot \underline{V} + \underline{\tau} : \nabla \circ \underline{V} \right) d\mathcal{V} \\ &+ \frac{d}{dt} \int_{\mathcal{V}(t)} p d\mathcal{V}. \end{aligned}$$

It is possible to substitute the last pressure term on the RHS by the RTT, Eq. (A.1). Doing so and after applying the definition of the material derivative for the pressure leads to,

$$\frac{d}{dt} \int_{\mathcal{V}(t)} \rho h d\mathcal{V} = \int_{\mathcal{V}(t)} \left(-\epsilon_E + \nabla \cdot \underline{q} + \underline{\tau} : \nabla \circ \underline{V} + \frac{Dp}{Dt} \right) d\mathcal{V}. \quad (2.55)$$

The point Lagrangian enthalpy statement would be in this case,

$$\frac{d(mh)}{dt} = \left(-\epsilon_E + \nabla \cdot \underline{q} + \underline{\tau} : \nabla \circ \underline{V} + \frac{Dp}{Dt} \right) \mathbb{V}. \quad (2.56)$$

2.4.5.2 Eulerian representation

It is necessary to work in this case with the analogous Eulerian representation of Eq. (2.55). Applying the RTT, Eq. (A.1), to Eq. (2.55) leads to,

$$\int_{\mathbb{V}} \left[\frac{\partial(\rho h)}{\partial t} + \nabla \cdot (\rho h \underline{V}) \right] d\mathbb{V} = \int_{\mathbb{V}} \left(-\epsilon_E + \nabla \cdot \underline{q} + \underline{\tau} : \nabla \circ \underline{V} + \frac{Dp}{Dt} \right) d\mathbb{V}. \quad (2.57)$$

Finally, the differential Eulerian conservation law for enthalpy can be obtained by differentiating Eq. (2.57) with respect to the volume,

$$\frac{\partial(\rho h)}{\partial t} + \nabla \cdot (\rho h \underline{V}) = -\epsilon_E + \nabla \cdot \underline{q} + \underline{\tau} : \nabla \circ \underline{V} + \frac{Dp}{Dt}. \quad (2.58)$$

MODELING OF TURBULENT ELECTROHYDRODYNAMIC FLOW

The problem regarding the computational simulations of industrially relevant flows was presented in chapter 1. There are, naturally, ways to reduce the range of wavenumbers involved in the solution of Eq. (1.4, 1.5). The widespread approach is to filter the velocity field in order to introduce a cutoff in the wavenumber range. Numerical simulations tackling the full resolution of the flow wavenumbers and frequencies are known as Direct Numerical Simulations (DNSs). The use of a low-pass cutoff filter in the frequency or wavenumber domain, in addition to some mathematical model replacing the effect of the time or length scales filtered out, is understood as the branch of filter-based turbulence modeling. Reynolds-Averaged Navier-Stokes (RANS) simulations or Large Eddy Simulations (LESs) are the most representative filter-based turbulence models. By modeling a range of the frequency or wavenumber range, these types of simulation methods are effectively less computationally intensive than DNSs. Filter based turbulence models are ideally applicable whenever the dynamics of the small, non-resolved scales are physically well understood and well separated from the large flow scale behavior. Speziale [60] and Chaouat [61] offer a very comprehensive review regarding the fundamentals and trends in RANS, LES, as well as hybrid RANS-LES turbulence models.

3.1 FUNDAMENTALS OF THE ONE-DIMENSIONAL TURBULENCE MODEL

A different approach for turbulence modeling is taken in this thesis. This approach does not rely on the filtering of the frequency or wavenumber range in order to perform feasible numerical simulations. The One Dimensional Turbulence (ODT) model focuses on the view of a turbulent field through a line-of-sight [62]. This reduces the complexity of the problem of the numerical simulations from a 3-D to a 1-D problem. Considering the simplest case of a turbulent eddy in a scalar density field, an instantaneous (and hence, time-discontinuous) representation of some turbulent instabilities, e.g. like the turbulent Rayleigh-Bénard (RB) instability, can be achieved by means of the linear transformation of a scalar profile. In the RB instability, an initially stable and stratified density field undergoes vortical motion due to the heating of the fluid from below. Consider the instant right before a turbulent eddy in Figure 3.1, where the density field profile increases

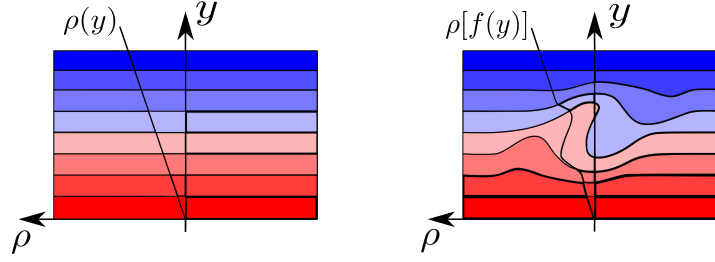


Figure 3.1: Effect of a turbulent eddy of an initially unstable thermally stratified Rayleigh-Bénard configuration (the fluid parcels have been coloured according to their temperature, where red parcels have a higher temperature than the blue ones). The image on the left is the instant right before the instability and the image on the right is the instant after the appearance of the 2-D turbulent eddy.

monotonically from the bottom to the top of the 1-D domain due to the heating effects. The heated fluid layers have a lower density than the cold fluid ones and thus, the weight of the cold layers acts as a destabilizing force in the system provoking mixing and breaking the thermal stratification (see Figure 3.1). This configuration is, indeed, unstable. It can be said that the gravitational force acts as the destabilizing force in the system. The effects of the 2-D turbulent eddy on the 1-D profile can be reproduced by a linear mapping of the density profile $\rho(y) \rightarrow \rho[f(y)]$. Note that the discussion of Figure 3.1 took place in a time-discontinuous context, and with a turbulent eddy produced by a non-local action [63].

The linear mapping is a measure preserving transformation, which guarantees that any material element is unaffected by the event [63]. Also, there are three random variables governing the mapping rule, namely, the instant $t_{0,eddy}$ and location of the eddy $y_{0,eddy}$, which will be referenced from now on as eddy event, and its size l_{eddy} . The mapping rule, called triplet map [62, 63], is a transformation for any scalar profile ψ (including the density profile ρ), i.e., a threefold compression and copy of the scalar profile within the range $[y_{0,eddy}, y_{0,eddy} + l_{eddy}]$, with the middle copy inverted,

$$\psi[f(y), t_{0,eddy}] = \begin{cases} \psi(3y - 2y_0, t_{0,eddy}) & y_0 \leq y \leq y_0 + \frac{l}{3}, \\ \psi(-3y + 4y_0 + 2l, t_{0,eddy}) & y_0 + \frac{l}{3} \leq y \leq y_0 + \frac{2l}{3}, \\ \psi(3y - 2y_0 - 2l, t_{0,eddy}) & y_0 + \frac{2l}{3} \leq y \leq y_0 + l, \\ \psi(y, t_{0,eddy}) & \text{otherwise.} \end{cases} \quad (3.1)$$

The subindex *eddy* was, and will be omitted for y_0 and l from now on.

Consider now a possible conceptual picture for an EHD instability. In a stable configuration prior to an eddy event, the electric field,

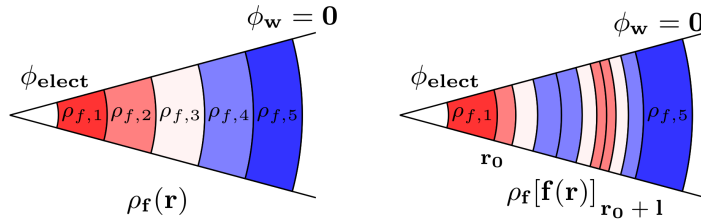


Figure 3.2: Discrete eddy event representation of a stable charge density field within a cylindrical system (wall and inner concentric electrode). The image on the left is the instant right before the appearance of an electrical convective current and the implementation of an eddy event. The image on the right is the instant after the appearance of the electrical convective current and the eddy event implementation.

interacting with the charge density field, causes an unipolar drift current between the inner concentric electrode at high voltage of the cylindrical system and the outer cylindrical wall (see Figure 3.2). Turbulence can locally modify the charge density field by convecting charge carriers, e.g., see Figure 3.2 after an eddy event. This implies the existence of convective currents, and thus, of an electrostatic potential energy difference distinct from the one in the stable configuration. In analogy to the RB case, such electrostatic potential energy difference can be released and transformed into fluid motion. However, unlike in the RB case, the origin of the fluid motion is indirect. It is caused by the disturbed charge density field (due to the convective currents), which causes changes in the electrostatic force, the latter inducing fluid motion. Similar to the gravitational force (or gravitational field) in the RB instability, the Coulomb force (or the electric field) is the destabilizing force in the system. For the ODT implementation of an eddy event, due to the measure preserving property of the triplet map, the charge density parcels close to $r = 0$ in the cylindrical coordinate system are not only mapped, but also resized in order to conserve the total charge density by means of the non-linear area differential rdr . That is, the measure preserving property in the planar system guarantees,

$$\int_{\mathfrak{V}(y_{0,l})} \psi^m(y) dy = \int_{\mathfrak{V}(y_{0,l})} \psi^m[f(y)] dy, \quad \text{for any } m, \quad (3.2)$$

while in the cylindrical coordinate system,

$$\int_{\mathfrak{V}(r_{0,l})} \psi^m(r) r dr = \int_{\mathfrak{V}(r_{0,l})} \psi^m[f(r)] r dr, \quad \text{for any } m. \quad (3.3)$$

It is noted that the resizing of fluid parcels seen in Figure 3.2 is due to a mesh adaption process. This process is discussed extensively in [64]. A brief summary of the process is also given in the next section.

Since the material elements are unaffected by the eddy event and the integral of ψ is measure preserving, it should be possible to state that

$$\frac{d}{dt} \int_{y_0}^{y_0+l} \psi dy = 0. \quad (3.4)$$

This is an advection equation for ψ in the 1-D domain (in this case specializing to planar coordinates)¹. This is just the Lagrangian representation of the continuity equation for ψ (see appendix A), i.e., an advection equation written in a conservative form. Due to the time-discontinuous character of the triplet map, the time derivative in the latter equation needs to be discretized. This leads then to the same measure preserving statement discussed before,

$$\left(\int_y \widehat{\psi} dy \right) - \left(\int_y \psi dy \right) = 0.$$

Here, $\widehat{\psi}(y) = \psi[f(y)]$, i.e., a notation for the mapped profiles. Note that whenever ψ is uniform, the statement is trivial. Hence, the interest is in the case that $\partial\psi/\partial y \neq 0$ (in the planar case). It is noted that Eq. (3.4) implies the existence of an advecting velocity v_ψ . Indeed, the application of the Reynolds Transport Theorem, Eq. (A.1), to Eq. (3.4), considering constant density in the 1-D domain, results in

$$\int_{y_0}^{y_0+l} \frac{\partial\psi}{\partial t} dy = (v_\psi\psi)_{y_0} - (v_\psi\psi)_{y_0+l}.$$

In a non-turbulent flow, v_ψ follows the zero gradient condition which results from the reduction of the zero divergence condition of the velocity field for incompressible flow to 1-D. That is, v_ψ is uniform, purely advective. However, the turbulent flow case necessarily obeys a 3-D velocity divergence condition, such that the nature of v_ψ is not trivial and can not be determined directly. Under the absence of uniform advection in the ODT line direction, the advecting velocity v_ψ is then associated to the changes of the 1-D deforming Lagrangian control volume,

$$v_\psi = \frac{dy}{dt}. \quad (3.5)$$

The latter expression can be approximated in a zero dimensional sense by means of the mixing length theory. For isentropic, homogeneous and stationary turbulence, in analogy to the mixing length theory [65], v_ψ is a characteristic velocity scale. The latter is associated to a turbulent diffusivity coefficient, or, in general, to a mixing time scale for the flow τ_{eddy} (along with the eddy length scale l), since

¹ Properties outside of the line direction, e.g. in x and z , are considered homogeneous. This suggests a representation of $dV = dy\Delta x\Delta z$. However, this may vary depending on the desired ODT formulation

$v_\psi \sim l/\tau_{eddy}$. This supposes, as stated before, statistical homogeneity in at least two (of three) spatial dimensions. This is the so-called temporal or T-ODT formulation. The mixing time scale could also be related to a streamwise mixing length scale by an advecting streamwise velocity. The latter is the spatial or S-ODT formulation.

Specializing to the T-ODT formulation, and considering the specific turbulent kinetic energy² derived from the previously mentioned mixing time scale, or eddy turnover time scale, τ_{eddy} , it can be said that, in a statistical isotropic and homogeneous turbulent flow for a scalar velocity $\psi = u$,

$$\left(\frac{l}{\tau_{eddy}}\right)^2 = \frac{1}{l^2} \left(\int_{y_0}^{y_0+l} u dy\right)^2. \quad (3.6)$$

This is the basis for the modeling of the eddy turnover time in the ODT model [62]. It is stressed that this formula is valid only for pure ideal, adiabatic mixing of velocity scalars (or of any scalar, in general) in an isentropic and homogeneous turbulence field. This is due to the assumption relating the kinetic energy of the velocity scalar u with the kinetic energy by v_ψ . In order to account for more complex phenomena, the RHS of Eq. (3.4) needs to account for molecular transport, such that conservation laws for momentum and energy can be obtained. Likewise, v_ψ , the velocity scale, need not be the flow characteristic velocity scale. The flow velocity field \underline{V} could be totally independent from v_ψ , e.g. in forced convective flows. The incorporation of molecular diffusion terms (and/or other general source terms), can be done by means of a relatively simple numerical treatment.

3.2 SAMPLING OF EDDY EVENTS

Specializing to the T-ODT formulation, the time scale determined by Eq. (3.6) (or its generalization, as discussed afterwards) is used to determine the instant of implementation of the eddy, $t_{0,eddy}$. An eddy rate can be calculated on the basis of the eddy turnover time scale τ_{eddy} , the eddy length l and position $r_{0,eddy}$. $r_{0,eddy}$ is used here to indicate that the eddy event discussion, from this point onwards, will take place in the context of the cylindrical coordinate system. The eddy rate per length and unit position, for one specific eddy can be calculated as [64, 66],

$$\lambda \sim \frac{1}{l^2 \tau_{eddy}} \rightarrow \lambda = \frac{C}{l^2 \tau_{eddy}}. \quad (3.7)$$

Here, C is a proportionality coefficient. It is an ODT parameter controlling the frequency of eddy events. Likewise, the global rate of eddies is given by,

$$\Lambda = \iint \lambda dr_0 dl. \quad (3.8)$$

² for constant density or incompressible flow

Direct sampling of an eddy for a given instant of time $t_{0,eddy}$, at a specific position r_0 and of a given length l , is governed by the Joint Probability Density Function of the eddy (JPDF),

$$\mathcal{F}_{eddy}(r_0, l; t_{0,eddy}) = \frac{\lambda}{\Lambda}. \quad (3.9)$$

Due to the discrete time-dependence, \mathcal{F}_{eddy} is actually the JPDF of a random process $\mathcal{F}_{eddy}(r_0, l; t)$ (see [32]). It is not possible to determine an analytical closed form of \mathcal{F}_{eddy} . Numerically, \mathcal{F}_{eddy} could be obtained by evaluating all of the possible numerical eddy events which could take place in the flow at every possible instant of time t . This is an unfeasible computational endeavour. In order to numerically approximate $\mathcal{F}_{eddy}(r_0, l; t)$ and simplify the computation process, a combination of the thinning and rejection methods is used [64, 67]. In the thinning method, eddies are sampled in time as a Poisson process with mean rate $n\Lambda$ ($n > 1$) and then accepted with probability $\Lambda/n\Lambda$. This eliminates the dependency on the unknown global rate Λ . In the rejection method, eddies are accepted based on the ratio between the unknown \mathcal{F}_{eddy} and a presumed JPDF $\mathcal{G}_{eddy}(r_0, l)$ as $\mathcal{F}_{eddy}/(b\mathcal{G}_{eddy})$ ($b > 1$). Dropping the subindex *eddy* for the JPDFs, the acceptance probability Ω of an eddy is calculated as,

$$\Omega = (\Omega_t) (\Omega_r) = \left(\frac{\Lambda}{n\Lambda} \right) \left(\frac{\mathcal{F}}{b\mathcal{G}(r_0, l)} \right). \quad (3.10)$$

Here, Ω_t and Ω_r refer to the probability of acceptance of an eddy event by the thinning and by the rejection method, respectively. Substituting $1/(nb\Lambda)$ by Δt_{samp} due to the arbitrary nature of the majorizing constants n and b , as well as the product $\mathcal{F}\Lambda$ by λ according to Eq. (3.9), results in,

$$\Omega = \frac{\lambda \Delta t_{samp}}{\mathcal{G}} \quad (3.11)$$

Δt_{samp} is chosen in such a way that the sampling time interval allows a sufficiently good reconstruction of the global eddy rate Λ . In practice, this can be done by ensuring that the sampling time is sufficiently smaller in comparison to the eddy turnover time scale τ_{eddy} . Since τ_{eddy} varies dynamically, Δt_{samp} must also be adjusted dynamically. The approximate JPDF of eddy sizes and positions, \mathcal{G} , is given by,

$$\mathcal{G} = h(l)g(r_0). \quad (3.12)$$

$g(r_0)$ is a uniform eddy location PDF and $h(l)$ is a presumed eddy size PDF. As detailed in [64], $h(l)$ is given by,

$$h(l) = \frac{2l_{\mathcal{F}}}{l^2} \left[\frac{e^{-\frac{2l_{\mathcal{F}}}{l}}}{e^{-\frac{2l_{\mathcal{F}}}{l_{max}}} - e^{-\frac{2l_{\mathcal{F}}}{l_{min}}}} \right]. \quad (3.13)$$

$l_{\mathcal{F}}$, l_{max} and l_{min} refer to the most probable, maximum and minimum expected length scales. l_{min} is generally considered the Kolmogorov length scale. The upper limit of l_{max} is taken as the physically maximum boundary layer thickness achievable by the internal flows studied here, i.e., half-width of the channel or the radius of the pipe, for channel and pipe flows, respectively. Likewise, the relation between the most probable and minimum length scales is assumed as $l_{\mathcal{F}} = 3l_{min}$ [68].

The (over)sampling procedure described above is a *memoryless* procedure, where the acceptance of each event is independent of the previously accepted event. In reality, due to the presence of the molecular transport described at the end of the previous section, the *catchup* diffusion advancement procedure smooths the gradients provoked by eddy events and adjusts the property profiles in order to satisfy the set of given boundary conditions³. This alternating stochastic and deterministic advancement, where each one feeds back on each other's previous advancement is a manifestation of the parabolic character of the ODT model. At a fundamental level, the ODT model is restricted to the application of dominantly parabolic (or hyperbolic) flows. Even in the case of the spatial formulation (S-ODT), this characteristic is maintained, with the subtle difference that the sampling process of the stochastic part is done for the streamwise position, instead of the time.

3.3 ADAPTIVE ODT FORMULATION

The Lagrangian character of the ODT formulation may involve the resizing of fluid parcels, as commented for the implementation of eddy events in the cylindrical system of Figure 3.2. The resizing of fluid parcels may also be present during the deterministic advancement part of ODT, in order to comply with mass conservation in the Lagrangian system, i.e., changes in density at constant mass mandate changes in volume. Therefore, a mesh adaption procedure was developed by [64]. The process of mesh adaption may take place in ODT under the following circumstances:

- Eddy events are implemented based on a threefold compression (and mid-copy inversion) of scalar profiles. Recurrent eddy events in a given section of the 1-D domain will render the simulations unfeasible. As a result, a mesh adaption process is performed after every eddy event implementation, in the range $[r_0, r_0 + l]$.
- In flows with non-trivial momentum and energy conservation due to the presence of diffusive fluxes (or some other source

³ This is an important aspect which will be discussed in a different context afterwards. Eddy events do not enforce boundary conditions directly

terms), mass conservation results in the change of the volume of the discrete fluid parcels (grid cells). Minimum and maximum thresholds for the grid cell sizes are specified as inputs for the simulations, Δr_{min} and Δr_{max} . If changes in the volume of a given grid cell (or a set of grid cells) results in the violation of this pre-specified thresholds, a process of mesh adaption takes place.

- In regions of the flow where eddy events are only seldomly implemented, diffusion may significantly smooth the property profiles, warranting further coarsening of the mesh. Due to this reason, the grid is adapted after an amount of time proportional to the CFL time-step condition (T-ODT formulation), or to the Kolmogorov length scale (S-ODT formulation). Alternatively, in regions of sustained volume change of the grid cells due to Lagrangian mass conservation, the difference between the sizes of neighbor cells in the boundaries of such regions may be exaggerate, resulting in distorted and inaccurate calculation of gradients. This is another reason for the regular grid adaption.
- Finally, any grid adaption procedure may result in the disproportionate size between cell neighbors. Each adaption step needs to comply with a 2.5 rule of proportion between cell neighbors's sizes. Otherwise, further adaption of the mesh is required [64].

In a grid cell with cell sizes Δr_i and corresponding property difference $\Delta \psi_i$ (both Δr_i and $\Delta \psi_i$ are evaluated at the cell faces), it is possible to normalize these quantities by the overall range size and the overall property difference in such range, i.e., $r_{max} - r_{min}$ and $\psi_{max} - \psi_{min}$ in the range. The nondimensional arc length Δa_i^* can then be calculated as,

$$\Delta a_i^* = \sqrt{(\Delta r_i^*)^2 + (\Delta \psi_i^*)^2}. \quad (3.14)$$

The total arc length can be uniformly redistributed based on a given nondimensional number density g_{Dens} , such that, as in [64],

$$\Delta a_u^* = \frac{\sum_i \Delta a_i^*}{int(g_{Dens} \sum_i \Delta a_i^*)}. \quad (3.15)$$

Here, $int()$ is the integer rounding of the factor inside the parenthesis. The new number of grid points is $int(g_{Dens} \sum_i \Delta a_i^*)$. With the definitions $a_0^* = a_{0,u}^* = 0$, $r_0^* = r_{0,u}^* = 0$, $r_{i \neq 0}^* = r_{i-1}^* + \Delta r_i^*$, $a_{i \neq 0}^* = a_{i-1}^* + \Delta a_i^*$, as well as $a_{j \neq 0,u}^* = a_{j-1,u}^* + \Delta a_u^*$, the new nondimensional grid can be found by interpolating the nondimensional cell face positions $r_{j,u}^*$ based on the calculated $a_{j,u}^*$ and the previous pairs $[r_i^*, a_i^*]$, i.e.,

$$r_{j,u}^* = r_{i-1,u}^* + \frac{r_i^* - r_{i-1}^*}{a_i^* - a_{i-1}^*} (a_{j,u}^* - a_{i-1}^*), \quad a_{j,u}^* \in [a_{i-1}^*, a_i^*]. \quad (3.16)$$

The new nondimensional grid cell sizes are then $\Delta r_{j,u}^* = r_{j,u}^* - r_{j-1,u}^*$. These cell sizes are then un-scaled to their dimensional counterparts and the new grid faces are calculated.

After the grid is processed in the previously described way, the 2.5 rule of proportion between cell neighbors's sizes is verified. Cells are then either merged or split in a conservative way (conserving mass in the T-ODT formulation and streamwise mass flux in the S-ODT formulation).

An additional mesh adaption procedure is performed in this thesis in order to enforce a fixed cell size at the origin (cell containing $r = 0$) in a cylindrical coordinate system. This is done due to the Finite Volume Method (FVM) used in this thesis. Essentially, due to the area differential in a cylindrical coordinate system, $dV = r dr$ (for homogeneous circumferential properties), any Lagrangian conservation law is nullified at $r = 0$. This implies a strict conservation of fluxes (in the absence of body source terms), which can not be achieved with a simple FV discretization unless the grid cell containing $r = 0$ is symmetric. For cylindrical coordinate systems, therefore, an additional input parameter Δr_c is required.

As commented previously, the grid is adapted regularly depending on the formulation, at time steps (or streamwise spatial steps) proportional to the CFL time-step condition (or the Kolmogorov length in S-ODT). The proportionality factor is in this case another mesh input parameter, $A_{TimeFac}$, i.e., $A_{TimeFac}$ is a proportionality factor for the time interval (or streamwise interval in S-ODT) after which a mesh adaption process takes place, regardless of eddy event implementations.

To finalize this section, a comment on the convergence of the numerical simulations by grid independence is given. Effectively, in the ideal case, all of the input parameters related to the grid adaption process should be irrelevant, once the grid is sufficiently refined, as in the sense that no real adaption is necessary at any time. In this sense, all of the parameters mentioned in this section are not considered as ODT model parameters.

3.4 VARIABLE DENSITY AND VECTOR ODT FORMULATION

This section discusses the generalization of the previously discussed concepts for the current ODT formulation used in this work. The generalized ODT formulation is discussed extensively in the Cartesian coordinate system by Ashurst and Kerstein [69, 70] and Lignell et al. [64]. Additionally, a detailed discussion of the cylindrical ODT formulation can be found in the work by Lignell et al. [66].

In the variable density and vector formulation, Eq. (3.4) is generalized to the conservation of mass, momentum and energy in the ODT line. Considering the stochastic part treatment only, scalars such as the density (mass conservation) or enthalpy (energy conservation) are

mapped as usual, $\rho \rightarrow \hat{\rho}$. However, due to the vector character of momentum, the treatment of each velocity component as a scalar also needs to comply with the overall mass and energy conservation. This is done by adding two kernel functions. Specializing to the planar Cartesian coordinate system, these are defined as,

$$K_{ODT} = y - f(y). \quad (3.17)$$

The notation used here is a convention adopted in ODT literature. As in Eq. (3.1), the convention implies that fluid at location $f(y)$ is mapped to location y . For the kernel function J_{ODT} , this is defined as,

$$J_{ODT} = |K_{ODT}|. \quad (3.18)$$

The treatment of the velocity components u_k , where $k \in \{1, 2, 3\}$, is, in T-ODT,

$$u_k \rightarrow \hat{u}_k + c_k K_{ODT} + b_k J_{ODT}. \quad (3.19)$$

Here, b and c are the corresponding kernel coefficients of J_{ODT} and K_{ODT} .

For the S-ODT formulation, due to flux conservation, a different version of the kernel application for the velocity components is applied in this work. In comparison to T-ODT, where the specific mass (trivial), specific momentum, and specific energy are mapped together with the density (e.g., u_k , h and ρ), the corresponding S-ODT mapped quantities are the volumetric density of mass, momentum and energy density (e.g., ρ , ρu_k and ρh). In S-ODT, thus, the kernels are applied not to the velocity components themselves, but rather, to the momentum components [71],

$$\rho u_k \rightarrow \widehat{\rho u_k} + c_k K_{ODT} + b_k J_{ODT}. \quad (3.20)$$

It is noted that ODT has traditionally used Eq. (3.19) as the only kernel mechanism, even in S-ODT. The use of Eq. (3.20) is new and will probably be superseded in the future. This is due to conservation issues in the diffusion catchup step used with this method in the only available publication to date using it [72]. Nonetheless, this method has been tested (as will be shown in the validation part of this thesis and in [72]), and has been verified to yield physically coherent results for crosswise (or radial) confined systems. Thus, this is the method used for S-ODT in this thesis. Mapped quantities, in general, can be calculated as,

$$\hat{\psi} = \frac{\widehat{\rho \psi}}{\hat{\rho}}. \quad (3.21)$$

Before deriving the generalized version of Eq. (3.6) in the variable density formulation, it is noted that there is a clear distinction between the velocity components subject to the kernel effects u_k and the

velocity of the (purely deforming) Lagrangian system, v_ψ , or $u_{2,\psi}$ in index notation. From a Lagrangian viewpoint, the velocity v_ψ is the deformation velocity of the Lagrangian volume. This is generally the opposite sign of the Eulerian measured velocity field, given that, by the calculation of relative velocities in a purely deforming system,

$$\underline{V}_\psi = \underline{V}_a - \underline{V}. \quad (3.22)$$

Here, \underline{V}_a is the advecting velocity of an inertial reference frame moving with the Lagrangian system. This is assumed at rest for the case of a purely deforming Lagrangian system ($\underline{V}_a = 0$). \underline{V} is then the Eulerian measured velocity field in this case. For a deforming and advecting system, the velocity \underline{V}_ψ , or specifically v_ψ measured in the ODT Lagrangian system (line), is only part of a more general Eulerian measured velocity field. Now we can interpret the subindex a in \underline{V}_a as symbolizing the absolute measure of the velocity (absolute with respect to a fixed coordinate system). In fact, the absolute (Eulerian) velocity field could be decomposed as,

$$\underline{V}_a = \underline{V} + \underline{V}_\psi. \quad (3.23)$$

In [73], Eq. (3.23) is written as $\underline{V}_A = \underline{V} + \underline{V}_D$, in [74] as $\underline{V}_L = \underline{V} + \underline{V}_D$ and in [72] as $\underline{V}_{tot} = \underline{V} + \underline{V}_D$. All statements refer to the same velocity decomposition. This decomposition can be seen either as a numerical splitting or as an analogy of a Helmholtz decomposition into solenoidal (\underline{V}) and irrotational (\underline{V}_ψ) components of the velocity. Further details of this treatment will be given in the discussion of the deterministic advancement. It is noted that Eq. (3.23) is introduced with the sole purpose of explaining the numerical treatment in ODT. Thus, in this thesis, everytime that the discussion is focused on ODT, the notation \underline{V} will refer to the solenoidal part of the Eulerian measured velocity field. For the cases that the discussion is general, e.g., the 3-D Navier-Stokes equations, \underline{V} refers instead to the complete Eulerian velocity field, i.e., \underline{V}_a in the notation of Eq. (3.23).

The generalized version of Eq. (3.6) in the variable density and vector ODT formulation can now be derived. Consider, as an example, the momentum balance before and after mapping based on Eq. (3.19),

$$\int_I (\widehat{\rho u}_k + \widehat{\rho} c_k K_{ODT} + \widehat{\rho} b_k J_{ODT}) d\mathbb{V} - \int_I \rho u_k d\mathbb{V} = 0. \quad (3.24)$$

Clearly, the latter expression is set to 0 due to (turbulent) momentum conservation. Here, $d\mathbb{V} = r dr = dr^2/2$ and the integral is evaluated in the range $[r_0, r_0 + l]$ according to the rule given by Eq. (C.1). Although ρu_k is not mapped in reality (in the T-ODT formulation), it is in any case a fact that due to the measure preserving property of the triplet map, $\int_I \rho u_k d\mathbb{V} = \int_I \widehat{\rho} \widehat{u}_k d\mathbb{V}$. Therefore,

$$c_k \int_I \widehat{\rho} K_{ODT} d\mathbb{V} = -b_k \int_I \widehat{\rho} J_{ODT} d\mathbb{V}. \quad (3.25)$$

For constant density, the LHS of this expression vanishes (according to Eq. (3.17) and the measure preserving property of the map) and, thus, $b_k = 0$. This means that the kernel J_{ODT} is responsible for enforcing variable density effects only. The kernel K_{ODT} is responsible for redistributing the kinetic energy among velocity components after a turbulent eddy event. Evaluating the kinetic energy change in a velocity component for constant density results in,

$$\begin{aligned}\Delta \Xi'_{kin,eddy,k} &= \frac{\rho}{2} \int_l (\hat{u}_k + c_k K_{ODT})^2 dV - \frac{\rho}{2} \int_l u_k^2 dV, \\ &= \rho c_k \left(\int_l u_k K_{ODT} dV + \frac{c_k}{2} \int_l K_{ODT}^2 dV \right).\end{aligned}\quad (3.26)$$

Maximizing this expression with respect to c_k ($d\Xi_{kin,k}/dc_k = 0$) results in the available kinetic energy for transfer per velocity component,

$$\Xi_{kin,eddy,k} = \frac{\rho}{2} \frac{\left(\int_l u_k K_{ODT} dV \right)^2}{\int_l K_{ODT}^2 dV}.\quad (3.27)$$

Although the latter energy is available for transfer, it is not necessary the case that all of it is actually transferred between velocity components. In fact, the actual energy changes imposed per velocity component are

$$\Delta \Xi'_{kin,eddy,k} = \alpha \sum_j G_{ij} \Xi_{kin,eddy,k}.\quad (3.28)$$

G_{ij} is the transfer matrix given by [75],

$$G_{ij} = \begin{pmatrix} -2 & 1 & 1 \\ 1 & -2 & 1 \\ 1 & 1 & -2 \end{pmatrix}.\quad (3.29)$$

In Eq. (3.28), the energy changes are selected in such a way that they are proportional to a tendency to produce a kinetic energy resembling an isotropic turbulence flow. The proportionality factor, α is an ODT model parameter.

Going back to the discussion regarding Eq. (3.27), and trying to follow the same analysis leading to Eq. (3.6), as well as considering the sum of all available energies as the total available kinetic energy would result in,

$$\left(\frac{l}{\tau_{eddy}} \right)^2 \frac{\rho}{2} \int_l dV = \frac{\rho}{2 \int_l K_{ODT}^2 dV} \sum_k \left(\int_l u_k K_{ODT} dV \right)^2.\quad (3.30)$$

There are definitely some similarities between Eq. (3.30) and (3.6). First of all, it is clear that Eq. (3.30) is the extensive counterpart of the intensive Eq. (3.6). Additionally, one may infer that due to the energy redistribution procedure, the correct available kinetic energy is the

same velocity integral from Eq. (3.6), but with the added multiplication by the kernel function (summed across all velocity components). The appearance of the kernel function also introduced the appearance of the integral $\int_l K_{ODT}^2 dV$. In ODT, the latter is an identity related to the mean square displacement of the fluid parcels due to the triplet map [63, 69],

$$\int_l K_{ODT}^2 dV = \frac{4}{27} l^2 \int_l dV. \quad (3.31)$$

Since there is no appearance of such mean square displacement factor in Eq. (3.6), although this is already an intrinsic property of the mapping process, it is left to conclude that the consistent version of Eq. (3.30) needs to remove the division by the factor $\int_l K_{ODT}^2 dV$ and instead introduce a factor $1/l^2$ on the RHS. Therefore, the appropriate equation for the eddy turnover time scale for the vector ODT formulation with constant density (in T-ODT) is,

$$\frac{\rho}{2} \left(\frac{l}{\tau_{eddy}} \right)^2 \int_l dV = K_0 \sum_k \Xi_{kin,eddy,k}, \quad (3.32)$$

where,

$$K_0 = \frac{\int_l K_{ODT}^2 dV}{l^2 \int_l dV}. \quad (3.33)$$

The last volume integral in the denominator of K_0 is introduced in order to make K_0 the necessary nondimensional scaling factor.

In the generalization of Eq. (3.32) to variable density, the factor ρ on the RHS is absorbed into the formula of the eddy available kinetic energy. Due to the previously mentioned influence of the kernel function J_{ODT} , the correct scaling of the density and the eddy length scale on the LHS is given by

$$\frac{1}{2} \left(\frac{1}{\tau_{eddy}} \right)^2 \int_l \hat{\rho} J_{ODT}^2 dV = K_0 \sum_k \Xi''_{kin,eddy,k}.$$

Here, the double dash in the kinetic energy term on the RHS, $\Xi''_{kin,eddy,k}$, is used to indicate, in analogy to the Favre average notation, that the kinetic energy refers to the variable density version of the available eddy kinetic energy. The detailed definition of $\Xi''_{kin,eddy,k}$ can be found in C. It is noted that $K_{ODT}^2 = J_{ODT}^2$. Therefore, due to the appearance of the additional kernel in the LHS density integral, a compensating factor K_0 is required on the LHS, in order to keep the consistency with Eq. (3.32). Therefore, the consistent scaling of the equation for τ_{eddy} in the variable density and vector formulation is,

$$\frac{1}{2K_0} \left(\frac{1}{\tau_{eddy}} \right)^2 \int_l \hat{\rho} K_{ODT}^2 dV = K_0 \sum_k \Xi''_{kin,eddy,k}. \quad (3.34)$$

In addition to the turnover time scaling by kinetic energy, it is traditional to incorporate in ODT additional forms of energy which can be transformed into kinetic energy. The viscous penalty factor is a kinetic energy loss (into heat) which is incorporated in Eq. (3.34) by means of a dimensional analogy. Starting from the same kinetic energy analogy,

$$\Xi_{vp,eddy} \sim \frac{1}{2} \rho_{eddy} v_{eddy,\psi}^2 \left(\int_I dV \right),$$

it is now possible to scale the eddy velocity v_{eddy} with the kinematic viscosity of the eddy. In doing so, and inserting another proportionality factor, Z , which is another ODT model parameter, the expression for the viscous penalty is obtained,

$$\Xi_{vp,eddy} = \frac{Z \rho_{eddy} v_{eddy}^2}{2l^2} \left(\int_I dV \right) = \frac{Z \mu_{eddy}^2}{2\rho_{eddy} l^2} \left(\int_I dV \right). \quad (3.35)$$

Here, $\nu_{eddy} = \mu_{eddy} / \rho_{eddy}$ is the kinematic viscosity of the eddy. μ_{eddy} and ρ_{eddy} are filtered values of the dynamic viscosity and the density in the eddy, i.e.,

$$\mu_{eddy} = \frac{\int_I \mu dV}{\int_I dV}, \quad \rho_{eddy} = \frac{\int_I \rho dV}{\int_I dV}. \quad (3.36)$$

Finally, within the scope of this thesis, an additional electrostatic potential energy term is added to the calculation of the eddy turnover time. The formulation of the term is discussed in the next section. The generalized formula for the eddy turnover time in the T-ODT formulation, thus, takes the form,

$$\frac{1}{2K_0} \left(\frac{1}{\tau_{eddy}} \right)^2 \int_I \hat{\rho} K_{ODT}^2 dV = K_0 \left(\sum_k \Xi''_{kin,eddy,k} \right) - \Xi_{vp,eddy} + K_0 \Xi_{pot,eddy}. \quad (3.37)$$

The last K_0 factor on the RHS in Eq. (3.37) is used to scale the eddy electrostatic potential energy term⁴ proportionally to the kinetic energy term. The detailed description of Eq. (3.37) for the planar and cylindrical coordinate systems, as well as its S-ODT counterpart is given in appendix C. The appendix also describes the functional form of the cylindrical triplet map and lists an algorithm overview of the ODT advancement process.

3.5 POTENTIAL ENERGY ODT FORMULATION

The last generalization of interest in ODT for this thesis is the treatment of the potential energy. Specifically for this thesis, a detailed discussion

⁴ Electrostatic potential energy which may or may not be transformed into kinetic energy

of the electrostatic potential energy treatment will be presented. In the limit of constant electric fields and charge density fields⁵, the electrostatic potential energy term in Eq. (2.52) does not contribute directly to the TKE (see appendix F). Rather, the contribution to the mean kinetic energy of the flow is done mainly via the Reynolds shear stress [76, 77]. More detailed considerations about the treatment for the transformation of potential energy into the mean kinetic energy follow next.

3.5.1 Case I: the limit of zero transfer of potential into kinetic energy

First, the case in which no transfer of potential into kinetic energy occurs is discussed next. This case was formally introduced by Jozefik et al. [73, 78] for the ODT modeling of the Darrieus-Landau instability. In the Darrieus-Landau (DL) formulation, the rate of eddy events is affected by the added potential energy term in Eq. (3.37). The influence to the turbulent flow is done by an intrinsic force, which is not part of the model dynamics due to the reduced order of the model (the DL instability is a 3-D dynamical instability). In practical terms, this means that the mechanism responsible for the instability is not directly present, or rather, not directly recognizable as an external body force transferring energy to the flow. Given that the deterministic PDEs solved in ODT may not directly involve the electroquasistatic body force, since, as it will be shown in the next section, it is assumed to act directly on the line direction, such a limit treatment can be justified. For the case of the DL instability, the flame front is unstable to perturbations of any wavelength due to the thermal expansion of the gas and the implied larger density of the reactants in comparison to the density of the combustion products.

For the DL formulation in [73], the corresponding potential energy term was modeled as,

$$\Xi_{DL,pot,eddy} = \int_1 \frac{\partial v_a}{\partial t} K_{ODT} (\hat{\rho} - \rho_{eddy}) dV. \quad (3.38)$$

Here, v_a is the absolute velocity in the line direction. The notation convention assumed here indicates that the second coordinate of the coordinate system always represents the direction of the line, which in the case of the internally forced convective flows studied in this thesis, always corresponds either to the wall normal direction or the radial direction. The first coordinate and the velocity component u is used to indicate the streamwise direction, or streamwise velocity component, respectively. The absolute velocity is calculated according to Eq. (3.23). The acceleration term in Eq. (3.38) is part of the intrinsic or fictitious force responsible for the DL instability.

⁵ Normally called One-Way Coupling (OWC) of electrostatics in the hydrodynamics of the flow

It is possible to express the electrostatic potential energy term in a way similar to the DL formulation. In order to do this, it is first important to examine Eq. (2.31). Given that boundary conditions are not directly enforced during eddy events, and considering that only fluid parcels are stirred due to turbulent advection, it is clear that the potential energy term required in ODT should be analogous to Eq. (2.31). Thus, the density terms in Eq. (3.38) must be substituted by charge density terms. Furthermore, understanding the acceleration term in Eq. (3.38) as the acceleration due to a conservative force, i.e., the result of the net effect of a scalar gradient field, it is possible to consider the equivalent of the acceleration term $\partial v_a / \partial t K_{ODT}$ in the electrodynamic case as $K_{ODT} \underline{E} \cdot \check{\underline{r}}_l$, where $\check{\underline{r}}_l$ is the unit position vector in the ODT line direction. This is because the electric field is unaffected by the fluid displacement due to the absence of the enforcement of the boundary conditions during eddy events (the electrostatic potential remains fixed). Therefore, the corresponding DL formulation for the electrostatic potential energy in ODT is,

$$\Xi_{E,pot-DL,eddy} = \int_l K_{ODT} (\hat{\rho}_f - \rho_{f,eddy}) \underline{E} \cdot \check{\underline{r}}_l d\mathcal{V}. \quad (3.39)$$

Due to the definition of the electric current density vector, Eq. (2.11), the latter expression can be rewritten for constant mobility β as,

$$\Xi_{E,pot-DL,eddy} = \frac{1}{\beta} \int_l K_{ODT} \left[\hat{\underline{J}} \cdot \check{\underline{r}}_l - (\underline{J} \cdot \check{\underline{r}}_l)_{eddy} \right] d\mathcal{V}. \quad (3.40)$$

Here, $(\underline{J} \cdot \check{\underline{r}}_l)_{eddy}$ is the current density average in the eddy range, analogous to Eq. (3.36).

3.5.2 Case II: Transfer of potential into kinetic energy

This section considers the ideas of the potential energy formulation discussed by [79–81] and of a technical communication sent to the author by M. Klein [82]. For the case of transfer of electrostatic potential energy into kinetic energy, the electrostatic potential energy term needs to be incorporated into the generalized version of the kinetic energy balance, Eq. (3.26),

$$\begin{aligned} \Delta \Xi'_{kin,eddy,k} &= \frac{1}{2} \int_l \hat{\rho} (\hat{u}_k + c_k K_{ODT} + b_k J_{ODT})^2 d\mathcal{V} - \frac{1}{2} \int_l \rho u_k^2 d\mathcal{V} \\ &+ \Xi_{E,pot,eddy,k}. \end{aligned} \quad (3.41)$$

Note that in this case, $\int_l \rho u_k^2 d\mathcal{V} = \int_l \widehat{\rho u_k^2} d\mathcal{V}$ due to the measure preserving property of the map. The latter mapped term was substituted on the LHS by the property of Eq. (3.21). For this case, the appropriate version of the formula for the electrostatic potential energy is that given by Eq. (2.31), i.e.,

$$\Xi_{E,pot,eddy} = \int_l \phi (\hat{\rho}_f - \rho_f) d\mathcal{V}. \quad (3.42)$$

The inclusion of the potential energy term in Eq. (3.41) implies that it will actually be part of the kinetic energy calculated as $\sum_k \Xi''_{kin,eddy,k}$. However, due to the presence of the factor K_0 multiplying the potential energy term in Eq. (3.37), there is no need to modify the equation, understanding that in this more generalized case,

$$\Xi_{kin+pot,eddy} = \sum_k \left(\Xi''_{kin,eddy,k} + \Xi_{E,pot,eddy,k} \right). \quad (3.43)$$

$\Xi_{E,pot,eddy,k}$ also influences the calculation of the kernel coefficients b_k and c_k . The calculation of these coefficients for the different planar, cylindrical, T-ODT and S-ODT formulations is presented in appendix C. In any case, one last important model parameter is required at this point, which is related to the redistribution of potential energy. Indeed, since,

$$\Xi_{E,pot,eddy} = \sum_k \Xi_{E,pot,eddy,k} \quad (3.44)$$

is the total electrostatic potential energy, a distribution of the potential energy per velocity component is modeled as,

$$\Xi_{E,pot,eddy,k} = \alpha_{pot,k} \Xi_{E,pot,eddy}. \quad (3.45)$$

$\alpha_{pot,k}$ is, therefore, the last one of the ODT model parameters (along with α , C and Z). $\alpha_{pot,k}$ is subject to,

$$\sum_k \alpha_{pot,k} = 1. \quad (3.46)$$

This of course excludes conflicts with the first case of the potential energy formulation discussed previously. In this thesis, a simple choice considering the parameters $\alpha_{pot,k} = [0, 1, 0]^T$ is used, where the second coordinate corresponds to the coordinate in the ODT line direction. The reasons for this choice will be clearer later, when the analysis of the charge continuity equation is carried out for the determination of the 1-D scalar governing equations used in the ODT deterministic advancement (see next section).

3.6 DETERMINISTIC ODT 1-D SCALAR GOVERNING EQUATIONS

3.6.1 Low Mach number EHD-asymptotics

This section is a formal dimensional analysis of the EHD governing equations, which is necessary in order to properly derive the correct 1-D scalar governing equations used in the deterministic ODT advancement. Equations (A.11) and (2.58) are first transformed from the Eulerian differential form to the Lagrangian differential form for a continuous system⁶, by substitution of the Eulerian continuity equation,

⁶ Not to confuse with the point Lagrangian representation that has been discussed so far and which is used in appendix A

Eq. (A.6), into the equations of momentum and energy (enthalpy), respectively⁷. Afterwards, the material derivative operator, Eq. (A.3) is used to simplify the expressions. In the case of the enthalpy equation, the LHS of the equation is given by the LHS of Eq. (2.55) differentiated with respect to the volume, due to the Lagrangian treatment.

$$\rho \frac{DV}{Dt} = -\nabla p + \nabla \cdot \underline{\underline{\tau}} + \rho \underline{\underline{g}} + \rho_f \underline{\underline{E}}. \quad (3.47)$$

$$\rho \frac{Dh}{Dt} = \rho c_p \frac{DT}{Dt} = \rho_f \underline{\underline{V}} \cdot \underline{\underline{E}} + \underline{\underline{J}} \cdot \underline{\underline{E}} + \nabla \cdot \underline{\underline{q}} + \underline{\underline{\tau}} : \nabla \circ \underline{\underline{V}} + \frac{Dp}{Dt}. \quad (3.48)$$

Here, c_p is the specific heat capacity at constant pressure, T is the temperature, and h is the specific enthalpy. Recall here the sign convention for $\underline{\underline{J}}$ defined in Chapter 2, which assumed positive current densities going from the outside to the interior of the control volume. This is normally the opposite of the traditional situation of, e.g., an electrode in the center of a channel or a pipe producing an electric discharge towards the walls. Recall also the definition of $\underline{\underline{J}}$ by Eq. (2.11), $\underline{\underline{J}} = \rho_f \beta \underline{\underline{E}}$, such that the last term on the RHS of Eq. (3.47) can be rewritten as $\underline{\underline{J}}/\beta$. Note also that in this specific section of the thesis the Navier-Stokes equations are discussed, which is the reason why $\underline{\underline{V}}$ is still referring here to the complete absolute Eulerian measured velocity field, neglecting the notation introduced for ODT in Eq. (3.23). In the next section of the thesis, 3.6.2, the ODT equations are discussed, such that the notation from Eq. (3.23) is adopted again.

The differential Lagrangian representation is used instead of the integral Lagrangian representation simply because it is easier to work directly with the temperature instead of the enthalpy. One important reason is that the flux equalization condition in the center cell of the ODT 1-D cylindrical grid, resolves an equalization of the heat flux, as per Eq. (3.48). In order to couple this in an implicit way, the variable advanced must be the temperature instead of the enthalpy. For low Mach number flows, a nonconservative formulation can yield very accurate results with high order methods, given that no pressure or density discontinuities are expected in the flow. In fact, for low Mach variable density 3-D DNSs, the majority of all publications to date use nonconservative versions of the governing equations, see e.g. [83–87].

Besides momentum and energy, the divergence condition for the velocity field given by the Lagrangian differential continuity equation is required⁸. This results in a divergence condition for the velocity field⁹. Additionally, the material derivative definition is also used to

⁷ The substitution of the continuity equation implies that for momentum and energy, mass conservation is implicit, as in any Lagrangian system.

⁸ This is obtained by inserting the material derivative definition into the Eulerian continuity equation, Eq. (A.6).

⁹ (Absolute) Eulerian measured velocity field.

obtain a differential expression for the current continuity equation from Eq. (2.26)¹⁰.

$$\nabla \cdot \underline{V} = -\frac{1}{\rho} \frac{D\rho}{Dt}. \quad (3.49)$$

$$\frac{D\rho_f}{Dt} = -\rho_f \nabla \cdot \underline{V} - \nabla \cdot \underline{J}. \quad (3.50)$$

Finally, Gauss's and Faraday's law, as well as the ideal gas equation of state of air are also required, i.e., Eqs. (2.13), (2.17) and (2.49).

$$\rho_f = \epsilon_0 \nabla \cdot \underline{E}. \quad (3.51)$$

$$\underline{E} = -\nabla \phi. \quad (2.17)$$

$$p = \rho R_{air} T. \quad (2.49)$$

This set of equations is next nondimensionalized. The electroquasistatic equations are discussed first. Due to Eq. (3.51), (2.17) and (2.11), Eq. (3.50) can be fully parameterized in terms of a reference electrostatic potential and a reference electrical mobility, $\beta = \beta_b \beta^*$ and $\phi = \phi_0 \phi^*$. For that, a characteristic length scale is required, due to Eqs. (3.51) and (2.17). In this sense, it is now time to enforce the desired 1-D character of the equations, by setting the length scale of the ODT domain as the characteristic length scale L . For the scope of this thesis, in the case of channel flows, L is the half-width of the channel. Conversely, in pipe flows, L is the radius of the pipe. These length scales correspond to the maximum boundary layer thickness in both configurations. Therefore, ρ_f is parameterized as $\rho_f = -(\epsilon_0 \phi_0 / L^2) \nabla^{2,*} \phi^*$ and \underline{J} as $\underline{J} = (\epsilon_0 \phi_0^2 \beta_b / L^3) (\nabla^{2,*} \phi^*) (\nabla^* \phi^*) \beta^*$. A reference scale for time and velocity is required as well. For that, a distinctive frequency and a bulk velocity are identified as reference scales¹¹, $t = t^* / f$ and $\underline{V} = U_b \underline{V}^*$. Using these reference scales, Eq. (3.50) can be rewritten as,

$$\begin{aligned} -\frac{\epsilon_0 \phi_0 f}{L^2} \frac{D(\nabla^{2,*} \phi^*)}{Dt^*} &= \frac{\epsilon_0 \phi_0 U_b}{L^3} (\nabla^{2,*} \phi^*) (\nabla^* \cdot \underline{V}^*) \\ &\quad - \frac{\epsilon_0 \phi_0^2 \beta_b}{L^4} \nabla^* \cdot [(\nabla^{2,*} \phi^*) (\nabla^* \phi^*) \beta^*]. \end{aligned}$$

If the latter equation is divided on the LHS and RHS by the factor $(\epsilon_0 \phi_0^2 \beta_b) / L^4$, the factor $\beta_b (\phi_0 / L)$ is obtained in the denominator of the LHS term and of the first RHS term. This factor is equivalent to the

¹⁰ Same as in the (density) continuity case.

¹¹ Same comments, implied here is the (absolute) Eulerian reference velocity field scale.

reference drift velocity of the charged media. As described by Atten et al. [88], it is possible to relate the electric field to the reference velocity scale. The correct scaling is carried out in terms of a reference velocity and a reference mobility. However, in the case of the nondimensional charge continuity equation, it is possible to rearrange the factors as,

$$\begin{aligned} & - \left(\frac{fL}{U_b} \right) \left(\frac{U_b L \rho_b}{\mu_b} \right) \left(\frac{\mu_b}{\rho_b \mathcal{D}_f} \right) \frac{\mathcal{D}_f}{\phi_0 \beta_b} \frac{D(\nabla^{2,*} \phi^*)}{Dt^*} \\ & = \left(\frac{\mathcal{D}_f}{\phi_0 \beta_b} \right) \left(\frac{\mu_b}{\rho_b \mathcal{D}_f} \right) \frac{U_b L \rho_b}{\mu_b} (\nabla^{2,*} \phi^*) (\nabla^* \cdot \underline{V}^*) \\ & \quad - \nabla^* \cdot [(\nabla^{2,*} \phi^*) (\nabla^* \phi^*) \beta^*]. \end{aligned}$$

Here, \mathcal{D}_f is the free charge (ionized air) diffusion coefficient and μ_b is the reference scale for the dynamic viscosity. With this substitution, the Strouhal number St and the Reynolds number are identified on the LHS and RHS. According to the IEEE nondimensional standard for electrohydrodynamics [54], the ion drift number F_E and the free charge (ionized air) Schmidt number Sc_f are also identified on the LHS and RHS,

$$\begin{aligned} - \frac{[St][Re][Sc_f] D(\nabla^{2,*} \phi^*)}{[F_E] Dt^*} &= \frac{[Re][Sc_f]}{[F_E]} (\nabla^{2,*} \phi^*) (\nabla^* \cdot \underline{V}^*) \\ &\quad - \nabla^* \cdot [(\nabla^{2,*} \phi^*) (\nabla^* \phi^*) \beta^*]. \end{aligned} \quad (3.52)$$

The factor $[Re][Sc_f]/[F_E]$ on the LHS and RHS of Eq. (3.52) is the mobility ratio M_β discussed by [88]. Therefore,

$$M_\beta = \frac{[Re][Sc_f]}{[F_E]}, \quad St = \frac{fL}{U_b}, \quad Sc_f = \frac{\mu_b}{\rho_b \mathcal{D}_f}, \quad F_E = \frac{\phi_0 \beta_b}{\mathcal{D}_f}. \quad (3.53)$$

It is noted that the ratio $[F_E]/[Sc_f]$ is also called electric Reynolds number, such that the definition of the mobility ratio is the ratio between the traditional Reynolds number and the electric Reynolds number of the flow [54]. For reference scales at standard temperature and pressure, the inverse of the electric Reynolds number Re_E^{-1} (and thus, the mobility ratio M_β) of ionized air, just as the Mach number for the scope of this thesis, approaches zero [88]. For the limit $M_\beta \rightarrow 0$, Eq. (3.52) leads to the statement of a constant nondimensional electric current density \underline{J}^* . Hence, it is convenient to define another reference scale for the electric current density, i.e., $\underline{J} = (I/S)\underline{J}^*$. It is now possible to define the complete list of nondimensional parameterizations,

$$\begin{aligned} \rho &= \rho_b \rho^*, & \underline{V} &= U_b \underline{V}^*, & \nabla &= \frac{1}{L} \nabla^*, & \rho_f &= -\frac{\epsilon_0 \phi_0}{L^2} \nabla^{2,*} \phi^* \\ \mu &= \mu_b \mu^*, & \underline{J} &= \frac{I}{S} \underline{J}^*, & \beta &= \beta_b \beta^*, & \underline{E} &= -\frac{\phi_0}{L} \nabla^* \phi^* \\ p &= p_b p^*, & T &= T_b T^*, & \underline{g} &= -g \underline{\check{g}}_{vert}, & \underline{\tau} &= \frac{\mu_b U_b}{L} \underline{\tau}^* \\ c_p &= c_{p,b} c_p^*, & \sigma_T &= \sigma_{T,b} \sigma_T^*, & t &= \frac{t^*}{f}, & \underline{q} &= \frac{\sigma_{T,b} T_b}{L} \underline{q}^*. \end{aligned}$$

(3.54)

Note that $\check{\underline{r}}_{vert}$ is the unit position vector in the vertical direction (acting direction of the gravitational acceleration g). The nondimensional versions of Eq. (3.47, 3.48, 3.49) and (2.49) are then¹²,

$$\nabla^* \cdot \underline{V}^* = -\frac{[St] D\rho^*}{\rho^* Dt^*}. \quad (3.55)$$

$$[St]\rho^* \frac{DV^*}{Dt^*} = -\frac{1}{\gamma[Ma]^2} \nabla^* p^* + \frac{1}{[Re]} \nabla^* \cdot \underline{\underline{\tau}}^* - \frac{1}{[Fr]^2} \rho^* \check{\underline{r}}_{vert} + \frac{[N_{EHD}]^2 J^*}{[Re]^2 \beta^*}. \quad (3.56)$$

$$\begin{aligned} [St]\rho^* c_p^* \frac{DT^*}{Dt^*} &= \frac{(\gamma-1)[Ma]^2[N_{EHD}]^2}{[Re]^2} \frac{1}{\beta^*} J^* \cdot \underline{V}^* \\ &\quad - \frac{(\gamma-1)[Ma]^2[N_{EHD}]^2}{[M_\beta][Re]^2} J^* \cdot \nabla^* \phi^* + \frac{1}{[Pr][Re]} \nabla^* \cdot \underline{q}^* \\ &\quad + \frac{(\gamma-1)[Ma]^2}{[Re]} \underline{\underline{\tau}}^* : \nabla^* \circ \underline{V}^* + \frac{(\gamma-1)[St] Dp^*}{\gamma Dt^*}. \end{aligned} \quad (3.57)$$

$$p^* = \rho^* T^*. \quad (3.58)$$

The bulk nondimensional numbers characterizing this set of equations are,

$$\begin{aligned} St &= \frac{fL}{U_b}, & Re &= \frac{\rho_b U_b L}{\mu_b}, & Sc_f &= \frac{\mu_b}{\rho_b \mathcal{D}_f}, & F_E &= \frac{\phi_0 \beta_b}{\mathcal{D}_f}, \\ Ma &= \frac{U_b}{\sqrt{\frac{\gamma p_b}{\rho_b}}}, & Fr &= \frac{U_b}{\sqrt{gL}}, & N_{EHD} &= \sqrt{\frac{IL^3 \rho_b}{S \beta_b \mu_b^2}}, & Pr &= \frac{c_{p,b} \mu_b}{\sigma_{T,b}}, \\ M_\beta &= \frac{Re}{Re_E}, & Re_E &= \frac{\rho_b \phi_0 \beta_b}{\mu_b} = \frac{F_E}{Sc_f}. \end{aligned} \quad (3.59)$$

If Eq. (3.56) is multiplied on the LHS and RHS by $[Ma]^2$, it is possible to obtain the Boussinesq number in the gravity term, i.e., $Bo = [Ma]^2/[Fr]^2$. Although this is merely speculative, it would be theoretically possible to state that there is an analogous electric Boussinesq number given by the factor $Bo_E = [Ma]^2[N_{EHD}]^2/[Re]^2$. In the limit where $Bo_E = 0$ and $Bo \rightarrow 0$, it is possible to derive the Boussinesq approximation for gaseous buoyant flows from the set of the previous nondimensional equations, see [89]. That is, a simplification

¹² Here again, the implied velocity is the absolute Eulerian measured velocity field

of the momentum equation and energy equation in order to treat the temperature as a quasi-passive scalar, neglecting its influence on fluid properties, e.g., ρ ¹³. In any case, it is not the objective of this thesis to derive such (hypothetical) asymptotic limits for Bo_E governed flows. Instead, it is only noted that, in the limit $Ma \rightarrow 0$, the multiplication of Eq. (3.56) by $[Ma]^2$ results in,

$$\nabla^* p^* = 0. \quad (3.60)$$

This is the classical result of the zero Mach limit asymptotics where the thermodynamic pressure is uniform in space. This is the pressure directly interacting in the ideal gas law, which makes density gradients, in leading Mach order, a sole function of the temperature [89, 90]. Due to this reason, the treatment of the thermodynamic pressure P , which is used for the ideal gas law and the temperature equation, is distinguished from the treatment of the hydrodynamic pressure p , which is used for the momentum equation. Additionally, for the type of flows treated in this thesis, the thermodynamic pressure remains constant in time, due to the open nature of the systems (pipes and channels). This means that $\partial P^*/\partial t^* = 0$ and due to Eq. (3.60), this implies,

$$\frac{DP^*}{Dt^*} = 0. \quad (3.61)$$

Without introducing additional asymptotic formalisms, it is noted that, in the limit $Ma \rightarrow 0$ and $M_\beta \rightarrow 0$, there is an indetermination of the term $\underline{J}^* \cdot \nabla^* \phi^*$ in Eq. (3.57). This implies that this term needs to be evaluated in a case by case basis, in order to decide whether or not its contribution can be neglected. Using then Eq. (3.58) and (3.57) in the limit $Ma \rightarrow 0$ and $M_\beta \rightarrow 0$, but retaining the term $\underline{J}^* \cdot \nabla^* \phi^*$ in Eq. (3.57), it is then possible to arrive at the expression for the material derivative of the density,

$$\begin{aligned} \frac{D\rho^*}{Dt^*} &= P^* \frac{D}{Dt^*} \left(\frac{1}{T^*} \right) \\ &= -\frac{1}{[St]c_p^*T^*} \left(\frac{1}{[Pr][Re]} \nabla^* \cdot \underline{q}^* - \frac{(\gamma-1)[Ma]^2[N_{EHD}]^2}{[M_\beta][Re]^2} \underline{J}^* \cdot \nabla^* \phi^* \right). \end{aligned} \quad (3.62)$$

Before summarizing the final expressions for the leading Mach and mobility ratio order quantities of velocity, temperature and electrostatic potential, one final nondimensional quantity is examined, namely, the skin friction coefficient,

$$C_f = \frac{2\tau_w}{\rho_b U_b^2}. \quad (3.63)$$

¹³ The use of the term ‘‘Boussinesq approximation’’ here should not be confused with the Boussinesq hypothesis used for the modeling of the Reynolds shear stress tensor by means of the mean shear stress tensor in RANS.

In Eq. (3.63), τ_w refers to the shear stress at the wall and the factor $(1/2)\rho_b U_b^2$ refers to the bulk hydrodynamic pressure. If the nondimensional parameterization for p^* is substituted back in the pressure gradient term in Eq. (3.56) and a new reference scale for the hydrodynamic pressure is chosen, namely, the wall shear stress, it is then possible to rewrite the nondimensional pressure gradient term in the momentum equation as $([C_f]/2)\nabla^* p^*$.

For the leading Mach order and leading mobility ratio order quantities of velocity, temperature and electrostatic potential, the governing equations are, thus¹⁴,

$$\nabla^* \cdot \underline{J}^* = 0. \quad (3.64)$$

$$\nabla^* \cdot \underline{V}^* = \frac{1}{\rho^* c_p T^*} \left(\frac{1}{[Pr][Re]} \nabla^* \cdot \underline{q}^* - \frac{(\gamma - 1) [Ma]^2 [N_{EHD}]^2}{[M_\beta][Re]^2} \underline{J}^* \cdot \nabla^* \phi^* \right). \quad (3.65)$$

$$[St] \rho^* \frac{D\underline{V}^*}{Dt^*} = -\frac{[C_f]}{2} \nabla^* p^* + \frac{1}{[Re]} \nabla^* \cdot \underline{\tau}^* - \frac{1}{[Fr]^2} \rho^* \underline{\dot{\gamma}}_{vert} + \frac{[N_{EHD}]^2}{[Re]^2} \frac{\underline{J}^*}{\beta^*}. \quad (3.66)$$

$$[St] \rho^* c_p \frac{DT^*}{Dt^*} = \frac{1}{[Pr][Re]} \nabla^* \cdot \underline{q}^* - \frac{(\gamma - 1) [Ma]^2 [N_{EHD}]^2}{[M_\beta][Re]^2} \underline{J}^* \cdot \nabla^* \phi^*. \quad (3.67)$$

$$\rho^* = \frac{P^*}{T^*}. \quad (3.68)$$

It is noted that, for the leading order solenoidal electric current density field, as per Eq. (3.64), leading order time invariant electric fields and charge density fields are also implied. Expanding ϕ^* and \underline{J}^* from Eq. (3.52) in mobility ratio powers, in analogy to asymptotic Mach number analysis [89, 90], it is possible to deduce that, for the leading order effects in terms of the mobility ratio, the charge continuity equation is written as,

$$-[St] \frac{D(\nabla^{2,*} \phi^*)}{Dt^*} = (\nabla^{2,*} \phi^*) (\nabla^* \cdot \underline{V}^*) - \nabla^* \cdot \underline{J}^{*,(1)}. \quad (3.69)$$

The superindex (1) indicates that $\underline{J}^{*,(1)}$ is the first order term, in the context of the mobility ratio, of the electric current density vector.

¹⁴ Same comments regarding \underline{V} , the absolute Eulerian measured velocity field is implied

The only zero order term (leading order effect) is the isolated term $\nabla^* \cdot \underline{J}^*$, which is the reason for the formulation of the solenoidal current density expression of Eq. (3.64). $\underline{J}^{*(1)}$ is, instead, in simpler terms, a perturbation of the current density. It is clear that the current density as such is not an independent variable. Rather, it is naturally given by a certain mobility and a certain electrostatic potential field. In that sense, the electrostatic potential appearing in Eq. (3.69) is also the first order term of the electrostatic potential ϕ^* , in terms of M_β . This finding is troublesome in the sense that Eq. (3.69) is yet another equation for the leading order velocity divergence condition. However, it is also interesting, in the sense that it has now been verified that there is a 'disturbance' component in the velocity field arising from current density fluctuations. This could be interpreted as the conceptual basis for considering the electrostatic potential energy in ODT as a source of turbulent advection. In fact, if the Boussinesq approximation for buoyant flows is used disregarding electrodynamic effects (a Boussinesq limit derived by classical zero Mach asymptotics as in [89]), the second order momentum equation¹⁵ relates the leading order velocity with the first order temperature. That is, there is a temperature 'disturbance' component in the velocity field responsible for turbulent advection, which is interpreted as the conceptual basis of the ODT gravitational potential energy formulation [79, 80].

3.6.2 *Reduction of the deterministic low Mach system to a scalar 1-D system*

Any velocity divergence condition involving any gradient other than the velocity gradient in the line direction in Eq. (3.69) or (3.65) implies an elliptic problem for the deterministic ODT solution. This is because the way to enforce the velocity divergence condition is by taking the divergence of Eq. (3.66). In the case that there was only a pressure gradient term on the RHS of Eq. (3.66), for any 2-D or 3-D velocity divergence condition the resulting equation for the pressure would be a 2-D or 3-D Poisson equation, respectively. Since the pressure is responsible for enforcing mass, momentum and energy conservation, this means that there could be 2-D or 3-D structures producing a feedback in the 1-D domain. Hence, this problem is called elliptic in ODT, because it would require 2-D or 3-D boundary conditions in order to be solved during the deterministic step. In [72], this divergence problem is discussed in more detail. The takeaway message is that, in ODT, it is only possible to enforce a 1-D divergence condition in the deterministic step. As discussed previously for Eq. (3.23), a decomposition of the velocity field is considered. One part of the

¹⁵ The second order momentum equation in the Boussinesq approximation for buoyant flows is the only nontrivial condition for the velocity field given the zero divergence condition for the leading order velocity used in the approximation

velocity field can be interpreted to evolve according to a deterministic 1-D scalar momentum equation and according to the stochastic eddy events and the corresponding ODT kernel treatment, Eq. (3.19) or (3.20). This is an advective contribution, i.e., the velocity \underline{V} in Eq. (3.23). Another part of the velocity field would be, in this sense, responsible for the deformation of the Lagrangian volume in ODT. During the deterministic step, the velocity divergence condition is derived as the material derivative of the density (see Eq. (3.55)). This is the change in the Lagrangian control volume. Therefore, it is interpreted that the velocity involved in the velocity divergence condition is the \underline{V}_ψ ¹⁶ contribution to \underline{V}_a , according to the notation in Eq. (3.23). Recall Eq. (3.5), specialized to the planar formulation,

$$v_\psi = \frac{dy}{dt}. \quad (3.70)$$

That is, the velocity divergence condition determines the deformation velocity of the Lagrangian system, at least according to a deterministic set of equations.

Additional considerations for the reduction of the set of Eqs. (3.64-3.67) to a 1-D scalar set of equations take into account other potential sources of ellipticity. In particular, any diffusion flux in any direction off the line is an elliptic operator. Due to the invariant character of the ∇ operator, however, the reduction to 1-D of vector diffusion fluxes must be done carefully. The reduction of the shear stress tensor divergence to the scalar approach is discussed in detail in appendix A of a previous work [72]. In planar coordinates, there is no distinction between the scalar and vector view of the velocity field or of the velocity components, respectively. This is because the operator ∇ is the same, regardless whether it is applied to vectors or scalars (the divergence of a vector is equivalent to the sum of the components of the gradient of a scalar). In cylindrical coordinates, however, this is not the case. In [72], this problem is resolved for the shear stress tensor divergence. It is proved that the vector and scalar views of the shear stress tensor divergence are equivalent, as long as a missing kinetic energy dissipation term is added to the scalar treatment of the velocity components in the directions off the line. For the heat diffusion flux, the problem is somehow alleviated in comparison to the shear stress tensor divergence, given that the ∇ operator is in this case applied to a vector, and not to a second order tensor. Nonetheless, the problem may still persist regarding how to model the diffusion flux. The practical conclusion is the same. That is, the reduction to the scalar 1-D equation of the 3-D Navier-Stokes equations can only take place after performing explicitly all of the corresponding vector operations. First, the explicit 3-D representation must be obtained, and then this 3-D representation should be reduced to consider gradients in the line direction only.

¹⁶ This is just v_ψ due to the 1-D system.

Another important observation is done regarding Eq. (3.64). The zero divergence condition (in zero mobility ratio order) for the electric current density vector is completely decoupled from the flow dynamics. Therefore, it can be solved without ODT, even in a 3-D configuration. However, using, e.g., a streamwise varying current density vector in Eq. (3.66), may result in a conflictive nonzero streamwise velocity divergence by applying the divergence operator in Eq. (3.66). This is of course because the 3-D electrostatic problem is decoupled from the velocity divergence condition in Eq. (3.69). Again, this results in the inability to operate with anything other than a 1-D electrostatic potential field, unless additional assumptions are taken. Since the current density vector is a constant in the line due to the 1-D treatment, its effect can be considered a bulk effect on the velocity in the line direction, which is zero due to the walls.

The treatment of the gravitational body force also requires some discussion. For (streamwise) vertical channel or pipe flows, the gravitational body force is added as a source term in the momentum equation. Given that the gravity is a constant, this does not cause any conflict with the velocity divergence condition (the divergence of the momentum equation is the same with or without the gravity term). For (streamwise) horizontal channel or pipe flows, the gravitational term only affects the velocity component in the line direction. Since v_ψ is already given by the divergence condition, the gravitational body force term can only have an effect on the \underline{V} ¹⁷ field. Hence, the gravitational body force term is considered as a source of turbulent advection in the ODT stochastic implementation for horizontal channel or pipe flows, but not during the deterministic diffusion step, in order to avoid double injection of potential energy into v ¹⁸. The same comments apply for the electric body force, which would normally only appear in the momentum equation for the velocity component pointing in the line direction.

Finally, the pressure gradient term in the momentum equation in ODT is omitted completely. Since all of the equations of momentum, energy and mass (the latter given by a 1-D velocity divergence condition) can be reduced to a scalar version, there is no need for enforcing a 2-D or 3-D divergence of the velocity field. The role of the pressure is, in this sense, superfluous. However, a side-constraint for enforcing a given streamwise bulk velocity, or for enforcing a (pre-specified) constant pressure gradient can be added to the momentum equation. Traditionally, this is taken as a mean streamwise pressure gradient in internally forced convective flows $\nabla \bar{p} \cdot \check{\underline{e}}_{str}$, where $\check{\underline{e}}_{str}$ is the unit vector in streamwise direction. However, this can also be generalized to the temperature equation, in case a source term is required, e.g., in order

¹⁷ According to the notation in Eq. (3.23)

¹⁸ This case of buoyant horizontal tubes is not discussed in this thesis. Therefore, no formula for the calculation of the gravitational potential energy contribution in the eddy turnover time was specified in appendix C.

to force a desired bulk temperature¹⁹. Note that for planar Cartesian coordinates, $\nabla \bar{p} \cdot \check{\underline{\underline{x}}}_{str}$ should take the form $\partial \bar{p} / \partial x$, while in cylindrical coordinates this is $\partial \bar{p} / \partial z$. For low Mach number constant property channel and pipe flows, it is possible to show that the average pressure is uniform along the crosswise or radial coordinate, for planar Cartesian and cylindrical coordinates, respectively [32]. With this, e.g., $\partial \bar{p} / \partial x$ becomes $d\bar{p} / dx$. This latter notation change is not considered in this thesis. Instead, the partial derivative notation is retained for straightforward association with the scalar reduction procedure.

The latter considerations allow a derivation of the scalar ODT 1-D deterministic governing equations. Starting with the set of nondimensional equations, Eqs. (3.64-3.67) and reverting the nondimensional parameterizations in the equations, the corresponding set of 1-D scalar conservation equations can be obtained after explicitly performing all of the vector calculus operations and then reducing to 1-D, and after accounting for all of the considerations discussed so far. In the planar case, this set of equations is²⁰,

$$\frac{\partial (\underline{J} \cdot \check{\underline{\underline{x}}}_{ODT})}{\partial y} = 0 \rightarrow \underline{J} \cdot \check{\underline{\underline{x}}}_{ODT} = \rho_f \beta \underline{E} \cdot \check{\underline{\underline{x}}}_{ODT} \text{ is a constant.} \quad (3.71)$$

$$\frac{DT}{Dt} = \frac{1}{\rho c_p} \left[\frac{\partial}{\partial y} \left(\sigma_T \frac{\partial T}{\partial y} \right) + \frac{(\underline{J} \cdot \check{\underline{\underline{x}}}_{ODT})^2}{\rho_f \beta} \right]. \quad (3.72)$$

$$\frac{DV}{Dt} = \frac{1}{\rho} \frac{\partial}{\partial y} \left(\mu \frac{\partial V}{\partial y} \right) + \underline{g} \cdot \check{\underline{\underline{x}}}_{vert} - \frac{1}{\rho} \nabla \bar{p} \cdot \check{\underline{\underline{x}}}_{str}. \quad (3.73)$$

$$\frac{\partial v_\psi}{\partial y} = \frac{1}{\rho c_p T} \left[\frac{\partial}{\partial y} \left(\sigma_T \frac{\partial T}{\partial y} \right) + \frac{(\underline{J} \cdot \check{\underline{\underline{x}}}_{ODT})^2}{\rho_f \beta} \right]. \quad (3.74)$$

Note the substitution of the electric field by its electric current density counterpart from Eq. (3.71) in Eq. (3.72). This is simply done for the sake of a clearer operational notation. These equations are solved together with the ideal gas law, Gauss's law and Faraday's law (in 1-D),

$$P = \rho R_{air} T. \quad (2.49)$$

$$\frac{\partial (\underline{E} \cdot \check{\underline{\underline{x}}}_{ODT})}{\partial y} = \frac{\rho_f}{\epsilon_0}. \quad (3.75)$$

¹⁹ This forcing is done for the enthalpy, however, given that the former is the conservative variable associated to the temperature

²⁰ Here again, the notation implied in Eq. (3.23) is used

$$\underline{E} \cdot \check{\underline{L}}_{ODT} = -\frac{\partial \phi}{\partial y}. \quad (3.76)$$

It is noted that Eq. (3.73) is the PDE of a vector quantity, and thus, a vector equation. However, if the equation is analyzed for each one of its (velocity) components, it can be verified that every velocity component evolves as an independent scalar. The specific form of these equations in the cylindrical coordinate system is given in appendix D, as well as a description of the implementation algorithm. In the next section, the T-ODT and S-ODT form of the previous set of equations is discussed, respectively.

3.6.3 Specialization to the T-ODT and S-ODT formulations

The Lagrangian formulation of the deterministic 1-D scalar equations (3.71-3.74) is a good point to finally discuss the differences between the temporal and spatial ODT formulations, T-ODT and S-ODT, respectively.

3.6.3.1 T-ODT formulation

So far, the discussion in this thesis has focused on the T-ODT formulation. This is the easiest one to conceptualize based on the understanding of the sampling and implementation of stochastic eddy events as part of a time-dependent random process. In T-ODT, as it has been discussed so far, the implementation of every eddy event intrinsically implies a deterministic catchup process from the time of the last event implementation to the time of the current event implementation, due to the operating splitting treatment between the stochastic turbulent advection and the deterministic diffusion implementation (including additional source terms). Specialization of Eqs. (3.71-3.74) to the T-ODT formulation is done, thus, by realizing that the material derivative in such equations corresponds, in T-ODT, to a total Lagrangian time derivative of the corresponding scalar. Since the Lagrangian volume is 1-D, the corresponding total velocity of the Lagrangian volume seen from an Eulerian reference system is v_a , according to the notation in Eq. (3.23). Eq. (3.74) is only applicable to the irrotational contribution of the velocity. For the solenoidal part, or the advecting contribution to the velocity, the analysis is done in the following way: the turbulent advection is formally incorporated in ODT by the effect of the stochastic eddy events, while the mean advection is considered in the deterministic advancement. Due to the geometric constraint of the walls for the case of the internal flows studied in this thesis, the mean advection in the direction of the line is zero. In terms of the T-ODT interpretation of the material derivative, this implies that the only remaining advecting contribution for the 1-D

deterministic system is v_ψ , which could have (in the case of variable density flows) a nonzero divergence condition (technically a gradient condition in 1-D),

$$\frac{D\psi}{Dt} \Big|_{T-ODT} \rightarrow \frac{d\psi}{dt} = \frac{\partial\psi}{\partial t} + v_\psi \frac{\partial\psi}{\partial y}. \quad (3.77)$$

It is stressed that this equation is only applicable for the ODT deterministic advancement of the internal flows studied in this thesis. Due to the Lagrangian treatment, the total time derivative is resolved as such, and the line velocity v_ψ is determined according to the result of the velocity divergence condition, Eq. (3.74). The corresponding advection of the grid cell faces with velocities v_ψ is performed afterwards according to Eq. (3.70), such that v_ψ is not an actual velocity field, but rather the representation of the corresponding deformation in the grid.

3.6.3.2 S-ODT formulation

S-ODT is a stationary quasi-2-D ODT formulation. In S-ODT, the JPDF of eddy events no longer depends on time, but rather on the streamwise position. In the planar formulation, the corresponding S-ODT formulation for Eq. (3.9) is,

$$\mathcal{F}_{eddy}(y_0, l; x_{0,eddy}) = \frac{\lambda}{\Lambda}. \quad (3.78)$$

The eddy rate and the eddy turnover time are therefore generalized to the spatial case, where the eddy turnover time becomes an eddy turnover length scale, as previously mentioned. Despite this, the formulation remains quasi-2-D due to the parabolic restrictions applied to the flow. This is because the nature of the operating splitting treatment obeying a catchup diffusion process to every implemented stochastic eddy event is preserved. For wall-bounded flows, this brings up an important discussion regarding the nature of the divergence condition. Indeed, although the divergence condition for the solenoidal contribution to the velocity may now be 2-D, the divergence condition of the irrotational part of the velocity is still 1-D, given that the Lagrangian volume does not expand or contract, in a bulk sense, due to the wall geometric constraint. This is also logical from the point of view that the line is still a 1-D domain. The line can not expand or contract in streamwise direction. Thus, there is no u_ψ velocity component, it is just zero. Eq. (3.74), remains, therefore, without additional modifications. In terms of the definition of the total Lagrangian time differential, these considerations force a distinct interpretation of the differential during the deterministic advancement depending on the corresponding intensive quantity that is being evaluated. For $\psi = 1$, corresponding to mass conservation, the applicable interpretation is, due to the 1-D divergence condition based on v_ψ , which represents the

material derivative of the density, or the changes in the Lagrangian volume,

$$\frac{d\rho}{dt} = \frac{\partial(\rho v_\psi)}{\partial y} = 0. \quad (3.79)$$

Consider now the material derivative definition for any other property excluding $\psi = 1$, that is, do not consider the differential Lagrangian statement for mass conservation as discussed before. The quasi-2-D system is parabolically advected in streamwise direction with an Eulerian velocity u by Eq. (3.23), given that $u_\psi = 0$. The equivalent Eulerian framework of the S-ODT quasi-2-D Lagrangian system, following Eq. (A.2), assuming stationarity, $\partial/\partial t = 0$, and decomposing the velocity in the line direction into its solenoidal and irrotational terms, with the advecting contribution considering only the zero mean part during the deterministic advancement, is, thus,

$$\frac{d(\rho\psi)}{dt} = \frac{\partial(\rho u\psi)}{\partial x} + \frac{\partial(\rho v_\psi\psi)}{\partial y}$$

Substitution of Eq. (3.79) here due to mass conservation implies taking the density out of the total differential on the LHS of the previous equation. Therefore, the definition for the material derivative in S-ODT is given by,

$$\rho \frac{D\psi}{Dt} \Big|_{S-ODT} \rightarrow \rho \frac{d\psi}{dt} = \frac{\partial(\rho u\psi)}{\partial x} + \rho v_\psi \frac{\partial\psi}{\partial y}.$$

The definition of u in terms of the total differential is,

$$u = \frac{dx}{dt}. \quad (3.80)$$

This allows to rewrite the total time differential in terms of a streamwise position differential

$$\frac{D\psi}{Dt} \Big|_{S-ODT} \rightarrow u \frac{d\psi}{dx} = \frac{1}{\rho} \frac{\partial(\rho u\psi)}{\partial x} + v_\psi \frac{\partial\psi}{\partial y}. \quad (3.81)$$

Note that for $\psi = u$, it is possible to arrive at a semi-conservative formulation of the form,

$$\frac{1}{2} \frac{du^2}{dx} = \frac{1}{\rho} \frac{\partial(\rho u^2)}{\partial x} + v_\psi \frac{\partial u}{\partial y}. \quad (3.82)$$

Eq. (3.81) or (3.82) are, thus, the corresponding material derivative interpretations in Eq. (3.72-3.73).

For incompressible (constant density) flows, the formulation can be fully conservative given that $\partial v_\psi/\partial y = 0$ and v_ψ can be inserted into the crosswise derivative. Although a conservative formulation is always desired (or in this case, the semi-conservative formulation), this is not always feasible for the type of internally forced convective flows

studied in this thesis. This is due to the simultaneous constraint of the quadratic character of u^2 and the exclusive acceptance of positive values of u due to the mandated or imposed parabolic character of the flow. For internally forced convective flows with a highly elliptic character, the semi-conservative formulation will be prone to produce negative velocity values, indicating recirculation and violating the parabolic requirement of the method. In such cases, the nonconservative formulation for u , i.e., Eq. (3.81), is used.

3.6.3.3 *Conservative T-ODT and S-ODT formulation for open systems*

The presentation of the deterministic part of the ODT model in this thesis is focused solely on the study of crosswise or radial confined flows, i.e., internal channel or pipe flows. The geometric wall constraint imposes a restriction on the expansion or contraction of the Lagrangian volume which can not be solved in a straightforward way using a fully conservative integral formulation, such as the one presented in [64, 66, 69] for T-ODT and S-ODT flows. For incompressible (constant density) T-ODT channel and pipe flows, the formulation presented here reduces (or is equivalent) to the previously cited traditional conservative integral formulations. For variable density T-ODT flows and (both constant and variable density) S-ODT flows, the decomposition of the velocity field into its solenoidal and irrotational contributions leads to a fundamentally different approach in comparison to the traditional open system formulations discussed in [64, 66, 69]. In open systems, the Lagrangian volume has the liberty to expand or contract during the deterministic step. Thus, the formulation for S-ODT boundary layer flows (or variable density T-ODT temporal jets) is different to the one found here. See [64, 66, 69] for more details regarding the deterministic equations for the S-ODT boundary layer type flows, or open T-ODT systems.

Part II

VALIDATION OF THE ODT MODEL:
APPLICATION TO INCOMPRESSIBLE
CONSTANT PROPERTY AND VARIABLE
DENSITY INTERNALLY FORCED CONVECTIVE
FLOWS

INCOMPRESSIBLE CONSTANT PROPERTY CHANNEL AND PIPE FLOWS WITH ODT

This chapter is an adaptation of part of the content submitted for publication in [91].

This chapter and the next chapter focus in turn on the preliminary validation of the ODT model for incompressible constant property and variable density internally forced convective flows.

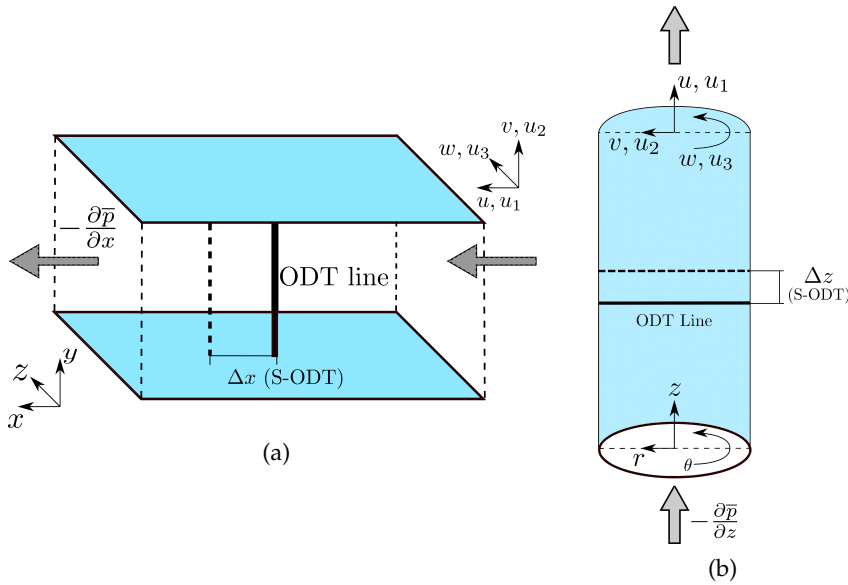


Figure 4.1: (a) Wall-normal ODT line in a channel flow. (b) Radial ODT line in a pipe flow. In both (a) and (b) cases, the T-ODT formulation produces a temporal representation of the scalar profiles within the line. In the S-ODT formulation, the line is advected in the streamwise direction, producing a stationary quasi-2-D scalar representation.

A large part of the body of research for purely incompressible flows focuses on the discussion regarding the universality and appropriate scaling of wall-bounded turbulent flows. As discussed in the introductory chapter, there is a large motivation in DNS research regarding the achievement of asymptotic turbulence states [23]. Thus, the question of the representativeness of either inner or outer scalings becomes relevant. As a reduced order model, ODT has much to offer in this regard, given that it can facilitate such large Reynolds number simulations, practically inaccessible for DNSs.

The absence of bulk flow acceleration in the statistically steady internal incompressible constant property channel and pipe flows is also an ideal test case for the evaluation of both the T-ODT and S-ODT

formulations. Due to the turbulence homogeneity in the streamwise direction, the statistically stationary flow can be directly compared to the statistically streamwise homogeneous flow. This is the Taylor's frozen turbulence hypothesis [92], which can be summarized in the statement,

$$dx = U_b dt \text{ (channel flow)}, \quad dz = U_b dt \text{ (pipe flow)}. \quad (4.1)$$

That is, the changes in the streamwise position can be equated to the product of a corresponding time interval and the streamwise bulk velocity of the flow. For a constant bulk velocity and constant fluid properties, and in the absence of body forces, U_b is related to the pressure gradient by the characteristic skin friction coefficient of the flow, C_f , Eq. (3.63).

Due to the reasons previously discussed, the numerical simulations of incompressible constant property internal channel and pipe flows without additional body forces are the first step in the validation of the ODT model. The numerical ODT simulations performed in this thesis used the base C++ code originally developed by D. Lignell [64, 66]. This code was subsequently modified and extended in order to include the treatment described in this work (see appendices C and D). In this chapter, the ODT formulation is heavily simplified due to the constant density assumption. Additionally, for all of the cylindrical simulations, as well as the planar S-ODT simulations, the treatment described in appendix C concerning the ODT kernel implementation step is also completely omitted due to the use of a single velocity component, i.e., $\alpha = 0$.

4.1 SETUP OF THE NUMERICAL SIMULATIONS

Figures 4.1a and 4.1b show a simplified sketch of the numerical domain in both the channel and pipe configuration cases, respectively. In both cases, the ODT line coincides with the direction of dominant shear, which is the wall normal direction. For both cases, buoyancy and EHD body forces are neglected. Tables 4.1 and 4.2 detail the ODT model parameters used for the channel and pipe flow simulations, respectively. Tables 4.3 and 4.4 detail the adaptive ODT and physical flow configuration parameters for the same simulations. The relevant nomenclature has been already introduced and can be found in the Nomenclature section at the beginning of the thesis. Uniform velocity profiles are considered as initial conditions. The streamwise velocity component is forced in all simulations by means of a fixed pressure gradient (FPG) forcing, $\partial\bar{p}/\partial x$ (see pressure gradient notation clarification in 3.6.2). After an initial transient period is elapsed, online averages for each one of the velocity components, the kinetic energy, and the crosswise (or radial) gradient of the streamwise velocity component, as well as cumulative sums of the changes per grid cell in the

streamwise velocity profile due to eddies are gathered and updated online. This statistical procedure is carried out in an equidistant statistics 1-D grid. The data is gathered until the process achieves statistical stationarity or statistical streamwise homogeneity, in T-ODT or S-ODT simulations, respectively.

Table 4.1: T-ODT and S-ODT model parameters used for channel flow simulations. Table adapted from [91].

ODT Model Parameter	T-ODT	S-ODT
C	6.5	3.0
Z	300.0	100.0
α	$2/3 \approx 0.6667$	0.0

Table 4.2: T-ODT and S-ODT model parameters used for pipe flow simulations. Table adapted from [91].

ODT Model Parameter	T-ODT	S-ODT
C	5.0	3.0
Z	350.0	100.0
α	0.0	0.0

Table 4.3: Adaptive ODT and flow configuration parameters used for channel flow simulations (T-ODT and S-ODT formulation). Table adapted from [91].

Parameter / Case	Case A	Case B	Case C
Domain Length $L_{ODT} = H$ (m)	2.0	2.0	2.0
ρ (kg/m ³)	1.0	1.0	1.0
ν (m ² /s)	1.6949×10^{-3}	1.0707×10^{-3}	0.9985×10^{-3}
$\partial \bar{p} / \partial x$ (Pa/m)	-1.0	-1.0	-4.0
Imposed Reynolds number	590	934	2000
$Re_{\tau} = u_{\tau} H / (2\nu)$			
$\Delta y_{min} = \eta / 3$ (m)	5.6496×10^{-4}	3.5688×10^{-4}	1.6642×10^{-4}
Δy_{max} (m)	0.04	0.04	0.04
\mathcal{S}^{Dens}	80.0	80.0	80.0
$A_{TimeFac}$	25.0 (T-ODT) & 4.0 (S-ODT)	25.0 & 4.0	25.0 & 4.0
Eddy-size PDF l_{max} / L_{ODT}	$1/3 \approx 0.3333$	$1/3 \approx 0.3333$	$1/3 \approx 0.3333$

Table 4.4: Adaptive ODT and flow configuration parameters used for pipe flow simulations (T-ODT and S-ODT formulation). Table adapted from [91].

Parameter / Case	Case A	Case B	Case C
Domain Length $L_{ODT} = D = 2R$ (m)	2.0	2.0	2.0
ρ (kg/m ³)	1.0	1.0	1.0
ν (m ² /s)	1.8182×10^{-3}	1.0×10^{-3}	0.9985×10^{-3}
$\partial\bar{p}/\partial z$ (Pa/m)	-2.0	-2.0	-8.0
Imposed Reynolds number $Re_\tau = u_\tau R/\nu$	550	1000	2000
Δr_C (m)	0.04	0.0222	0.0111
$\Delta r_{min} = \eta/3$ (m)	6.0606×10^{-4}	3.3333×10^{-4}	1.6642×10^{-4}
Δr_{max} (m)	0.04	0.04	0.04
\mathcal{S}^{Dens}	80.0	80.0	80.0
$A_{TimeFac}$	4.0	7.3	14.5
Eddy-size PDF L_{max}/L_{ODT}	$1/3 \approx 0.3333$	$1/3 \approx 0.3333$	$1/3 \approx 0.3333$

4.2 CALIBRATION OF THE MODEL INPUTS

4.2.1 Calibration of the ODT model parameters in T-ODT simulations

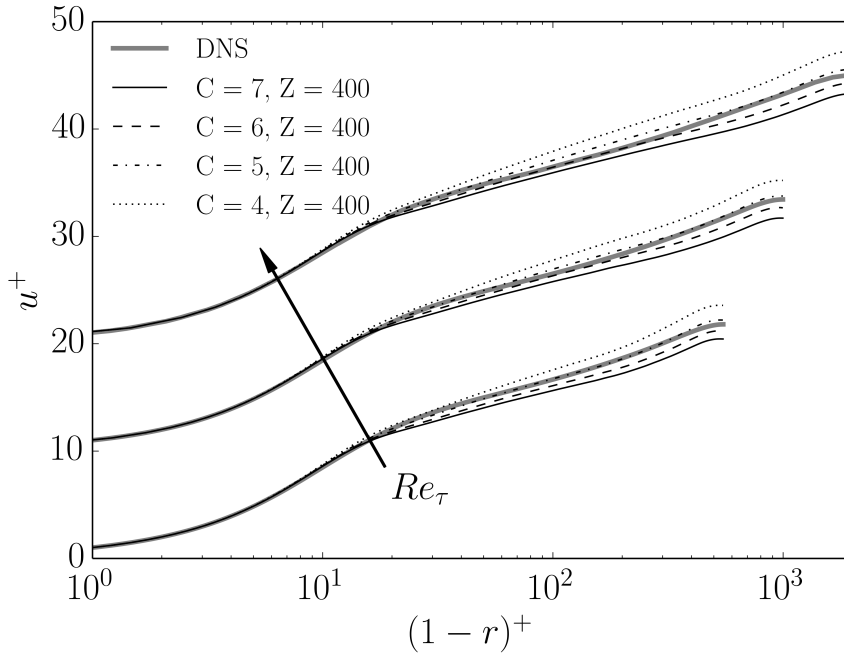
The presence of model parameters grants some degree of empiricism to ODT. Specifically the parameters C and Z must be calibrated in order to produce reliable simulation results. The aim of the parameter calibration is that, due to the physical analogy to the energy cascade achieved by the stochastic eddy event sampling procedure, the local dynamics, as in the Kolmogorov's similarity hypothesis [21], should remain universal. Thus, for large Reynolds numbers, the universality of the nondimensional ODT model parameters should hold, if the simulations are performed in a consistent way.

The calibration procedure for the parameters C and Z was carried out in this case by means of a sensitivity analysis to variations of initial estimated parameter values for the T-ODT and S-ODT channel and pipe flow simulations. The initial parameter values of C and Z were selected based on previous simulations performed by Lignell et al. [64] and Krishnamoorthy [93]. These results allowed the determination of the optimal values for C and Z written in Tables 4.1 and 4.2, which, as will be shown, resulted in a Reynolds number parameter independence for the range of conditions evaluated here. The parameter α was not subject to any sensitivity analysis. Values for α were simply chosen as 0 for the cylindrical T-ODT and all of the S-ODT formulations, since this was the first validation study of its nature¹. For T-ODT channel flow, α was set to $2/3$, since this is the theoretical value imposing equal kinetic energy redistribution among velocity components after an eddy event (see appendix C).

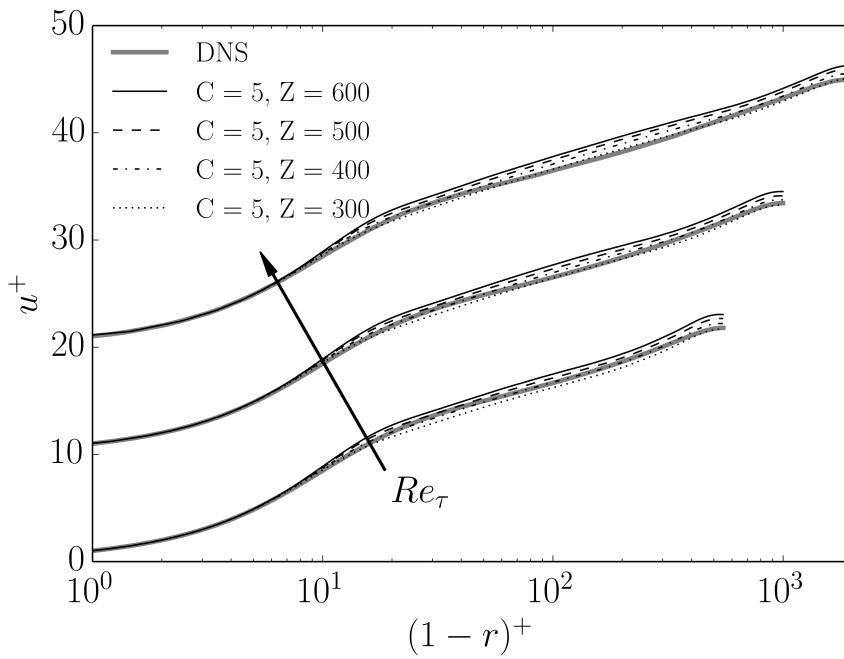
Figure 4.2 shows the sensitivity of the averaged streamwise velocity pipe flow profiles for different values of the parameters C and Z in T-ODT simulations. A review of the average operators and of the inner scaling of quantities in wall bounded flows can be found in the appendices E and G, respectively. All of the averages referenced in this chapter refer to time (T-ODT) or streamwise (S-ODT) averages gathered until the statistical stationarity is achieved². Channel flow profiles are not shown here due to redundancy. The effect of C is directly seen in the number of eddy events implemented during a simulation. This could be interpreted as a measure of the turbulence intensity. Smaller values of C shift the logarithmic region of the averaged velocity profile upwards. This also implies an increase in the slope of the profile in the outer layer. The behavior of the buffer layer is affected by the choice of the model parameter Z . However, in comparison to the phys-

¹ The first study directly comparing T-ODT and S-ODT simulations, and also the first detailed study for the application of the cylindrical formulation in pipe flow, based upon the results obtained in [66].

² For T-ODT, statistical stationarity is achieved. For S-ODT, perhaps a more appropriate term in this case would be statistical homogeneity in streamwise direction.



(a)



(b)

Figure 4.2: Influence of the ODT model parameters on the normalized wall-normal pipe flow mean velocity profile for $Re_\tau = 550, 1000, 2000$. The figures are taken from [91]. DNS results from Khoury et al. [94] ($Re_\tau = 550, 1000$) and Chin et al. [41] ($Re_\tau = 2003$) are shown for reference. Results at larger Reynolds numbers have a vertical offset of 10 nondimensional units for better visualization. a) Sensitivity to C and b) Sensitivity to Z .

ical interpretation of C , Z acts more like a tunable cutoff parameter which aims to reproduce physically reasonable results for the buffer layer representation. This is because for not large enough Reynolds numbers, there is a significant feedback from three-dimensional flow structures into the average flow, which cannot be represented with the parabolic ODT formulation. Increasing the value of Z implies also a shift in the logarithmic region, but with a constant profile slope. Small values of Z are responsible of a reduction of the extent of the buffer layer, and, thus, smaller y^+ starter values for the logarithmic region, as seen in [95].

4.2.2 Influence of the choice of l_{max}

As detailed in chapter 3, l_{max} is the upper limit of the eddy size PDF. The maximum value of l_{max} for the type of flows studied in this thesis is the value of the maximum achievable boundary layer thickness. This would be either half of the corresponding channel width, or the corresponding pipe radius. The effect of l_{max} in ODT channel and pipe flow simulations have been shown in previous studies, and refers to a modification of the outer layer of the averaged streamwise velocity profile [81, 93, 96]. This is shown in Figure 4.3. The parameter l_{max} has the same qualitative impact in both the planar and cylindrical formulations. Larger values are responsible for more mixing in the outer region, close to the centerline. This results in a flatter velocity profile near the centerline.

Motivated by the consistency between the planar and the cylindrical ODT formulation, a normalized value of $l_{max}/L_{ODT} = 1/3$ was selected for both formulations. This is the value of l_{max}/L_{ODT} which was selected for the cylindrical ODT formulation in the work of Krishnamoorthy [93].

4.2.3 Influence of the choice of $A_{TimeFac}$

Next, the influence of the choice of the $A_{TimeFac}$ factor is evaluated. This is the proportionality factor for the time interval (or streamwise interval in S-ODT) after which a mesh adaption process takes place, as detailed in Section 3.3. In the planar T-ODT formulation, the restriction of the time-step due to the CFL condition for the advancement of the diffusion even without implementation of eddy events, can be written in terms of the Kolmogorov length scale η , assuming an arbitrary value for the minimum grid cell size $\Delta y_{min} = \eta/n$, where n is any (integer) number of cells guaranteeing an adequate grid resolution,

$$\Delta t_{CFL} \approx \frac{\Delta y_{min}^2}{\nu} = \frac{\eta^2}{n^2 \nu}. \quad (4.2)$$

For low Reynolds numbers, e.g. the cases with $Re_\tau = 550$, it is very likely that the T-ODT simulations perform several successive diffusion

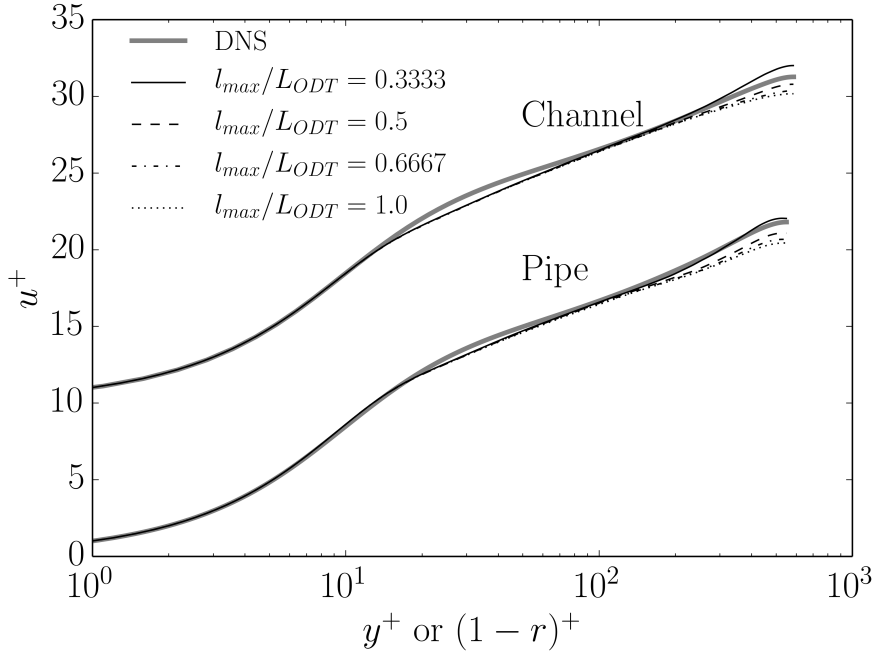


Figure 4.3: Influence of the upper limit of the eddy size PDF l_{max} on the normalized wall-normal pipe and channel flow mean velocity profiles. Pipe flow results are shown for $Re_\tau = 550$ and compared to DNS results from Khoury et al. [94]. Channel flow results are shown for $Re_\tau = 590$ and compared to DNS results from Moser et al. [27]. Channel flow results have been shifted upwards for better visualization. The figure is taken from [91].

catchup steps without the implementation of eddy events in between them. Besides the global low characteristic number of eddy events in low Reynolds number flows, it is also evident that within the 1-D flow itself, there are some regions of the flow with lower probability of implementation of stochastic events. An example of local reduced turbulence is the outer layer, or the region close to the centerline. There is a larger impact of the successive diffusion and corresponding mesh adaption (after sufficient diffusion) in such regions of reduced turbulence. These observations can be verified in Figure 4.4. As in the case of the influence of l_{max} , $A_{TimeFac}$ has approximately the same influence in both the planar and cylindrical formulations. It is noted that the factor $A_{TimeFac}$ has an almost negligible effect in the planar formulation.

The $A_{TimeFac}$ factor is a ratio between the diffusion CFL limited time step and the mesh adaption time scale. It can also be reinterpreted as a ratio between the characteristic eddy implementation time step and the CFL limiting time step, considering that there is a mesh adaption process after the implementation of every eddy event in ODT. This second interpretation allows to find a relation between the friction

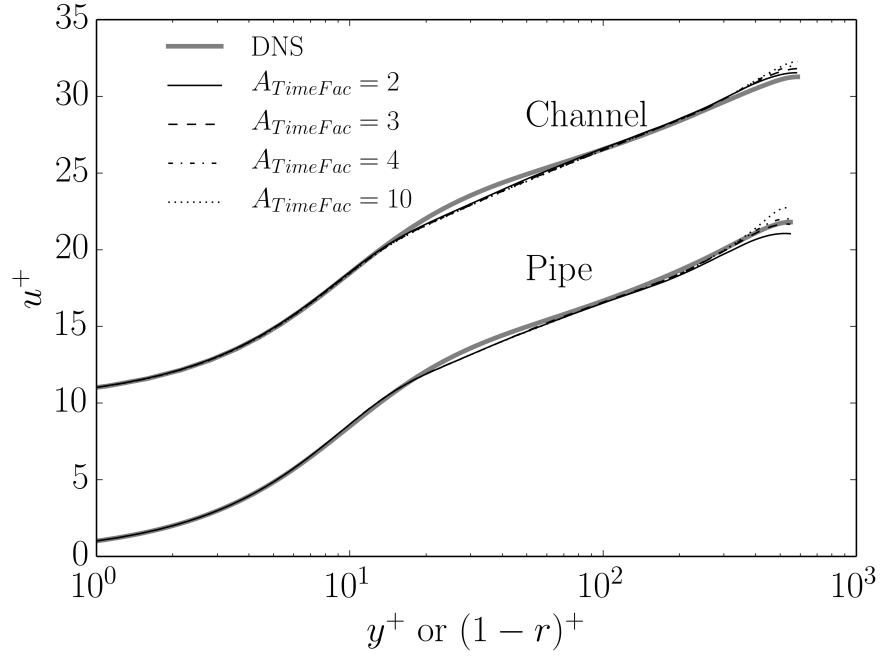


Figure 4.4: Influence of $A_{TimeFac}$ on the normalized wall-normal pipe and channel flow mean velocity profiles. Pipe flow results are shown for $Re_\tau = 550$ and compared to DNS results from Khoury et al. [94]. Channel flow results are shown for $Re_\tau = 590$ and compared to DNS results from Moser et al. [27]. Channel flow results have been shifted upwards for better visualization. The figure is taken from [91].

time scale³ and the CFL limited time step. In the planar formulation, this is,

$$A_{TimeFac} \sim \frac{\Delta t_\tau}{\Delta t_{CFL}} \rightarrow A_{TimeFac} \sim \frac{H}{2u_\tau} \frac{n^2\nu}{\eta^2}. \quad (4.3)$$

Eq. (4.2) was used in order to arrive to Eq. (4.3). The friction time scale, Δt_τ , is defined in the planar case as the ratio between the channel half-width (or half-height) $H/2$ and the friction velocity. Eq. (4.3) allows the formulation of a scaling law for $A_{TimeFac}$ in terms of Re_τ , the friction Reynolds number. This is because $u_\tau = 2Re_\tau\nu/H$. For two different friction Reynolds number flows which consider the same geometric configuration, the ratio between the 2 corresponding $A_{TimeFac}$ factors is,

$$A_{TimeFac,2} = A_{TimeFac,1} \frac{Re_{\tau,2}}{Re_{\tau,1}}. \quad (4.4)$$

Therefore, it is possible to calibrate $A_{TimeFac,1}$ for a given $Re_{\tau,1}$ and find the corresponding $A_{TimeFac,2}$ of another flow at $Re_{\tau,2}$. In this

³ The friction time scale is the local inner scaling factor for the time, which should be universal with the eddy implementation at the small scales

chapter of the thesis, the calibration of $A_{TimeFac}$ was done based on the results obtained in Figure 4.4 for Case A in the channel and pipe flow configuration. It is noted, however, that for planar channel flow configurations at larger values of Re_τ , the results were insensitive to the scaling of $A_{TimeFac}$. Since this has not been discussed in previous ODT investigations up to this date, it is expected that this parameter only plays a role, thus, in the cylindrical configuration. This is shown in Figure 4.5.

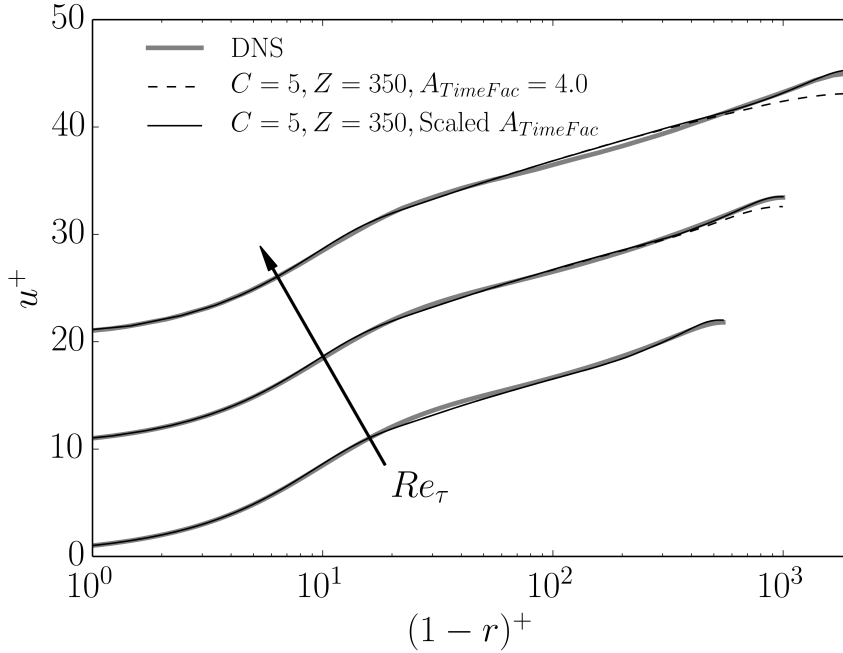


Figure 4.5: Influence of DATimeFac scaling on the normalized wall-normal pipe flow mean velocity profile for $Re_\tau = 550, 1000, 2003$. DNS results from Khoury et al. [94] ($Re_\tau = 550, 1000$) and Chin et al. [41] ($Re_\tau = 2003$) are shown for reference. The results for increasing Reynolds numbers have been shifted upwards in the plot for better visualization. The figure is taken from [91].

Sensitivity to the factor $A_{TimeFac}$ is attributed to the symmetric center cell treatment in the cylindrical ODT formulation, as detailed in chapter 3. Since the treatment is avoided in the planar formulation, the planar results are insensitive to the factor. The spatial cylindrical formulation is also affected in the same way by $A_{TimeFac}$. The same friction Reynolds number relation of Eq. (4.4) also holds for the spatial formulation.

4.3 SIMULATION RESULTS AND DISCUSSION

Comparisons between the T-ODT and S-ODT formulations were carried out as a validation method to evaluate the Taylor's hypothesis, which holds for fully developed incompressible internal flows. That is,

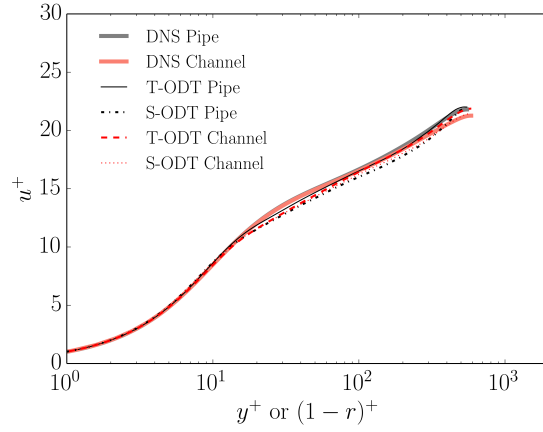
evaluating time averages for streamwise and spanwise (or circumferential) spatially homogeneous flows, is equivalent to the evaluation of streamwise averages of stationary and circumferentially homogeneous flows. Although the optimal parameters for C and Z chosen for the S-ODT formulation are very close to their counterpart values in the T-ODT formulation, both counterparts are not equal. This is due to the parabolic spatial advancement scheme being naturally distinct to the parabolic temporal advancement, both in the form of the deterministic equations, as well as in the formulation of the eddy turnover time in T-ODT, which is switched to an eddy turnover length in S-ODT.

4.3.1 Mean flow statistics

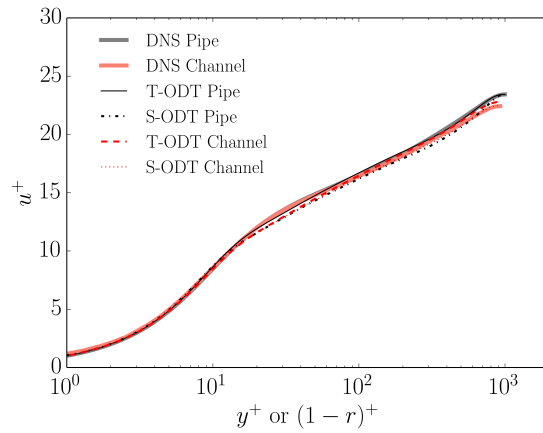
The S-ODT formulations in [64, 66, 69] all are stationary quasi-2-D formulations developed for the treatment of boundary layer type flows. This is because the boundary layer flow is the natural assumption of a stationary parabolic flow. However, the internally forced convective flows evaluated in this thesis do not resemble boundary layer flows, but rather, fully developed flows. In a boundary layer flow, the sum of the average pressure and the bulk kinetic energy are a constant in streamwise direction. For fully developed flows, the bulk kinetic energy itself is a constant in streamwise direction, the reason for which, the average pressure gradient has no other option but being a constant. For incompressible constant property flow, it is possible to relate the average streamwise pressure gradient with the wall shear stress, reason for which it is possible to force a certain friction Reynolds number with a FPG forcing method [32]. Therefore, a FPG forcing method is used in this chapter of the thesis, as detailed in Tables 4.1 and 4.2. It is noted that it is not possible to directly relate the wall shear stress with the pressure gradient in a variable density flow due to the inherent bulk flow acceleration produced by density gradients. In such cases, the constant average pressure gradient must be forced with a Constant Flow Rate (CFR) forcing method.

Figure 4.6 summarizes the simulation results for the wall-normal profiles of the mean streamwise velocity component for all Reynolds numbers evaluated in this chapter. Following the DNS work from Chin et al. [41], the friction Reynolds numbers $Re_\tau = 590$ and $Re_\tau = 934$ of the channel flow simulations are compared to the pipe friction Reynolds numbers $Re_\tau = 550$ and $Re_\tau = 1000$, respectively. The comparison is not intended as a one to one quantitative comparison given that the corresponding friction Reynolds numbers are not exactly the same. Having said that, the differences in the statistics shown here due to the differences in such Re_τ are expected to be negligible.

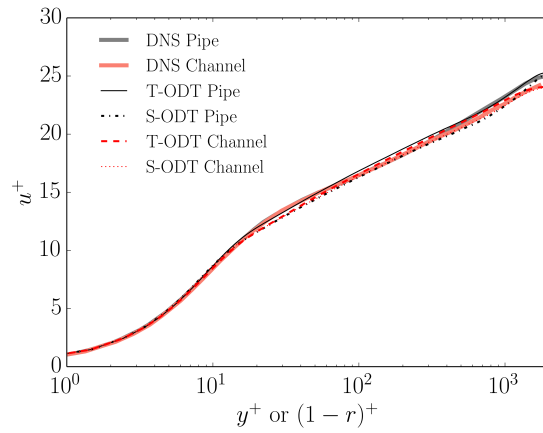
Good qualitative reproducibility of mean velocity profiles in ODT has been demonstrated in previous studies for channel flow simulations [81, 96]. The viscous layer is resolved in ODT. As such, the linear



(a)



(b)



(c)

Figure 4.6: Wall-normal profiles of mean streamwise velocity component in ODT channel and pipe flow simulations. a) The low friction Reynolds number case (Case A) is shown along with DNS results from Moser et al. [27] (channel) and Khoury et al. [94] (pipe). b) Case B results are shown along with DNS results from Hoyas and Jiménez [30] (channel) and Khoury et al. [94] (pipe). c) Case C results are shown along with DNS results from Hoyas and Jiménez [30] (channel) and Chin et al. [41] (pipe). The figures are taken from [91].

relation between the nondimensional velocity and the nondimensional distance from the wall in the viscous layer, $u^+ = y^+$, is observable for small y^+ values in Figure 4.6. The inner layer and the logarithmic layer are also well reproduced. The logarithmic layer is easily recognizable in all ODT cases by the extension of a lineal slope in y^+ values larger than 30. As commented previously, the presence of non-homogeneous three-dimensional structures has a large effect on the buffer layer of the mean flow streamwise velocity profile [81]. On one hand, there is no solid argument by which one could expect an accurate quantitative or qualitative match between DNS and ODT mean flow statistics in the buffer layer. The selection of an optimal Z parameter is a way to alleviate this issue. On the other hand, these non-homogeneous structures, which grant elliptic features to the flow, become smaller and less relevant at larger Reynolds numbers. The achievement of a truly one-dimensional turbulence characterized exclusively by the Reynolds number, and not by the bulk geometry of the problem, becomes then dominant. The better representation of the buffer layer with increasing Reynolds numbers can be seen by comparing the different profiles in Figure 4.6.

The ODT similarity between the channel and pipe flow simulations is also evident from Figure 4.6, as in the DNS results. Given the novel character of the cylindrical ODT formulation [66], this is an aspect worth noting. The chosen optimal ODT parameters, C and Z , for both the planar and cylindrical formulations exhibit this similarity as well. In the S-ODT formulation, C and Z are the same for both the pipe and channel flow configurations, i.e., $C = 3.0$ and $Z = 100.0$. By comparing ODT and DNS results, it is also clear that channel flows show an earlier departure into the logarithmic layer, in comparison to pipe flows [91].

The S-ODT mean velocity profiles lie in all cases below those obtained with the T-ODT formulation for the corresponding chosen input ODT model parameters, C and Z . In the S-ODT results, a larger velocity gradient is noticeable in the outer layer of the profile, close to the channel or pipe centerlines.

Next, the obtained ODT RMS velocity profiles are presented and compared against DNS data. This is shown in Figure 4.7. It is noted that the RMS profiles are obtained by the identity given in appendix E, Eq. (E.6),

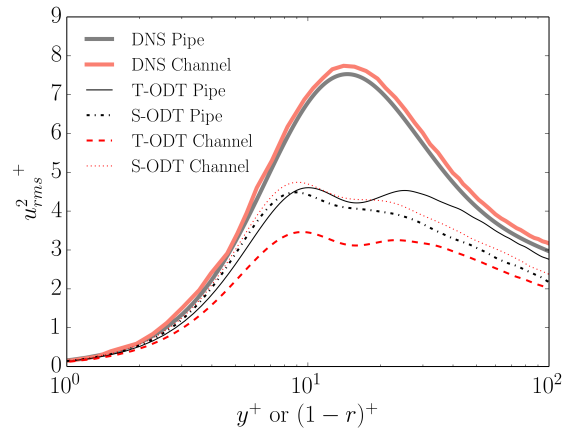
$$\psi_{RMS} = \sqrt{\langle \psi' \psi' \rangle} = \sqrt{\langle \psi^2 \rangle - \langle \psi \rangle^2}. \quad (\text{E.6})$$

That is, the RMS velocity profile of the velocity component u_k is the difference between the average kinetic energy of velocity component u_k and the kinetic energy of the mean flow by velocity component u_k . This definition is important because, despite having obtained a good representation of the mean flow as shown before, the representation of the kinetic energy in ODT may not be accurate. A derivation of

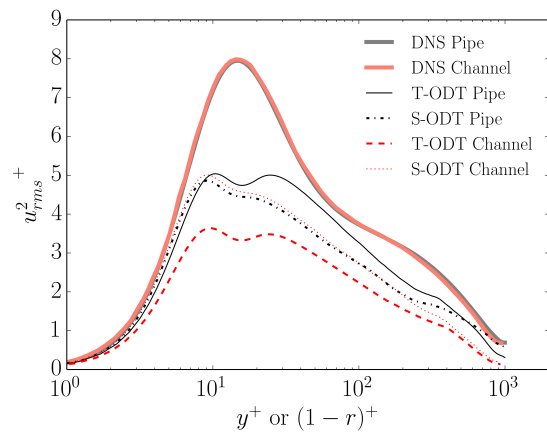
the average, mean and turbulent kinetic energy equations and their components or contributions can be found in appendix F. Momentarily, it is sufficient to say that the average kinetic energy in ODT is in any case smaller in magnitude than expected, in comparison to the conservation statement given by Eq. (2.53). This is due to the parabolic simplifications constraining the magnitude of the viscous dissipation by the shear stresses. The treatment of the pressure transport by the flow velocity in Eq. (2.53) is also not clear in ODT due to the constant streamwise pressure gradient assumption and the zero (or non-resolved) pressure gradient in any other direction off the line. Since the average kinetic energy is smaller than expected, the RMS velocity profiles are also smaller in magnitude than their DNS counterpart. This underestimation of the RMS velocity profiles shown in Figure 4.7 is consistent with previous ODT investigations [64, 81].

The dominance of the viscous shear stress in the viscous layer may be responsible for the slight parallel shift between ODT and DNS results seen in Figure 4.7. That is, as discussed before, the discrepancy between the ODT averaged kinetic energy and the 3-D DNS flow averaged kinetic energy of the corresponding velocity components. However, the deviation between ODT results and DNS data becomes more significant for the y^+ values after the ODT RMS peak close to the wall. The peak itself is underestimated. Nonetheless, the similarity between channel and pipe flow ODT simulations is also seen in the RMS plots. Before discussing apparent changes in the magnitude of the RMS profiles between the T-ODT and S-ODT formulations, it is noted that the RMS double peak seen in the T-ODT profile is simply an intrinsic *feature* of the ODT triplet maps [64]. Although it is common to find references to a second peak discussion in large Reynolds numbers DNSs such as [24, 41], the phenomena observed in ODT has a completely unrelated explanation, see [64]. The double peak *feature* is attenuated in the S-ODT results. The attenuation, or up to some extent, disappearance, of the not directly physical double peak T-ODT *feature* in S-ODT could be seen as an advantage of the spatial formulation. Nevertheless, given that the valley between both peaks in T-ODT approximately coincides with the y^+ value of the DNS peak RMS value, this is also an advantage of the T-ODT formulation, when compared with the simple offset of the single S-ODT RMS peak. Thus, the compromise in the trading of the peak *feature* is clear.

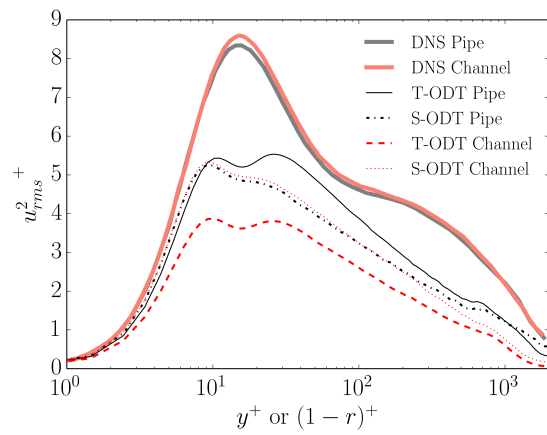
The discussion is now shifted to the discrepancy in the magnitude of the channel and pipe flow T-ODT RMS velocity profiles. The model parameter identified as responsible for this discrepancy is α . The model parameter α was set to 0 for the pipe flow T-ODT simulations, while it was $2/3$ in the channel flow T-ODT simulations. $\alpha = 0$ implies that the flow kinetic energy is fully contained in the streamwise velocity component. That is, there is no redistribution of kinetic energy after an eddy event. If the flow is assumed to start with a kinetic energy given



(a)



(b)



(c)

Figure 4.7: Wall-normal RMS profiles of streamwise velocity component. (a): the low friction Reynolds number case (Case A) is shown along with DNS results from Moser et al. [27] (channel) and Khoury et al. [94] (pipe). (b): Case B results are shown along with DNS results from Hoyas and Jiménez [30] (channel) and Khoury et al. [94] (pipe). (c): Case C results are shown along with DNS results from Hoyas and Jiménez [30] (channel) and Chin et al. [41] (pipe). The figures are taken from [91].

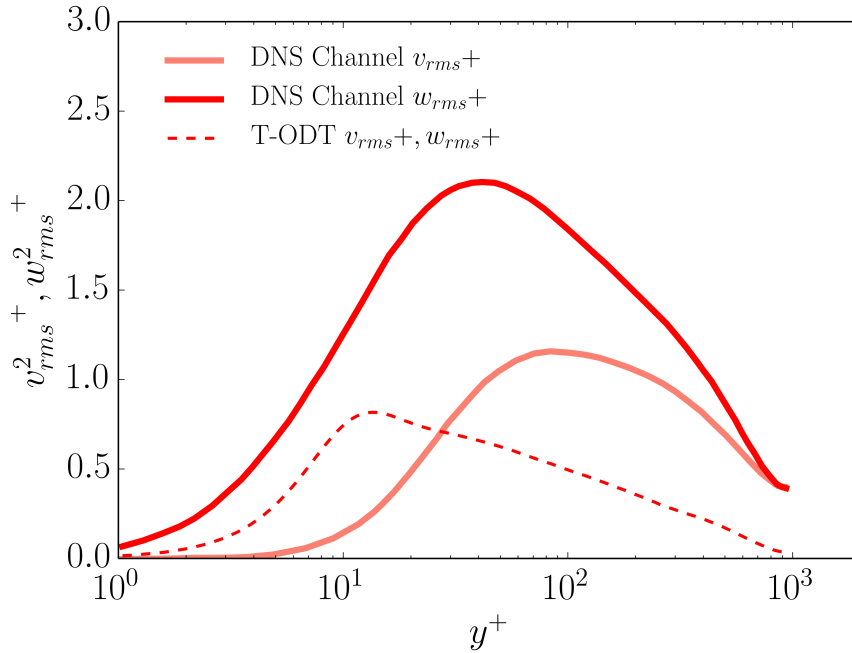


Figure 4.8: Case B results for channel crosswise and spanwise RMS velocity profiles compared to DNS results from Hoyas and Jiménez [30]. The figure is taken from [91].

exclusively by the streamwise velocity component (as it was effectively the case in all simulations), the kinetic energy will, therefore, remain in the streamwise velocity component during the whole simulation. Since there is no redistribution of kinetic energy, it is clear that the RMS profile of the streamwise velocity component should be larger in the $\alpha = 0$ simulations. This is also the reason why Figure 4.8 only shows the crosswise and spanwise RMS velocity profiles of the T-ODT channel flow simulations, given that there is no representation of v or w neither in the cylindrical simulations, nor in the S-ODT simulations due to the selection $\alpha = 0$. Furthermore, given that the initial conditions of the T-ODT channel flow simulations were the same for both v and w (essentially uniform zero velocity), the RMS profiles for v and w are the same⁴. As in the case of the streamwise RMS velocity profile, the crosswise and spanwise RMS velocity profiles are underpredicted in comparison to DNS results. This has already been shown in previous ODT channel flow simulations at lower Reynolds numbers [75, 96].

T-ODT and S-ODT results for the pre-multiplied mean velocity gradient in Case B simulations, together with the corresponding available DNS data for comparison, are shown in Figure 4.9. The most salient feature of this plot is the large signal noise in the outer layer. For Case B, there is a second peak of the signal in this large noise region, i.e., in the range $100 < y^+ < 1000$. This second peak indicates the change

⁴ This is in addition to the trivial fact that both $\langle v \rangle$ and $\langle w \rangle$ are zero.

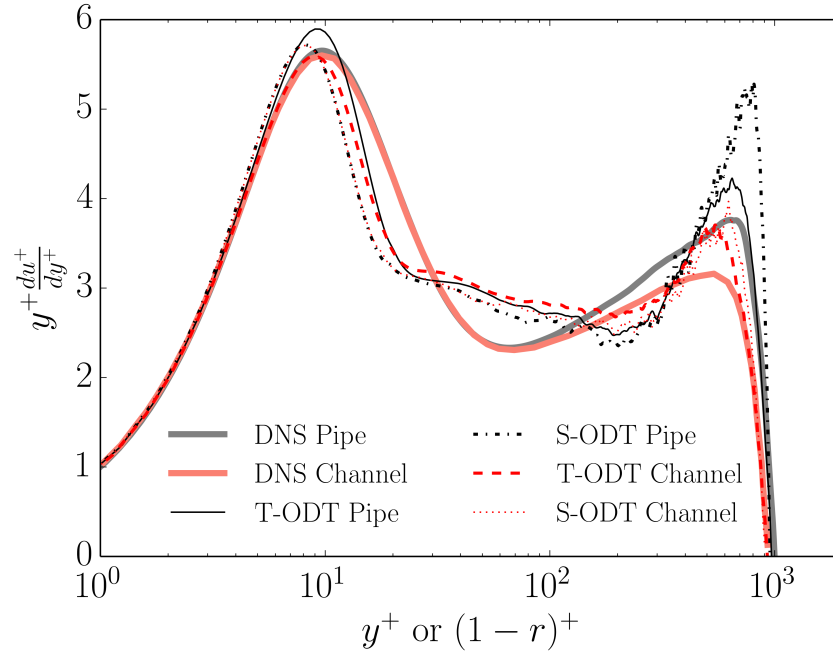


Figure 4.9: Pre-multiplied mean velocity gradient obtained in Case B simulations. DNS results from Jiménez et al. [97] (channel) and Khoury et al. [94] (pipe) are shown for reference. The figure is taken from [91]

in the average velocity gradient due to the bulk flow. The noise component is in this case indicating insufficient averaging due to seldom implementation of large (in size) eddy events, as would be expected from *bulk flow eddies*. Given that a larger averaging does not modify the qualitative results, and the fact that other second order statistical quantities (e.g., RMS profiles) already converged with the pre-selected averaging periods, the noise component is simply left as such in Figure 4.9. This bulk flow, or large scale representation, as it has been extensively discussed so far, is inadequate in ODT. In this case, this results in an overestimation of such second peak of the pre-multiplied velocity gradient. Nonetheless, one important finding from DNS can be corroborated with ODT. That is, there is no constant region of pre-multiplied velocity gradient beyond the point of departure of the outer buffer layer [91]. In that sense, there is no applicable logarithmic law, implying that there is no clear dominance of the turbulent transport. Still at a Reynolds number $Re_\tau = 1000$, it is not possible to talk about an asymptotic turbulence state. Such asymptotic state with a constant region of pre-multiplied mean velocity gradient only starts appearing at fairly large Reynolds numbers [94]. Even in $Re_\tau = 2000$ (Case C), the results are qualitatively not different. For channel flow, Lee and Moser [31] have shown that this constant region of the pre-multiplied velocity gradient only appears at $Re_\tau > 4200$.

The first peak of the pre-multiplied mean velocity gradient indicates the change in the mean velocity gradient due to the small turbulent scales. The position of this peak coincides with the position of the first peak of the streamwise RMS velocity profiles shown in Figure 4.7. This is a sign of consistency of the model. As discussed before, given that the mean flow is properly represented in ODT, as seen in Figure 4.6, and due to the universality of the small scale turbulent transport, the qualitative and quantitative agreement is reasonable for the first peak.

4.3.2 Reynolds shear stress and TKE Budgets

In ODT, the effect of the turbulent advection in the mean flow, i.e., the Reynolds shear stress, is given entirely by the effects of the stochastic eddy events. This is the reason why the Reynolds shear stress has been traditionally evaluated in ODT as the average change of the velocity or scalar profiles during eddy events. These calculation methods have been detailed in other ODT publications [62, 72, 75, 91] and are summarized again in appendix F for the constant and variable density flow cases, respectively.

Figure 4.10 corresponds to the Reynolds shear stress component $\langle u'v' \rangle$ of Case B simulations in both the planar and cylindrical formulation. Qualitatively, ODT is able to achieve a very good reproducibility of the DNS calculated Reynolds shear stress. The best match of the inner layer is obtained in the T-ODT planar formulation ($\alpha = 2/3$), while the best match of the outer layer is obtained for the S-ODT cylindrical formulation ($\alpha = 0$). In general, the good representation of the mean flow in ODT allows, thus, a good representation of the Reynolds shear stress.

To finalize this chapter, an overview of the incompressible TKE production and dissipation terms given in appendix G is shown next. Results for the pipe and channel flow Case B simulations are shown in Figure 4.11. Due to the reasonable agreement of both the mean flow and the Reynolds shear stress shown before, the TKE production budget is also qualitatively well matched in ODT. Discrepancies in the TKE dissipation have been also already addressed in previous comments along this chapter. The lesser dissipation magnitude in the viscous layer is linked to the reduced magnitude of the average kinetic energy. For the buffer layer, it is noted that there is an overestimation of the dissipation in the S-ODT formulation. This could be related to the disappearance of the second peak in the RMS velocity profiles shown in Figure 4.7, given that the position of the dissipation peak close to the wall coincides with the alleged position where the second peak in the RMS profile should be, if the ODT formulation were the T-ODT one, instead of the S-ODT one. Likewise, the dissipation budget sink close to the wall could also be interpreted as a feature of the ODT model,

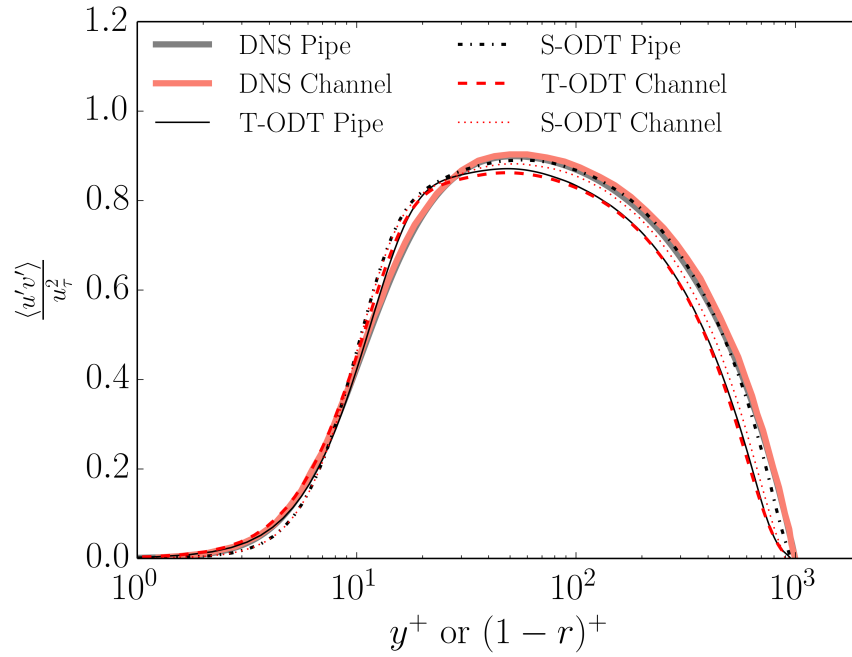


Figure 4.10: Case B nondimensional Reynolds shear stress component $\langle u'v' \rangle / u_\tau^2$. DNS results from Lee and Moser [31] (channel) and Khoury et al. [94] (pipe) are shown along for comparison. The figure is taken from [91].

where the dissipation is lower in regions of large production [98]. This is because of the way in which the diffusion catchup is implemented directly after the implementation of stochastic eddy events. The 1-D stochastic eddy events are created and then subject immediately to diffusive dissipation. This is of course not an accurate representation of the physical turbulence picture, and thus, is in disagreement with the DNS data.

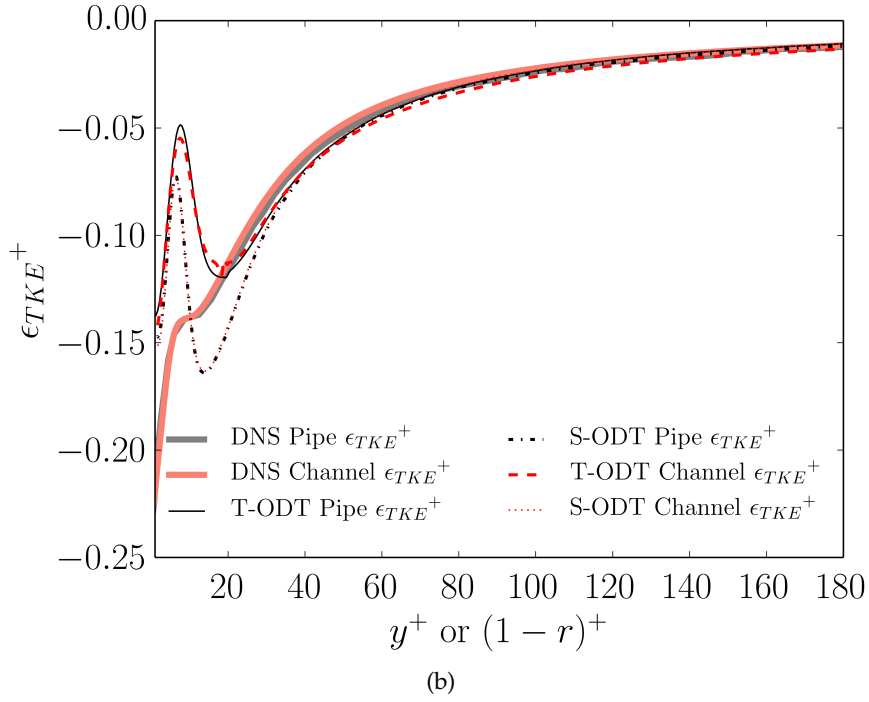
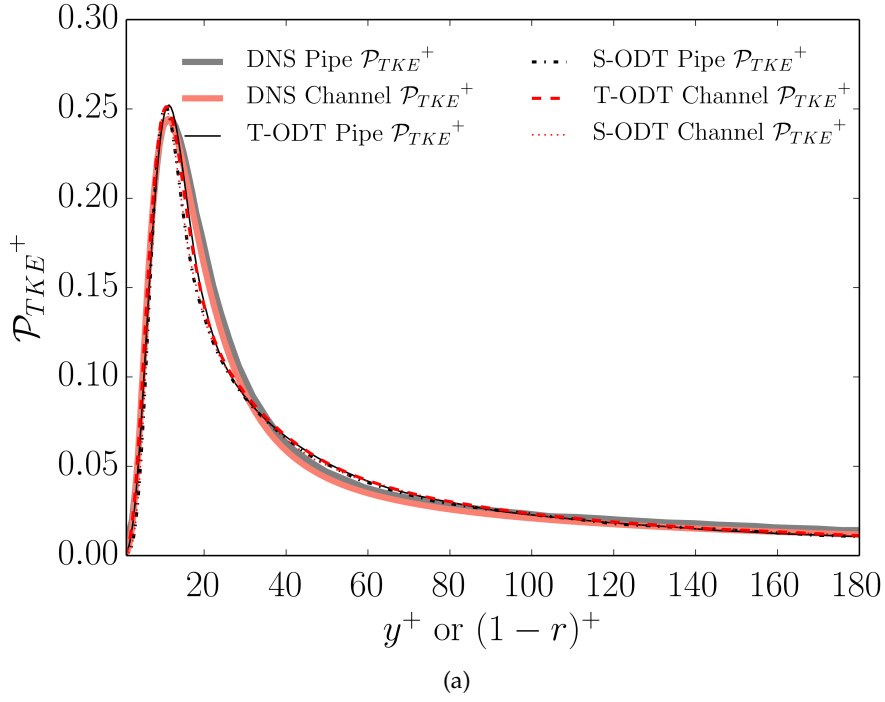


Figure 4.11: TKE Production (\mathcal{P}_{TKE}^+) and Dissipation (ϵ_{TKE}^+) budgets for T-ODT and S-ODT simulations (Case B). DNS results from Lee and Moser [31] (channel) and Khoury et al. [94] (pipe) are shown for comparison. (a) Production budget. (b) Dissipation budget. The figures are taken from [91].

This chapter is an adaptation of the content published in [72].

Additional to considering the work in [72] as a further validation case for ODT, it was also an extension of the variable density S-ODT formulation for confined flows (internal flows). Figure 5.1 illustrates the different applications for both the traditional S-ODT formulation in [64, 66, 69] and the alternative formulation in [72]. A detailed overview of the differences between the formulations, as well as an overview of the issues encountered by the traditional formulation in confined flows can be found in [72, 91]. The detailed comparison between the formulations, as well as the overview of issues is omitted from this thesis. This is because the alternative formulation is likely to be superseded in the future by a more general, fully conservative formulation, as suggested in a private communication with A. R. Kerstein. Nonetheless, the formulation used in [72] was the one selected for use in the evaluation of the EHD-enhanced flows studied in this thesis, and thus, it was the one that has been explained so far throughout the thesis.

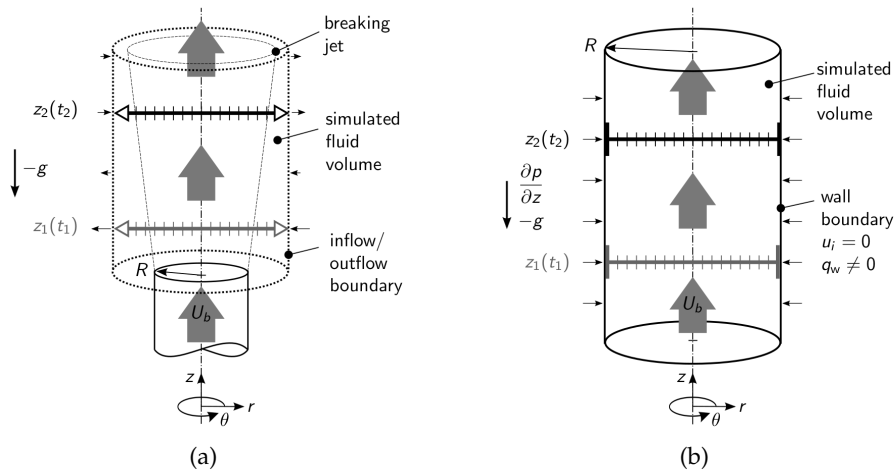


Figure 5.1: This figure shows two types of flows evaluated with ODT. (a) is a free shear flow, a cylindrical jet, which can be evaluated with both the T-ODT formulation, and the traditional S-ODT formulation [64, 66, 69]. (b) is an internally forced convective flow, a pipe flow, which can also be evaluated with the T-ODT formulation, but which motivated an alternative S-ODT formulation [72, 91]. Both (a) and (b) flows are simulated by a CFR constraint, i.e., fixed mass flux per unit area ρU_b . The figures are taken from [72].

Both flows described in Figure 5.1 (a) and (b) can be studied with the T-ODT formulation for the determination of statistically stationary

flow properties. For incompressible and constant property internally forced convective flows without body forces, such as the ones evaluated in the previous chapter, statistically streamwise homogeneous properties and statistically stationary properties are both equal. This is because a straightforward integration for time of Eq. (4.1) is possible, given that U_b is position independent at statistical stationarity,

$$dt = \frac{1}{U_b} dz \rightarrow \Delta t = \frac{1}{U_b} \Delta z. \quad (5.1)$$

In statistically stationary variable density flows, the streamwise density gradients are responsible for bulk flow acceleration or deceleration effects due to mass conservation, see Eq. (A.7). Since U_b is now a function of z , the direct integration of Eq. (5.1) is not possible. Hence, in this case, it is not possible to evaluate streamwise dependent properties with a T-ODT formulation, unless an ad-hoc transformation of time into space based on a numerical approximation of Eq. (5.1) is used. It is certainly of interest to evaluate the performance of such ad-hoc transformation, against a more suitable S-ODT formulation solution. In order to achieve this goal, a variable density internal pipe flow was considered. The variable density effect is achieved by a non-zero wall heat flux condition as illustrated in Figure 5.1, i.e., $q_w \neq 0$.

Only flow (a) in Figure 5.1 can be evaluated with the traditional S-ODT formulation from [64, 66, 69]. In flow (b), an alternative formulation is required due to the inability to expand or contract the Lagrangian system volume as the natural response for the enforcement of mass conservation. That is, the pipe walls constrain the gain or loss of radial mass flux at the walls, which would be the flux divergence response to the gain or loss of streamwise mass flux in the statistically stationary cylindrical jet flow. Given the theoretical motivation discussed so far, this chapter of the thesis describes then the results obtained for T-ODT and S-ODT simulations of a streamwise developing internal pipe flow with variable density effects due to heat transfer from the pipe wall.

5.1 SETUP OF THE NUMERICAL SIMULATIONS

The validation of the ODT simulations was done comparing the results obtained both for the T-ODT and S-ODT formulations with the results from the DNSs of Bae et al. [46]. Due to this reason, the flow configuration was setup as closely to the DNS as possible. In the DNS, strongly heated air flows in vertical ascending direction within a numerical pipe. The gravitational force is considered as a body force in the numerical simulations. However, no EHD body force is applied to the flow. Since the streamwise direction coincides with the vertical direction, the effects of the gravitational body force refer exclusively to an acceleration or deceleration effect either supporting or restraining the effect of the mean streamwise pressure gradient, or in this case, of

the applied CFR/streamwise mass flux constraint. The simulations are based on the case 618 of the DNS [46]. The working fluid considered is air at initial standard conditions of temperature and pressure. Air composition is assumed constant (21% O₂ and 79% N₂). Additionally, the air is assumed to behave as an ideal gas.

The simulations were done after a modification of the adaptive C++ ODT code from D. Lignell, as commented in the previous chapter. The stochastic and deterministic advancement algorithms in the ODT code are described both in appendix C and D, in addition to being described in detail in the original publication of the work, [72]. The calculation of the thermodynamic properties of air, which are updated during the deterministic advancement, before the enforcement of the divergence condition¹, is done using the NASA polynomials for standard air libraries contained in the software suite of Cantera [99]. The update of the enthalpy based on temperature values coming from the integration of the temperature equation, is also done with the same method. The update of the density based on the temperature is also solved by Cantera using the ideal gas law [99]. In the DNS study, a polytropic process is considered for air, and air properties are determined from power laws [46]. The use of these power laws results in slightly different fluid properties for the same values of temperature and pressure. This is, e.g., the reason behind the slightly different initial Grashof number in the ODT simulations, in comparison to the initial DNS Grashof number ($Gr_{0,DNS} = 6.78 \times 10^6$ vs. $Gr_0 = 6.10 \times 10^6$).

The initial conditions for both the T-ODT and S-ODT simulations were formulated in analogy to [46]. Initial conditions for the velocity field in the ODT line were obtained by simulating a fully developed incompressible and constant property pipe flow with a CFR (constant bulk velocity) constraint. The corresponding initial bulk velocity value was determined based on the initial bulk Reynolds number of the variable density simulations, considering initial air properties defined at standard temperature and pressure. Given that the objective of the simulations is the evaluation of streamwise dependent properties, there is a high sensitivity of the results to the initial conditions. In order to minimize the effects of the initial conditions, an ensemble of fully developed incompressible and constant property pipe flow simulations is used as initial conditions for the velocity profiles. The ensemble of initial conditions is generated by taking snapshots of the flow (either in the T-ODT or S-ODT incompressible constant property formulation), once the statistical stationarity of the flow is achieved. It is noted that every ensemble member of the streamwise velocity initial conditions achieves the desired $Re_{b,0}$, yet, only the entire ensemble (average) should be able to achieve the friction Reynolds number $Re_{\tau,0}$ that should correspond to the given $Re_{b,0}$ according either to the DNS

¹ The mass conservation enforcement in the Lagrangian framework.

specification or the approximation given by Colebrook's law and the corresponding skin friction coefficient [32].

The streamwise properties of the flow are also evaluated following the ensemble philosophy. Results are produced at equidistant streamwise intervals, and the fluid properties at specific streamwise positions are then either ensemble of Favre-averaged, as indicated in appendix E.

The input parameters regarding the flow conditions, as well as the mesh adaption parameters used in the simulations are specified in Tables 5.1 and 5.2. The ODT model parameters for the T-ODT formulation are selected based on the results presented in chapter 4, as well as the findings of a previous validation study using a variable density ODT formulation with a very low applied wall heat flux, resulting in the limit of an incompressible constant property flow, or incompressible constant property ODT formulation, where the temperature behaves as a passive scalar [100]. Unlike the results presented in chapter 4, no sensitivity analysis for the ODT model parameters is carried out in this chapter. This is because it is expected that approximately with the same order of magnitude, or in some cases even with the same parameters used in the incompressible constant property simulations from chapter 4, the simulations should yield physically consistent results. As in chapter 4, no sensitivity analysis for the influence of α is carried out. The value of $\alpha = 2/3$ is selected based on the simple theoretical choice demanding an equal kinetic energy redistribution after every implemented eddy event. Z values for the T-ODT and S-ODT simulations are the same ones used in chapter 4. C values for both the T-ODT and S-ODT simulations are adjusted at smaller values than those used in chapter 4 due to the expected reduction in the turbulence intensity, or expected reduction in C at lower Reynolds numbers [100]. This is because a value of $C = 0$ is indicative of a laminar flow, in which no eddy events are implemented.

5.2 SIMULATION RESULTS AND DISCUSSION

5.2.1 Bulk flow statistics

Bulk quantities are calculated at equidistant streamwise positions (or equidistant time intervals) in every ensemble member, and then averaged across the ensemble. In order to compare the T-ODT and S-ODT results, it is necessary to apply the ad-hoc temporal-to-spatial transformation alluded to previously. Echehki et al. [101] suggest the use of the following transformation in ODT,

$$z(t + \Delta t) = z(t) + \int_t^{t+\Delta t} U_b(t') dt', \quad (5.2)$$

Table 5.1: Physical, adaptive mesh, and ensemble settings of the variable density T-ODT and S-ODT simulations. Table adapted from [72].

Physical settings	Description / Value
Method used to generate initial conditions	Incompressible and constant property T-ODT simulation forcing constant $U_{b,0}$
Initial Reynolds number $Re_{b,0} = \rho_0 U_{b,0} D / \mu_0$	6000
Initial bulk velocity $U_{b,0}$	3.4896
Domain size $L_{ODT} = D = 2R$ (m)	0.0274
Initial Temperature T_0 (K)	298.15
Initial Pressure P_0 (Pa)	100000
Fixed nondimensional wall heat flux $q^* = q_w / (\rho_0 U_{b,0} T_0 c_{p,0})$	0.0018
Initial Grashof number $Gr_0 = (g q_w D^4 \rho_0^2) / (\mu_0^2 \sigma_{T,0} T_0)$	6.1030×10^6
Initial Prandtl number $Pr_0 = \mu_0 c_{p,0} / \sigma_{T,0}$	0.71
Adaptive mesh settings	Value
$\Delta r_{min} = \eta_0 / 6$ (m)	1×10^{-5}
Δr_{max} (m)	8.22×10^{-4}
Δr_C (m)	7.23×10^{-4}
g^{Dens}	80.0
$A_{TimeFac}$	1.48
Eddy-size PDF l_{max} / L_{ODT}	$1/2 = 0.5$
Ensemble settings	Value
Number of ensemble members N_{ens}	4800

Table 5.2: ODT model parameters of the variable density T-ODT and S-ODT simulations. Table adapted from [72].

Parameter / Formulation	T-ODT	S-ODT
C	3.5	2.5
Z	350	100
α	$2/3 \approx 0.6667$	$2/3 \approx 0.6667$

where t is any reference time instant and Δt is an arbitrary time interval. Just like U_b is a function of the streamwise position in the 2-D flow, U_b is a time-dependent function in the transient T-ODT simulation. U_b is estimated in T-ODT based on conservation of mass as,

$$U_{b,T-ODT} = \frac{\int_0^R \langle \rho u_1 \rangle dr^2}{\int_0^R \langle \rho \rangle dr^2}. \quad (5.3)$$

For the S-ODT formulation, the calculation of the bulk velocity is based on the conservation of streamwise mass flux,

$$U_{b,S-ODT} = \frac{\int_0^R \langle \rho u_1 \rangle dr^2}{\rho_b \int_0^R dr^2}, \quad (5.4)$$

such that ρ_b is given by the value of the density corresponding to the bulk temperature, T_b , according to the ideal gas law. In this context, the bulk temperature is estimated based on the conservation of streamwise enthalpy flux. The approximation given by [45] is used in this case,

$$T_{b,S-ODT} = \frac{\int_0^R \langle \rho u_1 T \rangle dr^2}{\int_0^R \langle \rho u_1 \rangle dr^2}. \quad (5.5)$$

It is noted that $\langle \rho u_1 T \rangle = (P_0/R_{air}) \langle u_1 \rangle$. In T-ODT, the bulk temperature is the temperature corresponding to the bulk density given by conservation of mass in the domain,

$$\rho_{b,T-ODT} = \frac{\int_0^R \langle \rho \rangle dr^2}{\int_0^R dr^2}. \quad (5.6)$$

The ODT results for the normalized bulk temperature and bulk velocity are shown in Figure 5.2, along with the DNS data from [46] for comparison. Since the wall heat flux is held constant in the ODT simulations, it is possible to obtain a representation of the bulk enthalpy in the stationary regime. In order to do that, Eq. (3.67) is rewritten in an Eulerian framework in terms of enthalpy,

$$\frac{\partial (\rho h)}{\partial t} + \nabla \cdot (\rho h \underline{V}) = \nabla \cdot (\sigma_T \nabla T). \quad (5.7)$$

This equation is now integrated with respect to the volume, considering a stationary regime for the flow and homogeneous properties in circumferential direction and no heat diffusion in streamwise direction. It is noted that this integration is performed over a sweep angle of π radians,

$$\begin{aligned} \frac{1}{2} \int_{z'=z_0}^{z'=z} \frac{\partial}{\partial z} \int_{r=0}^{r=R} \rho h u dr^2 dz' &= \int_{z'=z_0}^{z'=z} \int_{r=0}^{r=R} \frac{1}{r} \frac{\partial}{\partial r} \left(r \sigma_T \frac{\partial T}{\partial r} \right) r dr dz' \\ &= \int_{z'=z_0}^{z'=z} R q_w dz' \end{aligned}$$

The radial integral on the LHS of this equation is substituted by the product of the bulk quantities $\rho_b h_b U_b R^2$, being $\rho_b U_b R^2 = \rho_0 U_{b,0} R^2$ a constant due to the CFR constraint,

$$\frac{\rho_0 U_{b,0} R^2}{2} \int_{z'=z_0}^{z'=z} \frac{\partial h_b}{\partial z} dz' = R q_w (z - z_0) \rightarrow h_b = h_0 + \frac{2q_w}{\rho_0 U_{b,0} R} (z - z_0) \quad (5.8)$$

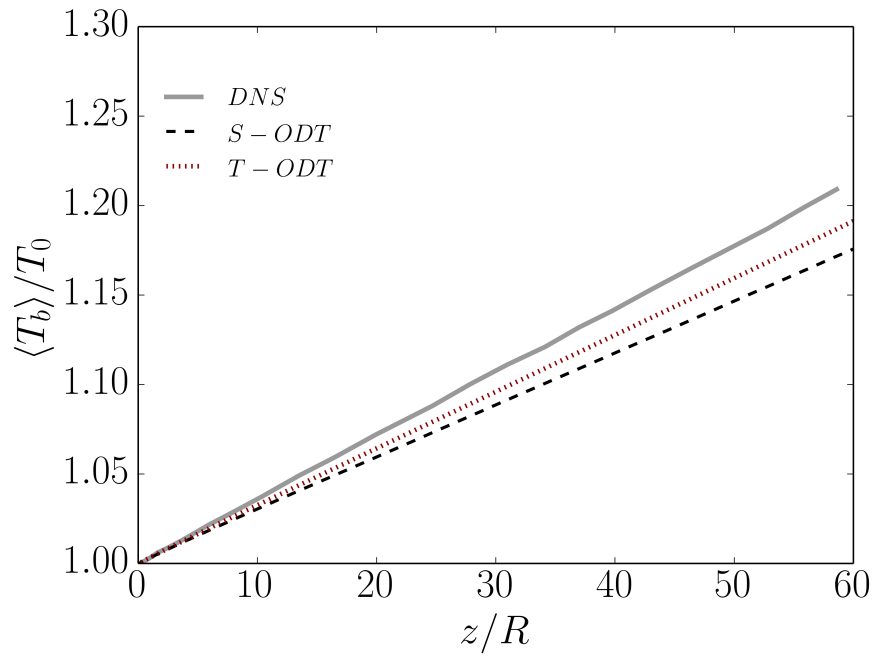
If the specific heat capacity at constant pressure, c_p is assumed to remain constant in streamwise direction², then Eq. (5.8) suggests also a lineal behavior for the temperature with respect to the streamwise position z . This statement agrees with the solution found by the DNS. Figure 5.2 shows that both the T-ODT and S-ODT formulations are unable to match the slope of the linear temperature behavior in z . The error in the slope is attributed to the difference in the filtered c_p and ρ values used in order to work with the discrete FVM used in the deterministic ODT catchup step. That is, the error in the slope is attributed to the low order of the nonconservative discretization scheme used to solve the deterministic ODT temperature diffusion equation, Eqs. (D.18) and (D.38), in the T-ODT and S-ODT formulations, respectively. It is noted that, given that Eq. (5.8) is obtained based on the representation of bulk quantities, the ad-hoc spatial transformation given by Eq. (5.2) and (5.3) is perfectly applicable, given that it considers the displacement of the bulk solution in time. The problem of the ad-hoc transformation is, instead, trying to apply it for the displacement of solutions which are not single-valued (or uniform) in the radial (or circumferential) direction. It is also noted that a linear representation of the bulk temperature implies, by the ideal gas law, Eq. (2.49), at constant composition and thermodynamic pressure, an hyperbolic function for the density of the approximate form,

$$\rho_b \approx \frac{P_0}{R_{air} \left[T_0 + \frac{2q_w}{\rho_0 U_{b,0} c_{p,0} R} (z - z_0) \right]}. \quad (5.9)$$

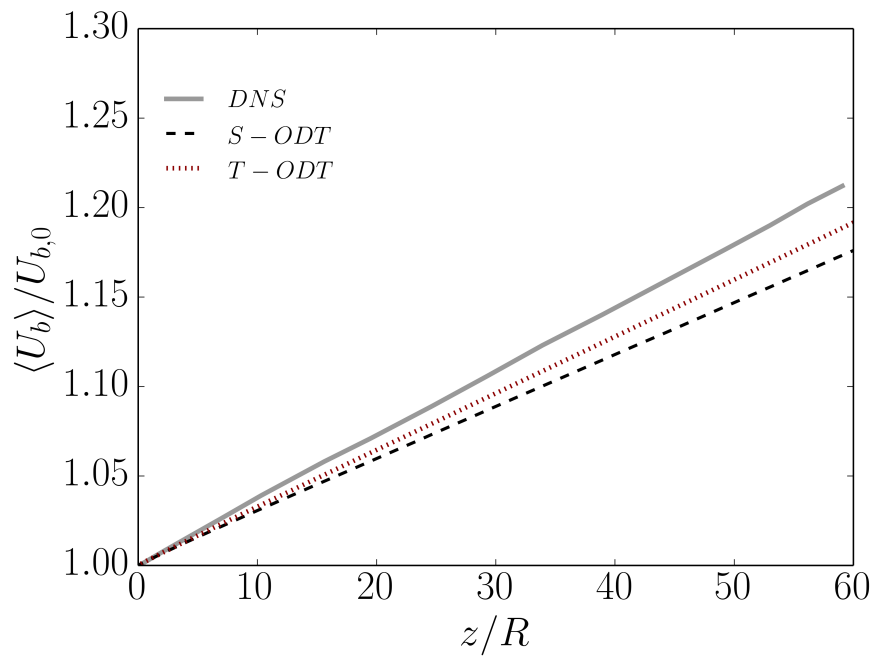
Since $\rho_b U_b$ is a constant due to the CFR constraint, then it is clear that U_b must also follow a linear streamwise dependence, just like h_b or T_b . In this sense, the same discretization error due to the FVM treatment of c_p and ρ is also shifted to the slope of $U_b(z)$.

Although there is no meaningful difference regarding the prediction of bulk quantities in both the S-ODT and T-ODT formulations, the analysis changes once the analysis of radial profiles in the pipe flow is done. The first quantity of interest in this context is the streamwise position dependence of the wall temperature. This is shown next in Figure 5.3. The S-ODT formulation clearly outperforms the prediction made by the T-ODT formulation in this case, as expected by

² This is a reasonable assumption for relatively low to moderate wall heat flux values. This is the case of the q_w value used for the simulation.



(a)



(b)

Figure 5.2: Normalized streamwise position dependence of the bulk temperature (a) and bulk velocity (b) in the T-ODT and S-ODT simulations. DNS data from [46] is shown for reference. The Figures are adapted from the original Figures published in [72].

the theoretical considerations discussed before. Mainly, the T-ODT formulation can not properly reproduce the streamwise dependence of the wall temperature due to the assumption that the temperature profile is being displaced uniformly at the bulk velocity value. The bulk temperature, which is being displaced at the bulk velocity value in T-ODT, can be found in the outer layer of the flow, close to the centerline. Close to the pipe wall, the temperature values are expected to differ significantly from those at the centerline. In S-ODT, every fluid parcel within the ODT line displaces with its own local velocity, which is the main advantage of the spatial formulation for flows in a stationary regime [102].

Figure 5.3 also shows the streamwise dependence of the bulk Nusselt number, Nu_b . The (bulk) Nusselt number is defined as the ratio of the convective heat transfer and conductive heat transfer. In a pipe flow, this is,

$$Nu_b = \frac{2\mathcal{H}_{cf,b}R}{\sigma_{T,w}} \rightarrow \langle Nu_b \rangle = \frac{2\langle \mathcal{H}_{cf,b} \rangle R}{\langle \sigma_{T,w} \rangle}. \quad (5.10)$$

Here, $\mathcal{H}_{cf,b}$ is the bulk convective heat transfer coefficient, defined by,

$$\mathcal{H}_{cf,b}(T_w - T_b)S = \frac{dQ}{dt}, \quad (5.11)$$

where S is the average heat transfer area and dQ/dt is the heat transfer rate. In a pure convection-diffusion system, the heat transfer rate is given by the molecular heat transport by diffusion, i.e., the heat conduction mechanism. This means that the corresponding integral expression for determining $\mathcal{H}_{cf,b}$ is related to the heat flux vector \underline{q} , in this case, by,

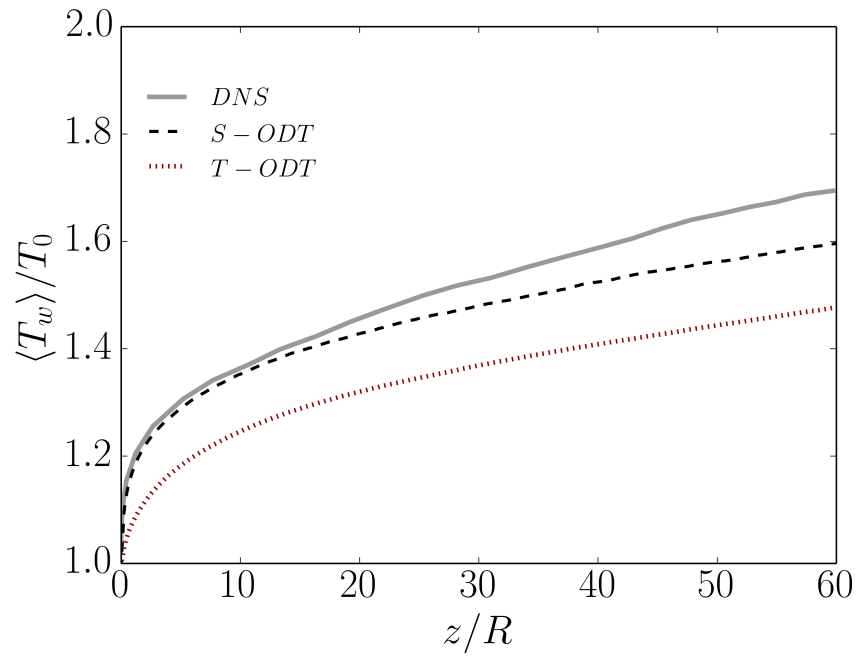
$$\mathcal{H}_{cf,b}(T_w - T_b) \oint dS = \oint \underline{q} \cdot d\underline{S} \rightarrow \mathcal{H}_{cf,b}(T_w - T_b) = q_w. \quad (5.12)$$

With the wall heat flux definition given in appendix G. For this case, then, the bulk Nusselt number can be calculated as,

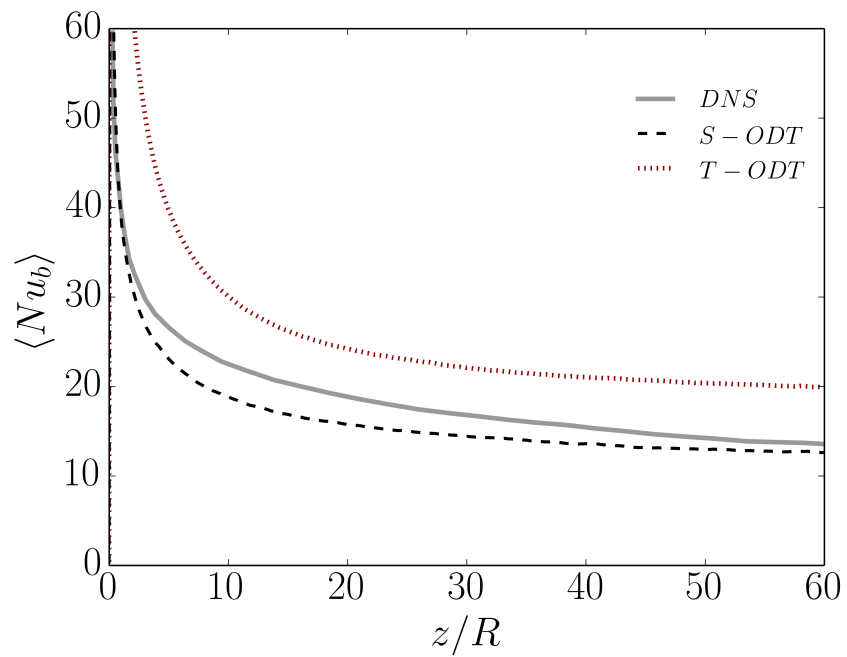
$$\langle Nu_b \rangle = \frac{2R \frac{\partial \langle T \rangle}{\partial r} \Big|_w}{\langle T_w \rangle - \langle T_b \rangle}. \quad (5.13)$$

It is clear that the better reproduction of the temperature profile (in this case for the wall temperature and wall temperature gradient), results in a much better match of the S-ODT formulation with the DNS data for Nu_b .

The streamwise position dependence of the skin friction coefficient, given by Eq. (3.63) (and the wall shear stress given by Eq. (G.1), is evaluated next in Figure 5.4. The almost constant streamwise dependence of C_f after the achievement of what appears to be the end of the transient phase of the flow for both ODT formulations, is strikingly different to the non-monotonic increase and subsequent decrease in C_f



(a)



(b)

Figure 5.3: Normalized streamwise position dependence of the wall temperature (a) and bulk Nusselt number (b) in the T-ODT and S-ODT simulations. DNS data from [46] is shown for reference. The Figures are adapted from the original Figures published in [72].

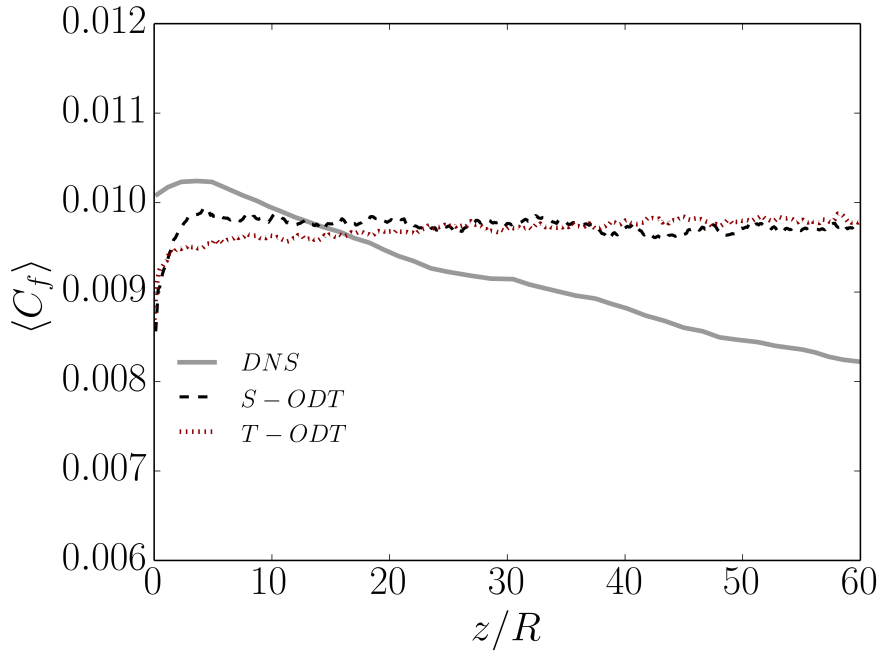


Figure 5.4: Normalized streamwise position dependence of the skin friction coefficient C_f . DNS data from [46] is shown for reference. The Figure is adapted from the original Figure published in [72].

shown in the DNS solution. This could be interpreted as an evidence of the flow parabolic restriction in ODT. Indeed, on the simulations was not only a CFR constraint imposed, but also a 1-D divergence condition for the flow, and, as a consequence, a constant mean streamwise pressure gradient. In ODT, this imposed condition results in a flow that is behaving, at least hydrodynamically, as a fully developed flow, with no substantial change in the kinematic properties (e.g., momentum and velocity components) of the flow in streamwise direction, despite the fact that thermally, the flow is still behaving as a developing boundary layer flow due to the advecting of the temperature PDE by the streamwise velocity component. Since there is no variation of the kinematic flow properties, or of the hydrodynamic boundary layer, the friction Reynolds number achieved after the transient flow phase finishes, remains constant. In the DNS, this may not be the case. Since there is no constraint on the divergence condition or on the pressure, the transient phase can be different, and the hydrodynamic character of the flow may still behave as a developing boundary layer throughout the whole simulation.

For streamwise positions $z/R < 30$, both the T-ODT and S-ODT formulations are able to yield the correct order of magnitude and qualitative trend for C_f . It is noted, though, that the initial C_f value in ODT is different to the initial C_f value of the DNS. This is because the initial conditions in ODT were produced by a T-ODT simulation forcing a constant bulk velocity, effectively yielding a desired $Re_{b,0}$

value, which did not agree with the corresponding initial $Re_{\tau,0}$ value produced by the incompressible and constant property DNS solution, or that predicted by the Colebrook law in pipe flow [32, 46, 94]. This was not necessarily a poor choice, given that the mean velocity profiles at the initial friction Reynolds number were checked to have a reasonable qualitative agreement with the corresponding nondimensionalized profiles at the suggested DNS $Re_{\tau,0}$. However, given that $Re_{\tau,0}$ is very low, small differences in the averaged value of the calculated mean streamwise pressure gradient (as a function of the forced U_b), have a big influence on the value of C_f . Thus, from the parameter calibration point of view, probably a better job matching U_b and the corresponding τ_w could have been done for the initial conditions. Yet again, this was not part of the scope of the work in this case. Here, a simple further use of more or less the same parameters used for the constant property flow simulations at larger Reynolds numbers in chapter 4 was intended. It is also noted from the results in Figure 5.4 that the S-ODT results for C_f show a steeper increase in the early stages of the transient, or in the early streamwise positions. This could be explained simply in the fact that the initial conditions used were from T-ODT simulations, instead of initial conditions produced with an inherent S-ODT formulation, and therefore, the transient dynamics are expected to be less subtle. Nonetheless, it is interesting to observe that, as the flow progresses towards the density weighted statistically stationary state in T-ODT and the density weighted statistically homogeneous state in S-ODT, both formulations yield approximately the same values for C_f .

5.2.2 *Streamwise velocity and temperature statistics*

The proper collapse of variable density flows into constant density flow profiles has been studied at least during the last 50 years in the field of compressible turbulence. Early works trace back to Van Driest [103], originating the transformation of the velocity profiles which now carries his name. The Van Driest transformation of the streamwise velocity profile is shown in Figure 5.5. The Van Driest transformation and its corresponding scaling in inner units is given in appendix G by Eqs. (G.16) and (G.17). In this case, the agreement of the ODT results with the DNS data is qualitatively reasonable for both the T-ODT and S-ODT formulations. The S-ODT formulation shows an overshoot of the velocity profile close to the centerline in early stages of the flow transient phase, and a subsequent underestimation of the outer layer in later streamwise positions. The overshoot is more moderate in the profiles obtained by the T-ODT formulation. It is noted that the overshoot close to the centerline is an artifact already observed in the mean channel and pipe flow profiles of the T-ODT and S-ODT simulation results from chapter 4, with varying degree

of severity. This is an issue that could be corrected with a sensitivity analysis of the model parameter choice in the variable density case. For downstream locations $z/R > 30$, as in the case of the bulk flow statistics already discussed, discrepancies between ODT and DNS results become more pronounced, either due to the inaccurate ODT transient phase result due to the nonconservative formulation used, or due to the unsuitable assumption of the achievement of a fully developed flow in the statistically stationary (or homogeneous) ODT results (i.e., the parabolic flow restriction), in comparison to the still developing boundary layer behavior shown in the DNS.

The counterpart of the kinematic statistics shown in Figure 5.5 is the inner scaled temperature statistics, represented in first order by the mean temperature profiles, as shown in Figure 5.6. Here again, the difference between the developing character of the thermal boundary layer achieved by the S-ODT formulation outperforms the predictions of the T-ODT formulation. The S-ODT temperature profiles match reasonably well with the DNS data in the entire investigated range of streamwise positions, $z/R < 50$. The systematically lower wall temperature obtained in T-ODT, Figure 5.3, is now contrasted with the systematically smaller temperature difference between the wall and the inner and outer layers of the flow, i.e., this is again a manifestation of the assumption of the displacement of solution with the single-valued bulk velocity. The displacement of fluid parcels which are far from the wall is the same as the displacement of those parcels located close to the wall. Given that this reasoning implies an overall slower movement of the fluid parcels in the outer layer, the solutions obtained by the T-ODT formulation and the ad-hoc transformation, Eq. (5.2), are delayed in the outer layer region, in comparison to the solutions obtained with the S-ODT formulation. For the temperature, this implies that the temperature profile obtained with the T-ODT formulation in the outer layer (away from the wall), still shows the effects of the initial uniform temperature conditions, even when the S-ODT solution has already achieved a different flow state. The S-ODT formulation is, thus, clearly a favorite, as long as a better representation of radial profiles is desired.

5.2.3 *Turbulent fluctuations*

It is now of interest to take a look at the statistics of fluctuating quantities. First, the results of the RMS profiles of velocity and temperature at a late downstream position, $z/R = 49.0$ are presented. The RMS profiles presented in Figure 5.7 are obtained using an ensemble (Reynolds) average method (see Eq. (E.6) in appendix E). For the case of the RMS velocity profiles, a similar trend to that presented in chapter 4 for incompressible and constant property flow is expected. In this case, the RMS profile is, again, the result between the ensemble averaged

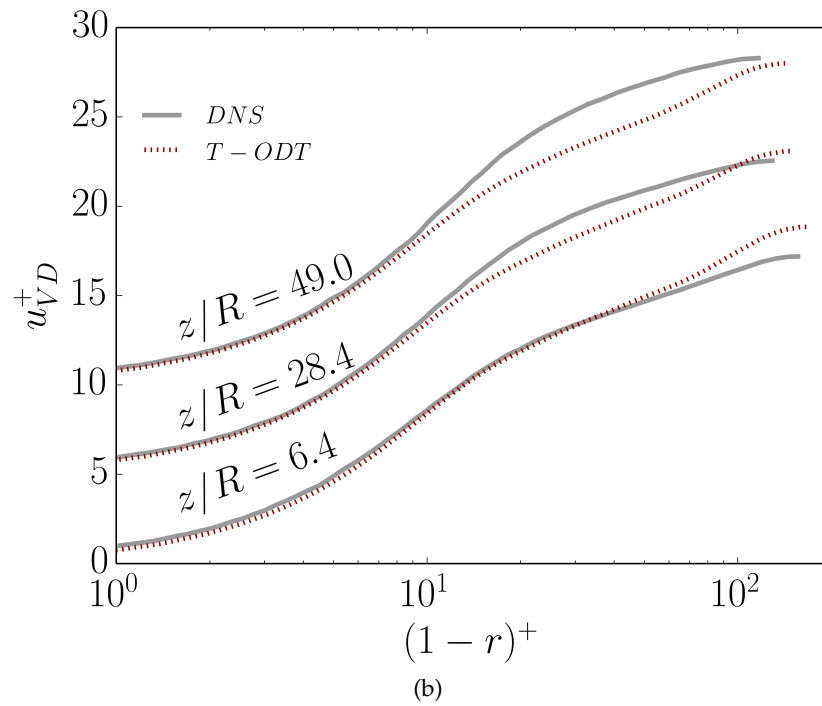
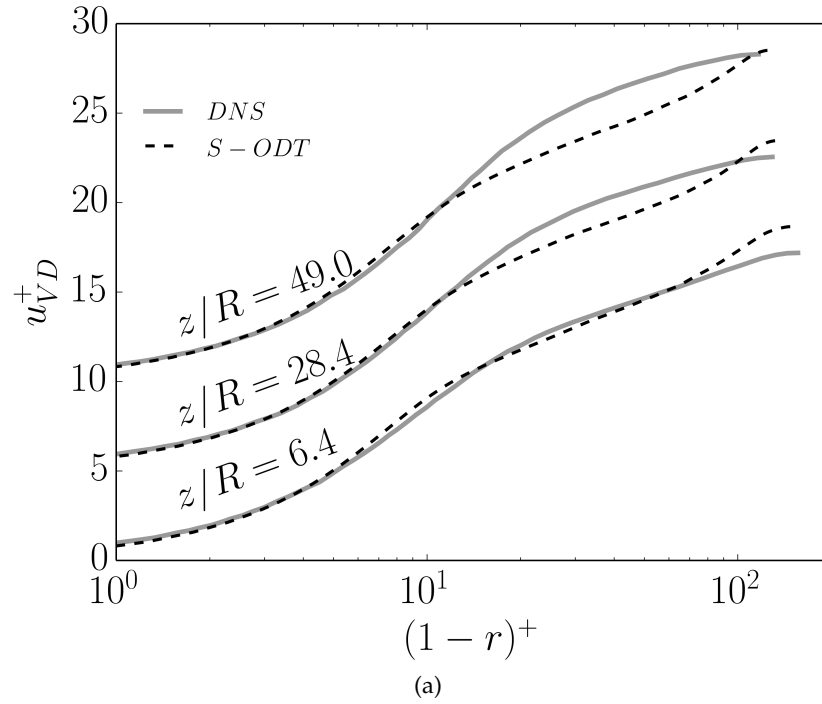


Figure 5.5: Wall scaling of the Van Driest streamwise velocity profile at normalized streamwise positions $z/R = 6.4$, $z/R = 28.4$ and $z/R = 49.0$. (a) Results obtained for S-ODT simulations. (b) Results obtained for T-ODT simulations. Profiles at $z/R = 28.4$ and $z/R = 49.0$ have been shifted in the vertical axis for better visibility and comparison. DNS data from [46] is shown for reference. The Figures are taken from [72].

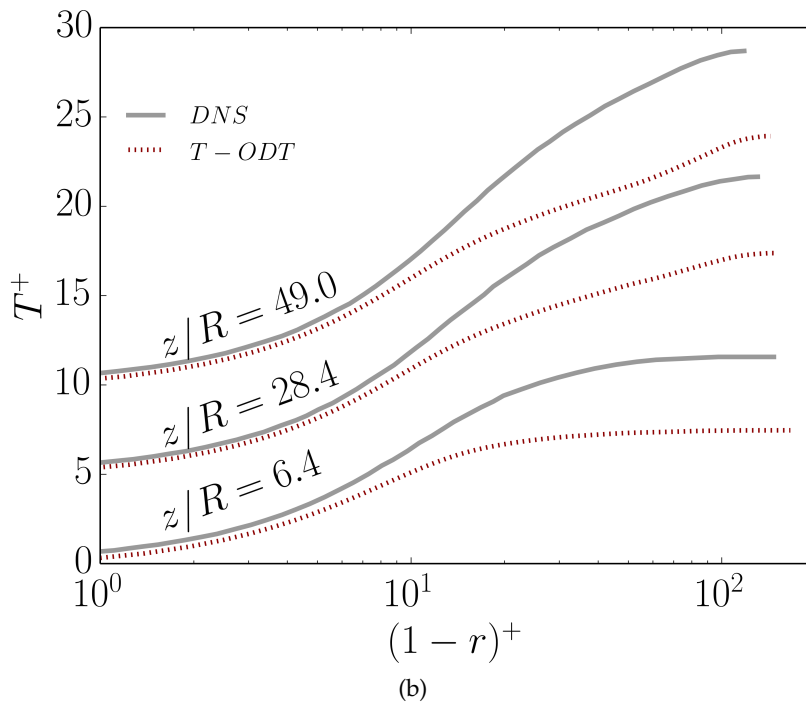
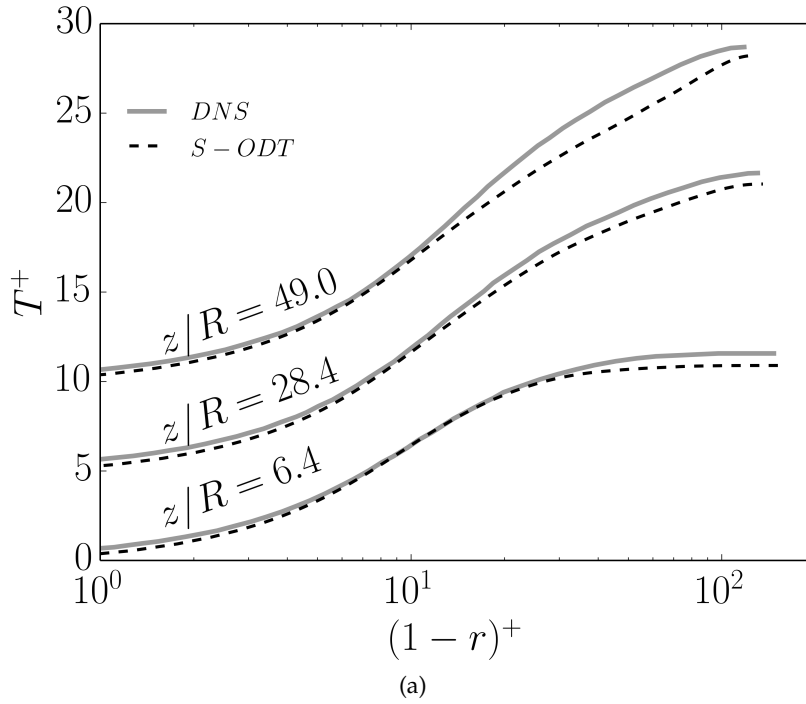


Figure 5.6: Wall scaling of the average temperature profiles at normalized streamwise positions $z/R = 6.4$, $z/R = 28.4$ and $z/R = 49.0$. (a) Results obtained for S-ODT simulations. (b) Results obtained for T-ODT simulations. Profiles at $z/R = 28.4$ and $z/R = 49.0$ have been shifted in the vertical axis for better visibility and comparison. DNS data from [46] is shown for reference. The Figures are adapted from the original Figures published in [72].

kinetic energy of the streamwise velocity component and the kinetic energy of the ensemble averaged mean streamwise flow. Given that these profiles are not density weighted, as in a Favre-average procedure, the sole effect of the fluctuations on the mean velocity signal, i.e., the sole effect of the solenoidal ODT velocity contribution responsible for turbulent advection, can be evaluated in a more suitable way. In general, both the T-ODT and S-ODT formulations fail to reproduce the DNS results, as in the case of constant property flow RMS velocity profiles. Although the scaling used for the figure is just a scaling based on the mean flow, it is seen that the magnitude of the turbulence intensity away from the wall, in the outer layer, is overestimated in comparison to the DNS solution. In this case, this could be the result of the overshoot in the mean velocity profile in the outer layer, as commented before.

The S-ODT results are generally closer to the DNS data, and, as such, S-ODT simulations produce larger turbulent fluctuations for both velocity and temperature, despite the curious fact that the value of the ODT model parameter C is lower in the S-ODT formulation. However, although the turbulent fluctuations of the velocity exceed the values predicted by DNS data away from the wall, this does not occur with the temperature fluctuations. Additionally, for both the RMS velocity and temperature profiles, the peak of the profile is offset closer to the wall in comparison to the DNS data. Although this is clearly an error due to the reduce order of the model, the fact that the radial position of the peak of both RMS velocity and temperature profiles coincide, is a sign of consistency. This is because the Prandtl number of the flow is very close to 1 ($Pr_0 \approx 0.71$), and in this context, it is expected that the behavior of the velocity as a scalar is not that different to the behavior of the temperature. The behavior of the temperature in the heated pipe is, thus, similar to that of a passive scalar in a channel flow [104].

The (Reynolds) ensemble-averaged RMS profiles presented in Figure 5.7 can be compared to the Favre-related velocity fluctuations in Figure 5.8, where $\langle \rho \rangle \langle u'' \rangle = -\langle \rho' u' \rangle$ by the identity from Eq. (E.14). In [46], the radial profile of the ensemble-averaged Favre velocity fluctuation is related to the buoyancy production term implied in the streamwise Reynolds stress $\widetilde{u''u''}$ transport equation (see the derivation of the term in [105]). Regardless of the normalization used, it is possible to understand this buoyancy production term in the context of a Boussinesq approximation for buoyant flows [89]. That is, in the context of a Boussinesq approximation, it is clear that the sole influence of the turbulent density fluctuations on the turbulent transport of momentum is done via the effects of the gravitational potential energy. Although the simulations carried out here did not consider this Boussinesq approximation, it is clear that the density weighted, or Favre-related fluctuations, are still a good accounting mechanism for

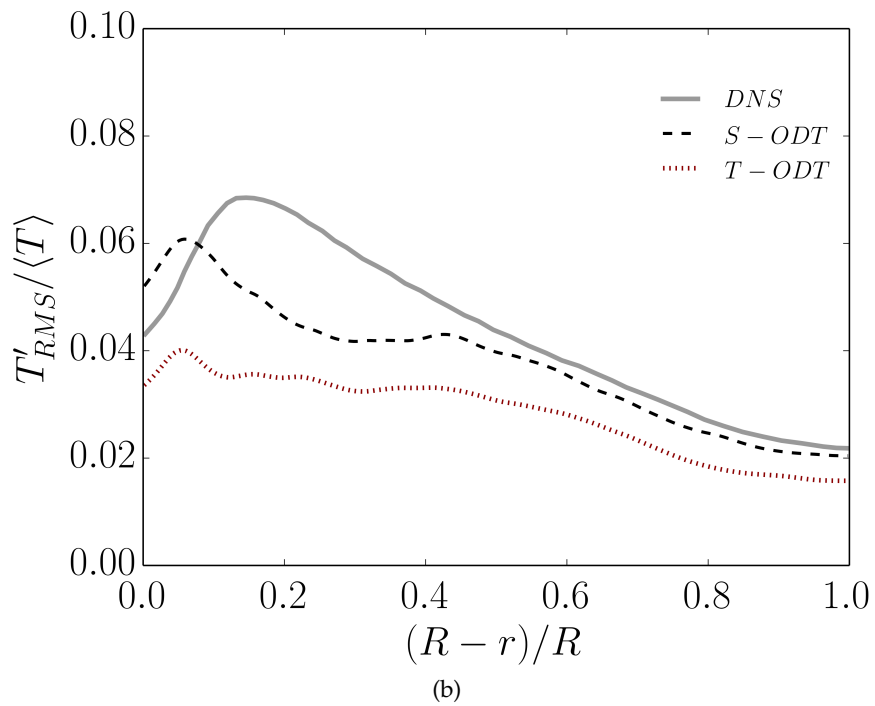
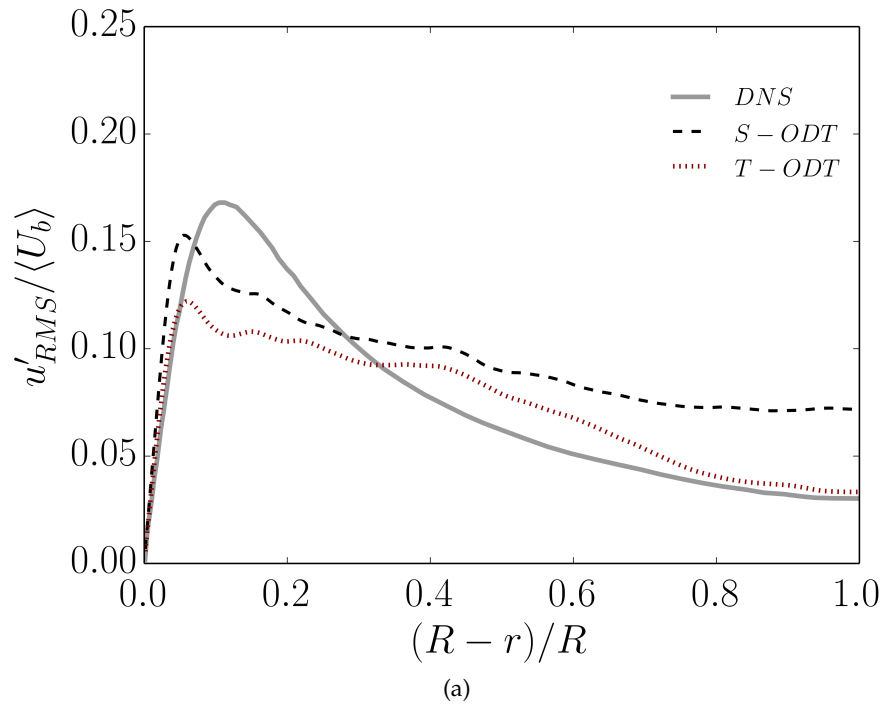


Figure 5.7: Radial RMS velocity profiles obtained via ensemble averaging for (a) Streamwise velocity and (b) Temperature. Both profiles are obtained at a normalized streamwise position $z/R = 49.0$. The Figures are adapted from the original Figures published in [72].

the influence of the gravitational potential energy effects, in contrast to the turbulent advection contribution done by the solenoidal contribution of the velocity field, i.e., the mere *kinematic* turbulence. According to the Favre-related streamwise velocity fluctuation profile presented in Figure 5.8, it is seen that the effects of gravity are modest in both the S-ODT and T-ODT formulations. In fact, according to the T-ODT results, the buoyancy contribution to turbulence is almost negligible at early stages of the transient flow, at $z/R = 6.4$. Nonetheless, both the T-ODT and S-ODT formulations underestimate the magnitude of the turbulence due to buoyancy effects if the DNS data is compared to the ODT results.

Finally, the turbulent momentum and heat transport are evaluated by the profiles of the Reynolds shear stress and the turbulent heat flux. First, the radial profile of the Reynolds shear stress is evaluated at a late downstream position, $z/R = 49.0$ in Figure 5.9, together with the average shear stress. The average shear stress is evaluated as the sum of the radial shear on the streamwise velocity and the streamwise shear on the radial velocity, i.e.,

$$\langle \tau \rangle \approx \langle \mu \rangle \left(\frac{\partial \langle u \rangle}{\partial r} + \frac{\partial \langle v \rangle}{\partial z} \right). \quad (5.14)$$

As in all previous radial profiles, the Reynolds shear stress is captured in a better way with the S-ODT formulation. However, it is noted that the S-ODT formulation produces an unphysical behavior of the average shear stress next to the wall, where the values of the stress exceed the values of the wall shear stress. This is attributed to the numerical error in the solution scheme, specifically in this case due to the mesh adaption procedure. The mesh adaption procedure works in a flux conservative way in the S-ODT formulation³, but switches to a mass conservative interpolation⁴ in the cell next to the wall in order to avoid expansions or contractions of the numerical domain due to mesh adaption. The conflicting interpolation scheme, together with the approximation of the stress neglecting the covariance between the dynamic viscosity and the velocity gradient may have provoked the anomalous behavior next to the wall. Given that this nonphysical behavior of the shear stress is not observed on the mean velocity profiles (or mean temperature profiles), this issue was not further investigated. It should be subject to a future discussion concerning the mesh adaption scheme in the S-ODT formulation for confined flows.

Figure 5.10 shows the radial profile of the turbulent heat flux component $\langle \rho h'' v'' \rangle$. Once again, the turbulent fluctuations obtained in the T-ODT formulation are significantly lower in comparison to those obtained in the S-ODT formulation. Nonetheless, both the T-ODT and S-ODT formulations are able to capture interesting qualitative

³ Conserving ρu weighted quantities.

⁴ Conserving ρ weighted quantities.

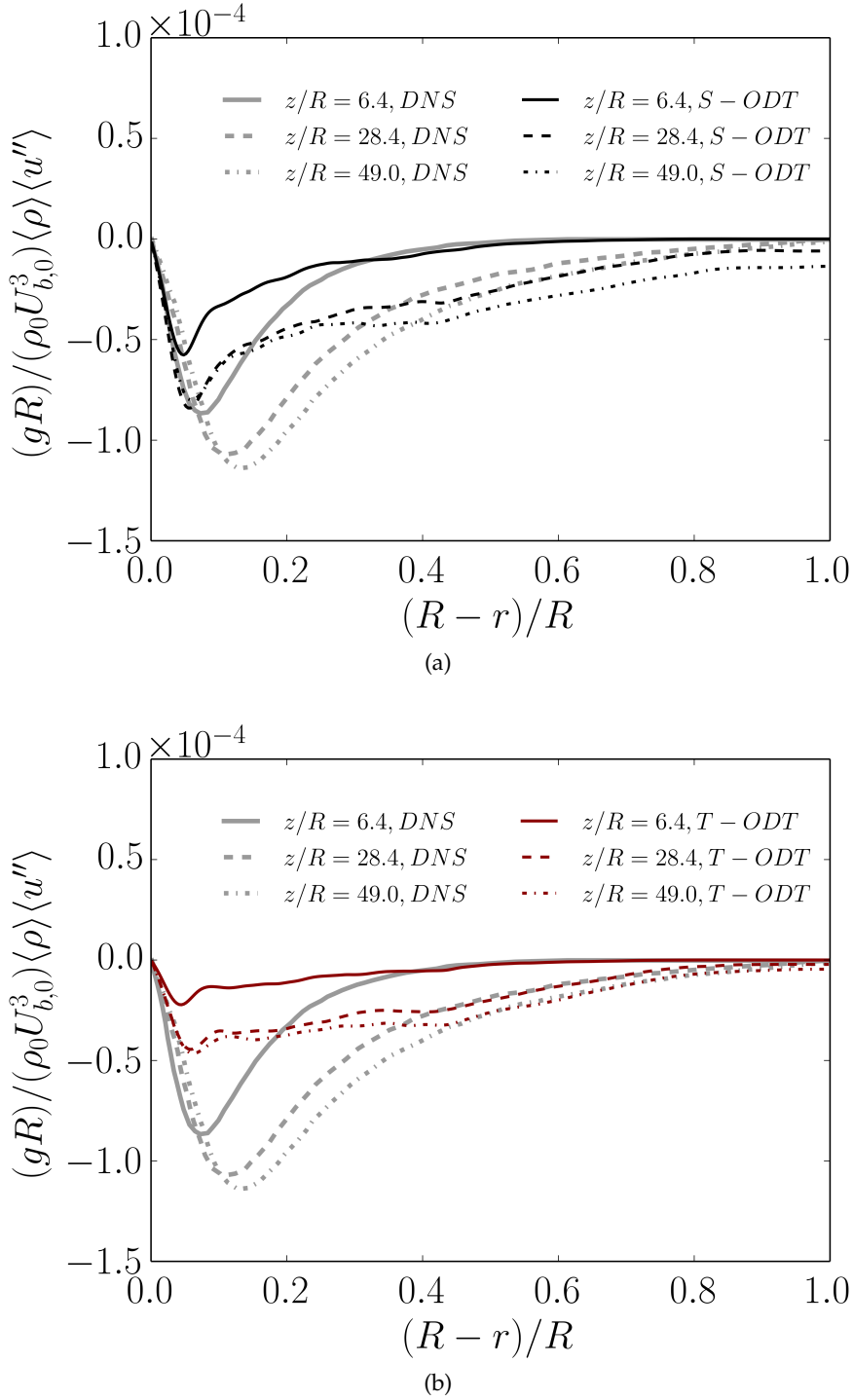


Figure 5.8: Radial profiles of density weighted Favre-related streamwise velocity fluctuations at different streamwise positions. (a) S-ODT simulation results, (b) T-ODT simulation results. It is noted that $\langle \rho \rangle \langle u'' \rangle = -\langle \rho' u' \rangle$. The term $\langle \rho' u' \rangle$ is associated to the buoyancy production term in [46]. DNS data from [46] is shown for reference. The Figures are adapted from the original Figures published in [72].

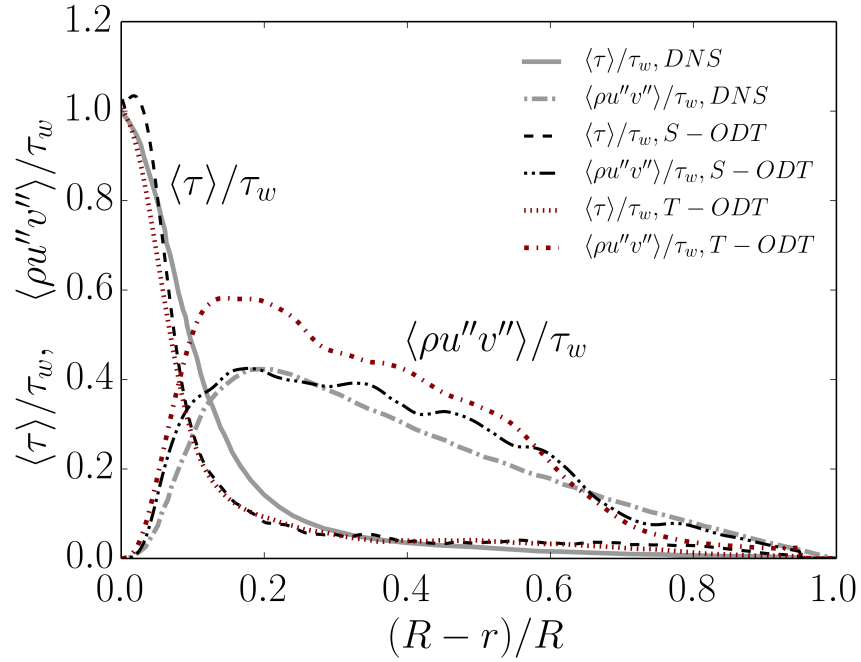


Figure 5.9: Average shear stress $\langle \tau \rangle$ and Reynolds shear stress component $\langle \rho u'' v'' \rangle$ in the S-ODT and T-ODT formulations at a normalized streamwise position $z/R = 49.0$. DNS data from [46] is shown for reference. The Figure is adapted from the original Figure published in [72].

features of the transient flow phase. Indeed, it is observed that the magnitude of the turbulent heat flux at $z/R = 28.4$ is larger than at the later position $z/R = 49$, as in the DNS data. This is a sign of the relaminarization of the flow, which was one of the main reasons motivating the DNS study [46, 105]. Before discussing this topic further, it is noted that the statistical convergence of the Reynolds shear stress, the turbulent heat flux and the skin friction coefficient, as presented in this work so far, were, by far, the most demanding computational requirements. All of these quantities are related to the intensity of the turbulence and the implementation of eddy events in ODT. For a relatively low Reynolds number, such as the one evaluated in this simulation, the number of eddy events implemented in every ensemble member is also small, while the effect of every eddy is relatively large on the statistics⁵. The computational cost of ODT regarding the calculation of turbulent fluxes, is, in this sense, expected to increase with the Reynolds number regarding the duration of every simulation or ensemble member realization. However, at the same time, the computational cost is also expected to be compensated by reducing the number of ensemble members required for converging statistics

⁵ The larger eddies characteristic of a more laminar flow transport more energy with them.

due to the increase in the number of implemented eddy events, also according to the Reynolds number.

5.2.4 Relaminarization effect and flow regimes

To finalize this chapter, a short comment regarding the relaminarization phenomena is made. This issue will be discussed again in the context of the EHD-enhanced heat transfer simulations in Chapter 7. The relaminarization seen in the DNS, as well as in ODT, agrees with the forced and natural convection boundaries from the diagram presented by the group of Tanaka et al. back in the 1980s [106]. It is possible to illustrate the change in the bulk Reynolds number in the ODT simulations from the initial conditions to the position $z/R = 50$ within such diagram. This is shown (for the values obtained in the S-ODT simulations) in Figure 5.11. The diagram shown in Figure 5.11 shows, first, in dashed red and green lines, the boundaries of laminar flow. The laminar flow was obtained in [106] by performing RANS simulations with the models suggested by Kawamura [107] and Jones and Launder [108]. In the simulations where the TKE converged to a value of zero, the flow was considered laminar [106]. The dashed black lines corresponding to the boundary between turbulent forced convection and turbulent mixed convection, as well as the boundary between turbulent mixed convection and turbulent natural convection follow the empirical relations from Tanaka et al. [109, 110],

$$Re_b = 50Gr_b^{\frac{8}{21}} \quad (\text{Forced and mixed convection boundary}), \quad (5.15)$$

$$Re_b = 16.5Gr_b^{\frac{8}{21}} \quad (\text{Mixed and natural convection boundary}). \quad (5.16)$$

The dotted black line in Figure 5.11 corresponds to the relaminarization boundary estimated by [106] as,

$$\frac{Gr_b}{Re_b^3} = 3 \times 10^{-6}. \quad (5.17)$$

Finally, the dotted purple line in Figure 5.11 is the regime distinction according to the nondimensional factor in the buoyancy term of the momentum equation, as derived in [111]⁶, i.e., $Gr/Re_b^2 = 1$. Note that for negligible Grashof numbers, $Gr \rightarrow 0$, the laminar boundary should approach the critical bulk Reynolds number for pipe flow, $Re_{b,cr} \approx 2040$ [8]. In that sense, the model for laminar flow suggested by Kawamura seems closer to reality.

Also shown in Figure 5.11 as star, square and cross symbols are the RANS simulation data of [106], where values of 80% of the initial Nusselt number, the minimum Nusselt number and a recovery to the

6 This is derived using a Boussinesq approximation.

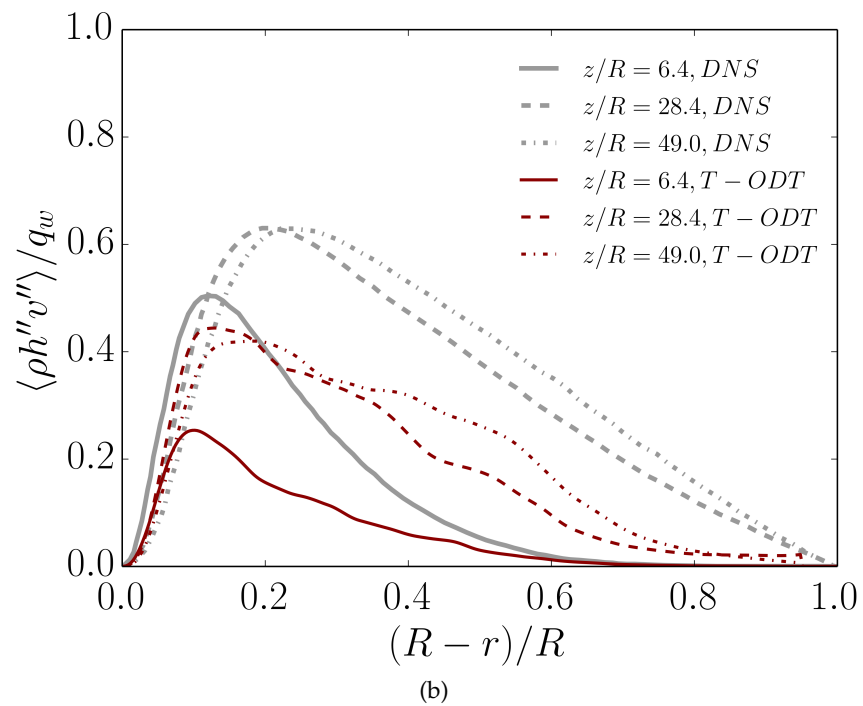
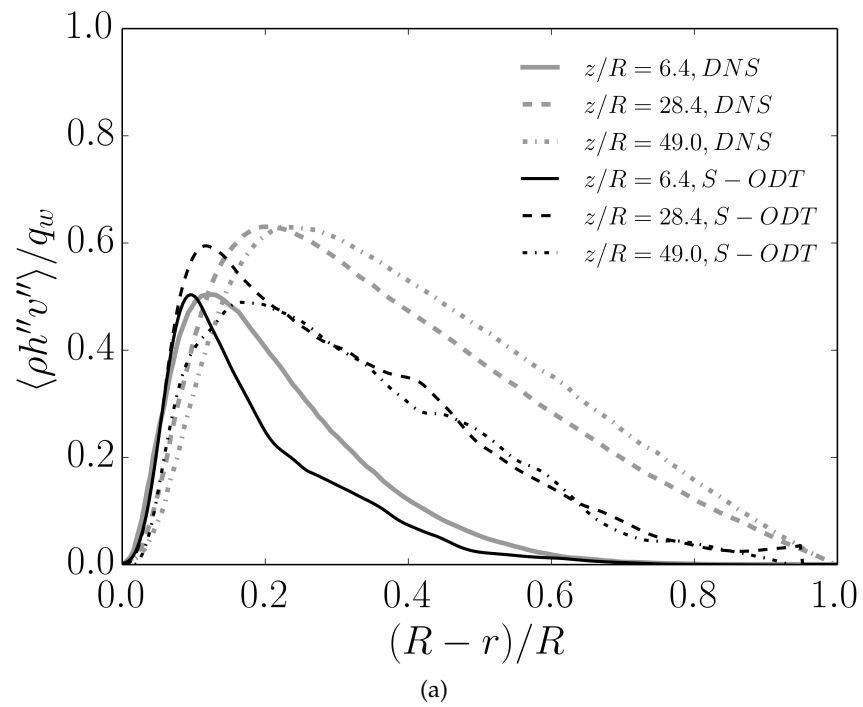


Figure 5.10: Radial profiles of turbulent heat flux component $\langle \rho h'' v'' \rangle$ at different streamwise positions. (a) S-ODT simulations. (b) T-ODT simulations. DNS data from [46] is shown for reference. The Figures are adapted from the original Figures published in [72].

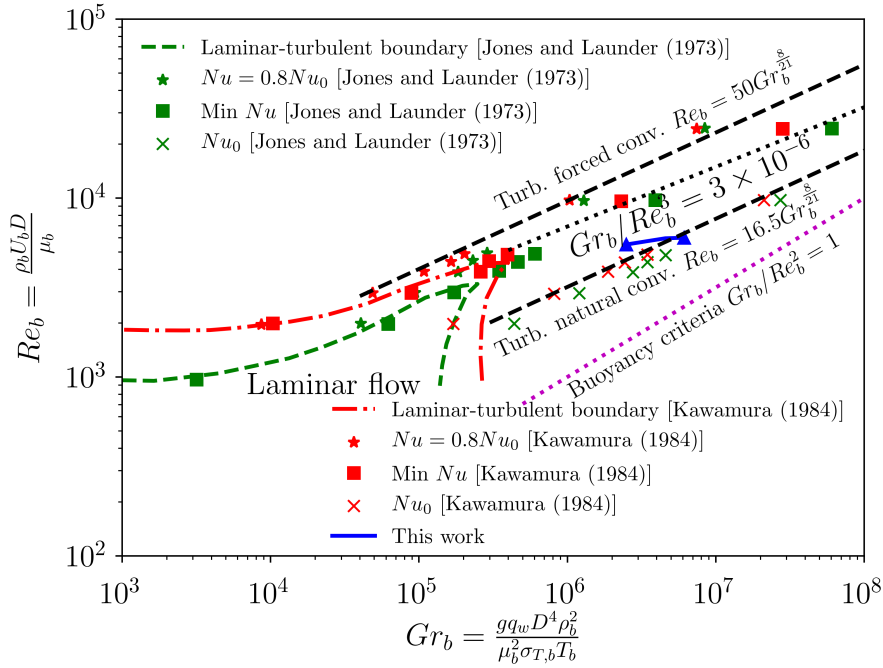


Figure 5.11: Natural and forced convection regime diagram presented in [106], with the change in the characteristic Grashof and Reynolds number obtained from the S-ODT simulations between the normalized positions $z/R = 0$ and $z/R = 50$ (blue line with triangular symbols). Note that $Re_{b,0} = 6000$ in the ODT simulations. See the text for a description of the diagram.

initial Nusselt number were achieved, respectively, with both models from [108] and [107]. The drop of the Nusselt number below 80% of the initial value and its later recovery to the original value at constant Re_b with varying Gr_b was indicative of a change in the flow regime.

Figure 5.11 shows that the relaminarization effect discussed in the DNS study of [46] agrees with the boundaries presented by [106], in the sense that the entire simulation starts at the turbulent natural convection regime and displaces towards the mixed convection regime, and towards the relaminarization boundary. Nonetheless, according to the buoyancy criteria, $Gr/Re_b^2 = 1$, this flow is still considered at all times as a forced convective flow [111]. This is an indication of how the effect of the body forces, in this case the gravitational body force, can influence the regime of the flow and the transition to turbulence. Indeed, the flow simulated in this chapter is, by no means, a classical example of a one-dimensional turbulence case, given that it must be represented, at least, in a two dimensional parametric space of Re_b and Gr_b , in addition to the already discussed streamwise dependency of flow quantities.

Part III

APPLICATION OF THE ODT MODEL TO EHD
INTERNALLY FORCED CONVECTIVE FLOWS

EHD FLOW IN A WIRE-PLATE ELECTROSTATIC PRECIPITATOR

This chapter is an adaptation of the content published in [112].

In this chapter, the S-ODT formulation is applied to evaluate the effects of the electroquasistatic body force, or EHD body force, within an incompressible constant property channel flow. It is stressed that the assumption of flow incompressibility with constant properties, considered in this chapter, implies neglecting any kind of temperature change. Therefore, all heat fluxes and Joule heating effect contributions into the temperature equation, Eq. (3.67), are neglected. This also implies that the divergence condition on the velocity, Eq. (3.65), results in a zero divergence of the velocity field. The EHD body force is produced by a periodic array of electrodes which ionize the surrounding air flow. This configuration resembles the wire-plate ESP configuration used in [51] and [113], and is an attempt to reproduce the results obtained in the DNS done by Soldati and Banerjee [53]. The ODT model implementation in the wire-plate ESP is shown in Figure 6.1. It shows, as an example, the implementation of an eddy event taking place at a streamwise position x_{eddy} . The eddy event has a left edge given by $y_{0,eddy}$ and a length l_{eddy} . This causes a distortion in the streamwise velocity profile, as discussed in chapter 3.

6.1 ROLE OF THE EHD BODY FORCE IN TURBULENCE AND ODT MODELING

Until this point, the reader may have found somehow arbitrary the treatment given to the EHD body force as part of the stochastic eddy event implementation in ODT. In fact, by examining the mean momentum and mean kinetic energy equations in appendix F, it is actually counterintuitive to discuss the EHD body force within the context of turbulent advection, given that it clearly affects directly only the mean kinetic energy (or the kinetic energy of the mean flow), and not the turbulent kinetic energy. This can be seen by the absence of the EHD term in the incompressible TKE equation (or in the variable density TKE equation as well), Eq. (F.9). It is noted that all comments made in this section, and in the thesis in general, refer to the asymptotic case of negligible mobility ratios $M_\beta \rightarrow 0$, as discussed in chapter 3.

In order to understand the role of the EHD body force in turbulence, it is first convenient to rewrite the electric current density vector given

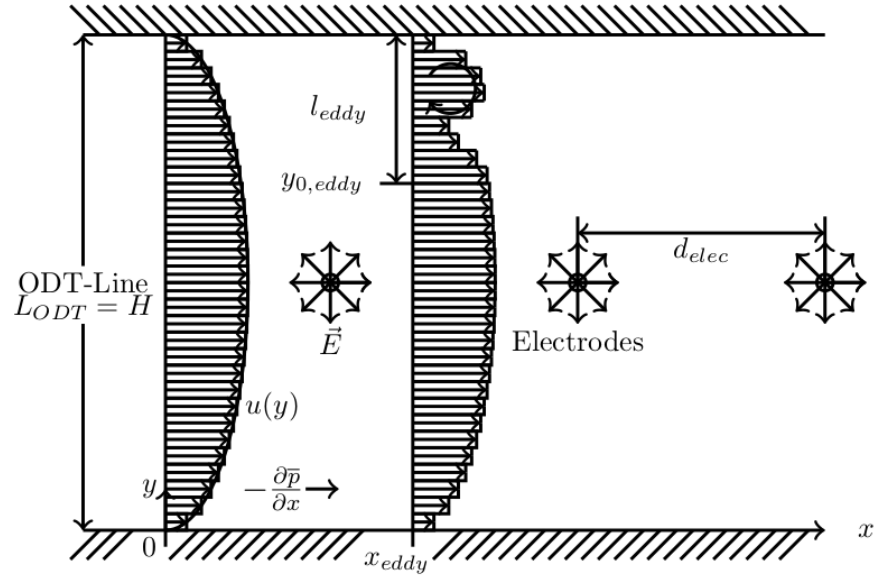


Figure 6.1: Configuration of the ODT model in a channel flow undergoing the effects of EHD body forces, resembling a wire-plate ESP. The ODT line coincides in this case with the channel crosswise direction and displaces in streamwise direction, according to the S-ODT formulation. Discharge electrodes are placed in a periodic array configuration at a distance d_{elec} . The EHD body force is generated due to the electrostatic potential difference between the electrode at ϕ_{elec} and the grounded channel walls at $\phi_{plate} = 0$. The Figure is adapted from the original Figure published in [112].

by Eq. (2.11). Indeed, using Eq. (2.13) (and Eq. (2.18)), the electric current density can be rewritten in terms of the electric field as,

$$\underline{J} = \rho_f \beta \underline{E} = \epsilon_0 \beta (\nabla \cdot \underline{E}) \underline{E}.$$

Using some convenient vector calculus identities, this can be rewritten as,

$$\frac{\underline{J}}{\beta} = \epsilon_0 \nabla \cdot (\underline{E} \circ \underline{E}) - \frac{\epsilon_0}{2} \nabla (\underline{E} \cdot \underline{E}) = \epsilon_0 \nabla \cdot (\underline{E} \circ \underline{E}) - \frac{\epsilon_0}{2} \nabla \cdot (|\underline{E}|^2 \underline{I}). \quad (6.1)$$

This representation of the EHD body force is the so-called Maxwell electroquasistatic stress tensor in an electrically linear medium [56]. Being a stress tensor, this implies that there is a normal stress associated to an irrotational component of the current and a shear stress associated to a rotational component of the current. This is similar to the analysis done by [76] and leads to the same conclusion. There is a component of the EHD body force, responsible for vortical motions which is not transferring translational kinetic energy into the flow, and a component which is only adding translational kinetic energy. The EHD body force behaves then equivalent to the pressure and the shear stress in the Navier-Stokes equations.

If there is a contribution to the EHD body force behaving just like the pressure gradient, then there should be an associated mean pressure gradient forcing the flow. In ODT, this contribution should be considered in the deterministic advancement treatment, as discussed previously in Chapter 3. **Is there then such a mean component forcing the flow in ODT?** The answer to this question in this thesis is no. This is motivated by the reduction from the vector Navier-Stokes equations to the scalar ODT equations also done in chapter 3. As commented in chapter 3, the ODT treatment supposes a parabolic flow, which formally requires a 1-D electric current density vector. E.g., for channel flow, this is a current density vector with a sole crosswise component. If this supposition holds, then there is necessarily no net effect of the EHD body force into the streamwise momentum component, and therefore, there is no contribution towards the mean streamwise pressure gradient. Hence, the EHD body force only acts on the crosswise momentum component. Consider now the Lagrangian momentum equation, Eq. (3.47), with all of the divergence terms of the EHD body force, as well as the pressure gradient and the shear stress tensor divergence grouped into a total stress tensor,

$$\rho \frac{DV}{Dt} = \nabla \cdot \left(-p\underline{\underline{I}} + \underline{\underline{\tau}} + \epsilon_0 \underline{\underline{E}} \circ \underline{\underline{E}} - \frac{\epsilon_0}{2} |\underline{\underline{E}}|^2 \underline{\underline{I}} \right) + \rho \underline{\underline{g}}. \quad (6.2)$$

It can be seen, according to Eq. (6.2), by supposing a 1-D electric field, e.g., in y direction, that the contribution of the EHD body force to the pressure gradient in the crosswise direction is simply $\epsilon_0 E_2^2/2$, which is the electrostatic potential energy density as per Eq. (2.36). Given that there is no mean streamwise pressure gradient associated to the EHD body force, and that the remaining contribution is just the potential energy acting on the momentum component responsible for turbulence within the 1-D domain, the ODT inclusion of the EHD body force as a potential energy term in the stochastic eddy event implementation is fully justified.

To summarize, it is noted that the role of the EHD body force in turbulence, for the asymptotic mobility ratio cases studied in this thesis, is equivalent to the role of the combined hydrodynamic pressure gradient and shear stress tensor divergence in the Navier-Stokes equations. In the internally forced convective flow cases studied with ODT, this role is restricted to a pressure-gradient type interaction in the direction of the ODT line. The EHD body force does not produce, nor dissipate turbulence directly, as seen by the absence of the EHD term in Eq. (F.9). Just like the pressure, its role is in the transport of turbulence, although this could also be an indirect mechanism for turbulence production due to modifications in the Reynolds shear stress. Therefore, the incorporation of the EHD body force term must be within the stochastic eddy event implementation part.

6.2 IMPLEMENTATION OF THE EHD BODY FORCE IN THE ODT WIRE-PLATE ESP

The findings from the previous section are in conflict with the EHD body force representation used in this chapter. As seen in Figure 6.1, the electric fields generated in the wire-plate ESP case are inherently two-dimensional. These electroquasistatic fields are independent of the flow dynamics, as discussed in chapter 3. The EQS fields are actually calculated before the flow simulations following the methods in appendix H. The existence of such a 2-D electric current density field grants the flow an inherently elliptic character. Since the body force is 2-D, there should be a corresponding associated 2-D pressure gradient type interaction. A mean pressure gradient-type of interaction in the streamwise momentum would result, for the incompressible flow intended in this study, in a direct modification of the streamwise bulk velocity. However, a bulk-filtering of the EHD body force considering the configuration suggested in Figure 6.1, results in a cancellation of the bulk effect of the streamwise EHD body force. Note that the bulk effect of the crosswise component of the EHD body force also cancels out. Such bulk filtering is simply an integration, e.g., over a control volume of length d_{elec} and height H with an electrode at the center. The implications of the latter consideration for the streamwise momentum component is that the EHD body force is not contributing, directly at least, with a change in the magnitude of the mean bulk streamwise momentum. This effect can also be visualized in the diagrams shown in [53]. Thus, there is no additional forcing necessary for the ODT simulations. This deductive analysis indicates that, for the case in Figure 6.1, the EHD body force does not inject energy at the large bulk scales (integral scales). This agrees with the phenomenological description presented in [52]. The characteristic length scale interaction for the EHD body force presented by [52] is, instead, located in the range between the integral length scale and the dissipation subrange (Kolmogorov length scale).

The question is then, how to implement such a 2-D generated electric field in ODT, in the most consistent way, in order to evaluate the flow as in [53]. The answer to this question is that the contribution of \underline{J} that needs to be considered is precisely the one associated to the turbulence, or the vortical motion¹. For that, the decomposition of the current onto its solenoidal and irrotational components suggested by [76] is used. The irrotational component is the one contributing to the mean flow motion, while the solenoidal component is the one contributing to turbulence. As explained in [76], in general, the electric current density can be described as rotational if its curl exists. The

¹ Again, this is motivated by the fact that there is no direct net contribution neither to the streamwise bulk flow due to the periodic electrode array, nor to the crosswise bulk flow due to the walls.

curl of the electric current density, or of the EHD body force, per Eq. (2.11) is,

$$\frac{1}{\beta} \nabla \times \underline{J} = \nabla \times (\rho_f \underline{E}) = \rho_f (\nabla \times \underline{E}) + \nabla \rho_f \times \underline{E}. \quad (6.3)$$

The first term in the RHS of Eq. (6.3) is zero as a consequence of Eq. (2.17). Therefore, the solenoidal part of the electric current density vector can be attributed to the charge density gradients.

Formally, given the precomputed 2-D EQS field, the calculation of the solenoidal or rotational component of the electric current density could be calculated by the vector identity,

$$\underline{J} = -\nabla j_{irrot} + \nabla \times \underline{J}_{sol}, \quad (6.4)$$

where the subindices *irrot* and *sol* refer to the irrotational and solenoidal components, respectively. These components can be calculated as in any Helmholtz decomposition, see [114],

$$\begin{aligned} j_{irrot} &= \frac{1}{4\pi} \int_{\mathcal{V}} \frac{\nabla' \cdot \underline{J}(\underline{r}')}{|\underline{r} - \underline{r}'|} d\mathcal{V} - \frac{1}{4\pi} \oint_S \frac{\underline{J}(\underline{r}')}{|\underline{r} - \underline{r}'|} \cdot \underline{n}' dS' \\ &= -\frac{1}{4\pi} \oint_S \frac{\underline{J}(\underline{r}')}{|\underline{r} - \underline{r}'|} \cdot \underline{n}' dS'. \end{aligned} \quad (6.5)$$

$$\begin{aligned} \underline{J}_{sol} &= \frac{1}{4\pi} \int_{\mathcal{V}} \frac{\nabla' \times \underline{J}(\underline{r}')}{|\underline{r} - \underline{r}'|} d\mathcal{V} - \frac{1}{4\pi} \oint_S \underline{n}' \times \frac{\underline{J}(\underline{r}')}{|\underline{r} - \underline{r}'|} dS' \\ &= \frac{\beta}{4\pi} \int_{\mathcal{V}} \frac{\nabla' \rho_f(\underline{r}') \times \underline{E}(\underline{r}')}{|\underline{r} - \underline{r}'|} d\mathcal{V}. \end{aligned} \quad (6.6)$$

Here, ∇' indicates that the nabla operator is taken with respect to the position vector \underline{r}' . The volume integral in Eq. (6.5) is neglected due to the zero divergence of the electric current density by Eq. (3.64). Furthermore, for the wire-plate ESP, the remaining surface integral term in Eq. (6.5) is zero if a 2-D control volume limited by the walls with an electrode in the center is considered. The surface integral term in Eq. (6.6) is neglected given that the electric current density vector is always parallel to the boundary surfaces². Given the 2-D field of \underline{J} , \underline{J}_{sol} is a 1-D vector in the z direction, which, for the purposes of ODT, is simply a scalar current density corresponding to the rotational contribution. Note also that $\nabla \rho_f \times \underline{E} = \nabla \times (\phi \nabla \rho_f)$.

The approach described above, although being the most methodical and formal one, was not the one followed in this chapter. Instead, a much simpler decomposition of the electric current density was considered,

$$\underline{J} = \rho_f \beta \underline{E} = -\beta \nabla (\rho_f \phi) + \beta \phi \nabla \rho_f. \quad (6.7)$$

² There are no tangential electric field lines at the surface of conductors or at the surface of the walls which are all at 0 electrostatic potential.

It is possible to think of Eq. (6.7) as a naive approach for the decomposition of \underline{J} . In fact, the curl of \underline{J} according to this decomposition is simply $\nabla \times (\beta\phi\nabla\rho_f)$, which is the same curl obtained by using Eq. (6.4) with Eqs. (6.5) and (6.6). Eq. (6.7), is, therefore, a Helmholtz decomposition [114], in which the term $\beta\phi\nabla\rho_f$ is the solenoidal contribution, i.e., the part associated to the charge density gradients, and the term $-\nabla(\rho_f\beta\phi)$ is the irrotational contribution, i.e., the part which can be written as a flux. The decomposition according to Eq. (6.7) is the approach followed in this chapter. The irrotational contribution is neglected. The streamwise rotational component of \underline{J} , i.e. $\beta\phi\partial\rho_f/\partial x$, was used as a streamwise dependent body force in the deterministic S-ODT advancement. The wall-normal rotational component, $\beta\phi\partial\rho_f/\partial y$, was used during eddy events as the actual crosswise current density component responsible for the potential energy contribution in the estimation of the eddy acceptance probability (see section 3.5).

The last discussion before proceeding into the simulation setup and listing of the input parameters is the decision of whether the electrostatic potential energy term in the ODT stochastic eddy event implementation involves or not a certain transformation of electrostatic potential energy into kinetic energy. That is, the discussion of the choice regarding the implementation of either Case I or Case II from section 3.5 in the S-ODT simulations. For that, the choice of Case I is motivated due to the decomposition performed for the electric current density vector by Eq. (6.7), and based on the reasoning presented in [76]. Given that the entire irrotational component of \underline{J} is discarded in the S-ODT simulations, there is, thus, no justification for considering a transfer of energy between the potential energy term and the kinetic energy available in the flow. A transfer of kinetic energy would be the case in the redistribution of kinetic energy among velocity components due to a pressure gradient-like effect. However, there is no such irrotational component of the electric current which would play this role. Therefore, the S-ODT simulations presented here consider the Case I treatment discussed in section 3.5.

6.3 SETUP OF THE NUMERICAL SIMULATIONS

Similar geometry and considerations to those from the DNS simulations were considered in an attempt to replicate the results from [53] with ODT. The flow is forced by a mean streamwise pressure gradient determined by a target friction Reynolds number (see 3.6.2). As it has been discussed previously, the correlation between a pressure gradient and a target friction Reynolds number is feasible in this case, given that it is possible to relate the wall shear stress with the pressure gradient by integration of the mean momentum equation [32], i.e., there is no bulk contribution of the EHD body force into the momentum of the flow. Buoyancy effects are also neglected in this chapter, given

that an incompressible constant property channel flow is considered. It is noted that the ODT simulations consider an infinitely long wire-plate ESP (with assumed spanwise periodicity), in comparison to the duct-type geometry of the DNS [53]. Nonetheless, for the purpose of the evaluation of the fundamental interactions intended here, this comparison suffices.

The electric field is generated by an infinitely long array of point electrodes, which operate at a discharge voltage ϕ_{elec} as indicated in Figure 6.1. The collector plates (walls of the channel) are grounded at a voltage $\phi_{plate} = 0$. The calculation method of the 2-D electroquasistatic fields, which remain fixed during the S-ODT simulations, is presented in appendix H. The current per unit length measured at the plate, I_{plate}/B , is used as a stopping criteria for the iteration procedure indicated in appendix H for the calculation of ϕ , \underline{E} and ρ_f . The EQS fields are obtained at the nodes of a 2-D grid of length $d_{elec}/2$. All fields are then interpolated into the centers of the cells of an equivalent equidistant 2-D grid, and mirrored across the channel centerline, in order to produce a 2-D array of height H , the distance between the walls of the channel. Since the channel is infinite (periodic) in streamwise direction, the 2-D EQS fields in a given discrete section of the channel of length d_{elec} are reused as many times as needed during the S-ODT simulations.

The low and high voltage cases evaluated in this chapter, and the required parameters for the calculation of the corresponding electroquasistatic fields in both cases can be found in Table 6.1. Figure 6.2 shows the field of the electrostatic potential in the high voltage case, or Case B from Table 6.1.

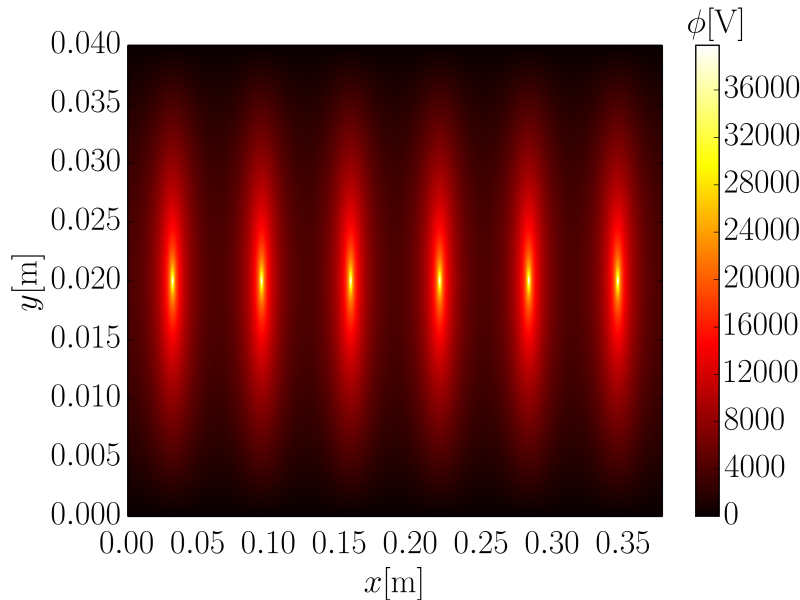


Figure 6.2: Distribution of the electrostatic potential in the wire-plate ESP (Case B, $\phi_{elec} = 42000\text{V}$). The channel height is $H = 0.04\text{m}$.

Table 6.1: Electrostatic field parameters for the different cases investigated. LV and HV refer to the low voltage and high voltage cases, respectively.

Parameter / Case	0 (Reference)	A (LV)	B (HV)
Distance between electrodes d_{elec} [m]	0.0628	0.0628	0.0628
Channel height or distance between channel walls $L_{ODT} = H$ [m]	0.04	0.04	0.04
Ionic mobility for positive discharge in air β [$\text{m}^2/(\text{V} \cdot \text{s})$]	0	1.43×10^{-4}	1.43×10^{-4}
Electrode discharge voltage ϕ_{elec} [V]	0	32000	42000
Grounded channel wall voltage ϕ_{plate} [V]	0	0	0
Electric current per unit length measured at the plate I_{plate}/B [A/m]	0	0.3×10^{-3}	0.75×10^{-3}

The flow simulations can be started once the electrostatic field is computed. A value of $\alpha = 0$ is chosen for simplicity in the simulations of this chapter. The ODT model parameters C and Z are calibrated for the mean streamwise velocity profiles in the pure incompressible constant property reference channel flow case (case 0 in Table 6.1). As in chapters 4 and 5, the sensitivity of the model parameters with respect to the change in the flow dynamics³ is expected to be small. However, a detailed sensitivity study concerning the choice of the model parameters was not carried out in this thesis. An exception to this rule in this chapter will be discussed later. The calibration process for the C and Z model parameters in the reference case is not shown here. However, it is stressed that, due to the very low characteristic Reynolds number of the flow ($Re_\tau = 108$), ODT already shows non-negligible qualitative differences with the corresponding DNS mean flow profiles in the outer layer of the normalized mean streamwise velocity profile. This is due to the appearance of structures which are characteristic of a low Reynolds number flow, and which have a more important character and a larger influence on the large scales, the

³ Change in the Reynolds number, or, in this case, change in the electrohydrodynamic number.

closer the flow approaches the critical transition Reynolds number⁴. As discussed in previous chapters, the lower value of the parameter C in comparison to values used in previous chapters is indicative of the lower Reynolds number of the simulation (more laminar character of the flow). Table 6.2 shows the physical and adaptive mesh settings for the S-ODT simulations. These settings are common for all of the three evaluated cases. Table 6.3 shows the ODT model parameters used.

Table 6.2: Physical and adaptive mesh settings of the S-ODT simulations.

Physical settings	Description / Value
Forcing method for u	FPG forcing
Target friction Reynolds number Re_τ	108
FPG $\partial\bar{p}/\partial x$ [Pa/m]	-0.5548
Domain size $L_{ODT} = H$ [m]	0.04
Air density ρ [kg/m ³]	1.38
Air kinematic viscosity ν [m ² /s]	1.6606×10^{-5}
Adaptive mesh settings	Value
$\Delta y_{min} = \eta_0/6$ [m]	3.0864×10^{-5}
Δy_{max} (m)	8.0×10^{-4}
g_{Dens}	80.0
$A_{TimeFac}$	1.0
Eddy-size PDF l_{max}/L_{ODT}	$1/2 = 0.5$

Table 6.3: ODT model parameters used for the wire-plate ESP simulations.

Parameter	Value
C	1.5
Z	100
α	0

6.4 SIMULATION RESULTS AND DISCUSSION

First, the changes in the mean streamwise velocity profiles and the Reynolds shear stresses in all of the three evaluated cases are analyzed. These results are shown in Figures 6.3a and 6.3b. It is noted that the average operator used in this case for the presentation of the results is, just like in chapter 4, a Reynolds-average operator; in this

⁴ For reference, for pipe flows, the critical Reynolds number is close to $Re_{b,cr} \sim 2000$ (defined based on the pipe diameter), while in channel flows, this critical value is approximately $Re_{b,cr} \sim 1400$ (defined based on the channel height or width H) [115].

case, though, it is convenient to stress that the averaging was done in streamwise direction, and hence, the use of the overline $\bar{\psi}$ in the presented results. It is also noted that, regardless of the choice of the ODT model parameter $\alpha = 0$, the crosswise Reynolds shear stress can still be obtained by the change in the streamwise velocity profile due to eddies, see appendix F. Although the effects are small, Figure 6.3a shows an increase of the mean velocity gradient in the outer layer of the flow at the HV simulation case. As a consequence, there is an increase in the bulk flow velocity which follows the increase in the voltage of the discharge electrodes. Similarly, Figure 6.3b shows a consistent overall increase in the magnitude of the crosswise Reynolds shear stress with the increase in the voltage of the discharge electrodes. The increase in the Reynolds stress agrees with the DNS data in the LV case only. Overall, an increased probability of eddy events occurs in the regions close to the electrodes due to the influence of the EHD forcing. This is seen in Figure 6.4.

The results shown in Figure 6.3a apparently contradict the discussion offered in the previous section regarding the alleged constancy of the bulk streamwise momentum, or of the bulk streamwise velocity, with respect to the EHD body force. The discussion in section 6.2 detailed, however, that there was an effect of the EHD body force on the transport of turbulence, yet, the effect was not directly on the large bulk flow scales. Hunt [77] details that, for body forces which are independent of the flow whilst being functions of space and time, the predominant characteristic is the local induction of mean flows characterized by eddy structures and oscillations. Thus, **can there be an increase in the bulk flow velocity without a net contribution from the EHD body force and at the same imposed mean pressure gradient, or wall shear stress?** According to the parameterization in Eq. (3.66), this is impossible, unless the value of the skin friction coefficient C_f is allowed to change. Precisely, it is noted that an increase or reduction in the kinetic energy of the mean flow, or mean flow induction, is normally translated as a corresponding drag reduction or drag increase effect, respectively. The drag is understood here by the effect in the skin friction coefficient C_f , given by Eq. (3.63). Consider the integral form of the kinetic energy equation given by Eq. (2.52), rewriting the shear stress tensor divergence as in Eq. (F.8),

$$\begin{aligned} \frac{d}{dt} \int_{\mathbf{V}(t)} \rho \zeta_{kin} d\mathbf{V} = & - \int_{\mathbf{V}(t)} \underline{V} \cdot \nabla p d\mathbf{V} + \int_{\mathbf{V}(t)} \mu \nabla^2 \zeta_{kin} d\mathbf{V} - \int_{\mathbf{V}(t)} \epsilon \zeta_{kin} d\mathbf{V} \\ & + \rho \underline{g} \cdot \int_{\mathbf{V}(t)} \underline{V} d\mathbf{V} + \int_{\mathbf{V}(t)} \rho_f \underline{E} \cdot \underline{V} d\mathbf{V}. \end{aligned} \quad (6.8)$$

Here, the integral of the kinetic energy contribution due to the EHD body force on the RHS is zero as detailed before, according to the periodic and symmetric electric field in Figure 6.2. If a statistically

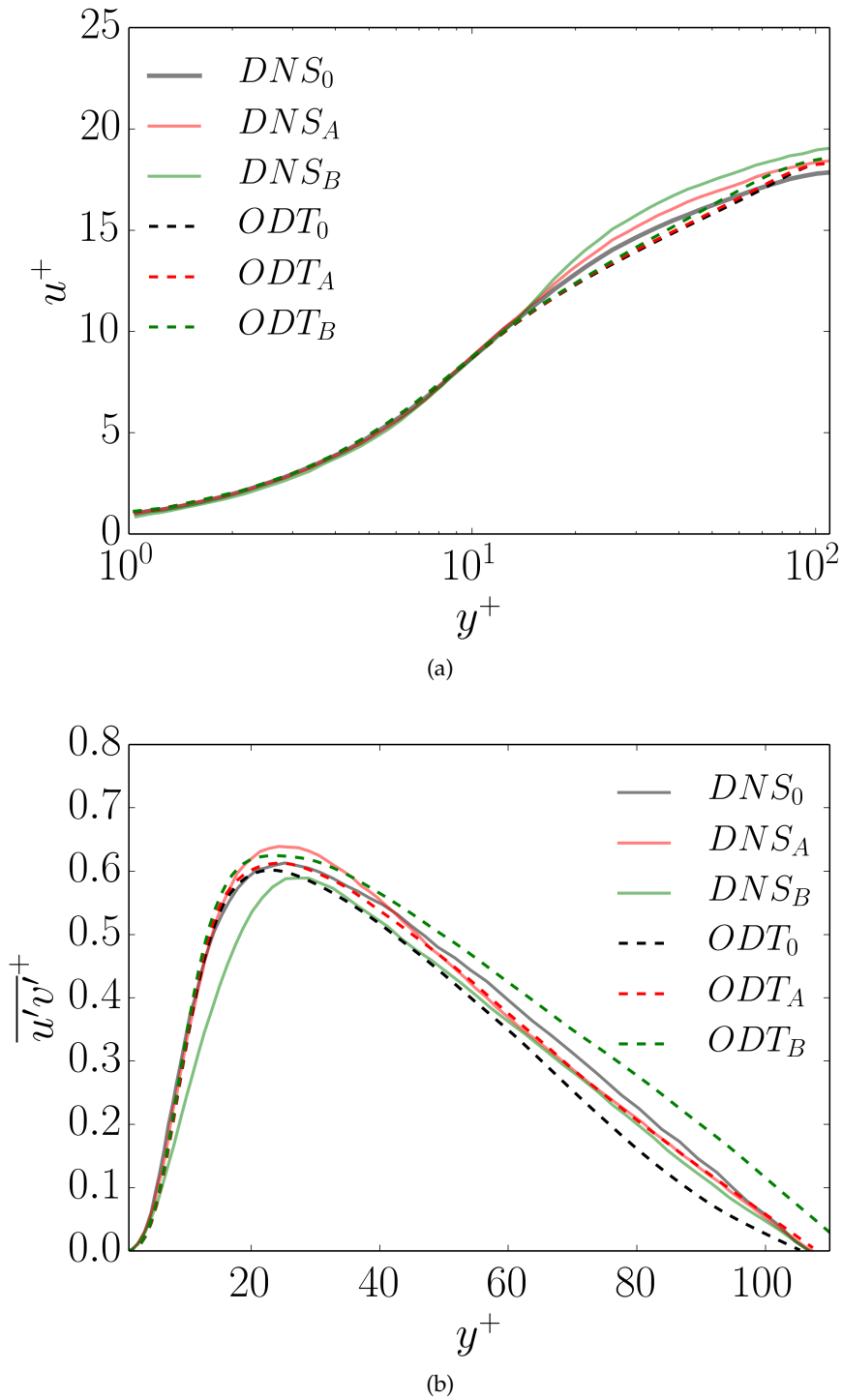
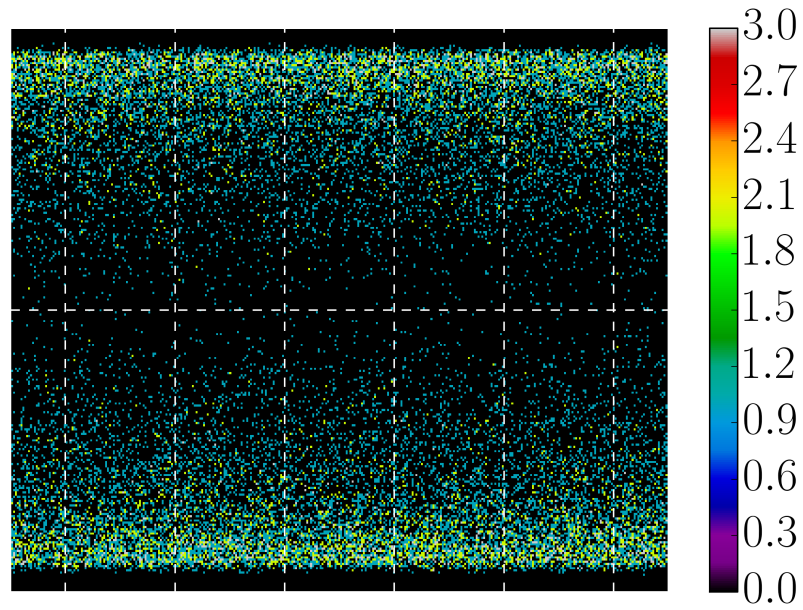
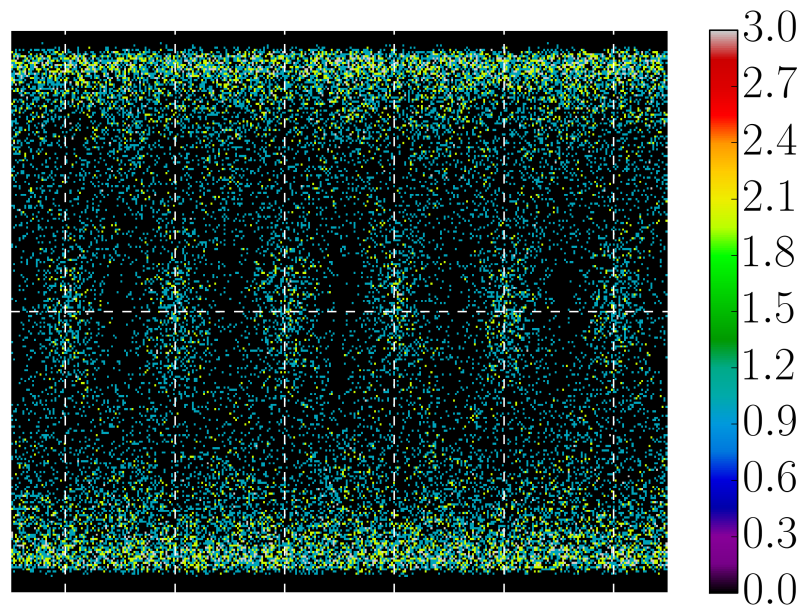


Figure 6.3: Normalized mean velocity profile and Reynolds shear stresses obtained in the three simulated cases of Table 6.1. Reference DNS data from [53] is shown for reference. Figures are taken from the original publication in [112].



(a)



(b)

Figure 6.4: Eddy event distribution in the S-ODT simulations of the wire-plate ESP. (a) Reference case, without EHD forcing. (b) Case B, HV case. The different colors in the plots indicate the density in the number of events according to the supplemented color scale. The intersection of the white dashed lines indicates the position of the electrodes. The Figure is adapted from the original publication in [112].

stationary and homogeneous kinetic energy field is assumed on the Lagrangian volume, the integral kinetic energy balance reduces to,

$$\int_{\mathcal{V}(t)} \underline{V} \cdot \nabla p d\mathcal{V} - \rho \underline{g} \cdot \int_{\mathcal{V}(t)} \underline{V} d\mathcal{V} = - \int_{\mathcal{V}(t)} \epsilon_{\zeta_{kin}} d\mathcal{V}. \quad (6.9)$$

Considering a non-negligible pressure gradient in streamwise direction only, and neglecting the effect of the gravitational potential energy, Eq. (6.9) is, according to the velocity field from Figure 6.1 in the channel case,

$$U_b \frac{\partial \bar{p}}{\partial x} H = -\mu \int_{x=0}^{x=d_{elec}} \int_{y=0}^{y=H} \left(\frac{\partial u}{\partial x} \frac{\partial u}{\partial x} + \frac{\partial u}{\partial y} \frac{\partial u}{\partial y} + \frac{\partial v}{\partial x} \frac{\partial v}{\partial x} + \frac{\partial v}{\partial y} \frac{\partial v}{\partial y} \right) dy dx. \quad (6.10)$$

This expression justifies the indirect changes in U_b , and subsequently in C_f , as a consequence of modifications in the kinetic energy dissipation. In fact, this is in perfect agreement with the second Kolmogorov hypothesis, which states that the large scale behavior is dictated by the TKE dissipation [21, 32]. In the FPG forcing, U_b is changed, not directly due to the EHD body force, but rather, indirectly due to the inherent change in the kinetic energy dissipation by the injection of energy from the EHD body force at an intermediate scale.

The results from Figure 6.3a confirm the previous analysis. The injection of the surplus energy due to the EHD body force is seen in the results shown by Figure 6.3b. That is, an increase in the Reynolds shear stresses due to the EHD body force, a statement which was also already analyzed by [76]. In fact, the EHD body force does not only increase the crosswise Reynolds shear stress $\overline{u'v'}$, but also the streamwise Reynolds shear stress $\overline{u'u'}$, which is part of the TKE. This indirect modification of the mean flow by the Reynolds shear stresses results in the observed drag reduction effect from Figure 6.3a. As stated before, the EHD body force does not induce a mean bulk flow directly, but rather, a modification of C_f due to modifications in the turbulent transport. The latter explanation agrees with the description commented in section 6.2.

An *exception* to the understood general rule of model parameter calibration in ODT is discussed now. Effectively, in chapters 4 and 5, the strategy for the selection of the model parameters was, in the case of chapter 4, a calibration at a moderate Reynolds number case, and in the case of chapter 5, a calibration of the model parameters based on the mean flow statistics of the simulated case. It is clear that the model parameters used in chapter 4 deviated from the values used in chapter 5. Although the dynamics between constant and variable density flow are clearly different with respect to each other, the change in the model parameters, specifically the change of C , is only attributed to the lower Reynolds number of the flow evaluated in chapter 5. That is, as commented in the previous section, C becomes case dependent

in an increasingly laminar-dominated regime. Since a value $C = 0$ is indicative of laminar flow in ODT (no implementation of eddy events), this is a consistent behavior of the model. The drag reduction effects shown in Figure 6.3a are a sign of *local flow relaminarization*, or at the very least, indicate the change in the fully turbulent character of the flow towards a transition regime. Since the dynamics of large scale eddy structures which are characteristic from transition regimes can neither be interpreted nor reproduced in ODT, this *local flow relaminarization* is modeled with a C parameter dependency, i.e., a reduction in the C parameter for increased magnitudes of the EHD body force.

Reviewing the nondimensional momentum equation, Eq. (3.66), it is noted that the EHD body force is scaled by the parameter N_{EHD}^2/Re^2 . C maintains a proportional relation with Re , that is, $C \rightarrow 0$ if $Re \rightarrow Re_{cr}$ (the critical Reynolds number for the transition between laminar and turbulent flow). This is equivalent to stating that $C \rightarrow 0$ if $Re_\tau \rightarrow 1$. For incompressible constant property flow, C_f can also be written as,

$$C_f = 2 \frac{u_\tau^2}{U_b^2} \rightarrow C_f = 2 \frac{Re_\tau^2}{Re^2}. \quad (6.11)$$

For a fixed value of Re_τ imposed on the simulations by the FPG forcing, the proper scaling of C_f goes then in inverse relation with Re . The analogy with the parameter C is then straightforward. If C_f scales inversely with N_{EHD}^2/Re^2 , then it should be possible to expect that C also does, i.e., $C \rightarrow 0$ if $N_{EHD}^2/Re^2 \rightarrow \infty$ in a very rough approximation. Indeed, it has been verified empirically in this work, that an appropriate qualitative behavior for the drag reduction trend, as well as the Reynolds shear stress behavior in the inner layer close to the wall (in comparison to the DNS data), can be found by scaling the C parameter as the following function of N_{EHD}^2/Re^2 ,

$$C_{scal} = C_0 \left(1 - \frac{4}{27} \frac{N_{EHD}^2}{Re^2} \right) \quad (6.12)$$

The bulk Reynolds number Re and bulk N_{EHD} Reynolds number are defined by Eq. (3.59), using the half-width of the channel $H/2$ as the characteristic length L , and defining the surface associated to the current as $S = HB/2$, where B is the depth of the channel or the length of the electrodes. This gives $N_{EHD}^2/Re^2 = I_{plate}/(B\rho_b\beta U_{b,0}^2)$, where $U_{b,0}$ is the bulk velocity obtained in the reference case. Also, C_0 is the nonscaled C value from Table 6.3. Eq. (6.12) satisfies the inverse relation between C and N_{EHD}^2/Re^2 . The factor $\frac{4}{27}$ is the analytical solution of the ODT kernel identity, Eq. (3.31), which signalizes the relation of C with the kinetic energy changes in the flow due to eddies. Since C is related to the turbulence intensity in ODT, it is hypothesized that this modification of C accounts for the missing mean kinetic energy introduced by the large scale structures, thus resulting in the

noted drag reduction effect. It is noted that Eq. (6.12) may produce negative C values for sufficiently high N_{EHD} values. This sets a limit for the S-ODT parabolic treatment, beyond which the solutions become indistinguishable from the pure still (no through-mean flow) EHD solution, given the complete absence of turbulent transport or eddy events. The still EHD solution is an inherently elliptical quiescent flow boundary value problem (BVP).

Using the suggested scaling, it is possible to obtain a better distinction between cases 0 and A in the mean velocity profiles, while also obtaining the same DNS trends in the Reynolds stress close to the wall. This is shown next in Figures 6.5a and 6.5b. Table 6.4 shows the change in the obtained bulk velocity values (and corresponding skin friction coefficient) for the nonscaled and scaled C -parameter simulations. The wall shear stress and friction velocity values corresponding to the constant forcing mean streamwise pressure gradient values used both in DNS and ODT are obtained by the integration of the streamwise incompressible constant property momentum equation, Eq. (F.7) (see also [32]).

Despite the improvement of the behavior in the crosswise Reynolds shear stress $\overline{u'v'}$ close to the wall, its qualitative disagreement in the outer layer still persists. According to the DNS data, there is a non-monotonic behavior in the near wall peak of the Reynolds shear stress; it increases in the LV case (case A), and then decreases below the reference case at HV (case B) [53]. Simultaneously, all three cases collapse in the outer layer away from the wall. This representation of the flow dynamics is not well reproduced in ODT for the reasons explained before regarding the inability of ODT to reproduce coherent structure information. The behavior of the crosswise Reynolds shear stress is explained in the DNS in terms of the reduction in the frequency of events producing negative Reynolds stresses⁵, and the increase in the frequency of events producing positive Reynolds stresses⁶ [53]. The latter frequency increase results in a decrease of the TKE production close to the wall, which could explain the apparent *relaminarization* of the flow away from the wall according to the inner scaling in Figures 6.5a (increased velocity values in the bulk region of the flow) and 6.5b (decrease of the Reynolds shear stress close to the wall). Given that, in addition to this apparent *relaminarization*, the overall effect of the EHD forcing increases the intensity of the turbulence events according to the DNS [53], the resulting increase in stochastic eddy events from Figure 6.4 with the corresponding drag reduction effects from Figures 6.5a and 6.5b, could be seen as a suitable representation of the flow in ODT, at least regarding the first order statistical moments and implied physics.

5 Events producing $u' < 0$ and $v' > 0$ or $u' > 0$ and $v' < 0$, considering zero average velocities.

6 Events producing $u' > 0$ and $v' > 0$ or $u' < 0$ and $v' < 0$, considering zero average velocities.

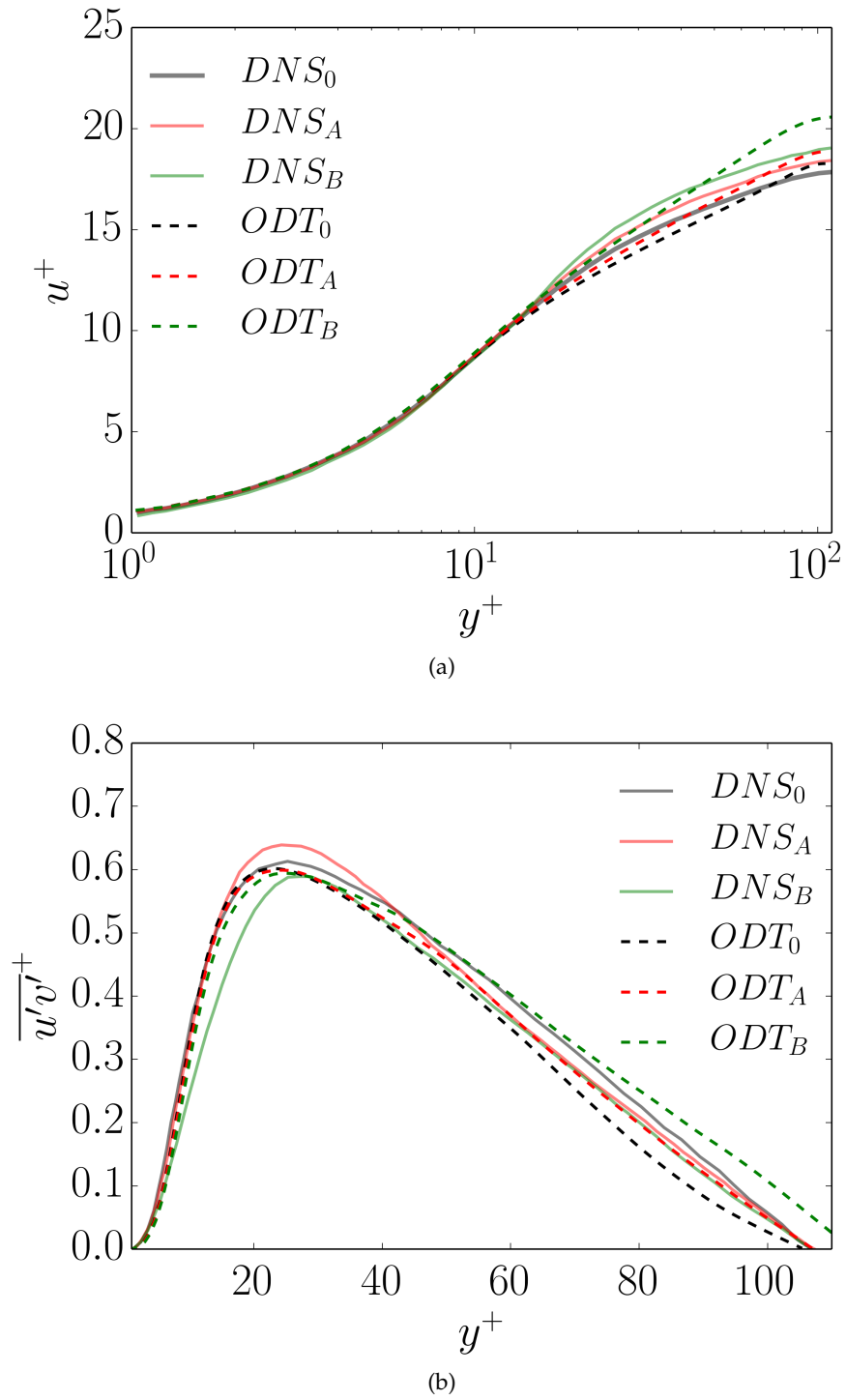


Figure 6.5: Normalized mean velocity profile and Reynolds shear stresses obtained in the three simulated cases of Table 6.1 with the scaled ODT model parameter C given by Eq. (6.12). Reference DNS data from [53] is shown for reference. The Figures are taken from the original publication in [112].

Figure 6.6a shows the non-dimensional mean shear stress obtained with the scaled C parameter values in the LV and HV cases. ODT is able to reproduce the increase in the mean velocity gradient in the buffer layer for increasing magnitudes of the EHD forcing. Although the values of the shear stress are different to those of the DNS, it is noted that the increase in the mean velocity gradient up to a position $y^+ \sim 30$ contrasts with the decrease in the Reynolds shear stress. This is a feature achieved in ODT which can not be reproduced with the classical Boussinesq turbulent viscosity approach or the eddy viscosity models used in traditional RANS simulations.

To complement the discussion of the crosswise Reynolds shear stress, Figure 6.6b shows the normalized streamwise RMS velocity profile. The apparent localized *relaminarization* effect, or its drag reduction counterpart, can be seen in a much clearer way in this figure by the reduction in the RMS velocity values away from the wall at the LV and HV cases.

It is not possible to evaluate the local increase or decrease of the TKE production stated by the DNS with the streamwise averaging used in the S-ODT simulations. This is because the quadrant analysis used in the DNS to evaluate the TKE production term supposes a velocity field with zero average. In the DNS, a triple decomposition is suggested, see [53]. E.g., for the streamwise velocity field,

$$u(x, y, z, t) = \bar{u}(y) + \langle u \rangle(x, y, t) + u'(x, y, z, t). \quad (6.13)$$

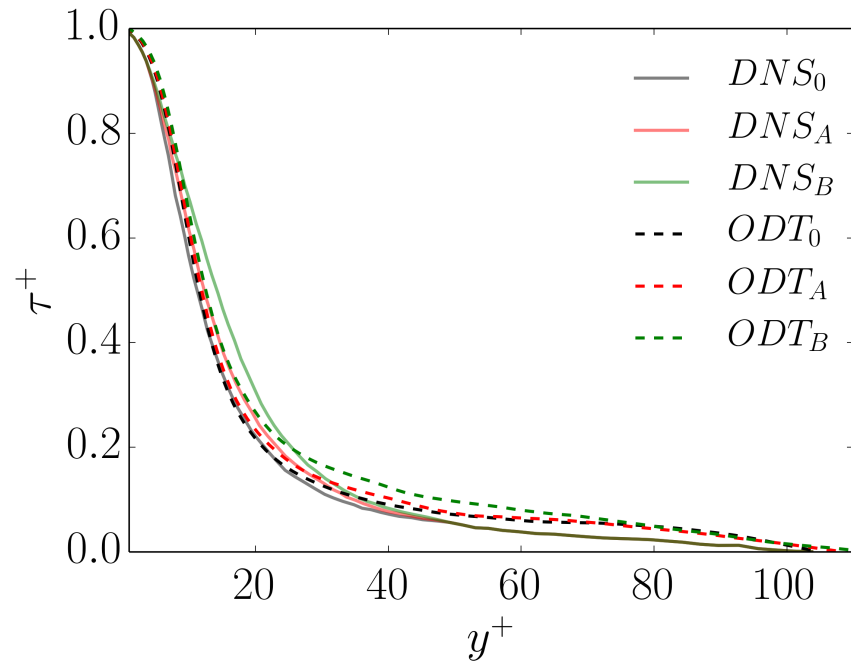
This is a decomposition into a mixed streamwise and temporal average $\bar{u}(y)$, plus an ensemble (phase) average $\langle u \rangle(x, y, t)$ of the homogeneous spanwise direction z . The corresponding ensemble average in ODT is given by the different realizations at the same wall-normal and streamwise positions, i.e.,

$$u(x, y, n) = \bar{u}(y) + \langle u \rangle(x, y) + u'(x, y, n). \quad (6.14)$$

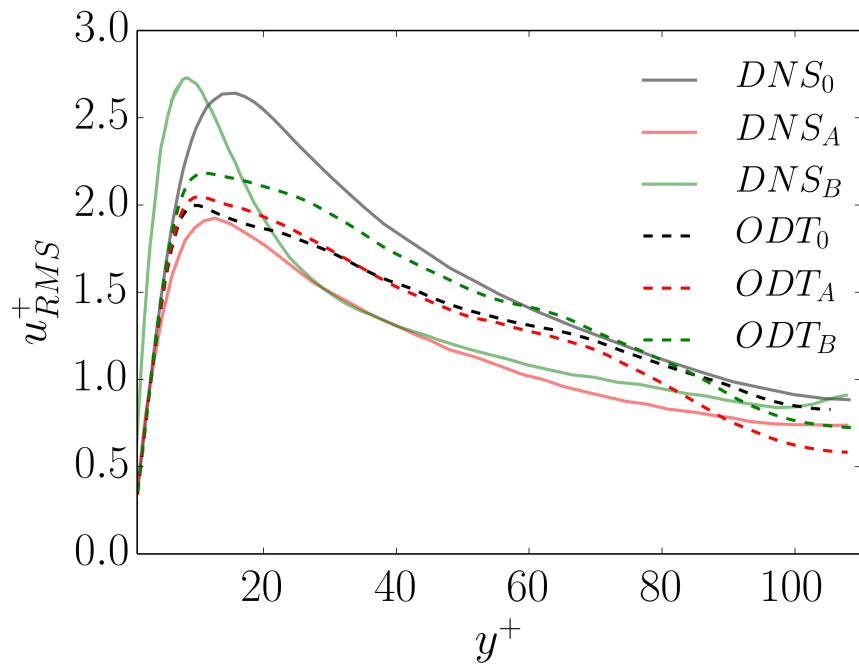
Here, \bar{u} is the average achieving the fully developed condition of the velocity field and $\langle u \rangle$ is an ensemble average corresponding to a discrete periodic position n between the discharge electrodes. Due to the imposed fully developed character of the flow, $\langle u(x, y) \rangle = \langle u \rangle(y) = \bar{u}(y)$ in ODT. Similarly, $\langle v \rangle = \bar{v} = 0$ ⁷, in contrast to $\langle v \rangle \neq 0$ in the DNS [53]. The lack of ellipticity is again, the reason why the model is unable to analyze organized motions of the non-streamwise velocity components⁸. Hence, the calculation of the TKE production and dissipation budgets in ODT is the same, given that the triple decomposition of the DNS simply reduces to the same traditional Reynolds decomposition in ODT. Therefore, it is impossible for ODT to capture differences in

⁷ Either due to the 1-D divergence (zero gradient) condition of v during the S-ODT deterministic step, the choice $\alpha = 0$, or the omission of the pressure gradient and the use of a FPG constraint.

⁸ Leaving aside the inability to obtain a w velocity component due to the choice $\alpha = 0$.



(a)



(b)

Figure 6.6: (a) Normalized mean shear stress and (b) streamwise RMS velocity profile obtained with scaled ODT C parameter values given by Eq. (6.12). $\tau^+ = \mu(\partial\bar{u}/\partial y)/\tau_w$ in (a). Reference DNS data from [53] is shown for reference. The Figures are taken from [112].

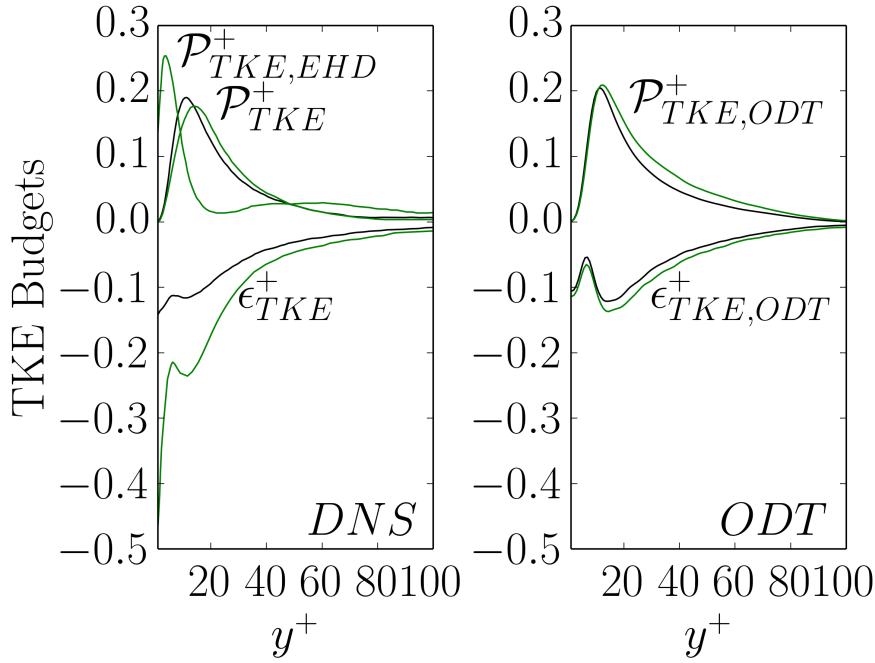


Figure 6.7: Normalized TKE production (\mathcal{P}_{TKE}^+) and dissipation (ϵ_{TKE}^+) budgets. The left figure shows the DNS data for the reference case 0 (black line) and case B (green line) [53]. The right Figure shows the S-ODT results. The organized motion EHD production term from [53] is also included for reference in the left Figure, $\mathcal{P}_{TKE,EHD}^+$. This term can not be reproduced in ODT. The Figure is adapted from the original publication in [112].

the TKE production term due to the organized flow velocity gradient as in the DNS. The same applies for the obtained triple decomposition TKE dissipation term [53]. ODT is not able to capture any dissipation effect other than the one due to shear in the streamwise direction produced by the crosswise gradient of the streamwise velocity⁹. This is seen in Figure 6.7, i.e., there is essentially no change in the TKE budgets obtained with ODT, regardless of the applied EHD body force. The only changes are due to the slight modification of the parameter C slightly affecting the dynamics in the outer layer, i.e., the change in C_f .

⁹ Again, v can only be taken as 0 in the S-ODT simulations done here, and $\partial\bar{u}/\partial x$ is also zero due to the achievement of the fully developed condition of the flow.

Table 6.4: Obtained bulk velocities and corresponding skin friction coefficients in the nonscaled and scaled C-parameter S-ODT simulations (C_0 and C_{scal} , respectively). The DNS obtained values are also shown for reference [53].

Parameter / Case	0	A	B
EHD number $N_{EHD} = \sqrt{IH^2\rho/(4B\beta\mu^2)}$	0.0	1484.9712	2347.9456
Forced friction velocity value in DNS and S-ODT u_τ [m/s]	0.0847	0.0847	0.0847
DNS obtained bulk velocity values $U_{b,DNS}$ [m/s]	1.16	1.19	1.23
DNS obtained skin friction coefficients $C_{f,DNS}$	0.0107	0.0101	0.0095
Nonscaled C S-ODT obtained bulk velocity values $U_{b,ODT}(C_0)$ [m/s]	1.29	1.34	1.44
Nonscaled C S-ODT obtained skin friction coefficients $C_{f,ODT}(C_0)$	0.0086	0.0080	0.0069
Ratio N_{EHD}^2/Re_0^2	0.0	0.9135	2.2838
C_{scal} parameter according to Eq. (6.12)	$C_0 = 1.5$	≈ 1.3	≈ 1
Scaled C S-ODT obtained bulk velocity values $U_{b,ODT}(C_{scal})$ [m/s]	1.29	1.37	1.56
Scaled C S-ODT obtained skin friction coefficients $C_{f,ODT}(C_{scal})$	0.0086	0.0076	0.0059

EHD FLOW IN A CYLINDRICAL ELECTROSTATIC PRECIPITATOR

In this penultimate chapter of the thesis, the effects of the electroquasistatic body force in a cylindrical geometry are evaluated in an incompressible constant property and a variable density framework. The constant property cylindrical ESP is evaluated following the same T-ODT and S-ODT methodology used in chapter 4 for incompressible constant property pipe flows. The methodology used in the variable density cylindrical ESP corresponds to that used in chapter 5.

A sketch of the flow is depicted in Figure 7.1. The basis configuration is that of an pipe flow forced by a given constant streamwise mass flow rate, i.e., $\int \rho u r dr = \dot{m}$, where \dot{m} is the constant mass flow rate in the pipe. One important difference with the pipe flow simulations from chapters 4 and 5 is the presence of an electrode wire, which is treated as an internal boundary in the radial computational domain. The electrode wire generates the corresponding radial electroquasistatic profiles of the electric field, charge density and electric current density. These profiles are calculated as described in appendix H and remain constant during the simulation. During eddy events, the internal boundary is treated just as another fluid parcel subject to the given mapping and kernel rules mentioned in appendix C. The corresponding no-slip (zero Dirichlet) BC corresponding to the internal boundary is enforced during the deterministic advancement. For the variable density cases, the treatment of the enthalpy (or temperature) during the deterministic advancement is indistinguishable from the treatment applied in chapter 5. This implies a treatment of the electrode wire as a perfectly thermal conducting fluid parcel, which guarantees a flux equalization condition at the radial center cell containing the origin, $r = 0$.

In the cylindrical configuration, the electric current density vector is fully irrotational. This is because the electroquasistatic fields are entirely assumed as 1-D radial profiles, and as such, the curl of the electric current density vector as a cross product, i.e., Eq. (6.3), is necessarily zero. Due to the additional zero divergence condition imposed on the electric current density vector, this results in a (radially-weighted) constant electric current density across the radius of the pipe, see Eq. (H.8). As such, the EHD body force term which would appear in the momentum equation can be treated as a part of a modified pressure gradient, as commented in chapter 6. Due to this reason, the EHD body force term is omitted from the deterministic ODT governing equations, and is just considered as part of the pressure

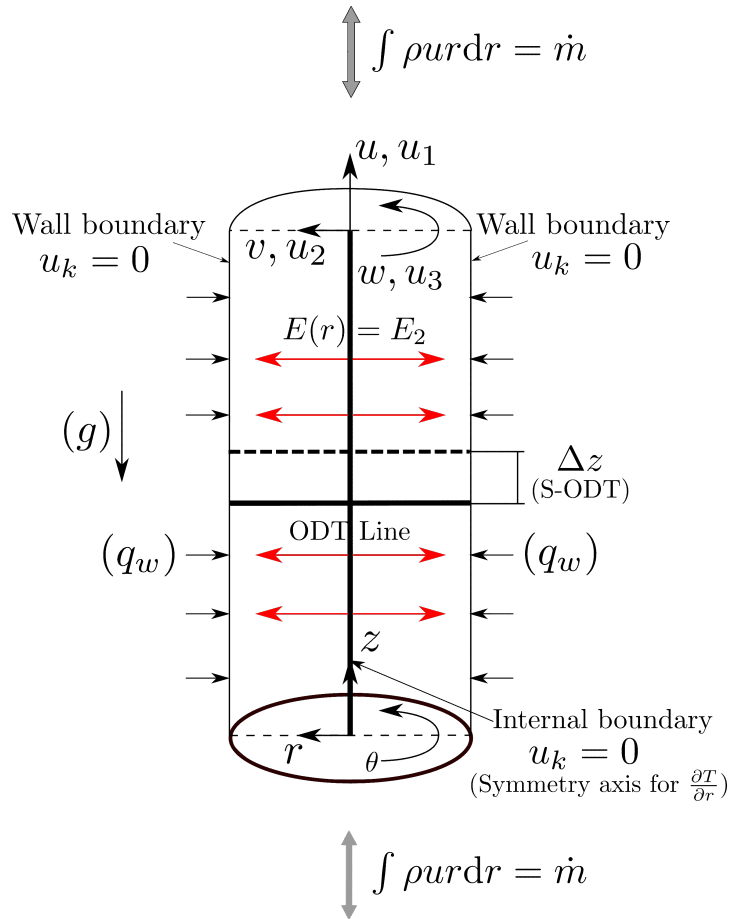


Figure 7.1: Cylindrical ESP model evaluated with ODT. The configuration is the same as that from the heated pipe in chapter 5, with the additional presence of an axial electrode wire concentric with the pipe walls, and which is responsible for the generation of the electroquasistatic variables E_2 , ρ_f and j_2 . The variables within parenthesis may be omitted in different parts in this chapter. This is clarified in the corresponding setups of the numerical simulations performed in this chapter. The flow is forced by means of a constant streamwise mass flow rate constraint \dot{m} . Both vertical and horizontal flows are evaluated in this chapter (for horizontal flows, $g = 0$. The vertical flows are evaluated in both upward and downward directions, as indicated by the thick gray arrow in the sketch.

scrambling process during eddy events in ODT. The EHD body force term is, thus, treated as a potential energy source term which is to be converted into kinetic energy. In practical terms, this means that the Case II treatment of the ODT potential energy formulation is used in all simulations carried out in this chapter.

7.1 INCOMPRESSIBLE CONSTANT PROPERTY FLOW IN A CYLINDRICAL ESP

The results presented in this section correspond to ODT simulations carried out in order to verify experimental measurements of the streamwise pressure drop as a function of the N_{EHD} number. These experiments were performed based on the understanding that a fully developed and incompressible constant property flow achieves a constant and radially homogeneous streamwise pressure gradient. The experimental results shown in this section were performed by the Chair of Particle Technology of the BTU Cottbus-Senftenberg. One part of these results is already published in [116], while another part of the results has not been published so far (at least not until the date of submission of this thesis). For consistency in the referencing, all of these experimental results will be cited as [116].

7.1.1 Setup of the numerical simulations

In an attempt to replicate the experimental results of the pressure drop as a function of the N_{EHD} number with ODT, the first assumption taken during the realization of this thesis was the consideration of the flow as a purely incompressible flow with constant fluid properties. That is, the buoyancy term, the Joule heating term, and any other type of heat or heat transfer were all neglected. These simulations were performed in a T-ODT fashion, obtaining the (temporally averaged) statistically stationary flow profiles. T-ODT simulations were performed for two different electrode wire diameters. The wire diameter influences the calculation of the characteristic nondimensional numbers of the flow by changing the hydraulic diameter of the pipe. In general, the diameter D and the hydraulic diameter D_H (and hydraulic radius R_H) of the pipe are related to the electrode diameter D_{elec} in the cylindrical ESP cases by,

$$D_H = 2R_H = D - D_{elec}. \quad (7.1)$$

The hydraulic lengths need to be substituted every time a characteristic length is required for the calculation of a nondimensional number. The fluid properties and further physical inputs for the T-ODT simulations are shown in Tables 7.1 and 7.2. All simulations consider the ionic mobility values for positive corona discharge in air taken from [117]. The constant mass flow rate constraint is enforced by the calculation of a pressure gradient, as in Eq. (D.24), but with the additional consideration of the presence of the electrode wire, which is excluded from the velocity integral,

$$\frac{\partial \bar{p}}{\partial x} \Delta t = \frac{\left[\sum_{i,-R}^{i,-R_{elec}} (\rho_i u_i \Delta r_i^2) + \sum_{i,R_{elec}}^{i,R} (\rho_i u_i \Delta r_i^2) \right] - \dot{m}}{\sum_{i,-R}^{i,-R_{elec}} \Delta r_i^2 + \sum_{i,R_{elec}}^{i,R} \Delta r_i^2}. \quad (D.24)$$

Table 7.1: Adaptive ODT and flow configuration parameters used for incompressible constant property cylindrical ESP simulations with $D_{elec} = 1\text{mm}$ (T-ODT).

Parameter / Case	Re_b = 2433.3333	Re_b = 4866.6667	Re_b = 7300.0
$L_{ODT} = D = 2R / D_H = 2R_H$ (m)	0.078 / 0.077	0.078 / 0.077	0.078 / 0.077
ρ (kg/m ³)	1.168	1.168	1.168
ν (m ² /s)	1.5822×10^{-5}	1.5822×10^{-5}	1.5822×10^{-5}
Imposed U_b (m/s)	0.5	1.0	1.5
Ionic mobility β [m ² /(V · s)]	1.5×10^{-4}	1.5×10^{-4}	1.5×10^{-4}
ESP length or electrode length B (m)	0.82	0.82	0.82
Target at $\phi_{elec} = 0\text{V}$ for $\partial\bar{p}/\partial x$ (Pa/m)	-0.0866	-0.4561	-0.8001
Δr_C (m)	0.001	0.001	0.001
$\Delta r_{min} = \eta/6$ (m) (from calibration target)	6.9806×10^{-5}	3.0415×10^{-5}	2.2964×10^{-5}
Δr_{max} (m)	0.0023	0.0023	0.0023
δ_{Dens}	80.0	80.0	80.0
$A_{TimeFac}$	1.0	1.5	2.0
Eddy-size PDF l_{max}/L_{ODT}	1/2	1/2	1/2

Table 7.2: Adaptive ODT and flow configuration parameters used for constant property cylindrical ESP simulations with $D_{elec} = 1.5\text{mm}$ (T-ODT).

Parameter / Case	$\text{Re}_b = 2417.5325$	$\text{Re}_b = 4835.0649$	$\text{Re}_b = 7252.5974$
$L_{ODT} = D = 2R / D_H = 2R_H$ (m)	0.078 / 0.0765	0.078 / 0.0765	0.078 / 0.0765
ρ (kg/m^3)	1.168	1.168	1.168
ν (m^2/s)	1.5822×10^{-5}	1.5822×10^{-5}	1.5822×10^{-5}
Imposed U_b (m/s)	0.5	1.0	1.5
Ionic mobility β [$\text{m}^2/(\text{V} \cdot \text{s})$]	1.5×10^{-4}	1.5×10^{-4}	1.5×10^{-4}
ESP length or electrode length B (m)	0.82	0.82	0.82
Target at $\phi_{elec} = 0\text{V}$ for $\partial\bar{p}/\partial x$ (Pa/m)	-0.0866	-0.4561	-0.8001
Δr_C (m)	0.0015	0.0015	0.0015
$\Delta r_{min} = \eta/6$ (m) (from calibration target)	7.0034×10^{-5}	3.0514×10^{-5}	2.3038×10^{-5}
Δr_{max} (m)	0.0023	0.0023	0.0023
g_{Dens}	80.0	80.0	80.0
$A_{TimeFac}$	1.0	1.5	2.0
Eddy-size PDF l_{max}/L_{ODT}	1/2	1/2	1/2

The ODT model parameters C and Z of the T-ODT simulations were calibrated based on the experimental results for the pressure drop obtained in the reference zero voltage case ($\phi_{elec} = 0$ and $I = 0$), i.e. without the EHD body force [116]. An additional calibration step was taken to adjust the value of C in the simulations with nonzero EHD body force. Although the value of C was changed in some simulations between the zero and nonzero EHD body force conditions, C was kept constant for all of the remaining values of N_{EHD} at the same bulk Reynolds number. That is, the only dependence of C is due to the very low Reynolds numbers, or turbulence, of some of the simulated flows, as in previous chapters in the thesis. Given that the presence of the EHD body force term induces additional turbulence in a low Reynolds number flow, C is expected to achieve a constant value at larger Re and N_{EHD} values. The T-ODT model parameters are presented in Table 7.3.

Table 7.3: T-ODT model parameters used for the constant property cylindrical ESP simulations ($D_{elec} = 1\text{mm}$ and $D_{elec} = 1.5\text{mm}$).

ODT Model Parameter	Reference pipe flow	Nonzero EHD body force
C	2.0	11.0
Z	350.0	350.0
α	$2/3 \approx 0.6667$	$2/3 \approx 0.6667$

Figure 7.2 shows the experimental characteristic voltage-current curves corresponding to the electrode diameters, $D_{elec} = 1\text{mm}$ and $D_{elec} = 1.5\text{mm}$ [116]. These curves are required in order to compute the electroquasistatic fields which will remain constant during the simulations. That is, these curves are part of the BCs of the simulations, such that they can not be obtained by the simulations themselves (see appendix H). It is noted that, as suggested in chapter 3, for most of the experimentally measured range, the characteristic voltage-current curves remain practically independent from the Reynolds number of the flow. This agrees in principle with the assumption of constant (with respect to the flow) electric field and charge density fields, or the so called one-way coupling of electroquasistatic variables due to the limit $M_\beta \rightarrow 0$ in Eq. (3.52). Large values of ϕ or I show certain sensitivity to the Reynolds number of the flow. Although it is not the scope of the thesis to evaluate what is happening in such regimes, it is expected that the change in temperature due to a non-negligible Joule heating term in Eq. (3.67), causes a change in the ionic mobility coefficient β , thus modifying the value of the measured voltage (or current).

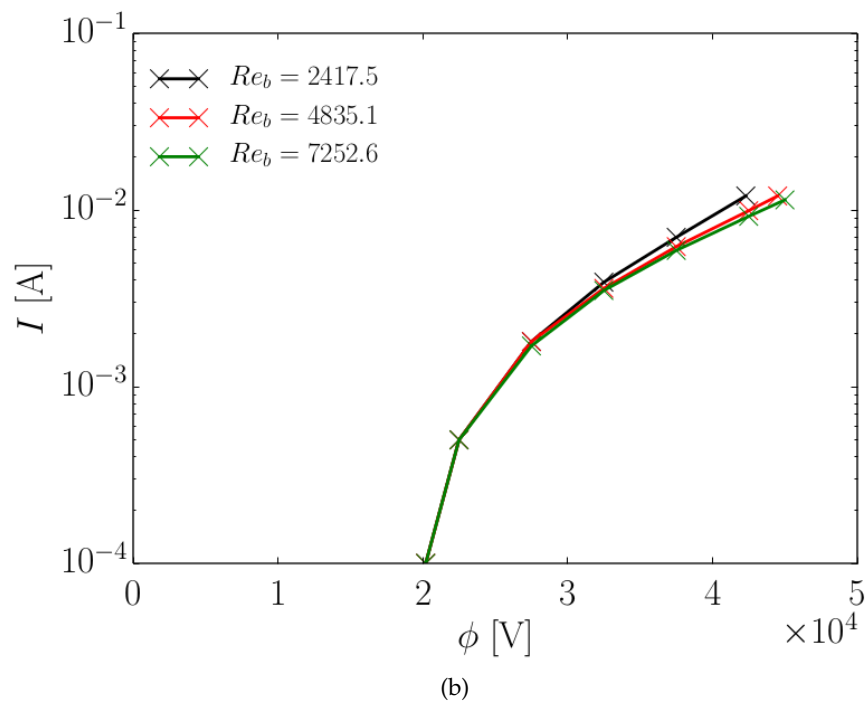
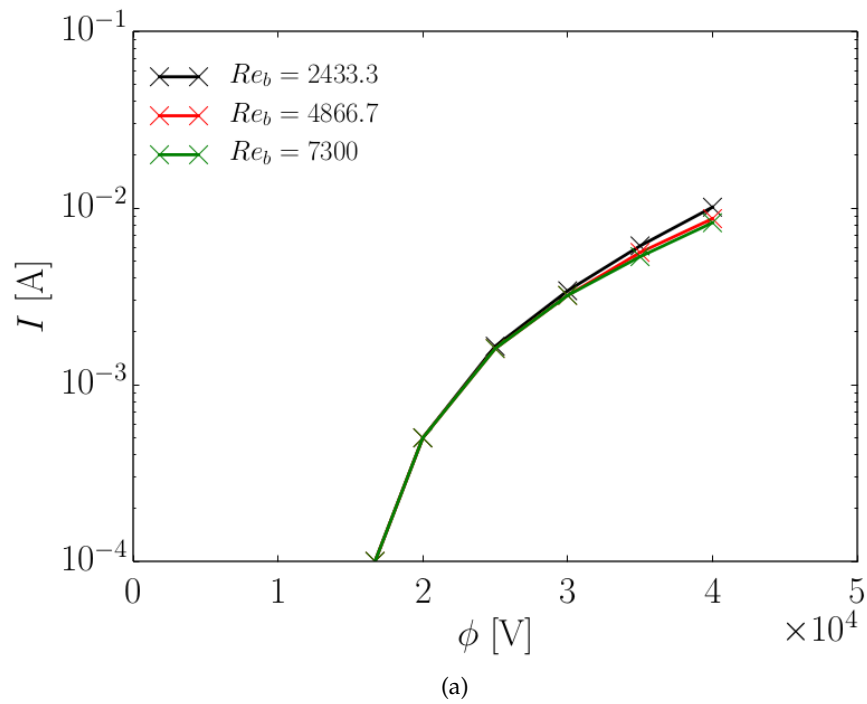


Figure 7.2: Experimental voltage-current curves measured at the different evaluated Reynolds numbers [116] (note the citation comment at the beginning of section 7.1). a) Electrode diameter $D_{elec} = 1\text{mm}$, and b) $D_{elec} = 1.5\text{mm}$.

7.1.2 Bulk flow results

Statistically stationary flows with negligible spatial inhomogeneities other than those present within the ODT line are ideal candidates for T-ODT simulations. Considering the case of a statistically stationary and streamwise homogeneous pipe flow (streamwise homogeneous velocity), without body forces and negligible spanwise velocity and spanwise velocity variations, the mean momentum equations of the flow, Eqs. (F.20) and (F.21), are,

$$0 = -\frac{\rho}{r} \frac{\partial (r \langle u'v' \rangle)}{\partial r} - \frac{\partial \langle p \rangle}{\partial z} + \frac{\mu}{r} \frac{\partial}{\partial r} \left(r \frac{\partial \langle u \rangle}{\partial r} \right), \quad (\text{F.20})$$

$$0 = -\frac{\rho}{r} \frac{\partial (r \langle v'v' \rangle)}{\partial r} - \frac{\partial \langle p \rangle}{\partial r}. \quad (\text{F.21})$$

In these equations, $\langle v \rangle = 0$ is assumed as a consequence of the streamwise homogeneity of the velocity and the zero divergence condition of the velocity field, Eq. (3.65). Integrating with respect to rdr between $r = r$ and $r = R$, the radius of the pipe, Eq. (F.21) transforms into,

$$-\left(Rp_w - \int_0^R \langle p \rangle dr \right) = 0.$$

The latter equation implies that the bulk pressure is equal to the pressure value at the wall. Such an expression can be derived with respect to z , in order to conclude that the bulk axial pressure gradient is equal to the pressure gradient at the wall of the pipe. Therefore, integrating Eq. (F.20) with respect to rdr leads to,

$$0 = -\frac{\partial p_w}{\partial z} \frac{R^2}{2} - R\tau_w \rightarrow \tau_w = -\frac{R}{2} \frac{\partial p_w}{\partial z},$$

where $\tau_w = -\mu \partial \langle u \rangle / \partial r|_{r=R}$. Note the deliberate use of $\partial p_w / \partial z$ instead of dp_w / dz in the previous expressions, simply as a way to harmonize the notation used so far (see notation clarification in 3.6.2).

With the presence of an internal boundary, i.e., the electrode wire, the corresponding expression relating the streamwise pressure gradient and the wall shear stress is obtained by considering the same magnitude of the wall shear stress at both the external pipe wall and the internal electrode boundary, but with an opposite sign. This results in the substitution of the radius in the above equation by the hydraulic radius,

$$-\frac{\partial p_w}{\partial z} = \frac{2\tau_w}{R_H}, \quad \tau_w = \mu \frac{\partial \langle u \rangle}{\partial r} \Big|_{r=R}. \quad (7.2)$$

Eq. (7.2) is used to obtain the pressure gradient in the incompressible constant property T-ODT simulations. The wall shear stress, represented in the form of the obtained Re_τ in the T-ODT simulations,

is shown in Figure 7.3. Alternatively, Figure 7.4 shows the pressure gradient normalized by the EHD stress. The EHD stress is a normalization quantity derived from the mean radial momentum equation considering the presence of the EHD body force, i.e.,

$$0 = -\frac{\rho}{r} \frac{\partial (r \langle v'v' \rangle)}{\partial r} - \frac{\partial \langle p \rangle}{\partial r} + \frac{j_z}{\beta}. \quad (\text{F.21})$$

Integrating the latter equation with respect to rdr , considering that the pressure at both the external pipe wall and the internal electrode boundary is the same, results in,

$$\int_{r=R_{elec}}^{r=R} \langle p \rangle dr - R_H p_w + \tau_{EHD} R_H = 0, \quad \tau_{EHD} = \frac{I}{2\pi B\beta}.$$

τ_{EHD} is referenced in the literature as the pressure differential maintaining the electric wind in a cylindrical ESP [13].

The results obtained show that the measurements done with the larger electrode diameter, $D_{elec} = 1.5\text{mm}$, concur with the T-ODT simulation results. Curiously, results obtained with the smaller electrode diameter, $D_{elec} = 1\text{mm}$, show larger deviation of the T-ODT results with increasing values of the electrohydrodynamic number, i.e., at larger voltage (or current) values. These results are analyzed on the context of the increased drag introduced by the larger electrode diameter. The favorable conditions for enhancement of turbulence in the configuration with the larger electrode diameter should allow a reduction in the hydrodynamic entry length, such that, effectively, the flow in the configuration with $D_{elec} = 1.5\text{mm}$, is a fully developed flow which agrees with the T-ODT hypothesis. Nonetheless, this may not be the case in the configuration with $D_{elec} = 1\text{mm}$. This analysis also neglects any other possible factor, such as the influence of the mesh used in the experimental device in order to force a turbulent flow at the entrance of the test section for the measure of the pressure drop, the assembly itself of the experimental device, and many other factors which could play a role in the inability of the flow to achieve a fully developed condition within the experimental test section. The transition to a fully developed turbulent flow is an aspect which can not be evaluated with ODT, given that the model is only capable of evaluating one dimensional asymptotic turbulence states, as discussed in chapter 3. However, it is possible to verify whether the flow is in transition without a collapse into a fully developed state, as in the case of a boundary layer, if an S-ODT formulation is used. This was precisely the case of the thermally developing pipe flow analyzed in chapter 5 of this thesis. This analysis is carried out in the next section.

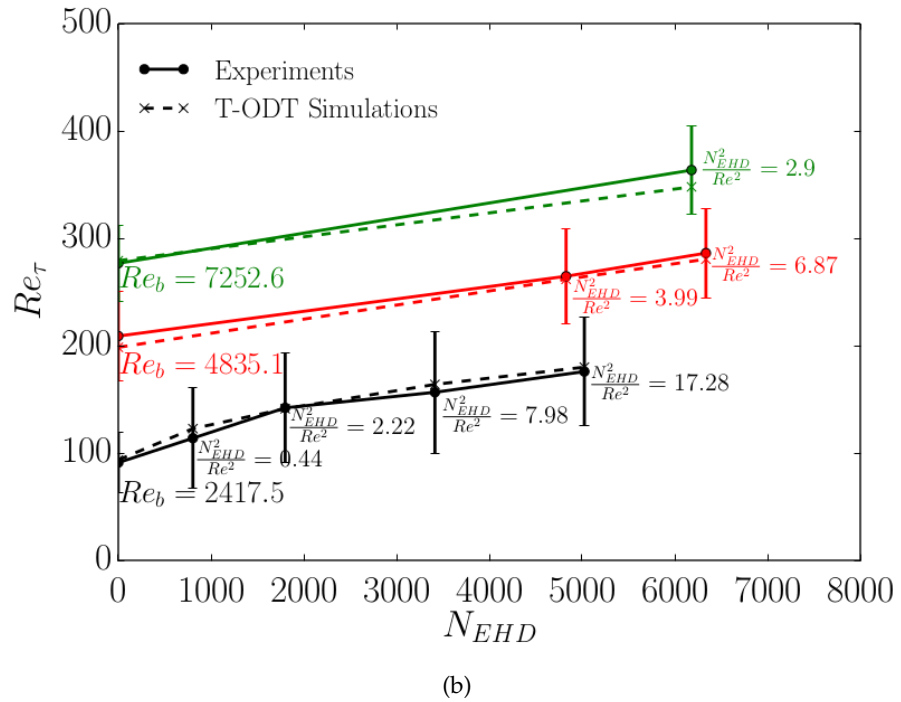
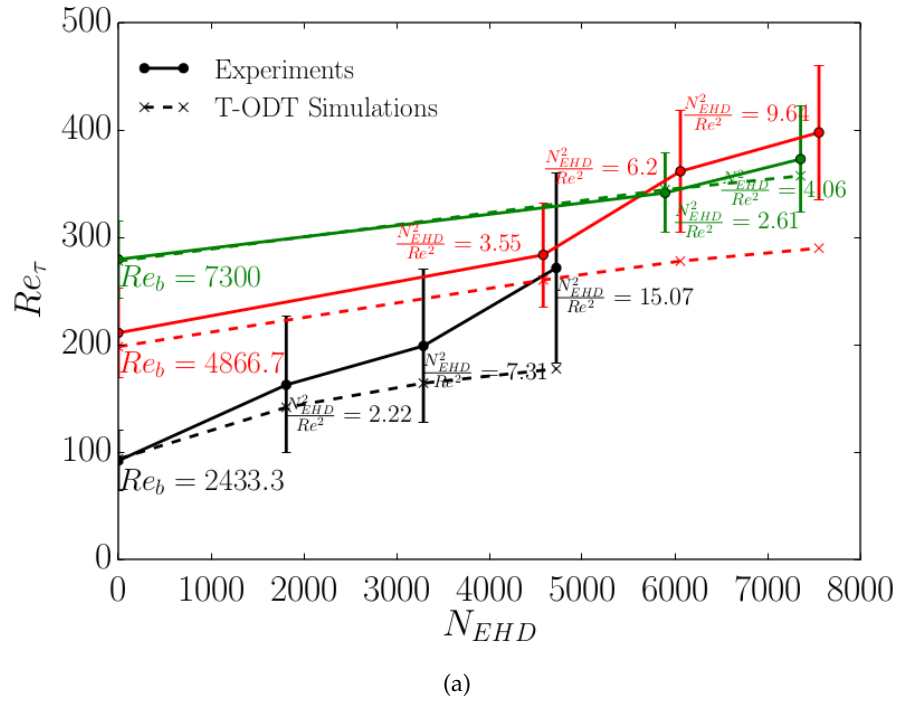
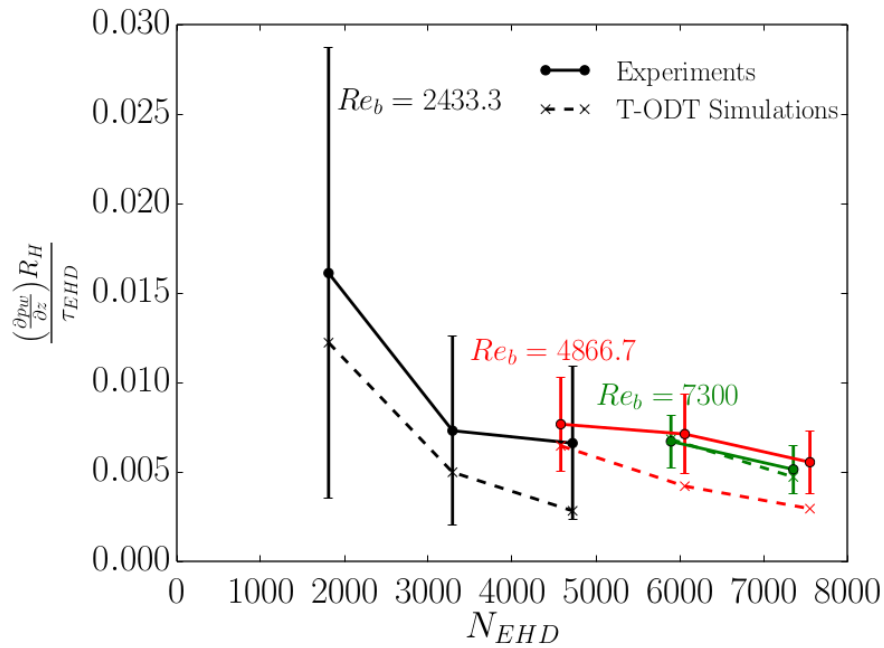
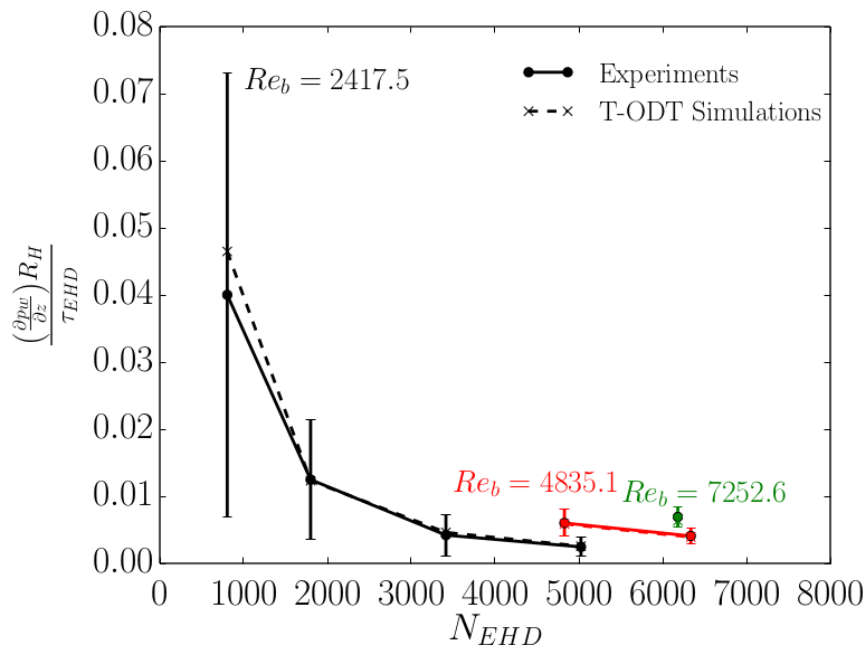


Figure 7.3: Friction Reynolds number Re_τ obtained in experiments and T-ODT simulations as a function of the electrohydrodynamic number N_{EHD} (defined based on the hydraulic radius of the pipe). The ratio N_{EHD}^2/Re^2 is shown along the results (with both numbers defined based on the radius of the pipe). a) Electrode diameter $D_{elec} = 1\text{mm}$. b) Electrode diameter $D_{elec} = 1.5\text{mm}$.



(a)



(b)

Figure 7.4: Normalized streamwise pressure gradient obtained in experiments and T-ODT simulations as a function of the electrohydrodynamic number N_{EHD} (defined based on R_H). a) Electrode diameter $D_{elec} = 1\text{mm}$. b) Electrode diameter $D_{elec} = 1.5\text{mm}$.

7.2 QUASI-INCOMPRESSIBLE AND TRANSITIONAL FLOW IN THE CYLINDRICAL ESP

In this section, the hypothesis of transitional flow for the cylindrical ESP configuration of the previous section with $D_{elec} = 1\text{mm}$ is evaluated with an S-ODT formulation. There are sufficiently good reasons to believe that the flow regimes evaluated in the previous section could be in a transition regime. These reasons are based on the analysis of Eq. (3.66) as follows. In chapter 5, the analysis of the flow regime in the context of turbulent forced convection, turbulent natural convection, or turbulent mixed convection, was presented in terms of different regime boundaries. One of these boundaries was the buoyancy criteria, $Gr/Re_b^2 = 1$, which is the nondimensional coefficient accompanying the buoyancy term in the nondimensional momentum equation [111]. The relevant nondimensional momentum equation for the types of flows evaluated in this thesis is Eq. (3.66), which has a nondimensional coefficient N_{EHD}^2/Re^2 accompanying the EHD body force term¹. It is possible, thus, to think of an electroquasistatic dominated regime criteria based on the ratio $N_{EHD}^2/Re^2 = 1$. As seen in Figure 7.3, most of the measurements or experimental data points fall within the criteria $N_{EHD}^2/Re^2 > 1$. This would be the equivalent of the buoyancy case with $Gr/Re_b^2 > 1$ (natural convection dominated regime). In the EHD case, $N_{EHD}^2/Re^2 > 1$ should also suggest that the radial motion is non-negligible in comparison to the streamwise motion, which would be the case in a fully forced convective flow. That is, $N_{EHD}^2/Re^2 > 1$ should indicate the presence of strong electric winds, capable of inducing a mixed and transitional regime, away from the fully developed turbulent flow case.

There is also another possible controversial issue regarding the T-ODT incompressible constant property simulations carried out in the previous section. That is, due to the Joule heating effect in Eq. (3.67), there may be non-negligible temperature and density gradients in the flow, which could alter the incompressible behavior. The direction of the flow in a vertical pipe may also introduce a gravity term and a buoyancy component into the pressure gradient, which could have uncertain effects. In order to clarify this issue, as well as the discussion regarding how the transitional character of the flow may affect the pressure gradient determined in the previous section, S-ODT simulations are performed for the flow conditions with characteristic number pairs $[N_{EHD}, Re_{b,0}] = [4722.56, 2433.33]$ and $[N_{EHD}, Re_{b,0}] = [4581.55, 4866.67]$ ², of the cylindrical ESP configuration with an electrode diameter of $D_{elec} = 1\text{mm}$. These two conditions

¹ Both N_{EHD} and Re defined based on the radius of the pipe, as declared in the nomenclature section of this thesis.

² Throughout this chapter, and as specified in the nomenclature, N_{EHD} and Re are always defined based on the pipe radius, while Re_b is defined based on the pipe diameter.

are very close to each other in Figures 7.3 and 7.4, in regards to the obtained (or measured) streamwise pressure gradient and the input magnitude of the EHD body force. However, they are very different in terms of the input bulk Reynolds number, and as such, have a very different ratio N_{EHD}^2/Re_0^2 .

7.2.1 Setup of the numerical simulations

The S-ODT simulations were run based on initial conditions of the fully developed cylindrical ESP flow at zero voltage (no EBF). In order to generate the initial conditions, the S-ODT simulations were run at zero voltage ($N_{EHD} = 0$) and without heat transfer until a statistically stationary velocity profile was obtained. The physical and mesh adaption parameters used in the simulations were exactly the same as those used in the incompressible constant property T-ODT simulations, see Table 7.1. The constant mass flow rate forcing a constant bulk velocity was also enforced. The initial uniform temperature and (thermodynamic) pressure of the flow, which remain constant in order to produce the initial conditions, were the temperature and pressure producing the fluid properties from Table 7.1, i.e., $T_0 = 298.15\text{K}$ and $P = 100000\text{Pa}$. The S-ODT simulations were repeated in order to calibrate the ODT model parameters, such that the same measured experimental pressure drop at zero voltage conditions is obtained. The latter coincides with the pressure drop obtained in the T-ODT simulations at zero voltage conditions. The calibrated ODT model parameters for the S-ODT simulations are shown in Table 7.4. Coincidentally, the C parameter values of the S-ODT simulations were exactly the same as those obtained in the T-ODT simulations, however, the Z parameter is slightly different and coincides with the value of Z used in the S-ODT simulations of chapter 5.

Table 7.4: S-ODT model parameters used in the cylindrical ESP simulations for the determination of the streamwise pressure gradient ($D_{elec} = 1\text{mm}$).

ODT Model Parameter	Initial conditions (incompressible constant property pipe flow)	Nonzero EHD body force
C	2.0	11.0
Z	100.0	100.0
α	$2/3 \approx 0.6667$	$2/3 \approx 0.6667$

Once the initial conditions of the fully developed, incompressible, and zero voltage cylindrical ESP flow are obtained, the S-ODT simulations are run in such a way that the Joule heating term of the temperature equation, Eq. (3.67) is now considered. The gravity term in the streamwise momentum equation is also considered. The gravity is considered to have the same sign as the pressure gradient for downward flows, and the opposite sign for upward flows. For the horizontal flow simulations, the gravity term is simply zero. The BCs for the temperature consider an imposed zero temperature gradient at the wall, i.e., normally associated to an adiabatic wall condition or an imposed value of $q_w = 0$ ³. This is an indication of the two different mechanisms for heat transfer in the EHD case: one is the traditional heat conduction mechanism by thermal diffusion, or collision between gas molecules according to their thermal velocity, the other one is the Joule heating effect, produced by the collision of the charge carriers according to their drift velocity within the electric field.

It is noted that the S-ODT simulations run in this chapter differ from the S-ODT simulations in chapter 5, in the sense that the flow being evaluated, as discussed before, is under a heavy influence of elliptical features. That is, the transitional character which could be induced according to the criteria $N_{EHD}^2 / Re^2 > 1$ is responsible for very strong elliptical features, which led to the regular violation of the parabolic assumption required by S-ODT flows. This was operationally resolved by distinguishing the streamwise velocity components u and u_D , as in [72], without ever performing the harmonization of the components during any deterministic step. That is, u and u_D evolved completely independent from each other, unlike in [72] or in chapter 5 of this thesis. This operational workaround has a physical interpretation. In the S-ODT simulations carried out in this section, the flow evolves according to the initial conditions in a thermally and hydrodynamically developing fashion. The coupling between the thermal and hydrodynamic boundary layers is, unlike in [72], only in a one-way fashion, where the thermal boundary layer evolves exclusively according to the initial conditions, but the hydrodynamic boundary layer evolves depending on the initial conditions and on the thermal boundary layer. Due to the harmonization of u and u_D in [72], S-ODT simulations in [72] and in the chapter 5 of this thesis, involve a two-way coupling of the thermal and hydrodynamic boundary layers, which allows the recovery of partial elliptical features of the flow.

Given that the scope of the results in this section of the thesis is limited to integral bulk quantities, the number of ensemble members used to generate the average results was limited to $N_{ens} = 40$ in each of the S-ODT simulated cases.

³ The zero radial temperature gradient is imposed, in the FV context, directly on the thermal diffusion term of the temperature equation.

7.2.2 Bulk flow results

As in chapter 5, it is possible to obtain an analytical expression for the streamwise rate of change of the bulk temperature and the bulk velocity. For that, consider the governing equation for the enthalpy, Eq. (2.58), considering only the terms retained after the asymptotic Mach and mobility ratio analysis performed in chapter 3, i.e., the Joule heating term and the molecular heat transport by conduction as in Eq. (3.67),

$$\frac{\partial(\rho h)}{\partial t} + \nabla \cdot (\rho h \underline{V}) = \nabla \cdot (\sigma_T \nabla T) - \underline{J} \cdot \nabla \phi. \quad (7.3)$$

The integration in circumferential and streamwise direction, considering homogeneous tangential properties over a sweep angle π , results in,

$$\begin{aligned} \frac{1}{2} \int_{z'=z_0}^{z'=z} \frac{\partial}{\partial z} \int_{r=0}^{r=R} \rho h u r^2 dz' &= \int_{z'=z_0}^{z'=z} \int_{r=0}^{r=R} \frac{1}{r} \frac{\partial}{\partial r} \left(r \sigma_T \frac{\partial T}{\partial r} \right) r dr dz' \\ &\quad - \int_{z'=z_0}^{z'=z} \int_{r=0}^{r=R} j_2 \frac{\partial \phi}{\partial r} r dr dz' \\ &= \int_{z'=z_0}^{z'=z} \left| \frac{I \phi_{elec}}{2\pi B} \right| dz' \end{aligned}$$

Note that the integration in radial direction is performed from 0 to R , as in chapter 5. Note also that the integration of the energy generation density term by heat conduction cancels out due to the imposed zero wall heat flux in the pipe or precipitator and the symmetric heat flux condition at both sides of the electrode, analogous to the achievement of a local maximum at $r = 0$. As discussed previously, the treatment of the temperature, or enthalpy, is indistinguishable from that of a heated pipe flow. Substituting the LHS of the previous expression by the corresponding bulk quantities, the linear change of the enthalpy in streamwise direction is given by,

$$\begin{aligned} \frac{\rho_0 U_{b,0} R^2}{2} \int_{z'=z_0}^{z'=z} \frac{\partial h_b}{\partial z} dz' &= \frac{I \phi_{elec}}{2\pi B} (z - z_0) \\ h_b &= h_0 + \frac{I \phi_{elec}}{\pi B \rho_0 U_{b,0} R^2} (z - z_0). \end{aligned} \quad (7.4)$$

As in chapter 5, the latter enthalpy equation allows the determination of the linear temperature behavior by assuming a constant, streamwise-independent value of the bulk specific heat capacity at constant pressure $c_{p,b}$. Since the mass flow rate $\rho_0 U_{b,0}$ is held constant, then U_b has, thus, a linear behavior in z as well.

The results for the normalized streamwise bulk temperature and velocity are presented next in Figure 7.5. The initial nonlinear behavior of U_b at the early stages of the simulation is attributed to the non-conservative nature of the formulation and the initial heavy changes

of the velocity profiles due to the modified ODT C parameter in the nonzero N_{EHD} condition, as well as the added effect of the injection of the electroquasistatic potential energy and the gravity, in comparison to the initial incompressible constant property conditions.

In order to derive the correct streamwise pressure gradient, the streamwise mean S-ODT mean momentum equation is analyzed, Eq. (F.62). In comparison to the T-ODT mean momentum equation, there is an added streamwise Reynolds stress term $\overline{u''u''}$ in the S-ODT formulation which can affect the calculation of the streamwise pressure gradient by adding an additional turbulent flow contribution. However, it has been acknowledged throughout this thesis, that the ODT representation of the RMS velocity profiles is underestimated, and as such, this may result in a wrong calculation of the resulting streamwise pressure gradient. Due to this reason, a bulk-filtered kinetic energy equation is used instead. That is, consider the Eulerian kinetic energy equation, Eq. (2.53),

$$\frac{\partial(\rho\tilde{\xi}_{kin})}{\partial t} + \nabla \cdot (\rho\tilde{\xi}_{kin}\underline{V}) = -\underline{V} \cdot \nabla p + \underline{V} \cdot \nabla \cdot \underline{\tau} + \rho\underline{V} \cdot \underline{g} + \frac{J \cdot \underline{V}}{\beta}. \quad (2.53)$$

This equation is integrated in rdr , considering homogeneous properties in the tangential direction and neglecting shear stress gradients in streamwise direction. By doing this, all quantities of interest are replaced by their bulk-filtered counterparts,

$$\frac{\partial(\rho_b\tilde{\xi}_{kin,b})}{\partial t} + \frac{\partial(\rho_b U_b \tilde{\xi}_{kin,b})}{\partial z} = -U_b \frac{\partial p_w}{\partial z} - 2 \frac{U_b \tau_w}{R_H} \pm \rho_b U_b g.$$

Note that the radial pressure gradient and the EHD body force term are neglected in this equation based on the assumption that the bulk radial velocity is simply zero. The type of flows that are being evaluated now are transitional flows, or at least that is the hypothesis that was stated in this section. Due to this reason, the time derivative term can not be simply neglected. Instead, consider now performing a Favre decomposition of U_b , such that $U_b = \widetilde{U}_b + U_b''$, noting that \widetilde{U}_b is a constant, and therefore, $U_b'' = 0$. Therefore,

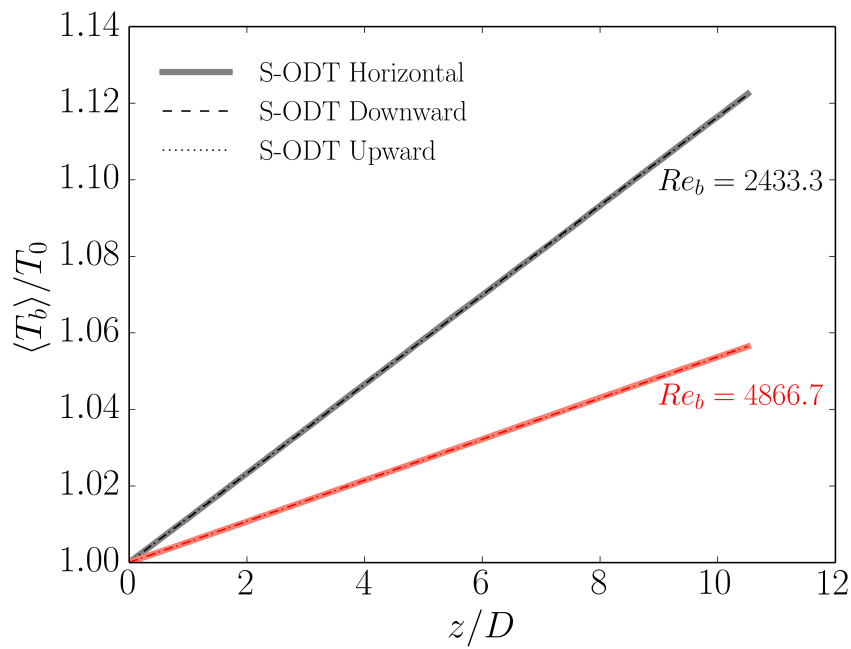
$$\frac{\partial(\rho_b\tilde{\xi}_{kin,b})}{\partial t} + \widetilde{U}_b \frac{\partial(\rho_b\tilde{\xi}_{kin,b})}{\partial z} = -\widetilde{U}_b \frac{\partial p_w}{\partial z} - 2 \frac{\widetilde{U}_b \tau_w}{R_H} \pm \rho_b \widetilde{U}_b g.$$

In order to remove the time derivative from the equation, a Reynolds average is performed and a statistical stationarity hypothesis is assumed. This results in the following expression for the average wall pressure gradient,

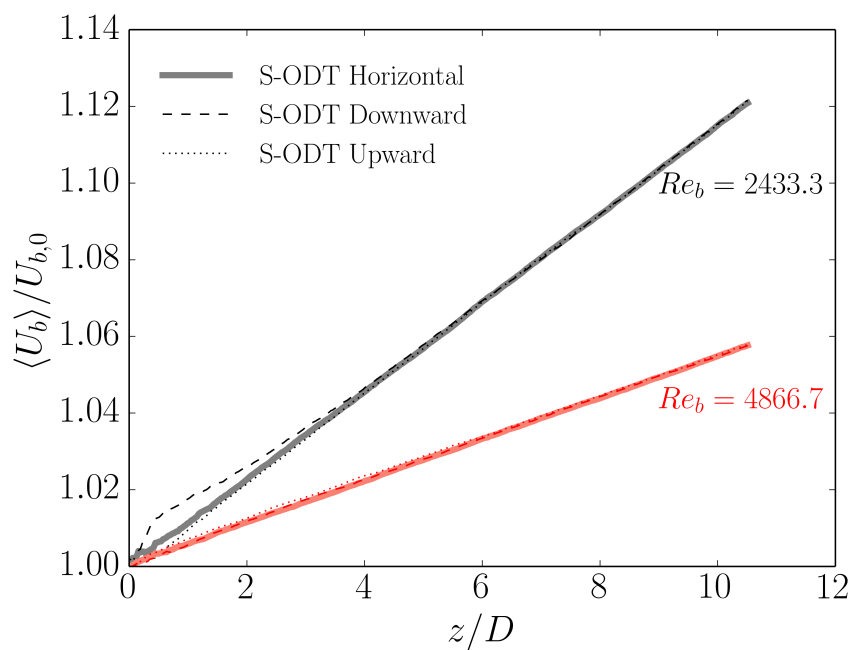
$$-\frac{\partial p_w}{\partial z} = \frac{\partial \langle \rho_b \tilde{\xi}_{kin,b} \rangle}{\partial z} + 2 \frac{\tau_w}{R_H} \pm \langle \rho \rangle g. \quad (7.5)$$

It is noted that the average bulk kinetic energy can be decomposed as the average kinetic energy of the bulk flow plus the bulk turbulent kinetic energy, i.e.,

$$\langle \rho_b \tilde{\xi}_{kin,b} \rangle = \langle \rho_b \rangle \widetilde{U}_b^2 + \langle \rho_b \rangle k_b. \quad (7.6)$$



(a)



(b)

Figure 7.5: a) Streamwise profile of normalized bulk temperature. b) Streamwise profile of normalized bulk velocity. The figures show the results of downward, horizontal, and upward S-ODT simulations. The black and red colors are indicative of different bulk Reynolds numbers.

Eq. (7.5) shows that there are four contributions into the pressure gradient. One is due to the streamwise change of the average kinetic energy of the bulk flow. This contribution can only take place in variable density flow, given that a density change is the only one responsible for a change in the bulk flow velocity due to the enforcement of a constant mass flow rate. The second contribution is due to the TKE. Since the EHD body force does not make any direct contribution into the mean flow, it is expected that the additional energy due to the EHD term is represented in a modification of the TKE magnitude, or in the streamwise transport of the TKE, given that the EHD body force also does not have any direct contribution into the TKE as per Eq. (F.43). The third contribution is the traditional wall shear stress part of the pressure gradient, which is the only contribution in an incompressible, fully developed (and statistically stationary) flow. The last contribution is an acceleration due to gravity.

In the experimental measurements, the pressure gradient value reported already involves a subtraction of the gravitational potential energy, or, in other words, of the contribution of the acceleration due to gravity. This contribution to the pressure gradient has exactly the same magnitude regardless of the downward or upward direction of the flow, but of course, has a different sign. This is because the change in density (if there is a change in density to be considered due to heating of the flow), is the same regardless of the direction of the flow, i.e., the change in temperature by Eq. (7.4) does not depend on the direction of the flow. It is important to remember that the gravitational contribution should not be confused with the bulk flow acceleration, or change in the bulk flow average kinetic energy.

Figures 7.6 and 7.7 show the S-ODT results of the pressure gradient in the two selected cases. Although the T-ODT results already fall into the standard deviation of the experimental expected value (abbreviated as SD in the figures), the S-ODT results are certainly closer to the mean reported value in both cases. Certainly, the added contribution to the pressure gradient by the streamwise developing TKE is a factor which could explain the deviation of some of the T-ODT results in the previous section. Furthermore, Figures 7.6 and 7.7 show that the bulk flow acceleration contribution due to the heating of the flow is almost negligible, indicating that the incompressible constant property assumption of the T-ODT simulations is perfectly justified. The decisive factor affecting the deviation between the T-ODT simulations and some of the experimental results in the previous section is, therefore, definitely, the transition (not fully developed) character of some of the reported flows.

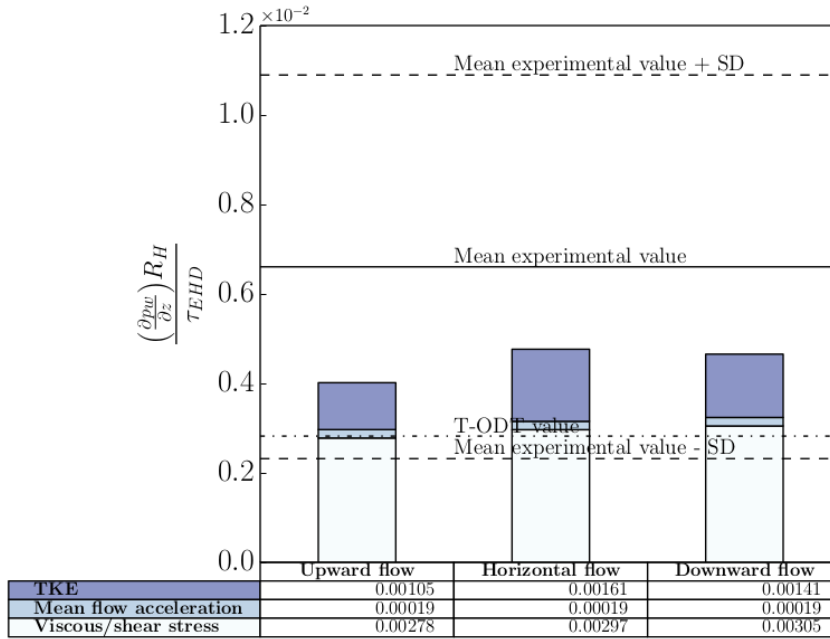


Figure 7.6: Normalized contributions to the pressure gradient in the downward, horizontal and vertical S-ODT simulations. The reported case is that at $N_{EHD} = 4722.56$ and $Re_{b,0} = 2433.33$. The horizontal solid lines indicate the reported mean experimental values, while the dashed lines indicate the mean plus or minus the standard deviation (SD) of the experimental values [116] (see the citation comment at the beginning of section 7.1). The horizontal dot-dashed line indicates the reported incompressible constant property T-ODT simulation value.

7.3 VARIABLE DENSITY FLOW IN A CYLINDRICAL ESP

In the previous section, the results for the pressure drop in the cylindrical ESP were analyzed in the context of temperature variations with an almost negligible influence. It is now of interest to evaluate the phenomenology of the flow in the context of larger temperature and density gradients, in order to evaluate the corresponding heat transfer enhancement or decrease in the presence of EHD body forces. S-ODT simulations are performed next with this objective in mind. The S-ODT simulations aim to replicate the experimental results published by Nelson et al [50].

7.3.1 Setup of the numerical simulations

The heat transfer enhancement or decrease is evaluated in this section by the ratio of the Nusselt numbers in the presence and absence of EHD body forces. In this case, the S-ODT simulations consider all of the variables sketched in Figure 7.1, excluding the action of the

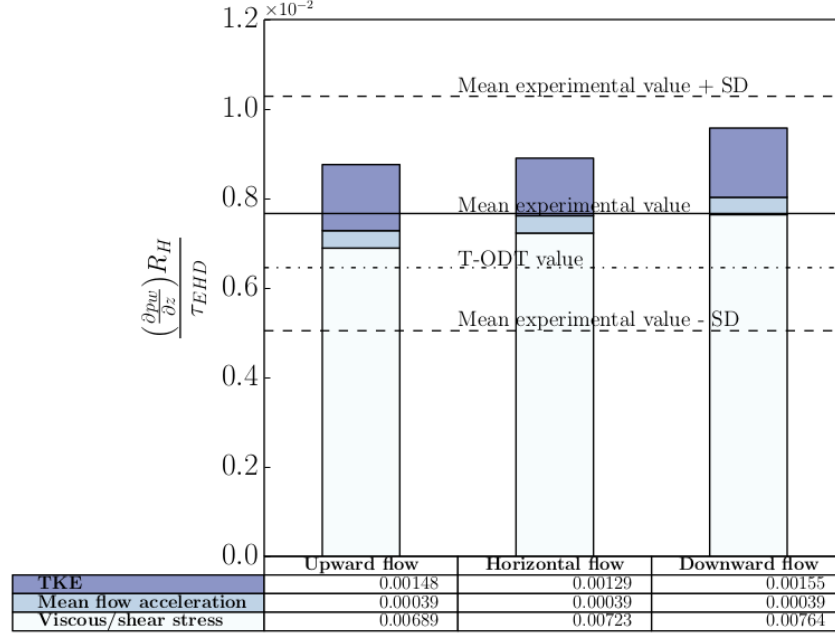


Figure 7.7: Normalized contributions to the pressure gradient in the downward, horizontal and vertical S-ODT simulations. The reported case is that at $N_{EHD} = 4581.55$ and $Re_{b,0} = 4866.67$. The horizontal solid lines indicate the reported mean experimental values, while the dashed lines indicate the mean plus or minus the standard deviation (SD) of the experimental values [116] (see the citation comment at the beginning of section 7.1). The horizontal dot-dashed line indicates the reported incompressible constant property T-ODT simulation value.

gravity, i.e., an horizontal flow is considered. This coincides with the orientation of the experimental device used by [50]. It is noted, that the experimental results reported here regarding the Nusselt number enhancement or decrease from [50] in the single wire electrode configuration are exactly the same as those reported in [49]. In fact, the work in [50] is considered an extension of the work undertaken in [49] by the same authors.

As in chapter 5, the Nusselt number is defined based on the ratio of convective heat transfer and conductive heat transfer,

$$Nu_b = \frac{2\mathcal{H}_{cf,b}R}{\sigma_{T,w}} \rightarrow \langle Nu_b \rangle = \frac{2\langle \mathcal{H}_{cf,b} \rangle R}{\langle \sigma_{T,w} \rangle}. \quad (5.10)$$

Note that, as discussed before, the description of the enthalpy (or temperature) PDE in ODT is indistinguishable from the heated pipe case outlined in Chapter 5. Therefore, the radius of the pipe is used here instead of the hydraulic radius. The bulk convective heat transfer coefficient is, as in Eq. (5.12), defined by the surface integrated heat flux,

$$\mathcal{H}_{cf,b}(T_w - T_b) \oint dS = \oint \underline{q}_{tot} \cdot d\underline{S}. \quad (5.12)$$

Note that the subscript *tot* was assigned to the heat flux vector \underline{q} . This is because, in this case, there is a contribution to the heat flux due to the EHD induced Joule heating effect. The corresponding flux contribution of the EHD energy source term can be found by the use of the divergence theorem. That is, consider the dimensional version of Eq. (3.67), this time in terms of the enthalpy,

$$\rho \frac{Dh}{Dt} = \nabla \cdot \underline{q} - \underline{J} \cdot \nabla \phi.$$

The LHS is the volume specific heat. If a volume integral is applied both on the LHS and RHS of the equation, the total heat is obtained. In order to transform the Joule heating source term into a heat flux term, it must be expressed in a divergence form. This is not a problem, given that the zero divergence condition imposed on the electric current density vector by Eq. (3.64) allows a straightforward and convenient rewriting. Doing this, the net heat flux which should be used in Eq. (5.12) is obtained,

$$\mathcal{H}_{cf,b}(T_w - T_b) \oint dS = \oint (\underline{q} - \phi \underline{J}) \cdot d\underline{S}. \quad (7.7)$$

Using the definition of the Nusselt number, Eq. (5.10), this results in,

$$\langle Nu_b \rangle = \frac{2R \langle \sigma_{T,w} \rangle \frac{\partial \langle T \rangle}{\partial r} \Big|_w + \frac{\phi_{elec} I}{\pi B}}{\langle \sigma_{T,w} \rangle (\langle T_w \rangle - \langle T_b \rangle)}. \quad (7.8)$$

The discussion is now shifted to the magnitude of the EHD body force applied in the S-ODT simulations. As before, the electroquasistatic fields are calculated according to the procedure described in appendix H. It is stressed that only three magnitudes of N_{EHD} are evaluated at each of the different simulated bulk Reynolds numbers. One is the threshold voltage, or the onset voltage of the corona discharge. The second one is an intermediate voltage condition. The third one is the spark-over voltage, prior to the electrical breakdown [49]. The voltage-current data is taken from [50]. The current values obtained from the reported dimensionless electric number in [50] are current measurements in the experimental heat transfer section. However, the current is generated by a discharge voltage in the electrode, which has a longer length than that of the heat transfer section. In order to account for this length difference, the current values for the heat transfer section are modified according to the following simple scaling law,

$$I = \frac{I_{elec} l_{elec}}{B}. \quad (7.9)$$

Here, I is the desired current value used for the calculation of the electroquasistatic fields, I_{elec} is the experimental reported current value based on the dimensionless electric number, l_{elec} is the reported electrode length and B is the test section length, all values reported in

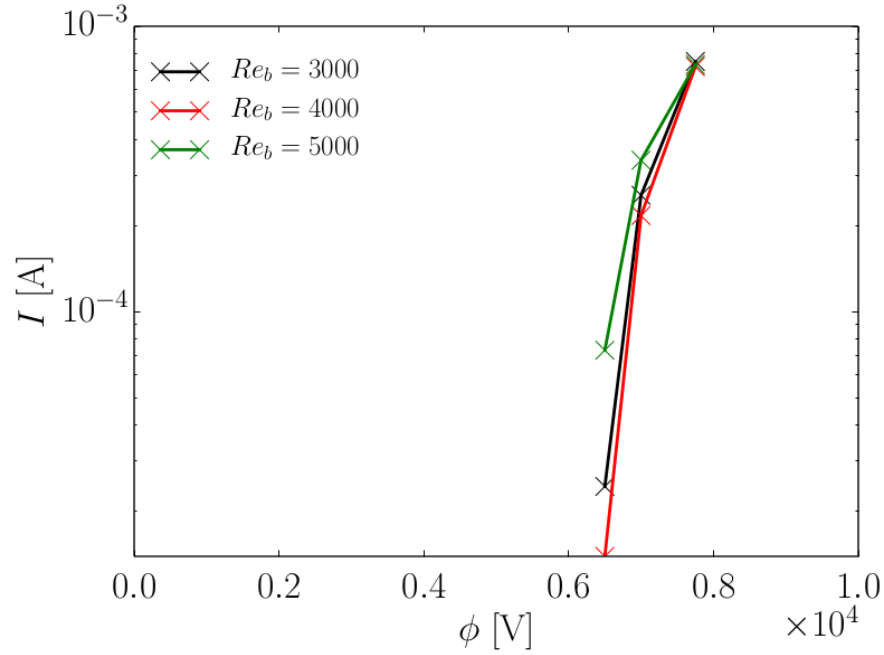


Figure 7.8: Experimental voltage-current curves used for the different variable density cylindrical ESP S-ODT simulations according to the reported experimental values in [50] and [49].

[50]. The corresponding voltage-current values used for the S-ODT simulations are then shown in Figure 7.8. As before, the characteristic curves are almost independent of the bulk Reynolds number of the flow.

Regarding the physical and mesh adaption parameters of the S-ODT simulations, Tables 7.5 and 7.6 show a summary of the required simulation inputs. The initial conditions for the S-ODT simulations are generated in the same way as in the previous quasi-incompressible S-ODT simulations, i.e., forcing a fully developed flow with a constant U_b at a zero voltage condition and without any type of heat transfer effects. It is noted that additional to the heat produced by the Joule heating effect, an additional wall heat flux produced by a resistive element in the experiment is also considered. This wall heat flux is estimated based on the initial fluid conditions summarized in Table 7.5, and the experimental constraint reported in [50], which indicates that a temperature difference of $\Delta T_{w,b} = 20\text{K}$ between the wall and the bulk flow is maintained at all times. That is, the wall heat flux due to the resistive element at the pipe wall is estimated as,

$$q_w = \frac{\rho_0 U_{b,0} c_{p,0} \Delta T_{w,b} (\pi R^2)}{2\pi BR} = \frac{\rho_0 U_{b,0} c_{p,0} \Delta T_{w,b} R}{2B}. \quad (7.10)$$

Table 7.5: Flow configuration parameters used for variable density cylindrical ESP simulations (S-ODT).

Physical settings / Case	$Re_{b,0} = 3000$	$Re_{b,0} = 4000$	$Re_{b,0} = 5000$
Domain size $L_{ODT} = D = 2R$ [m]	0.032	0.032	0.032
Electrode diameter D_{elec} [m]	0.25×10^{-3}	0.25×10^{-3}	0.25×10^{-3}
Test section length B [m]	0.76	0.76	0.76
Initial uniform temperature T_0 [K]	298.15	298.15	298.15
Initial Pressure P_0 [Pa]	100000	100000	100000
Initial bulk velocity $U_{b,0}$ [m/s]	1.494	1.992	2.490
Wall heat flux q_w [W/m ²]	369.659	492.879	616.099
Constant ionic mobility β [m ² /(V · s)]	1.4×10^{-4}	1.4×10^{-4}	1.4×10^{-4}

Table 7.6: Adaptive mesh settings and ensemble settings used for variable density cylindrical ESP simulations (S-ODT).

Adaptive mesh settings	Re_{b,0} = 3000	Re_{b,0} = 4000	Re_{b,0} = 5000
$\Delta r_{min} = \eta_0/6$ (m)	2.436×10^{-5}	1.888×10^{-5}	1.56×10^{-5}
Δr_{max} (m)	9.6×10^{-4}	9.6×10^{-4}	9.6×10^{-4}
Δr_C (m)	0.25×10^{-3}	0.25×10^{-3}	0.25×10^{-3}
ξ^{Dens}	80.0	80.0	80.0
$A^{TimeFac}$	1.0	1.0	1.0
Eddy-size PDF l_{max}/L_{ODT}	1/2 = 0.5	1/2 = 0.5	1/2 = 0.5
Ensemble settings			
Number of ensemble members N_{ens}	240	240	240

Once the initial conditions are generated, the S-ODT simulations at different electrohydrodynamic numbers are carried out only after a process of calibration of the ODT model parameters in the reference zero voltage condition ($\phi_{elec} = 0V$). The zero voltage condition is, thus, the reference case, which, despite not involving any type of EHD effects, still considers variable density flow simulations due to the wall heat flux due to the resistive element. This procedure is the same experimental procedure followed by Ohadi et al. [49] and Nelson et al. [50], who only report the final results as a ratio of the Nusselt number enhancement with respect to the zero voltage condition. The calibration of the ODT model parameters at the zero voltage condition is done in order to achieve the corresponding Nusselt number given by Abraham et al. [118] for a straight round pipe with an air flow of $Pr = 0.7$,

$$Nu_b = \frac{\frac{f_D}{8} (Re_b - 1000) Pr}{1 + 12.7 \sqrt{\frac{f_D}{8}} (Pr^{\frac{2}{3}} - 1)}. \quad (7.11)$$

The latter equation is a modification of the empirical relation postulated by Gnielinski for turbulent pipe flow [37]. It is valid for transitional and turbulent pipe flows ($Re_b > 2300$). This calibration procedure was the same used to calibrate the Nusselt number of the reference case in the experimental work of [49] and [50]. In Eq. (7.11), f_D is the friction factor estimated according to [118],

$$f_D = 3.03 \times 10^{-12} Re_b^3 - 3.67 \times 10^{-8} Re_b^2 + 1.46 \times 10^{-4} Re_b - 0.151. \quad (7.12)$$

This equation is valid for transitional Reynolds numbers in pipe flows, $2300 < Re_b < 4500$. For larger pipe flow bulk Reynolds numbers ($Re_b \geq 4500$), the friction factor is estimated by the the Colebrook law, as given by [119],

$$\frac{1}{\sqrt{f_D}} = -2 \log \left(\frac{K_\epsilon}{3.71 D_H} + \frac{2.51}{Re_b \sqrt{f_D}} \right), \quad (7.13)$$

where K_ϵ is the product of the relative roughness and the hydraulic diameter as in [119]. $K_\epsilon = 0$ for smooth pipes, such as those simulated here.

The Nusselt number obtained by Eq. (7.11) is assigned to the exit of the numerical pipe. That is, the calibration process was performed in order to achieve the desired Nu_b by Eq. (7.11) at the exit of the numerical pipe, which is the coordinate position $z = B$, since B is the length of the test section in the experiments. Due to the characteristically low and transitional bulk Reynolds numbers of the evaluated flows in [50], the achievement of the intended bulk Nusselt numbers as per Eq. (7.11) in the zero voltage reference case resulted in a dependency

of the C ODT model parameter with Re_b . Thus, different values of C were found for each one of the three evaluated Reynolds numbers. The calibrated ODT model parameters are shown next in Table 7.7.

Table 7.7: S-ODT model parameters used for the variable density cylindrical ESP simulations. Parameters calibrated to obtain values of Nu_b given by Eq. (7.11).

ODT Parameter	$Re_{b,0} = 3000$	$Re_{b,0} = 4000$	$Re_{b,0} = 5000$
C	1.7	4	6
Z	350.0	350.0	350.0
α	$2/3 \approx 0.6667$	$2/3 \approx 0.6667$	$2/3 \approx 0.6667$

7.3.2 Bulk flow results

Figure 7.9 shows the Nusselt number enhancement in the variable density cylindrical ESP obtained with S-ODT simulations in comparison to the reported experimental results in [49] and [50]. It is noted that the enhancement ratio is defined as the ratio between the average Nusselt number found at the exit of the numerical pipe in the nonzero EHD case and the Nusselt number found at the exit of the numerical pipe in the reference zero voltage case. The exit of the numerical pipe is the coordinate position $z = B$, given that B is the length of the test section. It is stressed here again, that the gravity term effects are neglected in these S-ODT simulations, i.e., g was taken as zero. The results show that the simulations are able to correctly predict the experimental results at the larger bulk Reynolds number case ($Re_{b,0} = 5000$). For smaller Reynolds numbers, which are normally categorized as transitional flows in engineering applications, at least according to the Colebrook law [119], i.e., $2300 \leq Re_b \leq 4000$, the S-ODT results underestimate the Nusselt number enhancement. The deviations between simulations and experimental results increase with smaller Reynolds numbers, and with larger nondimensional EHD body force coefficients N_{EHD}^2 / Re^2 .

These results are analyzed again in the context of the transition effects discussed in the previous section. It is hypothesized that the transition effects are not caused in this case due to the large values of N_{EHD}^2 / Re^2 , but rather, due to the small bulk Reynolds number values themselves, plus the very small pipe geometry used in the experiments. One of the difficulties at the time of evaluating Nusselt numbers resides precisely on the definition and the nature of the Nusselt number reported. In many cases, the experimental devices

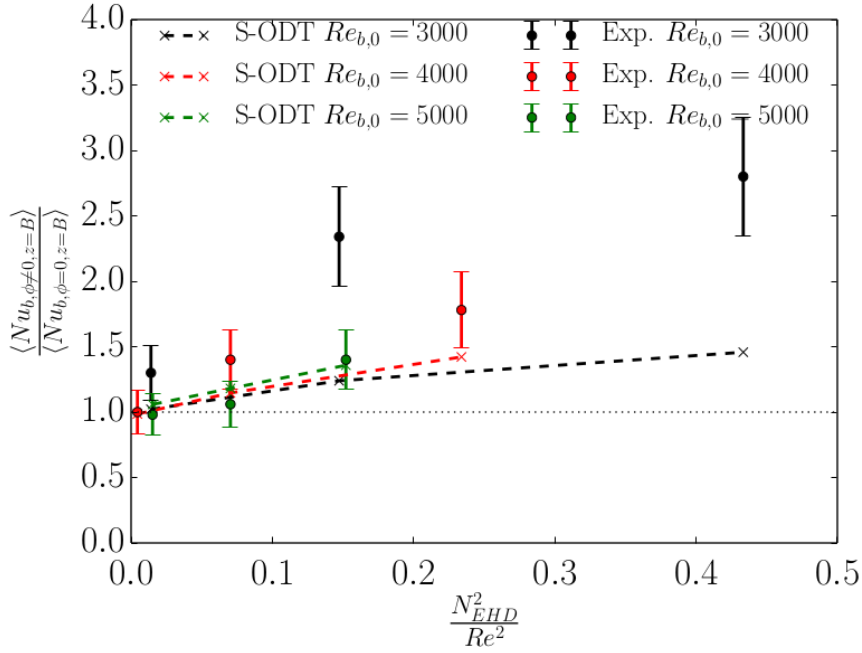


Figure 7.9: S-ODT simulation results for Nusselt number enhancement in the variable density cylindrical ESP. The experimental results obtained by [50] and [49] are reported for comparison.

are not able to report the so-called fully developed and stationary Nusselt number, given that the length of the experimental device is simply shorter than the hydrodynamic and the thermal entry length. In the case of the reported experimental results, the length of the entry section (prior to the test section) is sufficient to ensure a fully developed hydrodynamic flow. However, it is not clear whether the length of the test section itself is sufficient in order to exclude thermal entry effects. Abraham et al. [120] reports an approximation of the length of the thermal entry section (as a function of the Nusselt number behavior). According to [120], for $Re_b < 5000$, the length of the thermal entry region is larger than 75 pipe diameters, thus, larger than the length of both the entrance and test sections in the experimental devices of [50] and [49]. The length of 75D (experimental entrance and test section length in [50] and [49]) lies right at the end of the Nusselt transition region for $Re_b \sim 4000$, according to the data presented in [120]. For $Re_b \sim 3000$, the length of 75D lies right after the breakup of the laminar regime.

It is then hypothesized that, due to the calibration process performed in both the simulations and experiments, the S-ODT simulations should be able to achieve, in the integral quantity sense, the same steady and stationary nondimensional universal heat flux achieved by the experimental device. This nondimensional universal heat flux, or universal Nusselt number can be thought as the ratio between the

Nusselt number measured at the exit, $z = B$ and the Nusselt number at the fully developed condition (FDC),

$$Nu_{b,univ} = \frac{Nu_{b,z=B}}{Nu_{b,z=z_{FDC}}}. \quad (7.14)$$

In the absence of EHD body forces, the calibration process imposes $Nu_{b,univ} = 1$ both in the experiments and in the ODT simulations, given that the reported Nusselt number at the reference zero voltage case is forced to coincide with the value obtained by Eq. (7.11), which is the value for a fully developed condition.

Consider the case in which the flow at the exit of the test section in the experimental device coincides with the fully developed regime, i.e., $z = B = z_{FDC}$. In such a case, $Nu_{b,univ} = 1$, the calibration process is valid, and thus, ODT should be able to show the proper enhancement corresponding to the fully developed condition⁴. Conversely, if, by chance, the flow at the exit of the experimental device does not correspond to a fully developed condition, but rather, to a transitional condition, ODT should still be able to match the proper enhancement if the transitional characteristics of the flow are accounted for. In other words, the ODT results for Nusselt number enhancement should match the experimental results as long as $Nu_{b,univ} = 1$, which implies modifying the value of $Nu_{b,z=z_{FDC}}$ in Eq. (7.14) by the actual Nusselt number obtained with ODT at a fully developed condition. In the simulated flows with $Re_b \geq 5000$, this is precisely the case, at least according to the results obtained and the data provided by [120]. For $Re_b \geq 5000$, $z = B$ is a position larger than the hydrodynamic and thermal entry length. Thus, the reported S-ODT results match the experimental results.

For flows in which $z = B$ does not correspond to a position where the hydrodynamic and thermal entry length has been achieved, the correct ratio for Nusselt number enhancement needs to observe the actual fully developed condition in ODT, such that $Nu_{b,univ} = 1$ still holds. This can be interpreted by understanding that the transition dynamics in ODT need not be the same as in the real experiment⁵. Therefore, the ODT results can be corrected in such situations in order to properly reproduce the correct Nusselt number enhancement ratio Enh_{Nu} as,

$$Enh_{Nu} = \frac{\langle Nu_{b,\phi \neq 0,z=B} \rangle}{\langle Nu_{b,\phi=0,z >> B} \rangle} = \left(\frac{\langle Nu_{b,\phi \neq 0,z=B} \rangle}{\langle Nu_{b,\phi=0,z=B} \rangle} \right) \left(\frac{\langle Nu_{b,\phi=0,z=B} \rangle}{\langle Nu_{b,\phi=0,z >> B} \rangle} \right). \quad (7.15)$$

⁴ This is only valid in an integral quantity sense, given that the reduced dimensionality of the model does not allow any other conclusion in a non-parabolic flow

⁵ For sure, the transitional dynamics can not be the same, as it is the case that, generally, the transition dynamics of ODT and DNS can not be the same due to the restrictive parabolic character of the flows evaluated with ODT. A transitional flow exhibits, indeed, very strong elliptic features such as recirculation events.

In order to obtain the values for $\langle Nu_{b,\phi=0,z \gg B} \rangle$, new S-ODT simulations were performed at the zero voltage condition running for a much longer streamwise length $z \gg B$. The simulations ran until the behavior of $\langle Nu_b(z) \rangle$ was practically asymptotic.

The correction of the enhancement ratio by Eq. (7.15) was applied to all the S-ODT results which did not match the experimental results. That is, all of the results which are believed to have some kind of transitional effects. The corrected results are shown in Figure 7.10. For all data points at $Re_b = 4000$ and the data point at $Re_b = 3000$ and the lowest ratio N_{EHD}^2/Re^2 , the S-ODT simulations show now very good agreement with the reported experimental values.

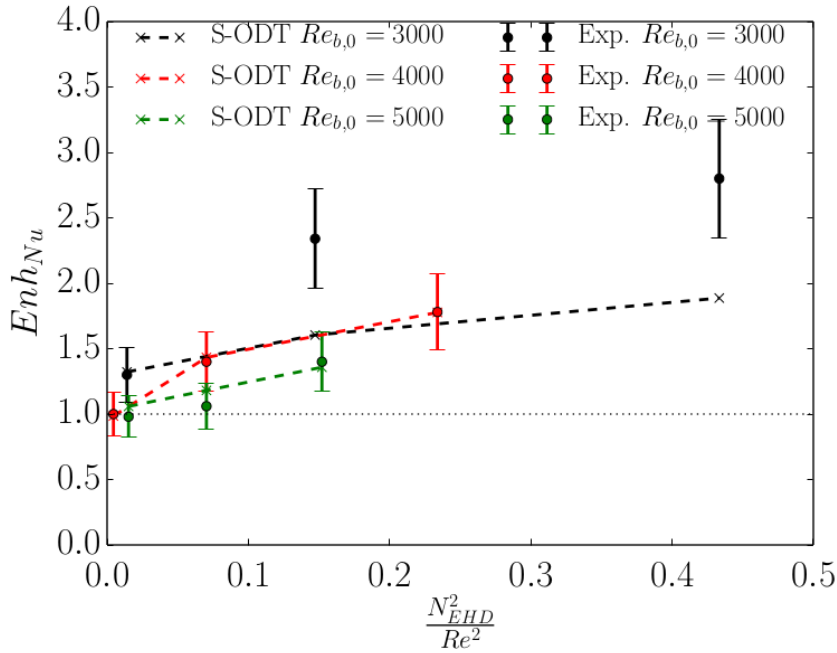


Figure 7.10: S-ODT simulation results for Nusselt number enhancement in the variable density cylindrical ESP after the correction for transition effects by Eq. (7.15). The experimental results obtained by [50] and [49] are reported for comparison.

For the data points at $Re_b = 3000$ and large ratios N_{EHD}^2/Re^2 in Figure 7.10, the transitional hypothesis can be extended. Consider now the case in which hypothetically, as in the regime diagram shown in chapter 5, Fig. 5.11, there is some relaminarization regime due to the EHD body force. **Would it then be possible that the actual corresponding fully developed condition in such a case is, not a turbulent flow, but rather, a laminar flow?** The Nusselt number for a laminar flow has a defined and constant solution, depending on the boundary conditions of the temperature. For the wall heat flux condition of the S-ODT simulations, this solution would be $Nu_{lam} = 4.36$ [111]. If the fully

developed condition is laminar, then $Nu_{b,z=z_{FDC}} = Nu_{b,lam,z_{FDC}} = 4.36$. This implies a correction of the form,

$$Enh_{Nu} = \frac{\langle Nu_{b,\phi \neq 0,z=B} \rangle}{Nu_{b,lam,z >> B}} = \left(\frac{\langle Nu_{b,\phi \neq 0,z=B} \rangle}{\langle Nu_{b,\phi=0,z=B} \rangle} \right) \left(\frac{\langle Nu_{b,\phi=0,z=B} \rangle}{Nu_{b,lam,z >> B}} \right). \quad (7.16)$$

Applying this correction to the data points deviating from the experimental results in Figure 7.10 results in the data shown in Figure 7.11. Although this last hypothesis is entirely speculative, what can actually be assured, with large confidence, is that there are transitional effects in the experimental flows reported by [50] and [49] in the low Reynolds number conditions with large ratios N_{EHD}^2/Re^2 .

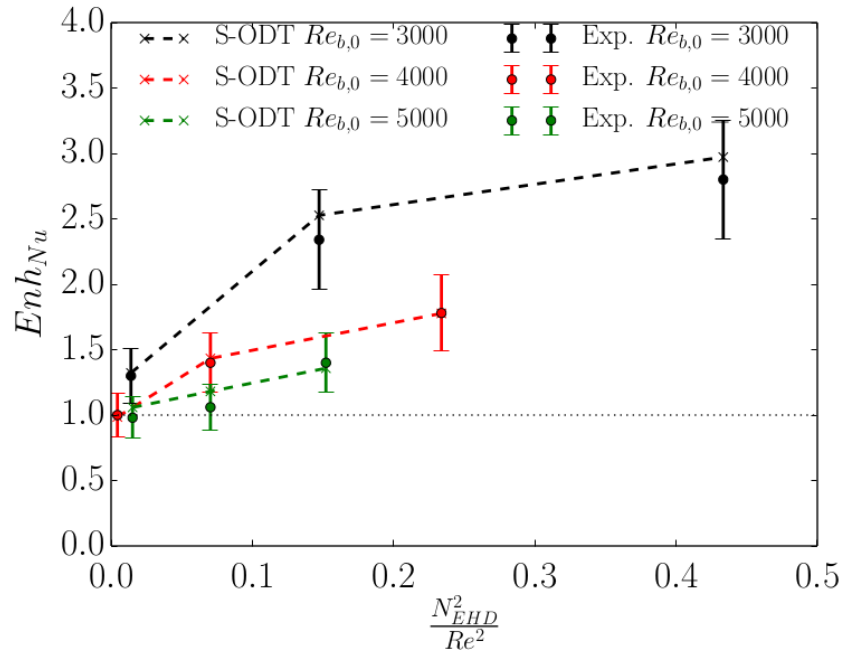


Figure 7.11: S-ODT simulation results for Nusselt number enhancement in the variable density cylindrical ESP after the correction for transition effects by Eqs. (7.15) and (7.16). The experimental results obtained by [50] and [49] are reported for comparison.

CLOSING COMMENTS

8.1 CONCLUSIONS

8.1.1 *Review and conclusions*

This chapter provides a review of selected issues of internally forced convective flows which was proposed at the beginning of the thesis.

In the first part of the thesis, a review of the current issues on wall-bounded flows was given. The current status of the research on EHD-enhanced channel and pipe flows was stressed, and the reasons why these types of flows could be of strategic importance in engineering applications was explained. With that in mind, the ODT model was presented in chapter 3. The presentation of the model was done with a sufficient degree of generality. As such, it allowed covering the study of incompressible constant property, variable density, and EHD-enhanced channel and pipe flows. In chapter 1, the problem of the confusing terminology, and, more importantly, the lack of a systemic framework to evaluate EHD-enhanced flows, was stressed. Using a reduced order model such as ODT, motivated, already in chapter 3 and due to the one-dimensionality of the model, a 1-D characteristic scaling of the Navier-Stokes equations with the presence of the EHD body force. This analysis brought some clarity in the nature of certain EHD flow regimes, and allowed the establishment of an initial pool of nondimensional numbers which could be used to describe these types of flows. These nondimensional numbers are by no means outsiders in the field of fluid dynamics, nor were they formulated in this thesis for the first time. In fact, they are even part of an international standard [54]. However, to the best knowledge of the author, a formalism such as the analysis carried out in chapter 3 regarding the derivation of the asymptotic one-way coupling regime of the electroquasistatic fields, i.e., where flow dynamics do not influence electroquasistatic fields of charge and electric fields, has not been carried out or published up to this date. This alone could be considered an advantage of doing turbulence modeling with ODT, in the sense that, if done in a systematic and correct way, the analysis required for the proper modeling of flows in ODT, can already deliver some interesting insights into the dynamics of turbulence.

In the second part of the thesis, channel and pipe flows were evaluated as single systems on their own, i.e., without the presence of external forces other than the gravitational force. An interesting analysis regarding the relaminarization phenomena which may occur in

streamwise developing pipe flows with a sufficiently large characteristic Grashof number was performed at the end of chapter 5. However, the main purpose of both chapters 4 and 5, was no other than to validate the use of the ODT model as a reliable turbulence model for the study of internally forced convective flows. Having compared in detail ODT results with DNSs in the aforementioned chapters, it is clear that, despite being a reduced order model, ODT is a reliable tool. This statement is valid at least when the discussion and analysis focuses on global quantities, as well as first and second order statistics of flow profiles, as it was the case of the results presented in chapters 4 and 5.

If the computational efficiency of the ODT model is compared to that of DNSs, it is noted that, for the incompressible constant property results obtained in chapter 4, all ODT simulations were computed using one core of an Intel i7-2600 CPU with 3.4 GHz and 8GByte memory [91]. In the largest friction Reynolds number case evaluated in this work ($Re_\tau = 2003$), an average of 2000 grid points were required during the simulation¹. As a reference, the nek5000 pipe flow code used by Khoury et al. [94], one of the DNSs used for comparison in chapter 4, required 2.1842×10^9 grid points, and employed an available infrastructure of 65536 cores for the calculation of simulations at $Re_\tau = 1000$. The channel flow $Re_\tau = 2003$ ODT simulations required 160 CPU-h (T-ODT). As a comparison, the DNS of Hoyas and Jiménez [30] required a computational time of 6×10^6 CPU-h. Indeed, the reduced dimensionality of the model obviously makes it significantly more computationally efficient in comparison to DNSs.

Regarding the distinct formulations of the model, the T-ODT and the S-ODT formulations, it was seen that the S-ODT formulation is, in general, more accurate when analyzing streamwise developing (stationary) flows than its T-ODT counterpart. E.g., the S-ODT formulation was able to capture the streamwise profiles of the wall temperature more accurately than in T-ODT for the heated pipe case of chapter 5. Furthermore, it is not necessary to use an ad-hoc time-to-space transformation in order to generate streamwise results in the S-ODT formulation. The streamwise representation is already built into the formulation of the model. The best possible results which can be obtained with the S-ODT formulation are those in which flows do not exhibit strong elliptic features, and a certain coupling between the hydrodynamic and thermal boundary layers can be achieved by solving a quadratic PDE for the streamwise velocity, as described in appendix D. In such cases, as in chapter 5 and [72], the solution of the quadratic PDE involves, indeed a larger computational cost in comparison to the cost of the corresponding T-ODT simulations. As

¹ This quantity varied during the simulation due to the adaptive nature of the ODT model previously discussed in this work.

an example, on average, the T-ODT simulations performed in chapter 5 and [72] ran for approximately 2400 CPU-h. Conversely, the S-ODT simulations required around 14400 CPU-h, i.e., approximately a factor 7 more demanding than their T-ODT counterpart.

In the third part of the thesis, the ODT model was formally applied to the EHD-enhanced channel and pipe flows. Specifically in chapter 6, an inherent 2-D planar elliptic flow was evaluated with the S-ODT formulation. Just by adding the EHD body force, this case is already significantly more complex than the simple incompressible constant property channel flow case. The fact that the electroquasistatic fields are inherently 2-D, despite being unaffected by the flow, confers a very strong elliptic character to the flow. Once again, motivated by the necessary dimensional reduction, or in this case, the parabolic constraint in ODT, an interesting analysis of the effects of the EHD body force due to its rotational component was achieved. This analysis agreed with previous considerations done by [76]. The results from chapter 6 confirmed that the effects of the EHD body force on turbulence are not direct. From an integral energy analysis, it is clear that adding some extra energy (in the form of electrostatic potential energy in this case) into the flow, necessarily leads to a larger turbulent dissipation. However, according to the mean equations shown in appendix F, this energy injection does not take place at the small scales, and it may also not necessarily take place at the large scales. Despite the sophisticated treatment used in order to couple the 2-D electroquasistatic fields with the S-ODT simulations in chapter 6, the qualitative results signaling drag reduction and localized increase of the Reynolds shear stress with the presence of the EHD body force were confirmed with ODT. At least for the integral quantities, as well as the first order statistical moments of the flow variables in the wall-normal profiles, the ODT results could also reasonably reproduce the DNS data.

As a contrast to the electric current density vector in chapter 6, which had both an irrotational and a solenoidal contribution, the wire-tube cylindrical ESP configuration from chapter 7 allows a purely irrotational electric current density vector. For ODT, this was an advantage, since the treatment could be heavily simplified in comparison to the planar 2-D treatment from chapter 6. Despite the simpler cylindrical treatment in ODT, there are no DNSs, to the best of the author knowledge, of such an EHD-enhanced pipe flow. As such, the ODT results in chapter 7 were only compared to experimental results. This of course also limited the analysis to integral quantities. Nonetheless, given the previous results obtained in chapters 4 and 6, it is expected that, at least for first order statistical moments, the radial flow profiles can be reproduced with a high degree of accuracy. Granted, such an achievement could also be done by a much simpler and more flexible RANS solver. Yet again, some modeling of the Reynolds stress would be required in RANS, which, as it was shown in chapter 6, would

require some knowledge of how to model this term as a function of the EHD body force. Of course, such knowledge is currently not available. Just from that point of view, the use of ODT is highly appealing. The ODT results of global integral quantities such as the pressure drop and the bulk Nusselt number in chapter 7 were, after a detailed analysis, surprisingly accurate. Again, this is a major milestone, given that no modeling of the Reynolds stress, or of a subgrid stress was required in ODT. The fact that, even when ODT is constrained to simulate parabolic flows, can still correctly account for some transition effects in internal flows, after a careful analysis is performed as shown in chapter 7, is truly promising. It is also clarifying, to say the least, the role that the ratio N_{EHD}^2/Re^2 may have on EHD-enhanced channel and pipe flows. Not only that, but, as shown at the end of chapter 7, even though the findings can not be confirmed, and it was a merely speculative hypothesis, the existence of a relaminarization regime in the EHD-enhanced internal flows, just as it is the case in plain variable density (or buoyant) flows, is certainly debatable. This could be the door towards unknown physical regimes. Overall, chapter 7 shows the superiority of the ODT model, in the sense that it is able to simulate flows with a surprising degree of precision², which, as of today, can not be simulated with DNSs.

8.1.2 *Closing comments regarding the fundamental question of this thesis*

As in any scientific work, this thesis was formulated based on a working hypothesis. Although the fundamental question postulated in chapter 1 could be considered by some research methodology colleagues as a rather informal, or, for the most formal colleagues, even a fully inappropriate research question, it is the purpose of this section to finally address, at least partially, such question, or at the very least, dedicate some comments.

Certainly, the numerical study of EHD-enhanced internal flows has shed some light into many aspects of wall-bounded turbulence. As an example, the following is a list of issues, which were discussed within this thesis³: rotational body force contributions to turbulence, injection of energy by body forces and its transfer into TKE, fully developed and transitional turbulence, turbulence modification by body forces or by density variations, and the one-dimensionality or higher-dimensionality of a turbulent flow from the geometric point of view and from the characteristic parameters point of view.

Adding a body force certainly complicates the analysis of the flow dynamics, however, as it was shown, by means of a one-dimensional model, a systematic framework can be developed which can help in

² This is of course in comparison to the available experimental data, and considering the reduced order of the model.

³ This is, by no means, a complete list of all issues addressed.

the task of elucidating several fundamental aspects of wall-bounded flows.

It is indeed possible to simulate more realistic flows, or at least, flows which can not be simulated by means of DNSs, with the ODT model. It is not only possible to achieve parametric spaces where DNSs can not reach, e.g., large Reynolds numbers. It is also possible to simulate flow conditions unfeasible for DNSs, only accessible by experiments, as in chapter 7. In the end, a vast area of new physical phenomena could be investigated, upon which existing applications can be optimized, and new potential applications can be developed.

8.2 RECOMMENDATIONS AND OUTLOOK ON FUTURE WORK

An outlook of ongoing investigations, as well as future new potential research topics is outlined below. As mentioned previously, this thesis may open the door to a vast new field of phenomena, which can not only serve for further validation of the ODT model against DNSs or experiments, but also, for the real use of ODT for the prediction of phenomena in applications, which are so far inaccessible for traditional DNSs. First, however, a list of recommendations for the improvement of the results presented in this work is listed.

8.2.1 Recommendations

8.2.1.1 Suggested improvements for the S-ODT numerical method

As detailed in appendices C and D, the numerical method used during the deterministic advancement in the S-ODT simulations is a nonconservative method. This is, per se, not a huge problem, since the numerical method used for variable density T-ODT simulations is also of a nonconservative nature. However, the aggravating factor in the S-ODT simulations, is the appearance of two distinct streamwise velocity components due to the eddy event implementation process. These distinct velocity components, u_D and u , arise from the mapping of the streamwise mass flux, and the kernel operation on the streamwise momentum flux and the streamwise kinetic energy flux, respectively. For internal flows with relatively weak elliptic features, this is not a problem, as it was the case of the simulated flows in chapter 5 and [72]. In such cases, u_D and u are harmonized during the deterministic advancement step. However, for the flows with the large ratio N_{EHD}^2/Re^2 in chapter 7, this was not possible, which leads to a somehow independent evolution of the thermal boundary layer by u_D , in comparison to the evolution of the hydrodynamic boundary layer by u .

For such reason, a new method for eddy event implementation in S-ODT internal flows is desired. This new method should consider a

conservative formulation. It is also desirable that the method is closer to the T-ODT implementation.

8.2.1.2 *Suggested improvements for the overall presented ODT results*

Except for the T-ODT and S-ODT simulations presented in chapter 4, the calibration process of the ODT model parameters for the rest of the simulations presented in this thesis was, at the very least, performed in a very coarse way. A systematic sensitivity analysis to model parameters was not performed in any of the simulations of chapters 5 or 6. In chapter 7, a coarse calibration based on integral quantities was performed, however, this may not be the optimal combination of parameters which achieve a reasonable reproduction of radial flow profiles. Granted, there is momentarily no information or data available regarding how such flow profiles look like. However, the issue at discussion here is that there is still a large room for improvement of the simulation results presented here.

8.2.2 *Outlook to future work*

Next, a short list of potential issues which can be evaluated in the future is presented. This list should be considered as a draft in progress, since many more potential issues may arise after the presentation of this thesis.

8.2.2.1 *Evaluation of the mass transfer enhancement by EHD effects*

Just as the heat transfer enhancement results outlined in chapter 7, an immediate logical step for the extension of the results presented in this thesis is the evaluation of the effects of the EHD body force on mass transfer. Given that different species have different mass transfer coefficients, the results could be surprising. A direct practical application for such research is the falling film technology which could be used to enhance the operation of ESPs. Absorption of particles by dissolution on the falling film, as well as the cooling function of the film, could be a major operational enhancement factor in ESPs. The most straightforward way to carry out mass transfer simulations with the framework presented in this thesis, is to simply implement mass species as passive scalars in the flow.

8.2.2.2 *Aerosol transport in ESPs*

In a true ESP, the flow is not quite as ideal as the type of flows presented in this thesis. Instead of considering the ions in air as the only charged particles in the flow, real ESPs involve different types of charges and different particle sizes. It could be possible to conceive the flow, or effects of such particles in the flow as continuous phases, and model the precipitation as in the mass transfer simulations suggested

previously. However, the effect of the charged particles still needs to be considered. This was mentioned while introducing the charge continuity equation in chapter 2, Eq. (2.27),

$$\sum_n \left[\frac{\partial \rho_{f,n}}{\partial t} + \nabla \cdot (\rho_{f,n} \underline{V} + \underline{I}_n) \right] = \sum_n \dot{\omega}_{f,n}. \quad (2.27)$$

The consequence of the introduction of several species in the charge continuity equation has an unexpected consequence on its nondimensional version used for the Mach and mobility ratio asymptotic analysis presented in chapter 3. This is because the new characteristic mobility ratio in Eq. (3.52) is some kind of weighted average of all of the species mobilities present in the system. Given that any present species in the flow has, in any case, a size significantly larger than that of an electron, the weighted average mobility is expected to drop significantly. Doing this implies a significant increase in the mobility ratio parameter M_β , which can no longer be assumed to have a value of zero. Hence, the asymptotic regime considering a constant electric current density vector is no longer applicable, and a sudden feedback of the flow on the electroquasistatic fields may occur due to the presence of convective currents in Eq. (3.52). This would lead to a two-way coupling between the electroquasistatic variables and the flow variables.

For such cases, an extension of the methods provided in this thesis is possible. Specifically, the numerical method proposed in appendix H needs to be used in order to calculate the varying electroquasistatic fields. Although the bulk electric current density can still be assumed as constant, if a constraint such as a constant charge streamwise flux is imposed on the ESP is imposed, the BCs for charged species and ions in air may be a bit different in comparison to the BCs used in this thesis. A good first approach would be to consider a zero Dirichlet BC for the charge species at the wire electrode. This assumes that only ions are produced close to the electrode, as it is the general consensus picture of what happens in any corona discharge process. Additionally, a zero Neumann BC could be used at the cylindrical ESP walls. For the ions, a zero Neumann BC could also be used at the precipitator walls, while a Dirichlet BC calculated from the bulk electric current density at the wire electrode could be used. For the calculation of the source term in Eq. (2.27), a quantization of the possible particle sizes and charges is desired. By doing this, methods used for the solution of population balance equations can be used, see e.g. [58].

8.2.2.3 EHD-enhanced mixed convection flows

Increasing the ratio N_{EHD}^2 / Re^2 could be expected to shift the forced convection regimes into natural convection regimes, as it is the case in buoyant flows with increased ratios of Gr / Re_b^2 . The latter is seen in the context of the regime diagram discussion of Figure 5.11 in chapter

5, see also [106]. The dynamics in EHD flows can be different, however, given that the injection of energy, unlike in the buoyant flow case, may not occur at the large scales [52]. Nonetheless, the existence of transition effects in the flow dynamics has been demonstrated in this thesis. Transition flows exhibit very strong elliptic features, such as recirculation, and so do natural convection flows. The existence of such regime shifts should be further investigated. The existence of a relaminarization regime is also debatable and could be investigated in the future. It is noted that Chang and Urashima [121] had already introduced an experimental diagram for different regimes in wire-plate ESPs, The findings in [121] are also a strong supporting argument of the theoretical discussion and simulation results produced in this thesis, and thus, should be investigated further in the future.

From the theory aspect, the existence of a quasi-Boussinesq approximation could also exist in EHD flows. This could and should be derived in the future based on the asymptotic analysis proposed in chapter 3.

Part IV

APPENDIX

NAVIER-STOKES EQUATIONS

In this thesis the term *Navier-Stokes equations* refers to the set of equations for conservation of mass, momentum and energy in the fluid flow. Postulates for mass, momentum and energy conservation were originally stated for point systems in classical mechanics. With the arrival of the concept of fields to physics, the Lagrangian perspective of a point system tracked in space (and time) had an Eulerian counterpart for the change of the field (in time).

A derivation of the Lagrangian Navier-Stokes equations based on the classical mechanics conception is presented in this appendix. Afterwards, the change to the commonly presented Eulerian framework is obtained by the application of the Reynolds Transport Theorem (RTT).

All of the relevant nomenclature in this and subsequent appendices is presented at the first time of introduction of the relevant quantity, index or mathematical operator, in the thesis. This means that there may be quantities, which are not explicitly explained here, but which can be found in the Nomenclature section at the beginning of the thesis.

The RTT is written in its integral form as,

$$\frac{d}{dt} \left(\int_{\mathcal{V}(t)} \rho \psi d\mathcal{V} \right) = \int_{\mathcal{V}(t)} \frac{\partial (\rho \psi)}{\partial t} d\mathcal{V} + \oint_{\mathcal{S}(t)} \rho \psi (\underline{V} \cdot \underline{n}) d\mathcal{S}. \quad (\text{A.1})$$

Here, ρ is the density, \mathcal{V} is the (control) volume, $\underline{S} = \mathcal{S}\underline{n}$ is the (control) surface vector represented by some unit surface vector \underline{n} , ψ is any intensive (mass specific) property corresponding to either mass ($\psi = 1$), momentum ($\psi = \underline{V}$) or total energy ($\psi = \zeta_{tot}$), and \underline{V} is the velocity of the (control) surface.

In a differential form, the surface integral on the RHS of Eq. (A.1) can be replaced by a volume integral of an equivalent divergence operator, as implied by the divergence theorem. If the volume is constant, or fixed, with respect to time, as in any Eulerian reference frame, then, after differentiating with respect to the volume,

$$\frac{d}{dt} \left(\frac{d\Psi}{d\mathcal{V}} \right) = \frac{d(\rho\psi)}{dt} = \frac{\partial (\rho\psi)}{\partial t} + \nabla \cdot (\rho\psi\underline{V}), \quad (\text{A.2})$$

where Ψ is any extensive property corresponding to either mass ($\Psi = m$), momentum ($\Psi = m\underline{V}$) or total energy ($\Psi = m\zeta_{tot}$). Alternatively, for intensive (mass specific) properties, in differential form, the following identity for material properties also holds,

$$\frac{D\psi}{Dt} = \frac{\partial \psi}{\partial t} + (\underline{V} \cdot \nabla) \psi, \quad (\text{A.3})$$

where $D\psi/Dt$ is the material derivative of ψ .

A.1 MASS CONSERVATION

A.1.1 Lagrangian representation

For $\Psi = m$ and the postulate that mass is neither created nor destroyed in our universe, it is possible to write,

$$\frac{dm}{dt} = 0. \quad (\text{A.4})$$

This is the differential Lagrangian statement on mass conservation (point system). For a finite size system, the mass is expressed in terms of the volume of the system, i.e., $m = \int_{\mathcal{V}(t)} \rho d\mathcal{V}$ ($\psi = 1$). Thus,

$$\frac{d}{dt} \int_{\mathcal{V}(t)} \rho d\mathcal{V} = 0. \quad (\text{A.5})$$

A.1.2 Eulerian representation

In order to obtain the differential Eulerian representation of mass conservation, the substitution $m = \rho\mathcal{V}$ is used in Eq. (A.4). As a consequence of the RTT, and as the counterpart of the Lagrangian representation, where mass remains constant in the system, in the Eulerian representation, the volume of the system is always fixed. For the LHS derivative resulting from Eq. (A.4), this implies that it is possible to pull the volume out of the total differential. Using Eq. (A.2) afterwards leads to,

$$\frac{\partial \rho}{\partial t} + \nabla \cdot (\rho \underline{V}) = 0. \quad (\text{A.6})$$

Similarly, for the integral representation of Eulerian mass conservation, substitute Eq. (A.1) into Eq. (A.5) (the divergence theorem may be applied as well),

$$\int_{\mathcal{V}} \left[\frac{\partial \rho}{\partial t} + \nabla \cdot (\rho \underline{V}) \right] d\mathcal{V} = 0. \quad (\text{A.7})$$

A.2 MOMENTUM CONSERVATION

A.2.1 Lagrangian representation

For $\Psi = m\underline{V}$, and due to Newton's second law of classical mechanics,

$$\frac{d(m\underline{V})}{dt} = \sum \underline{F}_{ext}. \quad (\text{A.8})$$

Here, \underline{F}_{ext} is any external force acting on the system. The following forces are considered for this thesis,

- **Body forces:**

- Gravitational force by the gravitational acceleration \underline{g} (in vertical direction), $\underline{F}_g = m\underline{g} \rightarrow dF_g = \rho\underline{g}dV$.
- Electromagnetic force by electric fields (neglecting magnetic fields), $\underline{F}_E = q\underline{E} \rightarrow dF_E = \rho_f\underline{E}dV$, where \underline{E} is the electric field vector, q is a (free) point charge and ρ_f is the free charge density.

- **Surface forces:**

- Hydrostatic pressure force by a pressure p , $\underline{F}_p = -p\underline{I} \cdot \underline{S}$. \underline{I} is the identity matrix. A point system has no effective surface. Therefore, by Newton's third law, this surface force is transformed into the equivalent reaction of the pressure difference force exerted by an external volume of fluid, i.e., $\underline{F}_p = -\nabla \cdot (p\underline{I}) V$. In differential terms, $d\underline{F}_p = -\nabla \cdot (p\underline{I}) dV$.
- Friction (viscous) force by a shear stress tensor $\underline{\tau}$, $\underline{F}_v = \underline{\tau} \cdot \underline{S}$. As before, by Newton's third law, this is equivalent to, $\underline{F}_v = \nabla \cdot \underline{\tau} V \rightarrow d\underline{F}_v = \nabla \cdot \underline{\tau} dV$.

Substituting the force definitions into Eq. (A.8),

$$\frac{d(mV)}{dt} = -\nabla \cdot (p\underline{I}) V + \nabla \cdot \underline{\tau} V + m\underline{g} + q\underline{E}, \quad (\text{A.9})$$

which is the differential Lagrangian statement on momentum conservation (noting that V refers to the external volume of fluid acting on the point system). For a finite size system, this expression is differentiated in terms of fluid parcels with infinitesimal momentum $d(mV)$, mass $dm = \rho dV$ and charge $dq = \rho_f dV$. The subsequent integration in terms of volume, considering the momentum of the finite size system as $mV = \int_{\mathbf{x}(t)} \rho V dV$, leads to the integral Lagrangian representation for momentum conservation,

$$\frac{d}{dt} \int_{\mathbf{x}(t)} \rho V dV = \int_{\mathbf{x}(t)} \left[-\nabla \cdot (p\underline{I}) + \nabla \cdot \underline{\tau} + \rho\underline{g} + \rho_f \underline{E} \right] dV. \quad (\text{A.10})$$

A.2.2 Eulerian representation

Substituting $m = \rho V$ as well as $q = \rho_f V$ in Eq. (A.9) leads to,

$$\frac{d(\rho V V)}{dt} = -\nabla \cdot (p\underline{I}) V + \nabla \cdot \underline{\tau} V + \rho\underline{g} V + \rho_f \underline{E} V.$$

For the constant control volume, this implies, together with the substitution of Eq. (A.2),

$$\frac{\partial(\rho V)}{\partial t} + \nabla \cdot (\rho V \circ \underline{V}) = -\nabla \cdot (p\underline{I}) + \nabla \cdot \underline{\tau} + \rho\underline{g} + \rho_f \underline{E}. \quad (\text{A.11})$$

The integral Eulerian representation is obtained after substituting Eq. (A.1) into Eq. (A.10),

$$\begin{aligned} & \int_{\mathcal{V}} \left[\frac{\partial(\rho \underline{V})}{\partial t} + \nabla \cdot (\rho \underline{V} \circ \underline{V}) \right] d\mathcal{V} \\ &= \int_{\mathcal{V}} \left[-\nabla \cdot (p \underline{I}) + \nabla \cdot \underline{\tau} + \rho \underline{g} + \rho_f \underline{E} \right] d\mathcal{V}. \end{aligned} \quad (\text{A.12})$$

A.3 ENERGY CONSERVATION

A.3.1 Lagrangian representation

For $\Psi = m\zeta_{tot}$, and due to the first law of thermodynamics, the rate of change of the total energy equals the sum of the heat transfer rate and the mechanical power,

$$\frac{d(m\zeta_{tot})}{dt} = \frac{\hat{\delta}Q}{dt} + \frac{\hat{\delta}W}{dt}. \quad (\text{A.13})$$

For mechanical work, all of the external forces in Eq. (A.9) are considered. The pressure force and the viscous force are non-conservative forces, and thus are able to produce mechanical work. The gravitational force and the electric force are conservative forces, since $m\nabla \times \underline{g} = 0$ and $q\nabla \times \underline{E} = 0$ (the latter one as a consequence of neglecting magnetic fields in Faraday's law). These forces do not yield an input or output of mechanical work on the system. Rather, they yield a change either in gravitational or in electrostatic potential energy. Since work can also be related to the change in potential energy, it is then possible to write,

$$\begin{aligned} \frac{\hat{\delta}W}{dt} &= (\underline{F}_p + \underline{F}_v + \underline{F}_g + \underline{F}_E) \cdot \underline{V} \\ &= [-\nabla \cdot (p \underline{I}) \cdot \underline{V} + \nabla \cdot \underline{\tau} \cdot \underline{V}] \mathcal{V} + m \underline{g} \cdot \underline{V} + q \underline{E} \cdot \underline{V} \end{aligned} \quad (\text{A.14})$$

Also, using the second law of thermodynamics in the point mass system, the heat difference δQ can be related to the changes in entropy s at a given temperature T ,

$$\frac{\hat{\delta}Q}{dt} = mT \frac{ds}{dt} \quad (\text{A.15})$$

Although this expression will not be used directly in this thesis, it is written here for the sake of generality. In common practice in this thesis, this heat transfer rate (or heat generation density rate, in terms per unit volume) is given by the molecular heat transport by conduction, Eq. (2.48), and the Joule heating effect, Eq. (2.38). Substituting then Eq. (A.14) and (A.15) into Eq. (A.13) leads to the Lagrangian differential statement of energy conservation (point system),

$$\frac{d(m\tilde{\zeta}_{tot})}{dt} = mT \frac{ds}{dt} + [-\nabla \cdot (p\underline{V}) + \nabla \cdot (\underline{\tau} \cdot \underline{V})] \mathbb{V} + m\underline{g} \cdot \underline{V} + q\underline{E} \cdot \underline{V}. \quad (\text{A.16})$$

Following the same procedure to obtain Eq. (A.10) from Eq. (A.9), it is possible to obtain the integral Lagrangian statement of total energy conservation,

$$\begin{aligned} \frac{d}{dt} \int_{\mathbb{V}(t)} \rho \tilde{\zeta}_{tot} d\mathbb{V} &= \int_{\mathbb{V}(t)} \left[\rho T \frac{ds}{dt} - \nabla \cdot (p\underline{V}) + \nabla \cdot (\underline{\tau} \cdot \underline{V}) \right] d\mathbb{V} \\ &+ \int_{\mathbb{V}(t)} \left(\rho \underline{g} \cdot \underline{V} + \rho_f \underline{E} \cdot \underline{V} \right) d\mathbb{V}. \end{aligned} \quad (\text{A.17})$$

A.3.2 Eulerian representation

In order to find the differential Eulerian representation for conservation of total energy, substitute $m = \rho\mathbb{V}$ in Eq. (A.16) and change the electrostatic potential energy term by the one corresponding to the Eulerian representation, given by Eq. (2.35). Afterwards, considering a constant control volume and applying the RTT, Eq. (A.2), leads to,

$$\begin{aligned} \frac{\partial(\rho\tilde{\zeta}_{tot})}{\partial t} + \nabla \cdot (\rho\tilde{\zeta}_{tot}\underline{V}) &= \rho T \frac{ds}{dt} - \nabla \cdot (p\underline{V}) + \nabla \cdot (\underline{\tau} \cdot \underline{V}) \\ &+ \rho \underline{g} \cdot \underline{V} - \frac{\epsilon_0}{2} \frac{\partial |\underline{E}|^2}{\partial t}. \end{aligned} \quad (\text{A.18})$$

The integral representation is obtained by integrating Eq. (A.18) with respect to the volume,

$$\begin{aligned} &\int_{\mathbb{V}} \left[\frac{\partial(\rho\tilde{\zeta}_{tot})}{\partial t} + \nabla \cdot (\rho\tilde{\zeta}_{tot}\underline{V}) \right] d\mathbb{V} \\ &= \int_{\mathbb{V}} \left[\rho T \frac{ds}{dt} - \nabla \cdot (p\underline{V}) + \nabla \cdot (\underline{\tau} \cdot \underline{V}) \right] d\mathbb{V} \\ &+ \int_{\mathbb{V}} \left(\rho \underline{g} \cdot \underline{V} - \frac{\epsilon_0}{2} \frac{\partial |\underline{E}|^2}{\partial t} \right) d\mathbb{V}. \end{aligned} \quad (\text{A.19})$$

RELEVANT THERMODYNAMIC RELATIONS

In terms of general thermodynamics, the equation of state is defined by a state function and its derivatives. The most relevant types of state functions, due to their relation with measurable thermodynamic parameters¹, are the enthalpy and the internal energy. The thermodynamic definition for the specific internal energy differential is,

$$d\zeta_{int} = -Pd\mathfrak{v} + Tds. \quad (\text{B.1})$$

Here, \mathfrak{v} is the specific volume, $\mathfrak{v} = \rho^{-1}$. Likewise, the thermodynamic definition for the specific enthalpy differential is,

$$dh = \mathfrak{v}dP + Tds. \quad (\text{B.2})$$

Substituting Tds from Eq. (B.1) into Eq. (B.2) leads to,

$$dh = d\zeta_{int} + d(P\mathfrak{v}). \quad (\text{B.3})$$

The specific heats are measurable quantities of interest in the equation of state. For thermodynamic processes at constant volume, due to Eqs. (A.15) and (B.1), the specific internal energy change is related to the change in temperature and the specific heat capacity at constant volume c_v ,

$$d\zeta_{int} = c_v dT. \quad (\text{B.4})$$

Likewise, for thermodynamic processes at constant pressure, due to Eqs. (A.15) and (B.2), the specific enthalpy change is related to the change in temperature and the specific heat capacity at constant pressure c_p ,

$$dh = c_p dT. \quad (\text{B.5})$$

Substituting $d\zeta_{int}$ from Eq. (B.4), dh from Eq. (B.5), and using the ideal gas law Eq. (2.49) in Eq. (B.3), it is possible to obtain a relation between the specific heats and the specific gas constant, i.e.,

$$c_p - c_v = R_{gas}. \quad (\text{B.6})$$

Another common quantity of interest is the heat capacity ratio γ , defined as,

$$\gamma = \frac{c_p}{c_v}. \quad (\text{B.7})$$

¹ Pressure, temperature, etc...

B.1 SOME ADDITIONAL ENERGY DEFINITIONS

Additionally to the specific enthalpy and specific internal energy, the concept of specific total energy is frequently used in this thesis. For the scope of this thesis, the specific total energy is defined as the sum of the specific internal energy and kinetic energy. Using, Eq. (B.3), the specific total energy is defined as,

$$\zeta_{tot} = h - \frac{P}{\rho} + \zeta_{kin}, \quad (\text{B.8})$$

where ζ_{kin} is the specific kinetic energy.

B.1.1 Kinetic energy

The specific kinetic energy is defined as,

$$\zeta_{kin} = \frac{1}{2} |\underline{V}|^2 = \frac{1}{2} (\underline{V} \cdot \underline{V}). \quad (\text{B.9})$$

The kinetic energy density is defined as,

$$\rho \zeta_{kin} = \frac{1}{2} \rho |\underline{V}|^2 = \frac{1}{2} \rho (\underline{V} \cdot \underline{V}). \quad (\text{B.10})$$

The rate of change of the kinetic energy density is obtained in chapter 2.

B.1.2 Gravitational potential energy

The specific gravitational potential energy is defined based on the gravitational force, $\underline{F}_g = m \underline{g}$,

$$\zeta_g = \int_{\Gamma} \underline{g} \cdot \underline{\check{\Gamma}} d\Gamma = \Gamma \underline{g} \cdot \underline{\check{\Gamma}}. \quad (\text{B.11})$$

The gravitational potential energy density is given by,

$$\rho \zeta_g = \rho \Gamma \underline{g} \cdot \underline{\check{\Gamma}}. \quad (\text{B.12})$$

The rate of change of the gravitational potential energy density is,

$$\frac{\partial (\rho \zeta_g)}{\partial t} = \rho \frac{D \zeta_g}{Dt} = \rho \underline{g} \cdot \underline{V}. \quad (\text{B.13})$$

It is possible to prove that for a constant gravitational acceleration, the latter expression is the same both in the Eulerian and Lagrangian frameworks. For the Lagrangian form, the verification is straightforward starting from the gravitational force,

$$\frac{d \Xi_g}{dt} = m \frac{d \zeta_g}{dt} \rightarrow \rho \frac{d \zeta_g}{dt} = \rho \frac{D \zeta_g}{Dt} = \frac{d \underline{F}_g}{dV} \cdot \underline{V} = \rho \underline{g} \cdot \underline{V}. \quad (\text{B.14})$$

For the Eulerian form, start with the definition of the gravitational potential energy,

$$\Xi_g = \int_{\Gamma} \underline{E}_g \cdot \underline{\check{r}} d\Gamma = \int_{\Gamma} \left(\int_{\mathbb{V}} \rho \underline{g} d\mathbb{V} \right) \cdot \underline{\check{r}} d\Gamma.$$

Now take the partial derivative with respect to time in order to find the rate of change of the electrostatic potential energy. Since the gravity is a constant, it can be taken out of all of the integrals,

$$\frac{\partial \Xi_g}{\partial t} = \frac{\partial}{\partial t} \left(\int_{\mathbb{V}} \rho \xi_g d\mathbb{V} \right) = \underline{g} \cdot \int_{\Gamma} \left(\int_{\mathbb{V}} \frac{\partial \rho}{\partial t} d\mathbb{V} \right) \underline{\check{r}} d\Gamma.$$

Substituting $\partial \rho / \partial t$ by means of Eq. (A.6),

$$\frac{\partial}{\partial t} \left(\int_{\mathbb{V}} \rho \xi_g d\mathbb{V} \right) = -\underline{g} \cdot \int_{\Gamma} \left(\int_{\mathbb{V}} \nabla \cdot (\rho \underline{V}) d\mathbb{V} \right) \underline{\check{r}} d\Gamma.$$

Reinserting the gravity into the divergence operator, switching the path and volume integrals, as well as the time and volume integrals, and differentiating with respect to the volume, yields then the desired identity²,

$$\frac{\partial (\rho \xi_g)}{\partial t} = -\rho \underline{g} \cdot \underline{V}. \quad (\text{B.15})$$

B.1.3 Electrostatic potential energy

All of the relevant quantities for the electrostatic potential energy are defined in chapter 2, sections 2.2.2 and 2.3.

² Note that an opposite sign is normally considered if this term is inserted into the energy equation, given that the work is defined as the opposite of the change of potential energy

This appendix is focused on the discussion of the details of implementation of eddy events in the stochastic ODT advancement. Despite being something intuitive, it must be stressed that the cylindrical coordinate system works with exclusively positive values of the radial coordinate. The handling of the cylindrical coordinate system in ODT, however, artificially treats one side of the numerical domain as a negative coordinate and the other side as a positive coordinate. This treatment allows the implementation of eddy events in the ODT line which cross $r = 0$, as it would be expected in any physical flow. For the scope of this thesis, it is stressed that, for the case of cylindrical coordinates, any effective volume integral is always calculated as,

$$\begin{aligned} \int () dV &= \int_a^b () r dr = \int_a^b () \frac{dr^2}{2} \\ &= \int_0^{|b|} () \frac{dr^2}{2} - \text{sgn}(b) \text{sgn}(a) \int_0^{|a|} () \frac{dr^2}{2}. \end{aligned} \quad (\text{C.1})$$

Each one of the corresponding volume integrals can be either positive or negative depending on the sign of the integral limits. $\text{sgn}()$ is the sign operator. For planar coordinates, the simple rule holds,

$$\int () dV = \int_a^b () dy. \quad (\text{C.2})$$

C.1 CYLINDRICAL TRIPLET MAP

The formula for the mapping of profiles in the planar Cartesian coordinate system was detailed in Eq. (3.1). The formula for the mapping of profiles in cylindrical coordinates is derived next.

Different formulations of the cylindrical triplet map are possible in contrast to the unique formulation for planar coordinates [66]. The Triplet Map A formulation (TMA) from [66] is derived in this appendix, since it is the easiest one to understand. In the cylindrical coordinate system, the profile of ψ in the range $[r_0, r_0 + l]$ defining an effective volume V_l ¹ is compressed to one third of its value, such that the gradients of the profile are steepened by a factor of 3,

$$V_{l/3} = \frac{1}{3} \left[\int_0^{|r_0+l|} \frac{dr^2}{2} - \text{sgn}(r_0 + l) \text{sgn}(r_0) \int_0^{|r_0|} \frac{dr^2}{2} \right]. \quad (\text{C.3})$$

¹ In the planar case, the effective volume refers to an effective length integral of grid cells of non-equal lengths but uniform width and height. In the cylindrical case, the effective volume refers to an effective area integral of radial wedge grid cells of non-equal radius but uniform opening angle and height

The resulting volume can be positive or negative depending on the sign of r_0 and $r_0 + l$. If each one of these compressed segments is defined by two internal boundaries $[r_{m-1}, r_m]$, where $m \in \{1, 2, 3\}$, such that $r_0 = r_{m-1}$ for $m = 1$, and $r_3 = r_0 + l$ for $m = 3$, then,

$$\mathbb{V}_{l/3} = \int_0^{|r_m|} \frac{dr^2}{2} - \text{sgn}(r_m) \text{sgn}(r_{m-1}) \int_0^{|r_{m-1}|} \frac{dr^2}{2}. \quad (\text{C.4})$$

Substituting Eq. (C.3) in Eq. (C.4), with $\mathbb{V}_l = 3\mathbb{V}_{l/3}$ from Eq. (C.3), and solving for r_m results in,

$$r_m = \text{sgn}(r_m) \left\{ \frac{1}{3} \mathbb{V}_l + \text{sgn}(r_m) \text{sgn}(r_{m-1}) r_{m-1}^2 \right\}^{\frac{1}{2}}. \quad (\text{C.5})$$

In terms of the algorithm used, the latter equation implies a sequential calculation of the internal boundaries r_m . Although the equation may seem implicit due to the appearance of the operator $\text{sgn}(r_m)$ on the RHS, this is misleading given that choosing the wrong sign of r_m leads to an imaginary solution.

In order to determine the map expression of a position $f(r)$ into a new position r , the procedure is similar to that used to determine the internal boundaries. The effective volume of an eddy segment which extends from r_0 to $f(r)$ is conserved and compressed to 1/3 of its magnitude,

$$\mathbb{V}_{f(r)} = \frac{1}{3} \left[\int_0^{|f(r)|} \frac{dr^2}{2} - \text{sgn}[f(r)] \text{sgn}(r_0) \int_0^{|r_0|} \frac{dr^2}{2} \right]. \quad (\text{C.6})$$

Likewise, for any mapped position r referenced to the boundary r_{m-1} ,

$$\mathbb{V}_r = \int_0^{|r|} \frac{dr'^2}{2} - \text{sgn}(r) \text{sgn}(r_{m-1}) \int_0^{|r_{m-1}|} \frac{dr'^2}{2}. \quad (\text{C.7})$$

Eqs. (C.6) and (C.7) are equal on the basis that $f(r)$ is mapped to r within any interval $[r_{m-1}, r_m]$. With the inversion of the middle segment as in the planar triplet map (change of the sign of the slope), the formula for mapping of the profiles in the cylindrical formulation is obtained,

$$\begin{aligned} & \psi[f(r)] \\ &= \begin{cases} \psi \left\{ \text{sgn}[f(r)] \left\{ \text{sgn}[f(r)] \text{sgn}(r_0) r_0^2 + 3 \left[r^2 - \text{sgn}(r) \text{sgn}(r_0) r_0^2 \right] \right\}^{1/2} \right\}, \\ \psi \left\{ \text{sgn}[f(r)] \left\{ \text{sgn}[f(r)] \text{sgn}(r_3) r_3^2 - 3 \left[r^2 - \text{sgn}(r) \text{sgn}(r_1) r_1^2 \right] \right\}^{1/2} \right\}, \\ \psi \left\{ \text{sgn}[f(r)] \left\{ \text{sgn}[f(r)] \text{sgn}(r_0) r_0^2 + 3 \left[r^2 - \text{sgn}(r) \text{sgn}(r_2) r_2^2 \right] \right\}^{1/2} \right\}, \\ \psi(r). \end{cases} \end{aligned} \quad (\text{C.8})$$

Each one of the four lines of Eq. (C.8) are applied depending on whether $r_0 \leq r \leq r_1$, $r_1 \leq r \leq r_2$, $r_2 \leq r \leq r_0 + l$, or $r \notin [r_0, r_0 + l]$, respectively. Figures C.1a and C.1b show a comparison of triplet maps for initially monotonic density profiles with the same size and left edge in the planar and cylindrical formulations.

C.2 ENERGY TERMS AND KERNEL COEFFICIENTS CALCULATIONS

Tables C.1 and C.2 detail the form of the momentum and kinetic energy balances, as well as available kinetic energy, viscous penalty and potential energy formulas for the T-ODT and S-ODT formulations (the S-ODT boundary layer formulation from [64, 66] is included for reference in Table C.3). The calculation formulas for the kernel coefficients is presented in the tables as well.

For T-ODT, the generalized eddy turnover time formula is given by Eq. (3.37),

$$\frac{1}{2K_0} \left(\frac{1}{\tau_{eddy}} \right)^2 \int_l \hat{\rho} K_{ODT}^2 dV = K_0 \left(\sum_k \Xi''_{kin,eddy,k} \right) - \Xi_{vp,eddy} + K_0 \Xi_{pot,eddy}. \quad (3.37)$$

In the S-ODT formulation, the eddy turnover time becomes a streamwise eddy turnover length scale, $L_{eddy} \neq l$, which is being advected with a streamwise velocity u_{eddy} (in the streamwise direction off the line),

$$\tau_{eddy} \text{ (T-ODT)} \rightarrow \frac{L_{eddy}}{u_{eddy}} \text{ (S-ODT)} \quad (C.9)$$

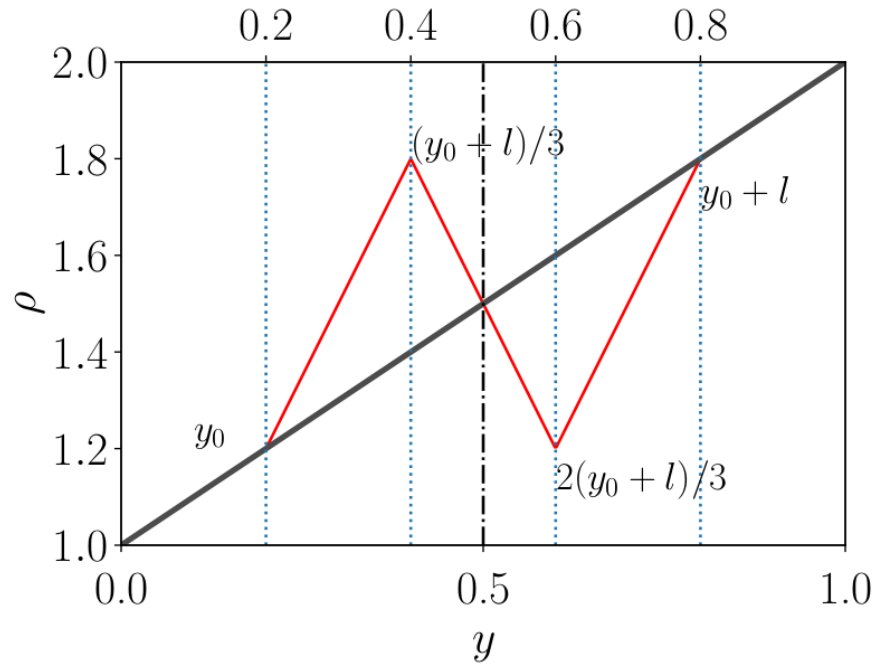
u_{eddy} is calculated as the density averaged streamwise velocity in the eddy range,

$$u_{eddy} = \frac{\int_l \rho u_1 dV}{\int_l \rho dV}. \quad (C.10)$$

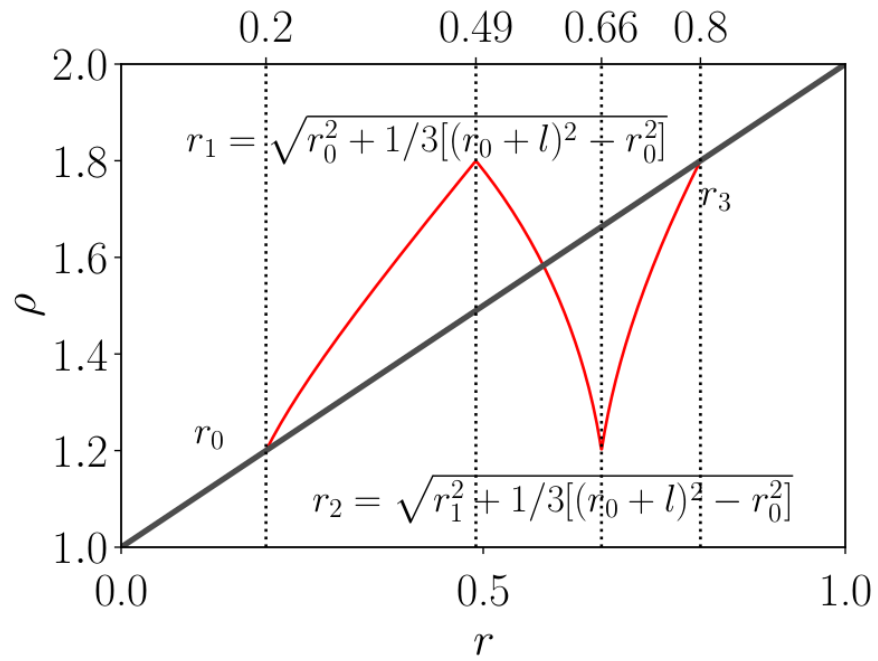
The S-ODT formulation is a quasi-2-D stationary formulation for ODT (it is not a fully 2-D formulation due to the restriction to parabolic problems). Due to the RTT, Eq. (A.1), the corresponding quantities to conserve in S-ODT, seen from the Eulerian perspective, are fluxes, instead of rate of changes of specific density quantities. Further development of this idea leads to the S-ODT generalization for boundary layers of the eddy turnover length formula, as in [64, 66, 69],

$$\frac{1}{2K_0} \left(\frac{u_{eddy}}{L_{eddy}} \right)^2 \int_l \hat{\rho} \hat{u}_1 K_{ODT}^2 dV = K_0 \left(\sum_k \Xi''_{u,kin,eddy,k} \right) - u_{eddy} \Xi_{vp,eddy} + K_0 \Xi_{u,pot,eddy}. \quad (C.11)$$

Here, the subindex u indicates that the quantity is now a streamwise-flux quantity (see Table C.3). For the S-ODT line-confined system



(a)



(b)

Figure C.1: (a) Planar triplet map of an initially monotonic density profile with eddy size $l = 0.6$ and left edge $y_0 = 0.2$. (b) Cylindrical triplet map of an initially monotonic density profile with eddy size $l = 0.6$ and left edge $r_0 = 0.2$.

formulation of [71, 72], the corresponding formula due to mapping of scalar densities, e.g. $\rho h \rightarrow \widehat{\rho h}$ is,

$$\frac{1}{2K_0} \left(\frac{\rho_{eddy} u_{eddy}}{L_{eddy}} \right)^2 \int_1 \frac{\widehat{\rho u_1}}{\widehat{\rho}^2} K_{ODT}^2 dV = K_0 \left(\sum_k \Xi''_{u,kin,eddy,k} \right) - u_{eddy} \Xi_{vp,eddy} + K_0 \Xi_{u,pot,eddy}. \quad (C.12)$$

C.3 STOCHASTIC ODT IMPLEMENTATION ALGORITHM

A simplified algorithmic description of the stochastic ODT implementation is listed next, summarizing part of the information contained in chapter 3 of this thesis. This algorithm is specialized for the T-ODT formulation, however, its generalization for S-ODT is straightforward. This algorithm is adapted from the ODT algorithms detailed in the thesis of R. McDermott and F. Meiselbach [68, 81].

By Eqs. (3.11) and (3.9), the acceptance probability of an eddy is,

$$\Omega = \frac{\Lambda \mathcal{F} \Delta t_{samp}}{\mathcal{G}}$$

Approximating \mathcal{F} as \mathcal{G} and averaging,

$$\overline{\Delta t_{samp}} = \frac{\overline{\Omega}}{\overline{\Lambda}} + \Delta_{\Delta t}. \quad (C.13)$$

Here, $\Delta_{\Delta t}$ represents the dynamic adjustment of $\overline{\Delta t_{samp}}$ during the stochastic implementation process. For the Poisson process, $\overline{\Lambda} = n\Lambda$ with an arbitrary $n > 1$.

The input data for algorithm 1 is the simulation time t_{end} , the ODT parameters $C, Z, \alpha, \alpha_{pot,k}$, mesh adaption parameters, initial and boundary conditions for conserved scalars, initial fluid properties, domain size L_{domain} , initial Kolmogorov length scale η_0 , average acceptance probability of eddy events $\overline{\Omega}$, and the maximum acceptance probability of eddy events Ω_{max} . Each adaption step in algorithm 1 must include the verification of the symmetric center cell size as commented previously in this chapter (for ODT cylindrical formulations).

The diffusion time step is calculated as,

$$\Delta t_{diff} = CFL \frac{(\Delta r_{min})^2}{\nu}, \quad (C.14)$$

where CFL is the CFL number condition and Δr_{min} is the minimum cell size in the grid. For S-ODT, the diffusion streamwise step takes the form,

$$\Delta z_{diff} = CFL \frac{(\Delta r_{min})^2}{u_{min} \nu}, \quad (C.15)$$

where u_{min} is the minimum streamwise velocity value in the grid.

```

1 Calculate mean sampling time as 10% of that given by Eq. (C.13)
  without the fluctuating part. The initial mean global rate of
  eddies is  $\bar{\Lambda} = n \frac{v_0}{(\Delta r_u)^2}$ , considering  $n$  as the number of grid cells
  and  $\Delta r_u$  as a uniform grid cell size given by  $L_{domain}/n$ ;
2 Calculate  $\Delta t_{diff}$  by Eq. (C.14);
3  $t = 0$ ;
4  $t_{diff} = 0$ ;
5  $t_{lastAdaption} = 0$ ;
6 while  $t \leq t_{end}$  do
7   if  $t - t_{diff} \leq \Delta t_{diff}$  then
8     Deterministic diffusion step for  $\Delta t = t - t_{diff}$ ;
9     Check for mesh adaption by  $\Delta r_{max}$  or  $\Delta r_{min}$ ;
10    if  $t - t_{lastAdaption} \geq A_{TimeFac} \Delta t_{diff}$  then
11      Adapt the mesh;
12      Recalculate  $\Delta t_{diff}$  by Eq. (C.14);
13       $t_{lastAdaption} = t$ ;
14    end
15     $t_{diff} = t$ ;
16  end
17  Perform a random eddy event as described in chapter 3.
  Calculate  $\Omega$  by Eq. (3.11). Perform this simultaneously with
  the dynamic adjustment of  $\bar{\Delta t}_{samp}$ , as detailed in Algorithm
  3.2 of McDermott [68];
18 if Eddy is accepted then
19   Adapt the mesh in the eddy region;
20   Deterministic diffusion step for  $\Delta t = t - t_{diff}$ ;
21   Check for mesh adaption by  $\Delta r_{max}$  or  $\Delta r_{min}$ ;
22   Re-adapt the mesh in the eddy region;
23   Recalculate  $\Delta t_{diff}$  by Eq. (C.14);
24   if  $t - t_{lastAdaption} \geq A_{TimeFac} \Delta t_{diff}$  then
25     Adapt the mesh;
26     Recalculate  $\Delta t_{diff}$  by Eq. (C.14);
27      $t_{lastAdaption} = t$ ;
28   end
29    $t_{diff} = t$ ;
30 end
31 Sample a random number  $n_r$  in  $(0;1]$ ;
32  $t = t + \Delta t_{samp}$ , with  $\Delta t_{samp}$  given by the Poisson process as,
   $\Delta t_{samp} = -\bar{\Delta t}_{samp} \ln |n_r|$ ;
33 end
34 if  $t_{diff} < t$  then
35   Deterministic diffusion step for  $\Delta t = t - t_{diff}$ ;
36 end

```

Algorithm 1: Stochastic T-ODT implementation

Table C.1: T-ODT eddy turnover time formula and kernel coefficients

Quantity / Term	Formula	Units
Mapped quantities	ρ, u_k, h, ρ_f	Dependent on the mapped scalar
Momentum balance	$\int_I (\widehat{\rho}u_k + \widehat{\rho}c_k K_{ODT} + \widehat{\rho}b_k J_{ODT}) dV - \int_I \rho u_k dV = 0$	$(\text{kg} \cdot \text{m/s})/\text{m}^2$ (Planar) or $(\text{kg} \cdot \text{m/s})/\text{m}$ (Cylindrical)
Kinetic energy balance	$\Delta E'_{kin,eddy,k} = \frac{1}{2} \int_I \widehat{\rho} (\widehat{u}_k + c_k K_{ODT} + b_k J_{ODT})^2 dV - \frac{1}{2} \int_I \rho u_k^2 dV + \Xi_{E,pot,eddy,k}$	J/m^2 (Planar) or J/m (Cylindrical)
Eddy turnover time relation	$\frac{1}{2K_0} \left(\frac{1}{\tau_{eddy}} \right)^2 \int_I \widehat{\rho} K_{ODT}^2 dV = K_0 \left(\sum_k \Xi''_{kin,eddy,k} \right) - \Xi_{ep,eddy} + K_0 \Xi_{pot,eddy}$	Units of τ_{eddy} : s
K_{ODT}	$y - f(y)$ (Planar) or $r - f(r)$ (Cylindrical)	m
J_{ODT}	$ K_{ODT} $	m
ρ_J	$\int_I \widehat{\rho} J_{ODT} dV$	kg/m (Planar) or kg (Cylindrical)
ρ_K	$\int_I \widehat{\rho} K_{ODT} dV$	kg/m (Planar) or kg (Cylindrical)
ρ_{JK}	$\int_I \widehat{\rho} J_{ODT} K_{ODT} dV$	kg (Planar) or $\text{kg} \cdot \text{m}$ (Cylindrical)
ρ_{KK}	$\int_I \widehat{\rho} K_{ODT}^2 dV$	kg (Planar) or $\text{kg} \cdot \text{m}$ (Cylindrical)
ρ_{kJ}	$\int_I \widehat{\rho} u_k J_{ODT} dV$	kg/s (Planar) or $\text{kg} \cdot \text{m}/\text{s}$ (Cyl.)

ρ_{kk}	$\int_I \widehat{\rho} \widehat{u}_k K_{ODT} dV$	kg/s (Planar) or kg · m/s (Cyl.)
H_{ODT}	ρ_K / ρ_I	-
$P_{k,ODT}$	$\rho_{kK} - H_{ODT} \rho_{kI}$	Same as ρ_{kK}
S_{ODT}	$\frac{1}{2} (H_{ODT}^2 + 1) \rho_{kK} - H_{ODT} \rho_{JK}$	Same as ρ_{JK}
$\Xi''_{kin,eddy,k}$	$\frac{P_{k,ODT}^2}{4S_{ODT}}$	J/m ² (Planar) or J/m (Cylindrical)
$\Xi_{vp,eddy}$	$\frac{Z_{eddy}^{H''}}{2\rho_{eddy}^2} (\int_I dV)$	J/m ² (Planar) or J/m (Cylindrical)
$\Xi_{E,pot-DL,eddy}$	$\frac{1}{\beta} \int_I K_{ODT} [\widehat{J} \cdot \widehat{\check{I}}_I - (\widehat{J} \cdot \widehat{\check{I}}_I)_{eddy}] dV$	J/m ² (Planar) or J/m (Cylindrical)
$\Xi_{E,pot,eddy}$	$\int_I \phi (\widehat{\rho}_f - \rho_f) dV$	J/m ² (Planar) or J/m (Cylindrical)

The kinetic energy balance can be rewritten as $\Delta \Xi'_{kin,eddy,k} = S_{ODT} c_k^2 + P_{k,ODT} c_k + \Xi_{E,pot,eddy,k,r}$ with the help of the notation in Table C.1. Solving for c_k results in,

$$c_k = \frac{1}{2S_{ODT}} \left[-P_{k,ODT} + \text{sgn}(P_{k,ODT}) \sqrt{P_{k,ODT}^2 + 4S_{ODT} (\Delta \Xi'_{kin,eddy,k} - \Xi_{E,pot,eddy,k})} \right]$$

The units of c_k are s⁻¹. Substituting $\Delta \Xi'_{kin,eddy,k}$ according to Eq. (3.28) and using the definition of kinetic energy $\Xi''_{kin,eddy,k}$ from Table C.1 leads to, using r, s, t as permutation of the indices 1, 2, 3,

$$c_r = \frac{1}{2S_{ODT}} \left\{ -P_{r,ODT} + \text{sgn}(P_{r,ODT}) \sqrt{(1 - \alpha) P_{r,ODT}^2 + \frac{\alpha}{2} P_{s,ODT}^2 + \frac{\alpha}{2} P_{t,ODT}^2 + \alpha_{pot,s} \frac{\alpha}{2} + \alpha_{pot,t} \frac{\alpha}{2}} \right\} 4S_{ODT} \Xi_{E,pot,eddy} \quad (C.16)$$

Table C.2: S-ODT eddy turnover length scale formula and kernel coefficients

Quantity / Term	Formula	Units
Mapped quantities	$\rho, \rho u_k, \rho h, \rho_f, \rho_f u_1$	Dependent on the mapped scalar
Streamwise momentum flux balance	$\int_{J_1} (\widehat{\rho u_1} u_k + \widehat{\rho u_1} c_k K_{ODT} + \widehat{\rho u_1} b_k J_{ODT}) dV - \int_{J_1} \rho u_1 u_k dV = 0$	J/m ² (Planar) or J/m (Cylindrical)
Streamwise kinetic energy flux balance	$\Delta E'_{u,kin,eddy,k} = \frac{1}{2} \int_{J_1} \widehat{\rho u_1} (\widehat{u}_k + c_k K_{ODT} + b_k J_{ODT})^2 dV - \frac{1}{2} \int_{J_1} \rho u_1 u_k^2 dV + \Xi_{u,E,pot,eddy,k}$	W/m (Planar) or W (Cylindrical)
Eddy turnover length scale relation	$\frac{1}{2K_0} \left(\frac{\rho_{eddy} u_{eddy}}{L_{eddy}} \right)^2 \int_{J_1} \frac{\widehat{\rho u_1}}{\widehat{\rho}^2} K_{ODT}^2 dV = K_0 \left(\sum_k \Xi''_{u,kin,eddy,k} \right) - u_{eddy} \Xi_{ep,eddy} + K_0 \Xi_{u,pot,eddy}$	Units of L_{eddy} : m
K_{ODT}	$y - f(y)$ (Planar) or $r - f(r)$ (Cylindrical)	m
J_{ODT}	$ K_{ODT} $	m
u_J	$\int_{J_1} \frac{\widehat{\rho u_1} J_{ODT}}{\widehat{\rho}} dV$	m ³ /s (Planar) or m ⁴ /s (Cyl.)
u_K	$\int_{J_1} \frac{\widehat{\rho u_1} K_{ODT}}{\widehat{\rho}} dV$	m ³ /s (Planar) or m ⁴ /s (Cyl.)

u_{JK}	$\int_1 \frac{\widehat{\rho} u_1 \text{K}_{ODT} \text{K}_{ODT}}{\widehat{\rho}^2} dV$	$\text{m}^7 / (\text{kg} \cdot \text{s})$ (Planar) or $\text{m}^8 / (\text{kg} \cdot \text{s})$ (Cylindrical)
u_{KK}	$\int_1 \frac{\widehat{\rho} u_1 \text{K}_{ODT}^2}{\widehat{\rho}^2} dV$	$\text{m}^7 / (\text{kg} \cdot \text{s})$ (Planar) or $\text{m}^8 / (\text{kg} \cdot \text{s})$ (Cylindrical)
u_{kJ}	$\int_1 \frac{\widehat{\rho} u_1 \widehat{\rho} u_k \text{K}_{ODT}}{\widehat{\rho}^2} dV$	m^4 / s^2 (Planar) or m^5 / s^2 (Cyl.)
u_{kK}	$\int_1 \frac{\widehat{\rho} u_1 \widehat{\rho} u_k \text{K}_{ODT}}{\widehat{\rho}^2} dV$	m^4 / s^2 (Planar) or m^5 / s^2 (Cyl.)
H_{ODT}	u_K / u_J	-
P_{kODT}	$u_{kK} - H_{ODT} u_{kJ}$	Same as u_{kK}
S_{ODT}	$\frac{1}{2} (H_{ODT}^2 + 1) u_{KK} - H_{ODT} u_{JK}$	Same as u_{JK}
$\Xi''_{u,kin,eddy,k}$	$\frac{P_{kODT}}{4S_{ODT}}$	W / m (Planar) or W (Cylindrical)
$\Xi_{vp,eddy}$	$\frac{Z_{t,eddy}}{2\rho_{eddy}^2} (\int_1 dV)$	J / m^2 (Planar) or J / m (Cylindrical)
$\Xi_{u,E,pot-DL,eddy}$	$\frac{1}{\beta} \int_1 \widehat{u}_1 \text{K}_{ODT} [\widehat{J} \cdot \widehat{\check{J}}_I - (\widehat{J} \cdot \widehat{\check{J}}_I)_{eddy}] dV$	W / m (Planar) or W (Cylindrical)
$\Xi_{u,E,pot,eddy}$	$\int_1 \phi (\widehat{\rho}_f \widehat{u}_1 - \rho_f u_1) dV$	W / m (Planar) or W (Cylindrical)

The kinetic energy balance can be rewritten as $\Delta \Xi'_{u,kin,eddy,k} = S_{ODT} c_k^2 + P_{kODT} c_k + \Xi_{u,E,pot,eddy,k}$, with the help of the notation in Table C.2. The units of c_k are $\text{kg} / (\text{m}^3 \cdot \text{s})$. Similar to Eq. (C.16), using the notation from Table C.2,

$$c_r = \frac{1}{2S_{ODT}} \left\{ -P_{r,ODT} + \text{sgn}(P_{r,ODT}) \sqrt{(1-\alpha) P_{r,ODT}^2 + \frac{\alpha}{2} P_{s,ODT}^2 + \frac{\alpha}{2} P_{t,ODT}^2} + \alpha_{pot,r} (1-\alpha) + \alpha_{pot,s} \frac{\alpha}{2} + \alpha_{pot,t} \frac{\alpha}{2} \right\} 4S_{ODT} \Xi_{u,E,pot,eddy} \quad (\text{C.17})$$

Table C.3: S-ODT eddy turnover length scale formula and kernel coefficients (boundary layer S-ODT formulation from [64, 66, 69])

Quantity / Term	Formula	Units
Mapped quantities	ρ, u_k, h, ρ_f	Dependent on the mapped scalar
Streamwise momentum flux balance	$\int_{J_l} (\widehat{\rho u_1 u_k} + \widehat{\rho u_1} c_k K_{ODT} + \widehat{\rho u_1} b_k J_{ODT}) dV - \int_{J_l} \rho u_1 u_k dV = 0$	J/m ² (Planar) or J/m (Cylindrical)
Streamwise kinetic energy flux balance	$\Delta E'_{u,kin,eddy,k} = \frac{1}{2} \int_{J_l} \widehat{\rho u_1} (\widehat{u_k} + c_k K_{ODT} + b_k J_{ODT})^2 dV - \frac{1}{2} \int_{J_l} \rho u_1 u_k^2 dV + \Xi_{u,E,pot,eddy,k}$	W/m (Planar) or W (Cylindrical)
Eddy turnover length scale relation	$\frac{1}{2K_0} \left(\frac{u_{eddy}}{L_{eddy}} \right)^2 \int_{J_l} \widehat{\rho u_1} K_{ODT}^2 dV = K_0 \left(\sum_k \Xi''_{u,kin,eddy,k} \right) - u_{eddy} \Xi_{ep,eddy} + K_0 \Xi_{u,pot,eddy}$	Units of L_{eddy} : m
K_{ODT}	$y - f(y)$ (Planar) or $r - f(r)$ (Cylindrical)	m
J_{ODT}	$ K_{ODT} $	m
ρ_{uJ}	$\int_{J_l} \widehat{\rho u_1} J_{ODT} dV$	kg/s (Planar) or kg · m/s (Cyl.)
ρ_{uK}	$\int_{J_l} \widehat{\rho u_1} K_{ODT} dV$	kg/s (Planar) or kg · m/s (Cyl.)

$\rho_{u K}$	$\int_I \hat{\rho} \hat{u}_1 \int_{ODT} K_{ODT} dV$	kg · m/s (Planar) or kg · m ² /s (Cylindrical)
ρ_{uKK}	$\int_I \hat{\rho} \hat{u}_1 K_{ODT}^2 dV$	kg · m/s (Planar) or kg · m ² /s (Cylindrical)
$\rho_{u k}$	$\int_I \hat{\rho} \hat{u}_1 \hat{u}_k \int_{ODT} dV$	kg · m/s ² (Planar) or kg · m ² /s ² (Cylindrical)
$\rho_{u kk}$	$\int_I \hat{\rho} \hat{u}_1 \hat{u}_k K_{ODT} dV$	kg · m/s ² (Planar) or kg · m ² /s ² (Cylindrical)
H_{ODT}	ρ_{uK} / ρ_u	-
$P_{k,ODT}$	$\rho_{u kk} - H_{ODT} \rho_{u k}$	Same as $\rho_{u kK}$
SODT	$\frac{1}{2} (H_{ODT}^2 + 1) \rho_{u kk} - H_{ODT} \rho_{u k}$	Same as $\rho_{u kK}$
$\Xi''_{u,kin,eddy,k}$	$\frac{P_{k,ODT}}{4S_{ODT}}$	W/m (Planar) or W (Cylindrical)
$\Xi_{vp,eddy}$	$\frac{Z_{k,eddy}^2}{2\rho_{eddy}^2} \left(\int_I dV \right)$	J/m ² (Planar) or J/m (Cylindrical)
$\Xi_{u,E,pot-DL,eddy}$	$\frac{1}{\beta} \int_I \hat{u}_1 K_{ODT} \left[\hat{J} \cdot \hat{\xi}_I - (\hat{J} \cdot \hat{\xi}_I)_{eddy} \right] dV$	W/m (Planar) or W (Cylindrical)
$\Xi_{u,E,pot,eddy}$	$\int_I \phi (\hat{\rho}_f \hat{u}_1 - \rho_f u_1) dV$	W/m (Planar) or W (Cylindrical)

The units of c_k are s⁻¹. The formula for the calculation of the kernel coefficients is the same as in Eq. (C.17), but using the notation and formulas from Table C.3.

DETERMINISTIC ODT IMPLEMENTATION

This appendix is focused on the practical implementation of the deterministic diffusion step specified in algorithm 1.

Due to the Lagrangian framework developed in this thesis, the ideal and most natural form of discretization which should ensure the implicit Lagrangian mass conservation is a FV discretization [122]. However, the governing equations derived in this thesis were obtained in a differential Lagrangian framework, which leads to an important dilemma. For that, an interpolation of values outside the flux terms is done, such that, discretely, the values can be inserted into the flux terms. Take, e.g., Eq. (3.72),

$$\frac{DT}{Dt} = \frac{1}{\rho c_p} \left[\frac{\partial}{\partial y} \left(\sigma_T \frac{\partial T}{\partial y} \right) + \frac{(J \cdot \check{\rho}_{ODT})^2}{\rho_f \beta} \right]. \quad (3.72)$$

It is possible to filter the terms ρ and c_p appearing on the RHS. Doing so, ρ_Δ and $c_{p,\Delta}$ terms are obtained, which are constant with respect to y within the discretized volume. This is a mean value approximation for ρ and c_p . The FVM uses values defined at the center of finite 1-D grid cells. Specializing to planar coordinates, the spatial variation of any scalar ψ can then be described via a Taylor series expansion around the center of a finite volume as [123],

$$\psi = \psi_c + (y - y_c) \frac{\partial \psi}{\partial y_c} + \frac{1}{2} (y - y_c)^2 \frac{\partial^2 \psi}{\partial y_c^2} + \frac{1}{3!} (y - y_c)^3 \frac{\partial^3 \psi}{\partial y_c^3} + \dots \quad (D.1)$$

For the mean value approximation at the center of a finite volume (grid cell), ψ is assumed to vary linearly and be represented by ψ_c . Since $y = y_c$, all second (and higher) order terms are omitted in Eq. (D.1). For the density ρ , this is,

$$\begin{aligned} \rho_\Delta &= \frac{1}{\Delta y} \int_{\Delta y} \rho dy \\ &= \frac{1}{\Delta y} \int_{\Delta y} \left[\rho_c + (y - y_c) \frac{\partial \rho}{\partial y_c} + O[(\Delta y)^2] \right] dy \\ &= \rho_c + O[(\Delta y)^2]. \end{aligned} \quad (D.2)$$

Similarly, for the specific heat capacity at constant pressure,

$$c_{p,\Delta} = c_{p,c} + O[(\Delta y)^2]. \quad (D.3)$$

The modified temperature equation that is solved, is, therefore,

$$\frac{DT}{Dt} = \frac{\partial}{\partial y} \left(\frac{\sigma_T}{\rho_\Delta c_{p,\Delta}} \frac{\partial T}{\partial y} \right) + \frac{(J \cdot \check{\rho}_{ODT})^2}{\rho c_p \rho_f \beta} + O[(\Delta y)^2]. \quad (D.4)$$

That is, the temperature flux conservation is only hold with a second order error by grid discretization. This equation can be discretized with a FVM by integrating with respect to y ,

$$\int_{\Delta y} \frac{DT}{Dt} dy = \frac{1}{\rho \Delta c_p \Delta} \left[\left(\sigma_T \frac{\partial T}{\partial y} \right)_{y+\frac{\Delta y}{2}} - \left(\sigma_T \frac{\partial T}{\partial y} \right)_{y-\frac{\Delta y}{2}} \right] + \int_{\Delta y} \frac{(\underline{J} \cdot \check{\gamma}_{ODT})^2}{\rho c_p \rho_f \beta} dy + O(\Delta y). \quad (D.5)$$

The mean value approximation for the material derivative on the LHS results again in a second order error per grid discretization. The leading order error term is, thus, first order per grid discretization. Similar consequences are carried over to the conservation of mass, by the divergence condition, Eq. (3.74). Formulas for the calculation of the fluxes or derivatives and derivative coefficients at the grid cell boundaries demanded in Eq. (D.5) can be found in [81]. It is noted that in the case of constant properties, all equations become fully conservative and the only error in the calculations is the second order error due to the mean value approximations at the cell centers (plus the error due to time integration).

As a contrast to the FVM applied for the hydrodynamic treatment, the electrodynamic treatment is done in this thesis following a Finite Difference Method (FDM). This is motivated, at a fundamental level, on the brief comment made in chapter 2 regarding the ill-definition of electric fields within Lagrangian frameworks. Another reason for the FD treatment of the electrostatics is that the calculation of electrostatic potential problems involves a very delicate treatment of the boundary conditions. Dirichlet boundary conditions are interpolated in any standard FVM [122], which proved as a major inconvenience during the numerical generation of the electrostatic fields. Finite difference formulas for the calculation of derivatives required, e.g., in the planar coordinate system for Eqs. (3.71), (3.75-3.76) can be found in any standard Computational Fluid Dynamics (CFD) book, e.g. [122].

In the following subsections, the spatial discretization and time integration of the hydrodynamic equations is discussed. The solution algorithm for the electrodynamic equations is discussed in another appendix.

D.1 T-ODT GOVERNING EQUATIONS

The time integration of T-ODT governing equations is done with a first order implicit integration method for momentum and temperature. Details of the time integration methods can be found in any standard CFD textbook, e.g. [122]. The momentum equation is usually solved in an operator splitting fashion, first omitting the mean pressure gradient effect, and then updating the velocity in order to account for it. Mass

conservation is enforced by the divergence condition at the end of the Lagrangian time advancement. Next, the integral form and the discretized form of the deterministic T-ODT governing equations is discussed. This is based on the model equations, Eqs. (3.71-3.74), and the material derivative definition for T-ODT, Eq. (3.77).

D.1.1 Cartesian coordinates

The integral and discretized hydrodynamic equations are listed next. For the discretized equations, the subindex i refers to the grid cell index, while the superindex n refers to the discrete time-step index. A superindex $*$ indicates an intermediate time-step. Indices $i + \frac{1}{2}$ or $i - \frac{1}{2}$ indicate the position of a grid cell face. In all integral or integrated equations, $O(\Delta)$ is $O(\Delta y)$ if $\rho, c_p \neq \text{constant}$ or $O(\Delta) = 0$ otherwise. In all discretized equations, $O(\Delta)$ is $O(\Delta t, \Delta y)$ if $\rho \neq \text{constant}$ or $O(\Delta) = O[\Delta t, (\Delta y)^2]$ otherwise.

- **Momentum equation:**

$$\int_{\Delta y} \frac{dV}{dt} dy = \frac{1}{\rho_{\Delta}} \left[\left(\mu \frac{\partial V}{\partial y} \right)_{y+\frac{\Delta y}{2}} - \left(\mu \frac{\partial V}{\partial y} \right)_{y-\frac{\Delta y}{2}} \right] + \int_{\Delta y} \underline{g} \cdot \check{\underline{\tau}}_{vert} dy - \int_{\Delta y} \frac{1}{\rho_{\Delta}} \nabla \bar{p} \cdot \check{\underline{\tau}}_{str} dy + O(\Delta). \quad (D.6)$$

- **Discretized momentum equation:**

$$\frac{V_i^{n,*} - V_i^n}{\Delta t} \Delta y_i^n = \frac{1}{\rho_i^n} \left[\left(\mu^n \frac{\partial V_i^{n,*}}{\partial y^n} \right)_{i+\frac{1}{2}} - \left(\mu^n \frac{\partial V_i^{n,*}}{\partial y^n} \right)_{i-\frac{1}{2}} \right] + \underline{g} \cdot \check{\underline{\tau}}_{vert} \Delta y_i^n + O(\Delta). \quad (D.7)$$

- **Temperature equation:**

$$\int_{\Delta y} \frac{dT}{dt} dy = \frac{1}{\rho_{\Delta} c_{p,\Delta}} \left[\left(\sigma_T \frac{\partial T}{\partial y} \right)_{y+\frac{\Delta y}{2}} - \left(\sigma_T \frac{\partial T}{\partial y} \right)_{y-\frac{\Delta y}{2}} \right] + \int_{\Delta y} \frac{(\underline{J} \cdot \check{\underline{\tau}}_{ODT})^2}{\rho c_p \rho_f \beta} dy + O(\Delta). \quad (D.8)$$

- **Discretized temperature equation:** Note that β is a constant due to the electric field, charge density and current density assumed as constants. For the planar case, the current density is also a constant.

$$\frac{T_i^{n+1} - T_i^n}{\Delta t} \Delta y_i^n = \frac{1}{\rho_i^n c_{p,i}^n} \left[\left(\sigma_T^n \frac{\partial T_i^{n+1}}{\partial y^n} \right)_{i+\frac{1}{2}} - \left(\sigma_T^n \frac{\partial T_i^{n+1}}{\partial y^n} \right)_{i-\frac{1}{2}} \right] + \frac{j_{2,i}^2}{\rho_i^n c_{p,i}^n \rho_{f,i} \beta} \Delta y_i^n + O(\Delta). \quad (D.9)$$

- **Divergence condition:** The definition given by Eq. (3.5) is used, $v_\psi = dy/dt$, together with the ideal gas law, Eq. (2.49),

$$\frac{\partial}{\partial y} \left(\frac{dy}{dt} \right) = \frac{\partial}{\partial y} \left(\frac{R_{air} \sigma_T}{Pc_{p,\Delta}} \frac{\partial T}{\partial y} \right) + \frac{R_{air} (J \cdot \check{\zeta}_{ODT})^2}{Pc_p \rho_f \beta} + O(\Delta).$$

Thus,

$$\begin{aligned} \frac{d\Delta y}{dt} &= \frac{R_{air}}{Pc_{p,\Delta}} \left[\left(\sigma_T \frac{\partial T}{\partial y} \right)_{y+\frac{\Delta y}{2}} - \left(\sigma_T \frac{\partial T}{\partial y} \right)_{y-\frac{\Delta y}{2}} \right] \\ &+ \int_{\Delta y} \frac{R_{air} (J \cdot \check{\zeta}_{ODT})^2}{Pc_p \rho_f \beta} dy + O(\Delta). \end{aligned} \quad (D.10)$$

- **Discretized divergence condition:**

$$\begin{aligned} \frac{\Delta y_i^{n+1} - \Delta y_i^n}{\Delta t} &= \frac{R_{air}}{Pc_{p,i}^{n+1}} \left[\left(\sigma_T^{n+1} \frac{\partial T^{n+1}}{\partial y^n} \right)_{i+\frac{1}{2}} - \left(\sigma_T^{n+1} \frac{\partial T^{n+1}}{\partial y^n} \right)_{i-\frac{1}{2}} \right] \\ &+ \frac{R_{air} j_{2,i}^2}{Pc_{p,i}^{n+1} \rho_{f,i} \beta} \Delta y_i^n + O(\Delta). \end{aligned} \quad (D.11)$$

- **Discretized mean pressure gradient constraint:**

$$\overline{V}_i^{n+1} - \overline{V}_i^{n,*} = -\frac{1}{\rho_i^{n+1}} \frac{\partial \overline{p}}{\partial x} \Delta t \begin{pmatrix} 1 \\ 0 \\ 0 \end{pmatrix}. \quad (D.12)$$

With the pressure gradient either being pre-defined or given by a pre-defined streamwise mass flux constraint $\dot{m} = U_b \rho_b L$, where L is the ODT domain length,

$$\frac{\partial \overline{p}}{\partial x} \Delta t = \frac{\sum_i (\rho_i^{n+1} u_i^{n,*} \Delta y_i^{n+1}) - U_b \rho_b L}{\sum_i \Delta y_i^{n+1}}. \quad (D.13)$$

D.1.2 Cylindrical coordinates

Note the use of the identity given by Eq. (C.1) in this section. Note also the form of the shear stress tensor divergence in ODT, as in [72],

$$\nabla \cdot \underline{\underline{\tau}} = \begin{pmatrix} \frac{1}{r} \frac{\partial}{\partial r} \left(r \mu \frac{\partial u}{\partial r} \right) \\ \frac{1}{r} \frac{\partial}{\partial r} \left(r \mu \frac{\partial v}{\partial r} \right) - \frac{v}{r^2} \frac{\partial (r \mu)}{\partial r} \\ \frac{1}{r} \frac{\partial}{\partial r} \left(r \mu \frac{\partial w}{\partial r} \right) - \frac{w}{r^2} \frac{\partial (r \mu)}{\partial r} \end{pmatrix}. \quad (D.14)$$

Filtering $(v/r)_\Delta$ and $(w/r)_\Delta$ in the tensor divergence and integrating over $dr^2/2$ (effective volume integral), results in,

$$\begin{aligned} & \tau_{r+\frac{\Delta r}{2}} - \tau_{r-\frac{\Delta r}{2}} \\ &= \left(\begin{array}{c} \left(r\mu \frac{\partial u}{\partial r} \right)_{r+\frac{\Delta r}{2}} - \left(r\mu \frac{\partial u}{\partial r} \right)_{r-\frac{\Delta r}{2}} \\ \left(r\mu \frac{\partial v}{\partial r} \right)_{r+\frac{\Delta r}{2}} - \frac{v_\Delta}{r_\Delta} (r\mu)_{r+\frac{\Delta r}{2}} - \left(r\mu \frac{\partial v}{\partial r} \right)_{r-\frac{\Delta r}{2}} + \frac{v_\Delta}{r_\Delta} (r\mu)_{r-\frac{\Delta r}{2}} \\ \left(r\mu \frac{\partial w}{\partial r} \right)_{r+\frac{\Delta r}{2}} - \frac{w_\Delta}{r_\Delta} (r\mu)_{r+\frac{\Delta r}{2}} - \left(r\mu \frac{\partial w}{\partial r} \right)_{r-\frac{\Delta r}{2}} + \frac{w_\Delta}{r_\Delta} (r\mu)_{r-\frac{\Delta r}{2}} \end{array} \right). \end{aligned} \quad (\text{D.15})$$

In all integral or integrated equations, $O(\Delta)$ is $O(\Delta r)$ if $\rho, c_p \neq \text{constant}$ or $O(\Delta) = 0$ otherwise. In all discretized equations, $O(\Delta)$ is $O(\Delta t, \Delta r)$ if $\rho \neq \text{constant}$ or $O(\Delta) = O[\Delta t, (\Delta r)^2]$.

- **Momentum equation:**

$$\begin{aligned} \frac{1}{2} \int_{\Delta r} \frac{dV}{dt} dr^2 &= \frac{1}{\rho_\Delta} \left[\tau_{r+\frac{\Delta r}{2}} - \tau_{r-\frac{\Delta r}{2}} \right] + \frac{1}{2} \int_{\Delta r} \underline{g} \cdot \check{\tau}_{vert} dr^2 \\ &\quad - \frac{1}{2} \int_{\Delta r} \frac{1}{\rho_\Delta} \nabla \bar{p} \cdot \check{\tau}_{str} dr^2 + O(\Delta). \end{aligned} \quad (\text{D.16})$$

- **Discretized momentum equation:** Velocities in the shear stress term on the RHS are discretized at time-step $n, *$. Properties and grid cell sizes are evaluated at time step n .

$$\begin{aligned} \frac{V_i^{n,*} - V_i^n}{\Delta t} \Delta r_i^{2,n} &= \frac{2}{\rho_i^n} \left[\tau_{i+\frac{1}{2}} - \tau_{i-\frac{1}{2}} \right] + \underline{g} \cdot \check{\tau}_{vert} \Delta r_i^{2,n} + O(\Delta). \end{aligned} \quad (\text{D.17})$$

- **Temperature equation:**

$$\begin{aligned} \frac{1}{2} \int_{\Delta r} \frac{dT}{dt} dr^2 &= \frac{1}{\rho_\Delta c_{p,\Delta}} \left[\left(r\sigma_T \frac{\partial T}{\partial r} \right)_{r+\frac{\Delta r}{2}} - \left(r\sigma_T \frac{\partial T}{\partial r} \right)_{r-\frac{\Delta r}{2}} \right] \\ &\quad + \frac{1}{2} \int_{\Delta r} \frac{(\underline{J} \cdot \check{\tau}_{ODT})^2}{\rho c_p \rho_f \beta} dr^2 + O(\Delta). \end{aligned} \quad (\text{D.18})$$

- **Discretized temperature equation:**

$$\begin{aligned} \frac{T_i^{n,*} - T_i^n}{\Delta t} \Delta r_i^{2,n} &= \frac{2}{\rho_i^n c_{p,i}^n} \left[\left(r^n \sigma_T^n \frac{\partial T^{n,*}}{\partial r^n} \right)_{i+\frac{1}{2}} - \left(r^n \sigma_T^n \frac{\partial T^{n,*}}{\partial r^n} \right)_{i-\frac{1}{2}} \right] \\ &\quad + \frac{j_{2,i}^2}{\rho_i^n c_{p,i}^n \rho_{f,i} \beta} \Delta r_i^{2,n} + O(\Delta). \end{aligned} \quad (\text{D.19})$$

- **Optional constant bulk enthalpy constraint:** A constraint for enforcing constant bulk enthalpy (constant bulk temperature) can be enforced by means of a bulk mean streamwise enthalpy gradient. In a constant properties flow, this is equivalent to the forcing of the temperature profile by means of a streamwise temperature gradient, see [124],

$$h(T)_i^{n+1} - h(T)_i^{*,n} = -u_i^{n,*} \frac{\partial \bar{h}}{\partial x} \Delta t. \quad (\text{D.20})$$

The mean streamwise enthalpy gradient is either pre-defined or given by a target bulk enthalpy H_b ,

$$\frac{\partial \bar{h}}{\partial x} \Delta t = \frac{\sum_i \left(h_i^{n,*} \Delta r_i^{2,n} \right) - H_b \sum_i \Delta r_i^{2,n}}{\sum_i u_i^{n,*} \Delta r_i^{2,n}}. \quad (\text{D.21})$$

- **Divergence condition:** Due to properties of the ∇ operator for cylindrical coordinates, the cylindrical analogous of the planar equation using $v_\psi = dr/dt$ is,

$$\frac{1}{r} \frac{\partial}{\partial r} \left(r \frac{dr}{dt} \right) = \frac{1}{r} \frac{\partial}{\partial r} \left(\frac{r R_{air} \sigma_T}{Pc_{p,\Delta}} \frac{\partial T}{\partial r} \right) + \frac{R_{air} (\underline{J} \cdot \check{\gamma}_{ODT})^2}{Pc_p \rho_f \beta} + O(\Delta).$$

Thus,

$$\begin{aligned} \frac{1}{2} \frac{d\Delta r^2}{dt} &= \frac{R_{air}}{Pc_{p,\Delta}} \left[\left(r \sigma_T \frac{\partial T}{\partial r} \right)_{r+\frac{\Delta r}{2}} - \left(r \sigma_T \frac{\partial T}{\partial r} \right)_{r-\frac{\Delta r}{2}} \right] \\ &+ \frac{1}{2} \int_{\Delta r} \frac{R_{air} (\underline{J} \cdot \check{\gamma}_{ODT})^2}{Pc_p \rho_f \beta} dr^2 + O(\Delta). \end{aligned} \quad (\text{D.22})$$

- **Discretized divergence condition:**

$$\begin{aligned} \frac{\Delta r_i^{2,n+1} - \Delta r_i^{2,n}}{\Delta t} &= \frac{2R_{air}}{Pc_{p,i}^{n+1}} \left[\left(r^n \sigma_T^{n+1} \frac{\partial T^{n+1}}{\partial r^n} \right)_{i+\frac{1}{2}} - \left(r^n \sigma_T^{n+1} \frac{\partial T^{n+1}}{\partial r^n} \right)_{i-\frac{1}{2}} \right] \\ &+ \frac{R_{air} j_{2,i}^2}{Pc_{p,i}^{n+1} \rho_{f,i} \beta} \Delta r_i^{2,n} + O(\Delta). \end{aligned} \quad (\text{D.23})$$

- **Discretized mean pressure gradient constraint:** The pressure gradient constraint is the same as in the planar case, Eq. (D.12). The mean pressure gradient is either pre-defined or given by a pre-defined streamwise bulk mass flux constraint. Here, R is the radius of the ODT pipe domain,

$$\frac{\partial \bar{p}}{\partial x} \Delta t = \frac{\sum_i \left(\rho_i^{n+1} u_i^* \Delta r_i^{2,n+1} \right) - 2U_b \rho_b R^2}{\sum_i \Delta r_i^{2,n+1}}. \quad (\text{D.24})$$

D.1.3 Advancement algorithm

An overview of the advancement algorithm can be found in [72]. It is noted that the electric fields remain constant during the simulation. These are calculated beforehand with a method specified in appendix H. The electric fields play no role in the deterministic advancement scheme. In a coarse perspective, the advancement algorithm updates first the temperature and momentum of the flow (including optional bulk enthalpy correction in case of isothermal constant Dirichlet temperature boundary conditions). The fluid properties, as a function of the temperature (including the density) are updated next. This step is done in the simulations with the help of the open source software Cantera [99], using default libraries for air properties. Mass conservation is then enforced by calculating the new grid cell sizes in the numerical domain. Finally, the mean pressure gradient constraint is enforced.

D.2 S-ODT GOVERNING EQUATIONS

The model equations, Eqs. (3.71-3.74), are now evaluated by means of the S-ODT material derivative definition, Eqs. (3.81) and (3.82). Due to the way in which the eddy event implementation works in the S-ODT formulation used in this thesis, and in [72], two different streamwise velocity fields are obtained at the end of the stochastic events. The inconsistency is due to the mapping of the streamwise mass flux and the application of the kernel for the streamwise velocity component u . This produces a velocity u obtained from the kernel procedure, and a velocity u_D originated from the mapping of the streamwise mass flux, the latter according to the notation in [72]. u_D would be the equivalent of u_ψ in the notation of this thesis. However, it has already been clarified that there is no such velocity component. As such, the surge of u_D is a mere numerical artefact, as it is discussed in [72]. The harmonization of u_D and u takes place during the deterministic advancement scheme, for the cases where the flow does not exhibit a highly elliptic character. Otherwise, u and u_D remain as two different and independent contributions for the streamwise velocity. The notation u_D from [72] is used here in all of the following equations.

Due to the formulation of Eq. (3.82), a different treatment is required for the streamwise advancement of momentum, in order to conserve the total differential of u^2 . The method used here is explained in [72]. It is noted that, discretely, the approximation of Eq. (3.82) can be taken as,

$$\frac{1}{2} \frac{u^{2,n+1} - u^2}{\Delta x} = \frac{(u^{n+1} + u^n)}{2} \frac{u^{n+1} - u^n}{\Delta x} = u^{n+\frac{1}{2}} \frac{u^{n+1} - u^n}{\Delta x} = f(u). \quad (\text{D.25})$$

Here, n is a superindex for the streamwise position and $f(u)$ is the RHS of the S-ODT momentum equation, as per Eq. (3.73) in the planar case. This is, any method that produces a solution for the advancement of u^2 (that is, $u^{2,n+1}$) as an average of the solutions at the current and advanced streamwise positions can be used for the approximation of the streamwise derivative. In [72], the method used is an iterative method, which was developed in analogy to the approximation of square roots by the Babylonian method [125]. The method is a simplification of the general Newton's method. In the Babylonian method, if a is an approximation to \sqrt{N} , then the average $1/2(a + N/a)$ is a better approximation to \sqrt{N} [125]. In this way, the streamwise velocity component u can be computed in an iterative way at the next streamwise position.

For the cases where the flow exhibits a highly elliptic character, most notably the cases with variable density and a large EHD body force term, the nonconservative version of the formulation for u , Eq. (3.81), is used. This is also the formulation used for any other variable, $\psi \neq u$ in all S-ODT simulations, i.e.,

$$u \frac{d\psi}{dx} = u_D^n \frac{\psi^{n+1} - \psi^n}{\Delta x} = f(u). \quad (\text{D.26})$$

In the next set of discretized equations, the subindex i refers to the grid cell index and the superindex n refers to the discrete streamwise position index. A superindex $*$ indicates an intermediate streamwise position. Besides the streamwise momentum integration, the other momentum components and the temperature use a second order Crank-Nicolson streamwise integration method.

D.2.1 Cartesian coordinates

In all integral or integrated equations, $O(\Delta)$ is $O(\Delta y)$ if $\rho, c_p \neq \text{constant}$ or $O(\Delta) = 0$ otherwise. In all discretized equations, $O(\Delta)$ is $O(\Delta x, \Delta y)$ if $\rho \neq \text{constant}$ or $O(\Delta) = O[\Delta x, (\Delta y)^2]$ otherwise.

- **Momentum equation:**

$$\begin{aligned} \int_{\Delta y} u \frac{dV}{dx} dy = \frac{1}{\rho_\Delta} \left[\left(\mu \frac{\partial V}{\partial y} \right)_{y+\frac{\Delta y}{2}} - \left(\mu \frac{\partial V}{\partial y} \right)_{y-\frac{\Delta y}{2}} \right] \\ + \int_{\Delta y} \underline{g} \cdot \underline{\check{r}}_{vert} dy - \int_{\Delta y} \frac{1}{\rho_\Delta} \nabla \bar{p} \cdot \underline{\check{r}}_{str} dy + O(\Delta). \end{aligned} \quad (\text{D.27})$$

- **Discretized momentum equation:** for the streamwise component, an iterative integration to find u^2 is performed in the flow

simulations with a relatively low elliptic character, i.e., where the solution does not yield negative velocity values for u ,

$$\begin{aligned} \frac{u_i^{2,n,*} - u_{D,i}^n u_i^n}{\Delta x} \Delta y_i^n &= \frac{1}{\rho_i^n} \left[\left(\mu^n \frac{\partial u^{n,*}}{\partial y^n} \right)_{i+\frac{1}{2}} - \left(\mu^n \frac{\partial u^{n,*}}{\partial y^n} \right)_{i-\frac{1}{2}} \right] \\ &+ O(\Delta), \end{aligned} \quad (\text{D.28})$$

For the crosswise and spanwise velocity components ($k \in \{2, 3\}$), as well as the streamwise velocity component in the cases with a highly elliptic character ($k \in \{1, 2, 3\}$), a Crank-Nicolson integration method is used. No buoyant planar flows are evaluated in this thesis.

$$\begin{aligned} u_{D,i}^n \frac{u_{k,i}^{n,*} - u_{k,i}^n}{\Delta x} \Delta y_i^n &= \frac{1}{2\rho_i^n} \left[\mu_{i+\frac{1}{2}}^n \left(\frac{\partial u_k^{n,*}}{\partial y^n} + \frac{\partial u_k^n}{\partial y^n} \right)_{i+\frac{1}{2}} - \mu_{i-\frac{1}{2}}^n \left(\frac{\partial u_k^{n,*}}{\partial y^n} + \frac{\partial u_k^n}{\partial y^n} \right)_{i-\frac{1}{2}} \right] \\ &+ O(\Delta). \end{aligned} \quad (\text{D.29})$$

- **Temperature equation:**

$$\begin{aligned} \int_{\Delta y} u \frac{dT}{dx} dy &= \frac{1}{\rho_{\Delta} c_{p,\Delta}} \left[\left(\sigma_T \frac{\partial T}{\partial y} \right)_{y+\frac{\Delta y}{2}} - \left(\sigma_T \frac{\partial T}{\partial y} \right)_{y-\frac{\Delta y}{2}} \right] \\ &+ \int_{\Delta y} \frac{(J \cdot \check{\chi}_{ODT})^2}{\rho c_p \rho_f \beta} dy + O(\Delta). \end{aligned} \quad (\text{D.30})$$

- **Discretized temperature equation:** a Crank-Nicolson integration method is used.

$$\begin{aligned} u_{D,i}^n \frac{T_i^{n+1} - T_i^n}{\Delta x} \Delta y_i^n &= \frac{1}{2\rho_i^n c_{p,i}^n} \left[\sigma_{T,i+\frac{1}{2}}^n \left(\frac{\partial T^{n+1}}{\partial y^n} + \frac{\partial T^n}{\partial y^n} \right)_{i+\frac{1}{2}} - \sigma_{T,i-\frac{1}{2}}^n \left(\frac{\partial T^{n+1}}{\partial y^n} + \frac{\partial T^n}{\partial y^n} \right)_{i-\frac{1}{2}} \right] \\ &+ \frac{j_{2,i}^2}{\rho_i^n c_{p,i}^n \rho_{f,i} \beta} \Delta y_i^n + O(\Delta). \end{aligned} \quad (\text{D.31})$$

- **Divergence condition:** In analogy with Eq. (D.10),

$$\begin{aligned} u \frac{d\Delta y}{dx} &= \frac{R_{air}}{Pc_{p,\Delta}} \left[\left(\sigma_T \frac{\partial T}{\partial y} \right)_{y+\frac{\Delta y}{2}} - \left(\sigma_T \frac{\partial T}{\partial y} \right)_{y-\frac{\Delta y}{2}} \right] \\ &+ \int_{\Delta y} \frac{R_{air} (J \cdot \check{\chi}_{ODT})^2}{Pc_p \rho_f \beta} dy + O(\Delta). \end{aligned} \quad (\text{D.32})$$

- **Discretized divergence condition:**

$$\begin{aligned} \frac{\Delta y_i^{n+1} - \Delta y_i^n}{\Delta x} &= \frac{R_{air}}{P u_i^{n,*} c_{p,i}^{n+1}} \left[\left(\sigma_T^{n+1} \frac{\partial T^{n+1}}{\partial y^n} \right)_{i+\frac{1}{2}} - \left(\sigma_T^{n+1} \frac{\partial T^{n+1}}{\partial y^n} \right)_{i-\frac{1}{2}} \right] \\ &\quad + \frac{R_{air} j_{2,i}^2}{P u_i^{n,*} c_{p,i}^{n+1} \rho_{f,i} \beta} \Delta y_i^n + O(\Delta). \end{aligned} \quad (D.33)$$

- **Discretized mean pressure gradient constraint:** The procedure is the same as in the T-ODT formulation, Eqs. (D.12) and (D.13). In the nonconservative formulation cases, the pressure gradient constraint is imposed both on the u and u_D velocity components.

D.2.2 Cylindrical coordinates

The shear stress tensor divergence is given by Eq. (D.14) and (D.15). In all integral or integrated equations, $O(\Delta)$ is $O(\Delta r)$ if $\rho, c_p \neq \text{constant}$ or $O(\Delta) = 0$ otherwise. In all discretized equations, $O(\Delta)$ is $O(\Delta z, \Delta r)$ if $\rho \neq \text{constant}$ or $O(\Delta) = O[\Delta z, (\Delta r)^2]$.

- **Momentum equation:**

$$\begin{aligned} \frac{1}{2} \int_{\Delta r} u \frac{dV}{dz} dr^2 &= \frac{1}{\rho_\Delta} \left[\tau_{r+\frac{\Delta r}{2}} - \tau_{r-\frac{\Delta r}{2}} \right] + \frac{1}{2} \int_{\Delta r} \underline{g} \cdot \check{\tau}_{vert} dr^2 \\ &\quad - \frac{1}{2} \int_{\Delta r} \frac{1}{\rho_\Delta} \nabla \bar{p} \cdot \check{\tau}_{str} dr^2 + O(\Delta). \end{aligned} \quad (D.34)$$

- **Discretized momentum equation:** The sign of the gravity term is positive for downward flows, and negative for upward flows. In the conservative formulation for u , the corresponding discretization is,

$$\begin{aligned} \frac{u_i^{2,n,*} - u_{D,i}^n u_i^n}{\Delta z} \Delta r_i^{2,n} &= \frac{2}{\rho_i^n} \left[\left(r^n \mu^n \frac{\partial u^{n,*}}{\partial r^n} \right)_{i+\frac{1}{2}} - \left(r^n \mu^n \frac{\partial u^{n,*}}{\partial r^n} \right)_{i-\frac{1}{2}} \right] \\ &\quad \pm g \Delta r_i^{2,n} + O(\Delta), \end{aligned} \quad (D.35)$$

For the radial and tangential velocity components ($k \in \{2, 3\}$), as well as the streamwise velocity component in the nonconservative formulation ($k \in \{1, 2, 3\}$), the corresponding discretization is,

$$\begin{aligned}
 & u_{D,i}^n \frac{u_{k,i}^{n,*} - u_{k,i}^n}{\Delta z} \Delta r_i^{2,n} \\
 &= \frac{1}{\rho_i^n} \left\{ r_{i+\frac{1}{2}}^n \mu_{i+\frac{1}{2}}^n \left[\left(\frac{\partial u_k^{n,*}}{\partial r^n} + \frac{\partial u_k^n}{\partial r^n} \right)_{i+\frac{1}{2}} \right] \right. \\
 &\quad \left. - r_{i-\frac{1}{2}}^n \mu_{i-\frac{1}{2}}^n \left[\left(\frac{\partial u_k^{n,*}}{\partial r^n} + \frac{\partial u_k^n}{\partial r^n} \right)_{i-\frac{1}{2}} \right] \right\} \pm g \Delta r_i^{2,n} + O(\Delta), \quad k = 1.
 \end{aligned} \tag{D.36}$$

$$\begin{aligned}
 & u_{D,i}^n \frac{u_{k,i}^{n,*} - u_{k,i}^n}{\Delta z} \Delta r_i^{2,n} \\
 &= \frac{1}{\rho_i^n} \left\{ r_{i+\frac{1}{2}}^n \mu_{i+\frac{1}{2}}^n \left[\left(\frac{\partial u_k^{n,*}}{\partial r^n} + \frac{\partial u_k^n}{\partial r^n} \right)_{i+\frac{1}{2}} - \left(\frac{u_{k,i}^{n,*}}{r_i^n} + \frac{u_{k,i}^n}{r_i^n} \right) \right] \right. \\
 &\quad \left. - r_{i-\frac{1}{2}}^n \mu_{i-\frac{1}{2}}^n \left[\left(\frac{\partial u_k^{n,*}}{\partial r^n} + \frac{\partial u_k^n}{\partial r^n} \right)_{i-\frac{1}{2}} - \left(\frac{u_{k,i}^{n,*}}{r_i^n} + \frac{u_{k,i}^n}{r_i^n} \right) \right] \right\} \\
 &\quad + O(\Delta), \quad k \in \{2, 3\}.
 \end{aligned} \tag{D.37}$$

• **Temperature equation:**

$$\begin{aligned}
 \frac{1}{2} \int_{\Delta r} u \frac{dT}{dz} dr^2 &= \frac{1}{\rho_{\Delta} c_{p,\Delta}} \left[\left(r \sigma_T \frac{\partial T}{\partial r} \right)_{r+\frac{\Delta r}{2}} - \left(r \sigma_T \frac{\partial T}{\partial r} \right)_{r-\frac{\Delta r}{2}} \right] \\
 &\quad + \frac{1}{2} \int_{\Delta r} \frac{(J \cdot \check{\chi}_{ODT})^2}{\rho c_p \rho_f \beta} dr^2 + O(\Delta).
 \end{aligned} \tag{D.38}$$

• **Discretized temperature equation:**

$$\begin{aligned}
 u_{D,i}^n \frac{T_i^{n+1} - T_i^n}{\Delta z} \Delta r_i^{2,n} &= \frac{1}{\rho_i^n c_{p,i}^n} \left[r_{i+\frac{1}{2}}^n \sigma_{T,i+\frac{1}{2}}^n \left(\frac{\partial T^{n+1}}{\partial r^n} + \frac{\partial T^n}{\partial r^n} \right)_{i+\frac{1}{2}} \right. \\
 &\quad \left. - r_{i-\frac{1}{2}}^n \sigma_{T,i-\frac{1}{2}}^n \left(\frac{\partial T^{n+1}}{\partial r^n} + \frac{\partial T^n}{\partial r^n} \right)_{i-\frac{1}{2}} \right] \\
 &\quad + \frac{j_{2,i}^2}{\rho_i^n c_{p,i}^n \rho_{f,i} \beta} \Delta r_i^{2,n} + O(\Delta).
 \end{aligned} \tag{D.39}$$

- **Divergence condition:** Due to properties of the ∇ operator for cylindrical coordinates, the cylindrical analogous of the planar equation using $v_\psi = u dr/dx$ is,

$$\frac{1}{r} \frac{\partial}{\partial r} \left(u r \frac{dr}{dz} \right) = \frac{1}{r} \frac{\partial}{\partial r} \left(\frac{r R_{air} \sigma_T}{P c_{p,\Delta}} \frac{\partial T}{\partial r} \right) + \frac{R_{air} (J \cdot \check{\chi}_{ODT})^2}{P c_p \rho_f \beta} + O(\Delta).$$

Thus,

$$\begin{aligned} \frac{u}{2} \frac{d\Delta r^2}{dz} &= \frac{R_{air}}{Pc_{p,\Delta}} \left[\left(r\sigma_T \frac{\partial T}{\partial r} \right)_{r+\frac{\Delta r}{2}} - \left(r\sigma_T \frac{\partial T}{\partial r} \right)_{r-\frac{\Delta r}{2}} \right] \\ &+ \frac{1}{2} \int_{\Delta r} \frac{R_{air} (J \cdot \check{\gamma}_{ODT})^2}{Pc_p \rho_f \beta} dr^2 + O(\Delta). \end{aligned} \quad (\text{D.40})$$

- **Discretized divergence condition:**

$$\begin{aligned} &\frac{\Delta r_i^{2,n+1} - \Delta r_i^{2,n}}{\Delta z} \\ &= \frac{2R_{air}}{Pu_i^{n,*} c_{p,i}^{n+1}} \left[\left(r^n \sigma_T^{n+1} \frac{\partial T^{n+1}}{\partial r^n} \right)_{i+\frac{1}{2}} - \left(r\sigma_T^{n+1} \frac{\partial T^{n+1}}{\partial r^n} \right)_{i-\frac{1}{2}} \right] \\ &+ \frac{R_{air} j_{2,i}^2}{Pu_i^{n,*} c_{p,i}^{n+1} \rho_{f,i} \beta} \Delta r_i^{2,n} + O(\Delta). \end{aligned} \quad (\text{D.41})$$

- **Discretized mean pressure gradient constraint:** The procedure is the same as in the T-ODT formulation, Eqs. (D.12) and (D.24). In the nonconservative formulation cases, the constraint is imposed on both the u and u_D velocity components.

D.2.3 Advancement algorithm

An overview of the advancement algorithm can be found in [72]. It is noted that the electric fields remain constant during the simulation. These are calculated beforehand with a method specified in appendix H. The electric fields play no role in the deterministic advancement scheme. The advancement algorithm updates first the streamwise momentum of the flow, and then the other momentum components, as well as the temperature. The fluid properties, as a function of the temperature (including the density) are updated next. This step is done in the simulations with the help of the open source software Cantera [99], using default libraries for air properties. Mass conservation is then enforced by calculating the new grid cell sizes in the numerical domain. Finally, the mean pressure gradient constraint is enforced.

AVERAGE OPERATORS

E.1 TIME AND STREAMWISE AVERAGES

The time-average operator is defined for any quantity (scalar or vector) ψ as,

$$\bar{\psi} = \frac{1}{\Delta t_{avg}} \int_{t - \frac{\Delta t_{avg}}{2}}^{t + \frac{\Delta t_{avg}}{2}} \psi dt, \quad (\text{E.1})$$

where Δt_{avg} is a sufficiently large time period. This average operator is used in the T-ODT formulation.

Conversely, the streamwise-average operator is defined for ψ in a planar coordinate system as,

$$\bar{\psi} = \frac{1}{\Delta x_{avg}} \int_{x - \frac{\Delta x_{avg}}{2}}^{x + \frac{\Delta x_{avg}}{2}} \psi dx. \quad (\text{E.2})$$

The notation used is the same as for the time average operator. Given that the streamwise operator will be used exclusively for the S-ODT formulation, there is no conflict in the notation. For cylindrical coordinates, the streamwise direction is z . Therefore,

$$\bar{\psi} = \frac{1}{\Delta z_{avg}} \int_{z - \frac{\Delta z_{avg}}{2}}^{z + \frac{\Delta z_{avg}}{2}} \psi dz. \quad (\text{E.3})$$

E.2 ENSEMBLE AVERAGE

The ensemble average $\langle \psi \rangle$ is a generalization for a time or streamwise average of any scalar or vector ψ . The ensemble average is defined as,

$$\langle \psi \rangle = \frac{1}{N} \sum_n \psi \Delta n, \quad (\text{E.4})$$

where Δn may refer either to a time or streamwise step, Δt or Δx (or Δz), respectively, and N to an averaging period in terms of time or streamwise advancement. In the most general case, $\Delta n = 1$ refers to an ensemble realization and $N = N_{ens}$ refers to the total number of ensemble members involved in the average operation. The ensemble average $\langle \psi \rangle$ is related to the quantity ψ by the decomposition,

$$\psi = \langle \psi \rangle + \psi'. \quad (\text{E.5})$$

In cases where a generalized ensemble realization and an additional time or streamwise averaging window is implied, the notation $\langle \bar{\psi} \rangle$ is used.

The RMS value for a scalar ψ is defined, according to Eq. (E.5) as,

$$\psi_{RMS} = \sqrt{\langle \psi' \psi' \rangle} = \sqrt{\langle \psi^2 \rangle - \langle \psi \rangle^2}. \quad (\text{E.6})$$

Likewise, the covariance between two scalars, e.g. ψ and θ is defined as,

$$\langle \psi' \theta' \rangle = \langle \psi \theta \rangle - \langle \psi \rangle \langle \theta \rangle. \quad (\text{E.7})$$

Along with the definition of the RMS by Eq. (E.6), and of the ensemble average decomposition by Eq. (E.5), another property of the ensemble average operator is,

$$\langle \psi' \rangle = 0. \quad (\text{E.8})$$

Due to this reason, the ensemble average operator is also known as a Reynolds average operator.

E.3 FAVRE AVERAGE

A special type of ensemble average is the Favre average. For variable density flows, the Favre average of a tensor ψ is defined as,

$$\tilde{\psi} = \frac{\langle \rho \psi \rangle}{\langle \rho \rangle}. \quad (\text{E.9})$$

The counterpart of Eq. (E.5) for the Favre average is,

$$\psi = \tilde{\psi} + \psi''. \quad (\text{E.10})$$

Similarly, the calculation of RMS values and covariances in the Favre average case, is given by,

$$\widetilde{\psi_{RMS}} = \sqrt{\widetilde{\psi'' \psi''}} = \sqrt{\widetilde{\psi^2} - \tilde{\psi}^2}. \quad (\text{E.11})$$

Likewise, the covariance between two scalars, e.g. ψ and θ is defined as,

$$\widetilde{\psi'' \theta''} = \tilde{\psi} \tilde{\theta} - \tilde{\psi} \tilde{\theta}. \quad (\text{E.12})$$

In analogy to the ensemble average, the fundamental property of the Favre average is,

$$\widetilde{\psi''} = 0. \quad (\text{E.13})$$

Also, the ensemble (Reynolds) and Favre averages are related by [126],

$$\langle \psi \rangle - \tilde{\psi} = \psi'' - \psi' = \langle \psi'' \rangle = -\frac{\langle \rho' \psi'' \rangle}{\langle \rho \rangle} = -\frac{\langle \rho' \psi' \rangle}{\langle \rho \rangle}. \quad (\text{E.14})$$

And, as a consequence,

$$\langle \psi' \theta'' \rangle = \langle \psi' \theta' \rangle. \quad (\text{E.15})$$

MEAN FLOW AND TKE EQUATIONS

In order to discuss the form of the Reynolds shear stress profiles, as well as the form of the TKE budget profiles, it is necessary to derive the ODT TKE equation. This is done next for incompressible constant property and variable density flow.

F.1 GENERALIZED INCOMPRESSIBLE CONSTANT PROPERTY MEAN MOMENTUM AND TKE EQUATIONS

In order to derive the vector form of the incompressible TKE equation, according to the average and fluctuating quantities relation, Eq. (E.5), while also considering Eq. (E.7), it is necessary to subtract the kinetic energy of the mean flow from the average kinetic energy [32]. This is, at least considering the partial time derivative of the TKE,

$$\rho \frac{\partial k}{\partial t} = \frac{\rho}{2} \frac{\partial \langle \underline{V}' \cdot \underline{V}' \rangle}{\partial t} = \rho \left(\frac{\partial \langle \zeta_{kin} \rangle}{\partial t} - \langle \underline{V} \rangle \cdot \frac{\partial \langle \underline{V} \rangle}{\partial t} \right). \quad (\text{F.1})$$

where k is the Turbulent Kinetic Energy (TKE),

$$k = \frac{1}{2} \langle \underline{V}' \cdot \underline{V}' \rangle. \quad (\text{F.2})$$

Note that this is a simplification of the more general variable density case,

$$k = \frac{1}{2} \widetilde{\underline{V}'' \cdot \underline{V}''}. \quad (\text{F.3})$$

Note that although the average operator is commutative with partial derivatives, it is not commutative with the Lagrangian material derivative operator. That is,

$$\frac{D \langle \psi \rangle}{Dt} = \frac{\partial \langle \psi \rangle}{\partial t} + (\underline{V} \cdot \nabla) \langle \psi \rangle, \quad (\text{F.4})$$

however, due to the relation given by Eq. (E.7),

$$\left\langle \frac{D\psi}{Dt} \right\rangle = \frac{\partial \langle \psi \rangle}{\partial t} + (\langle \underline{V} \rangle \cdot \nabla) \langle \psi \rangle + \langle (\underline{V}' \cdot \nabla) \psi' \rangle. \quad (\text{F.5})$$

Therefore, the average material derivative operator of a tensor ψ is defined as,

$$\frac{\langle D \rangle \psi}{\langle D \rangle t} = \frac{\partial \psi}{\partial t} + (\langle \underline{V} \rangle \cdot \nabla) \psi. \quad (\text{F.6})$$

The first task is then to find the average momentum equation. This must be done in an Eulerian framework. Consider the average of the Eulerian version of the momentum equation, Eq. (A.11), with the definition of the shear stress tensor, Eq. (2.46), the divergence condition for incompressible and constant property flow, Eq. (1.2), and assuming constant fluid properties, as well as a constant electric current density vector per Eq. (3.64),

$$\rho \frac{\langle \mathbf{D} \rangle \langle \underline{\mathbf{V}} \rangle}{\langle \mathbf{D} \rangle t} = \rho \frac{\partial \langle \underline{\mathbf{V}} \rangle}{\partial t} + \rho (\langle \underline{\mathbf{V}} \rangle \cdot \nabla) \langle \underline{\mathbf{V}} \rangle = -\rho \nabla \cdot \langle \underline{\mathbf{V}}' \circ \underline{\mathbf{V}}' \rangle - \nabla \langle p \rangle + \mu \nabla^2 \langle \underline{\mathbf{V}} \rangle + \rho \underline{\mathbf{g}} + \frac{\underline{\mathbf{J}}}{\beta}. \quad (\text{F.7})$$

Here, the definition given by Eq. (F.6) was used. The average kinetic energy equation, $\zeta_{kin} = (\underline{\mathbf{V}} \cdot \underline{\mathbf{V}})/2$, is obtained by averaging Eq. (2.53),

$$\begin{aligned} \rho \frac{\langle \mathbf{D} \rangle \langle \zeta_{kin} \rangle}{\langle \mathbf{D} \rangle t} &= \rho \frac{\partial \langle \zeta_{kin} \rangle}{\partial t} + \rho (\langle \underline{\mathbf{V}} \rangle \cdot \nabla) \langle \zeta_{kin} \rangle = -\frac{\rho}{2} \nabla \cdot \langle \underline{\mathbf{V}}' \circ \underline{\mathbf{V}}' \cdot \underline{\mathbf{V}}' \rangle \\ &\quad - \rho (\langle \underline{\mathbf{V}} \rangle \cdot \nabla) \langle \underline{\mathbf{V}}' \circ \underline{\mathbf{V}}' \rangle + \mathcal{P}_{TKE} - \nabla \cdot (\langle p \rangle \langle \underline{\mathbf{V}} \rangle) - \nabla \cdot \langle p' \underline{\mathbf{V}}' \rangle \\ &\quad + \mu \nabla^2 \langle \zeta_{kin} \rangle - \epsilon_{\langle \zeta_{kin} \rangle} + \rho \langle \underline{\mathbf{V}} \rangle \cdot \underline{\mathbf{g}} + \langle \underline{\mathbf{V}} \rangle \cdot \frac{\underline{\mathbf{J}}}{\beta}. \end{aligned} \quad (\text{F.8})$$

Subtracting then the scalar product of $\langle \underline{\mathbf{V}} \rangle$ with Eq. (F.7) from Eq. (F.8), leads to the generalized incompressible TKE equation [32],

$$\rho \frac{\langle \mathbf{D} \rangle k}{\langle \mathbf{D} \rangle t} = \rho \frac{\partial k}{\partial t} + \rho \langle \underline{\mathbf{V}} \rangle \cdot \nabla k = -\nabla \cdot \left(\frac{\rho}{2} \langle \underline{\mathbf{V}}' \cdot \underline{\mathbf{V}}' \circ \underline{\mathbf{V}}' \rangle + \langle \underline{\mathbf{V}}' p' \rangle \right) + \mu \nabla^2 k + \mathcal{P}_{TKE} - \epsilon_{TKE}. \quad (\text{F.9})$$

$\epsilon_{\langle \zeta_{kin} \rangle}$ is the viscous dissipation of average kinetic energy,

$$\epsilon_{\langle \zeta_{kin} \rangle} = \mu \langle \nabla \circ \underline{\mathbf{V}} : \nabla \circ \underline{\mathbf{V}} \rangle. \quad (\text{F.10})$$

Also, \mathcal{P}_{TKE} is the production of TKE, defined as,

$$\mathcal{P}_{TKE} = -\rho \langle \underline{\mathbf{V}}' \circ \underline{\mathbf{V}}' \rangle : \nabla \circ \langle \underline{\mathbf{V}} \rangle, \quad (\text{F.11})$$

while ϵ_{TKE} is the viscous dissipation of TKE, defined as,

$$\epsilon_{TKE} = \mu \langle \nabla \circ \underline{\mathbf{V}}' : \nabla \circ \underline{\mathbf{V}}' \rangle. \quad (\text{F.12})$$

F.2 ODT INCOMPRESSIBLE CONSTANT PROPERTY MEAN MOMENTUM AND TKE EQUATIONS

F.2.1 Planar ODT mean flow and TKE equations

The explicit representation of the mean flow in Cartesian coordinates, Eq. (F.7) is,

$$\rho \frac{\langle \mathbf{D} \rangle \langle u_k \rangle}{\langle \mathbf{D} \rangle t} = -\rho \sum_{l=1}^3 \frac{\partial \langle u_l' u_k' \rangle}{\partial x_l} - \frac{\partial \langle p \rangle}{\partial x_k} + \mu \sum_{l=1}^3 \frac{\partial^2 \langle u_k \rangle}{\partial x_l^2} + \frac{j_k}{\beta}. \quad (\text{F.13})$$

The gravity term has been neglected in this expression. Neither buoyant horizontal channels nor vertical channels are evaluated in this thesis.

Likewise, the explicit representation of the TKE in Cartesian coordinates, Eq. (F.9), is,

$$\rho \frac{\langle D \rangle k}{\langle D \rangle t} = \mu \sum_{l=1}^3 \frac{\partial^2 k}{\partial x_l^2} - \frac{\rho}{2} \sum_{k=1}^3 \sum_{l=1}^3 \frac{\partial \langle u'_l u'_k u'_l \rangle}{\partial x_l} - \sum_{k=1}^3 \frac{\partial \langle u'_k p' \rangle}{\partial x_k} + \mathcal{P}_{TKE} - \epsilon_{TKE}. \quad (\text{F.14})$$

The cartesian representation for \mathcal{P}_{TKE} and ϵ_{TKE} can be found in appendix G.

In order to derive the ODT mean flow momentum equation, simply average the planar ODT momentum equation, substituting the turbulent advection term, i.e., the Reynolds shear stress, by the net average effect of the stochastic eddy events, $\langle M_k + \mathcal{T}_k + \mathcal{S}_k \rangle$, where M_k , \mathcal{T}_k and \mathcal{S}_k represent the effects of the mappings, the turbulent transport and the pressure scrambling on the velocity component k , respectively [75].

$$\rho \frac{\langle D \rangle \langle u_k \rangle}{\langle D \rangle t} = \left[-\rho \frac{\partial \langle u'_k u'_1 \rangle}{\partial x} \right]_{S-ODT} + \rho \langle M_k + \mathcal{T}_k + \mathcal{S}_k \rangle - \frac{\partial \bar{p}}{\partial x} \delta_{1k} + \mu \frac{\partial^2 \langle u_k \rangle}{\partial y^2}. \quad (\text{F.15})$$

$\langle M_k + \mathcal{T}_k + \mathcal{S}_k \rangle$ is the representation of the turbulent advection of the velocity component k by v_ψ . It is the result of the change in the profiles due to implementation of eddy events [75]. Due to the measure preserving property of the map, $\int M_k dy = 0$ per definition. Furthermore, the transport term also integrates to zero, $\int \mathcal{T}_k dy = 0$ due to the zero bulk contribution to momentum due to transport [75]. In constant density, according to Eq. (3.25), the only kernel function implemented in ODT is K_{ODT} , which also integrates to zero $\int K_{ODT} dy = 0$. Therefore, no momentum sources are implemented during eddy events, and as a consequence, the integral of \mathcal{S}_k is also zero, i.e., $\int \mathcal{S}_k dy = 0$. Due to the absence of a pressure scrambling contribution in Eq. (F.13), \mathcal{S}_k is defined as zero for every y position. This implies the presence of a single transport term agreeing with the mapping process and the redistribution of kinetic energy among velocity components, $\partial \mathcal{R}_k / \partial y$,

$$\langle M_k + \mathcal{T}_k \rangle = \frac{\partial \mathcal{R}_k}{\partial y}.$$

There is no direct representation of the pressure gradient term in ODT. Its only role is in the redistribution of kinetic energy among velocity components, as dictated by the Poisson equation of an incompressible and constant property flow (enforcement of the divergence condition for the velocity field). The pressure gradient term can, thus, be omitted

from a momentum analysis. Regarding the EHD body force term which may also be present in the flow, as per Eq. (F.13), the analysis regarding the representation of the body force as part of the Maxwell electroquasistatic stress tensor in chapter 6 is recalled. For the 1-D electric current density vectors demanded in the wall-bounded flows evaluated with ODT, the only contribution of the EHD body force is as an irrotational current contribution. The irrotational contribution is then assumed as part of a modified pressure gradient. Thus, the electric current density term can also be omitted from the ongoing analysis. Comparing then Eq. (F.15) and (F.13), it is then deduced that,

$$\langle M_k + \mathcal{T}_k \rangle = \frac{\partial \mathcal{R}_k}{\partial y} = -\frac{\partial \langle u'_k v'_\psi \rangle}{\partial y}. \quad (\text{F.16})$$

The definition of the average material derivative in ODT needs to be interpreted according to the type of formulation, as detailed in chapter 3. This is the reason for the appearance of the streamwise Reynolds shear stress in the S-ODT formulation in Eq. (F.15) [62]. The latter term, however, is zero for fully developed hydrodynamic boundary layers (statistically streamwise homogeneous flows)

In order to derive the ODT TKE equation, follow the same procedure given by Eq. (F.1). A detailed derivation can be found in [62, 75],

$$\begin{aligned} \rho \frac{\langle \text{D} \rangle k}{\langle \text{D} \rangle t} = & \mu \frac{\partial^2 k}{\partial y^2} + \left\{ \left[-\frac{\rho}{2} \frac{\partial}{\partial x} \left(\sum_{k=1}^3 \langle u'_1 u'_k u'_k \rangle \right) \right]_{S-ODT} \right. \\ & \left. + \rho \sum_{k=1}^3 \left[\frac{\partial}{\partial y} \left(\frac{\mathcal{R}_{kk}}{2} - \langle u_k \rangle \mathcal{R}_k \right) + \frac{\langle \mathcal{S}_{kk} \rangle}{2} \right] \right\} \\ & + \mathcal{P}_{TKE,ODT} - \epsilon_{TKE,ODT}. \end{aligned} \quad (\text{F.17})$$

\mathcal{R}_{kk} is the bulk effect of the turbulent transport due to stochastic eddies [75], i.e.,

$$\langle M_{kk} + \mathcal{T}_{kk} \rangle = \frac{\partial \mathcal{R}_{kk}}{\partial y}. \quad (\text{F.18})$$

$\langle \mathcal{S}_{kk} \rangle$ is the ODT quantity representing the pressure strain contribution to the TKE [75]. \mathcal{S}_{kk} can not be evaluated directly. However, its sum across k corresponds to the transfer of potential into kinetic energy during eddy events. This transfer prevents the strict conservation of kinetic energy among velocity components. For flows without EHD body forces, thus, $\mathcal{S}_{kk} = 0$, as in [75]. In general, the TKE transport and budget terms M_{kk} , \mathcal{T}_{kk} and \mathcal{S}_{kk} are obtained due to changes in the kinetic energy profiles as in [75],

$$\begin{aligned} M_{kk} + \mathcal{T}_{kk} + \mathcal{S}_{kk} &= 2u_k (M_k + \mathcal{T}_k + \mathcal{S}_k) \\ &= 2u_k \frac{\Delta u_k}{\Delta t} \Bigg|_{\text{stoch. part}} = \frac{\Delta u_k^2}{\Delta t} \Bigg|_{\text{stoch. part}}. \end{aligned} \quad (\text{F.19})$$

Δt corresponds to the catchup diffusion time step associated to the implementation of an eddy event. The change in the profile can also be counted as zero if no eddy was implemented in a given deterministic advancement step. The definition of the ODT TKE production and dissipation terms, $\mathcal{P}_{TKE,ODT}$ and $\epsilon_{TKE,ODT}$, from Eq. (F.17), can be found in appendix G.

F.2.2 Cylindrical ODT mean flow and TKE equations

The explicit representation of the mean flow in cylindrical coordinates, Eq. (F.7), is different for the streamwise momentum component in comparison to the radial and circumferential component. This is due to the distinctive component-wise representation of the operator ∇ in cylindrical coordinates [127]. Assuming that gravity acts in streamwise direction, the streamwise, radial and circumferential mean momentum components are, respectively,

$$\begin{aligned} \rho \frac{\langle D \rangle \langle u \rangle}{\langle D \rangle t} = & -\rho \left(\frac{\partial \langle u'u' \rangle}{\partial z} + \frac{1}{r} \frac{\partial (r \langle u'v' \rangle)}{\partial r} + \frac{1}{r} \frac{\partial \langle u'w' \rangle}{\partial \theta} \right) - \frac{\partial \langle p \rangle}{\partial z} \\ & + \mu \left[\frac{\partial^2 \langle u \rangle}{\partial z^2} + \frac{1}{r} \frac{\partial}{\partial r} \left(r \frac{\partial \langle u \rangle}{\partial r} \right) + \frac{1}{r^2} \frac{\partial^2 \langle u \rangle}{\partial \theta^2} \right] - \rho g + \frac{j_1}{\beta}, \end{aligned} \quad (\text{F.20})$$

$$\begin{aligned} \rho \frac{\langle D \rangle \langle v \rangle}{\langle D \rangle t} = & -\rho \left[\frac{\partial \langle v'u' \rangle}{\partial z} + \frac{1}{r} \frac{\partial (r \langle v'v' \rangle)}{\partial r} + \frac{1}{r} \frac{\partial \langle v'w' \rangle}{\partial \theta} - \frac{\langle w'w' \rangle}{r} \right] - \frac{\partial \langle p \rangle}{\partial r} \\ & + \mu \left[\frac{\partial^2 \langle v \rangle}{\partial z^2} + \frac{1}{r} \frac{\partial}{\partial r} \left(r \frac{\partial \langle v \rangle}{\partial r} \right) + \frac{1}{r^2} \frac{\partial^2 \langle v \rangle}{\partial \theta^2} - \frac{\langle v \rangle}{r^2} - \frac{2}{r^2} \frac{\partial \langle w \rangle}{\partial \theta} \right] \\ & + \frac{j_2}{\beta}, \end{aligned} \quad (\text{F.21})$$

$$\begin{aligned} \rho \frac{\langle D \rangle \langle w \rangle}{\langle D \rangle t} = & -\rho \left[\frac{\partial \langle w'u' \rangle}{\partial z} + \frac{1}{r} \frac{\partial (r \langle w'v' \rangle)}{\partial r} + \frac{1}{r} \frac{\partial \langle w'w' \rangle}{\partial \theta} + \frac{\langle v'w' \rangle}{r} \right] \\ & + \mu \left[\frac{\partial^2 \langle w \rangle}{\partial z^2} + \frac{1}{r} \frac{\partial}{\partial r} \left(r \frac{\partial \langle w \rangle}{\partial r} \right) + \frac{1}{r^2} \frac{\partial^2 \langle w \rangle}{\partial \theta^2} - \frac{\langle w \rangle}{r^2} + \frac{2}{r^2} \frac{\partial \langle v \rangle}{\partial \theta} \right] \\ & - \frac{1}{r} \frac{\partial \langle p \rangle}{\partial \theta} + \frac{j_3}{\beta}. \end{aligned} \quad (\text{F.22})$$

The explicit representation of the TKE in cylindrical coordinates, Eq. (F.9), is,

$$\begin{aligned} \rho \frac{\langle \mathbf{D} \rangle k}{\langle \mathbf{D} \rangle t} = & \mu \left[\frac{\partial^2 k}{\partial z^2} + \frac{1}{r} \frac{\partial}{\partial r} \left(r \frac{\partial k}{\partial r} \right) + \frac{1}{r^2} \frac{\partial^2 k}{\partial \theta^2} \right] \\ & - \left(\frac{\partial \langle u' p' \rangle}{\partial z} + \frac{1}{r} \frac{\partial (r \langle v' p' \rangle)}{\partial r} + \frac{1}{r} \frac{\partial \langle w' p' \rangle}{\partial \theta} \right) \\ & - \frac{\rho}{2} \left[\frac{\partial}{\partial z} \left(\sum_{k=1}^3 \langle u'_k u'_k u' \rangle \right) + \frac{1}{r} \frac{\partial}{\partial r} \left(r \sum_{k=1}^3 \langle u'_k u'_k v' \rangle \right) \right. \\ & \left. + \frac{1}{r} \frac{\partial}{\partial \theta} \left(\sum_{k=1}^3 \langle u'_k u'_k w' \rangle \right) \right] + \mathcal{P}_{TKE} - \epsilon_{TKE}. \end{aligned} \quad (\text{F.23})$$

The cylindrical representation for \mathcal{P}_{TKE} and ϵ_{TKE} can be found in appendix G.

In order to derive the ODT mean flow momentum equation, average the cylindrical ODT momentum equation, substituting the turbulent advection term, i.e., the Reynolds shear stress, by the net average effect of the stochastic eddy events, $\langle M_k + \mathcal{T}_k + \mathcal{S}_k \rangle$ [75]. As in the generalized equation, the distinct component-wise representation of the shear stress tensor divergence results in different momentum equations for the streamwise, radial and circumferential velocity components,

$$\begin{aligned} \rho \frac{\langle \mathbf{D} \rangle \langle u \rangle}{\langle \mathbf{D} \rangle t} = & \left[-\rho \frac{\partial \langle u' u' \rangle}{\partial z} \right]_{S-ODT} + \rho \langle M_1 + \mathcal{T}_1 + \mathcal{S}_1 \rangle - \frac{\partial \bar{p}}{\partial z} \\ & + \mu \frac{1}{r} \frac{\partial}{\partial r} \left(r \frac{\partial \langle u \rangle}{\partial r} \right) - \rho g, \end{aligned} \quad (\text{F.24})$$

$$\begin{aligned} \rho \frac{\langle \mathbf{D} \rangle \langle v \rangle}{\langle \mathbf{D} \rangle t} = & \left[-\rho \frac{\partial \langle v' u' \rangle}{\partial z} \right]_{S-ODT} + \rho \langle M_2 + \mathcal{T}_2 + \mathcal{S}_2 \rangle \\ & + \mu \left[\frac{1}{r} \frac{\partial}{\partial r} \left(r \frac{\partial \langle v \rangle}{\partial r} \right) - \frac{\langle v \rangle}{r^2} \right], \end{aligned} \quad (\text{F.25})$$

$$\begin{aligned} \rho \frac{\langle \mathbf{D} \rangle \langle w \rangle}{\langle \mathbf{D} \rangle t} = & \left[-\rho \frac{\partial \langle w' u' \rangle}{\partial z} \right]_{S-ODT} + \rho \langle M_3 + \mathcal{T}_3 + \mathcal{S}_3 \rangle \\ & + \mu \left[\frac{1}{r} \frac{\partial}{\partial r} \left(r \frac{\partial \langle w \rangle}{\partial r} \right) - \frac{\langle w \rangle}{r^2} \right]. \end{aligned} \quad (\text{F.26})$$

The considerations for M_k , \mathcal{T}_k and \mathcal{S}_k from the planar case also hold in the cylindrical case. Thus, the crosswise Reynolds shear stress is, in this case,

$$\langle M_k + \mathcal{T}_k \rangle = -\frac{1}{r} \frac{\partial \left(r \langle u'_k v'_\psi \rangle \right)}{\partial r} = \frac{1}{r} \frac{\partial (r \mathcal{R}_k)}{\partial r}. \quad (\text{F.27})$$

As before, $\langle M_k + \mathcal{T}_k + \mathcal{S}_k \rangle$ is evaluated by the changes in the velocity profile k due to eddies [75] (recalling that $\mathcal{S}_k = 0$). Also, as in the planar

case, the material derivative is interpreted differently, depending on the type of ODT formulation used, thus explaining the presence of the streamwise Reynolds shear stress in S-ODT. The streamwise Reynolds shear stress is zero for fully developed hydrodynamic boundary layers (statistically streamwise homogeneous flows).

In order to derive the ODT TKE equation, the procedure is the same as in the planar case. The detailed derivation can be found in [91],

$$\begin{aligned} \rho \frac{\langle D \rangle k}{\langle D \rangle t} = & \mu \frac{1}{r} \frac{\partial}{\partial r} \left(r \frac{\partial k}{\partial r} \right) + \left\{ \left[-\frac{\rho}{2} \frac{\partial}{\partial z} \left(\sum_{k=1}^3 \langle u'_k u'_k u'_1 \rangle \right) \right]_{S-ODT} \right. \\ & \left. + \rho \sum_{k=1}^3 \left\{ \frac{1}{r} \frac{\partial}{\partial r} \left[r \left(\frac{\mathcal{R}_{kk}}{2} - \langle u_k \rangle \mathcal{R}_k \right) \right] + \frac{\langle \mathcal{S}_{kk} \rangle}{2} \right\} \right\} \quad (\text{F.28}) \\ & + \mathcal{P}_{TKE,ODT} - \epsilon_{TKE,ODT}. \end{aligned}$$

As before, Eq. (F.19) holds. \mathcal{S}_{kk} can not be determined directly, yet its sum across k corresponds to the transfer of potential energy into kinetic energy during an eddy event. An equivalent definition for \mathcal{R}_{kk} also holds,

$$\langle M_{kk} + \mathcal{T}_{kk} \rangle = \frac{1}{r} \frac{\partial (r \mathcal{R}_{kk})}{\partial r}. \quad (\text{F.29})$$

The definition of the ODT TKE production and dissipation terms, $\mathcal{P}_{TKE,ODT}$ and $\epsilon_{TKE,ODT}$, can be found in appendix G.

F.3 GENERALIZED VARIABLE DENSITY MEAN FLOW AND TKE EQUATIONS

As before, first the non-commutativity of the average operator with the material derivative operator is noted. This time, consider the ensemble average of both the density (which is variable now) and the material derivative operator,

$$\left\langle \rho \frac{D\psi}{Dt} \right\rangle = \left\langle \rho \frac{\partial \psi}{\partial t} \right\rangle + \left\langle \rho (\underline{V} \cdot \nabla) \psi \right\rangle.$$

As it is now, this expression does not allow to draw any further conclusions. The proper starting point is, instead, the averaging of the total Eulerian differential for conservation of ψ , Eq. (A.2),

$$\left\langle \frac{d}{dt} \left(\frac{d\Psi}{d\underline{V}} \right) \right\rangle = \left\langle \frac{d(\rho\psi)}{dt} \right\rangle = \frac{\partial \langle \rho\psi \rangle}{\partial t} + \nabla \cdot \langle \rho\psi \underline{V} \rangle.$$

The latter expression can be rewritten by means of the Favre average definition, Eq. (E.9), and the relation given by Eq. (E.12), as

$$\left\langle \frac{d(\rho\psi)}{dt} \right\rangle = \frac{\partial \langle \rho \rangle \tilde{\psi}}{\partial t} + \nabla \cdot \left(\langle \rho \rangle \tilde{\psi} \underline{\tilde{V}} \right) + \nabla \cdot \left(\langle \rho \rangle \widetilde{\psi'' \underline{V}''} \right). \quad (\text{F.30})$$

For $\psi = 1$, the corresponding average expression for conservation of mass is,

$$\left\langle \rho \frac{d\rho}{dt} \right\rangle = \frac{\partial \langle \rho \rangle}{\partial t} + \nabla \cdot (\langle \rho \rangle \tilde{\underline{V}}) = 0. \quad (\text{F.31})$$

Inserting Eq. (F.31) into Eq. (F.30) results in the average of the density weighted material derivative, i.e., the material derivative for average mass conservation,

$$\left\langle \rho \frac{d\psi}{dt} \right\rangle \rightarrow \left\langle \rho \frac{D\psi}{Dt} \right\rangle = \langle \rho \rangle \frac{\partial \tilde{\psi}}{\partial t} + \langle \rho \rangle (\tilde{\underline{V}} \cdot \nabla) \tilde{\psi} + \nabla \cdot (\langle \rho \rangle \widetilde{\psi'' \underline{V}''}). \quad (\text{F.32})$$

Therefore, the Favre averaged material derivative operator of a tensor ψ is defined as,

$$\frac{\tilde{D}\psi}{\tilde{D}t} = \frac{\partial \psi}{\partial t} + (\tilde{\underline{V}} \cdot \nabla) \psi. \quad (\text{F.33})$$

The proper method for the calculation of the TKE equation in the variable density case is, thus, given by,

$$\frac{\tilde{D}k}{\tilde{D}t} = \frac{1}{2} \frac{\tilde{D} \widetilde{\underline{V}'' \cdot \underline{V}''}}{\tilde{D}t} = \frac{\tilde{D} \tilde{\tau}_{kin}}{\tilde{D}t} - \tilde{\underline{V}} \cdot \frac{\tilde{D} \tilde{\underline{V}}}{\tilde{D}t}. \quad (\text{F.34})$$

First, the average momentum equation is found by Favre-averaging Eq. (A.11), considering variable fluid properties, and then substituting the average statement for conservation of mass, Eq. (F.31),

$$\begin{aligned} \langle \rho \rangle \frac{\tilde{D} \tilde{\underline{V}}}{\tilde{D}t} &= \langle \rho \rangle \frac{\partial \tilde{\underline{V}}}{\partial t} + \langle \rho \rangle (\tilde{\underline{V}} \cdot \nabla) \tilde{\underline{V}} = -\nabla \cdot \langle \rho \underline{V}'' \circ \underline{V}'' \rangle - \nabla \langle p \rangle \\ &\quad + \nabla \cdot \tilde{\underline{\tau}} + \nabla \cdot \langle \underline{\tau}'' \rangle + \langle \rho \rangle \underline{g} + \frac{I}{\beta}. \end{aligned} \quad (\text{F.35})$$

In order to arrive at this equation, the following decompositions were applied, see [126],

$$\begin{aligned} \rho &= \langle \rho \rangle + \rho', & \underline{V} &= \tilde{\underline{V}} + \underline{V}'', & p &= \langle p \rangle + p', \\ \underline{\tau} &= \tilde{\underline{\tau}} + \underline{\tau}'', & \mu &= \langle \mu \rangle + \mu'. \end{aligned} \quad (\text{F.36})$$

The Favre-averaged and fluctuating components of the shear stress tensor are,

$$\begin{aligned} \tilde{\underline{\tau}} &= \langle \mu \rangle \left[\nabla \circ \tilde{\underline{V}} + (\nabla \circ \tilde{\underline{V}})^T \right] - \frac{2}{3} \langle \mu \rangle (\nabla \cdot \tilde{\underline{V}}) \underline{I}, \\ \underline{\tau}'' &= \langle \mu \rangle \left[\nabla \circ \underline{V}'' + (\nabla \circ \underline{V}'')^T \right] - \frac{2}{3} \langle \mu \rangle (\nabla \cdot \underline{V}'') \underline{I}. \end{aligned} \quad (\text{F.37})$$

These equations have been derived considering that the correlations of the fluctuating dynamic viscosity with other turbulent fluctuations are negligible [126].

It is also possible to formulate an average temperature equation. However, this is a rather poor choice considering the introduction of further correlations between the specific heat capacity and the temperature. Instead, it is more suitable to work with an average enthalpy equation. The Favre-averaged enthalpy equation is found by averaging the Eulerian enthalpy equation, Eq. (2.58), considering only the molecular heat flux transport term and the constant Joule heating term $\underline{J} \cdot \underline{E}$ as a consequence of the Mach asymptotic analysis carried out in chapter 3,

$$\begin{aligned} \langle \rho \rangle \frac{\widetilde{D}\tilde{h}}{\widetilde{D}t} = \langle \rho \rangle \frac{\partial \tilde{h}}{\partial t} + \langle \rho \rangle \left(\widetilde{\underline{V}} \cdot \nabla \right) \tilde{h} = & -\nabla \cdot \langle \rho \underline{V}'' h'' \rangle + \nabla \cdot \left(\langle \sigma_T \rangle \nabla \tilde{T} \right) \\ & + \nabla \cdot \left(\langle \sigma_T \rangle \nabla \langle T'' \rangle \right) + \underline{J} \cdot \underline{E}. \end{aligned} \quad (\text{F.38})$$

Here again, the correlation of the fluctuating thermal conductivity with the temperature was neglected, as suggested by [126]. The corresponding decompositions are, in this case,

$$T = \tilde{T} + T'', \quad h = \tilde{h} + h'', \quad \sigma_T = \langle \sigma_T \rangle + \sigma_T'. \quad (\text{F.39})$$

Next, the average kinetic energy expression is found by averaging Eq. (2.53) in its proper Eulerian representation, considering variable fluid properties, and then substituting the average statement for conservation of mass, Eq. (F.31),

$$\begin{aligned} \langle \rho \rangle \frac{\widetilde{D}\widetilde{\xi}_{kin}}{\widetilde{D}t} = \langle \rho \rangle \frac{\partial \widetilde{\xi}_{kin}}{\partial t} + \langle \rho \rangle \left(\widetilde{\underline{V}} \cdot \nabla \right) \widetilde{\xi}_{kin} = & -\frac{1}{2} \nabla \cdot \left(\langle \rho \rangle \widetilde{\underline{V}'' \circ \underline{V}'' \cdot \underline{V}''} \right) \\ & - \left(\widetilde{\underline{V}} \cdot \nabla \right) \langle \rho \underline{V}'' \circ \underline{V}'' \rangle + \mathcal{P}_{TKE} \\ & - \widetilde{\underline{V}} \cdot \nabla \langle p \rangle - \langle \underline{V}'' \rangle \cdot \nabla \langle p \rangle - \nabla \cdot \langle p' \underline{V}'' \rangle + \langle p' \nabla \cdot \underline{V}'' \rangle \\ & + \widetilde{\underline{V}} \cdot \nabla \cdot \widetilde{\underline{\tau}} + \widetilde{\underline{V}} \cdot \nabla \cdot \langle \underline{\tau}'' \rangle + \langle \underline{V}'' \rangle \cdot \nabla \cdot \widetilde{\underline{\tau}} + \nabla \cdot \langle \underline{\tau}'' \cdot \underline{V}'' \rangle \\ & - \epsilon_{TKE} + \langle \rho \rangle \widetilde{\underline{V}} \cdot \underline{g} + \langle \underline{V} \rangle \cdot \frac{\underline{J}}{\beta}. \end{aligned} \quad (\text{F.40})$$

Note that, as a consequence of Eq. (3.64), \underline{J} is a constant, implying that the electric field in leading mobility ratio order is time-invariant. Due to the Galilean invariance of the quasistatic formulations of electromagnetism [56], this results in a leading order conservation of electroquasistatic potential energy. That is, considering Eq. (2.44),

$$\rho \frac{D\xi_E}{Dt} = 0 = -\underline{J} \cdot \underline{E} - \rho_f \underline{V} \cdot \underline{E}. \quad (\text{F.41})$$

The term $\underline{J} \cdot \underline{E}$ can be averaged with a Favre-average operator or with a Reynolds average operator and it will still remain the same. Therefore, in leading order, it is possible to approximate

$$-\underline{J} \cdot \underline{E} = \rho_f \langle \underline{V} \rangle \cdot \underline{E} = \langle \underline{V} \rangle \cdot \frac{\underline{J}}{\beta} \approx \rho_f \widetilde{\underline{V}} \cdot \underline{E} = \widetilde{\underline{V}} \cdot \frac{\underline{J}}{\beta}. \quad (\text{F.42})$$

Finally, the TKE equation in the variable density case is obtained as suggested by Eq. (F.34), by subtracting the scalar product of \tilde{V} with Eq. (F.35) from Eq. (F.40), considering the identity in Eq. (F.42),

$$\begin{aligned} \langle \rho \rangle \frac{\tilde{D}k}{\tilde{D}t} = & \langle \rho \rangle \frac{\partial k}{\partial t} + \langle \rho \rangle \left(\tilde{V} \cdot \nabla \right) k = -\frac{1}{2} \nabla \cdot \left(\langle \rho \rangle \widetilde{V'' \circ V'' \cdot V''} \right) \\ & + \mathcal{P}_{TKE} - \langle V'' \rangle \cdot \nabla \langle p \rangle - \nabla \cdot \langle p' V'' \rangle + \langle p' \nabla \cdot V'' \rangle \\ & + \langle V'' \rangle \cdot \nabla \cdot \underline{\underline{\tau}} + \nabla \cdot \langle \underline{\underline{\tau}} \cdot V'' \rangle - \epsilon_{TKE}. \end{aligned} \quad (\text{F.43})$$

For the variable density case,

$$\mathcal{P}_{TKE} = -\langle \rho \rangle \widetilde{V'' \circ V''} : \nabla \circ \tilde{V}, \quad (\text{F.44})$$

$$\epsilon_{TKE} = \langle \underline{\underline{\tau}} : \nabla \circ V'' \rangle. \quad (\text{F.45})$$

F.4 ODT VARIABLE DENSITY MEAN FLOW AND TKE EQUATIONS

F.4.1 Planar ODT mean flow and TKE equations

The explicit representation of the mean flow in Cartesian coordinates, Eq. (F.35) is,

$$\begin{aligned} \langle \rho \rangle \frac{\tilde{D}\tilde{u}_k}{\tilde{D}t} = & -\sum_{l=1}^3 \frac{\partial \left(\langle \rho \rangle \widetilde{u_l'' u_k''} \right)}{\partial x_l} - \frac{\partial \langle p \rangle}{\partial x_k} + \sum_{l=1}^3 \left(\frac{\partial \tilde{\tau}_{kl}}{\partial x_l} + \frac{\partial \langle \tau_{kl}'' \rangle}{\partial x_l} \right) \\ & - \langle \rho \rangle g \delta_{k2} + \frac{j_k}{\beta}. \end{aligned} \quad (\text{F.46})$$

The gravity term was assumed here acting in the vertical direction (buoyant horizontal channel). As a reference, the explicit representation of the shear stress tensor components τ_{xx} , τ_{xy} , τ_{xz} , τ_{yy} , τ_{yz} and τ_{zz} can be found in the Appendix B of Bird et al. [59],

$$\begin{aligned} \tau_{xx} = & 2\mu \frac{\partial u}{\partial x} - \frac{2}{3}\mu \left(\frac{\partial u}{\partial x} + \frac{\partial v}{\partial y} + \frac{\partial w}{\partial z} \right), \\ \tau_{yy} = & 2\mu \frac{\partial v}{\partial y} - \frac{2}{3}\mu \left(\frac{\partial u}{\partial x} + \frac{\partial v}{\partial y} + \frac{\partial w}{\partial z} \right), \\ \tau_{zz} = & 2\mu \frac{\partial w}{\partial z} - \frac{2}{3}\mu \left(\frac{\partial u}{\partial x} + \frac{\partial v}{\partial y} + \frac{\partial w}{\partial z} \right), \\ \tau_{xy} = & \tau_{yx} = \mu \left(\frac{\partial v}{\partial x} + \frac{\partial u}{\partial y} \right), \\ \tau_{yz} = & \tau_{zy} = \mu \left(\frac{\partial w}{\partial y} + \frac{\partial v}{\partial z} \right), \\ \tau_{xz} = & \tau_{zx} = \mu \left(\frac{\partial u}{\partial z} + \frac{\partial w}{\partial x} \right). \end{aligned} \quad (\text{F.47})$$

For the mean enthalpy, the corresponding expression for Eq. (F.38) is,

$$\begin{aligned} \langle \rho \rangle \frac{\widetilde{D}\widetilde{h}}{\widetilde{D}t} = & - \sum_{k=1}^3 \frac{\partial \left(\langle \rho \rangle \widetilde{u_k'' h''} \right)}{\partial x_k} + \sum_{k=1}^3 \left\{ \frac{\partial}{\partial x_k} \left(\langle \sigma_T \rangle \frac{\partial \langle T \rangle}{\partial x_k} \right) \right\} \\ & + \sum_{k=1}^3 j_k E_k. \end{aligned} \quad (\text{F.48})$$

Likewise, the explicit representation of the TKE in Cartesian coordinates, Eq. (F.43), is, according to [126],

$$\begin{aligned} \langle \rho \rangle \frac{\widetilde{D}k}{\widetilde{D}t} = & \sum_{l=1}^3 \frac{\partial}{\partial x_l} \left(\sum_{k=1}^3 \langle \tau_{kl}'' u_k'' \rangle \right) - \sum_{l=1}^3 \frac{\partial}{\partial x_l} \left(\frac{\langle \rho \rangle}{2} \sum_{k=1}^3 \widetilde{u_l'' u_k'' u_k''} + \langle p' u_l'' \rangle \right) \\ & + \langle p' \sum_{k=1}^3 \frac{\partial u_k''}{\partial x_k} \rangle + \left[- \sum_{k=1}^3 \langle u_k'' \rangle \frac{\partial \langle p \rangle}{\partial x_k} + \sum_{k=1}^3 \sum_{l=1}^3 \langle u_k'' \rangle \frac{\partial \widetilde{\tau}_{kl}}{\partial x_l} \right] \\ & + \mathcal{P}_{TKE} - \epsilon_{TKE}. \end{aligned} \quad (\text{F.49})$$

The cartesian representation for \mathcal{P}_{TKE} and ϵ_{TKE} can be found in appendix G.

The ODT mean flow momentum equation in the variable density case is found by averaging Eq. (3.73), and substituting the Reynolds shear stress, by the net average effect of the stochastic eddy events, $\langle M_k + \mathcal{T}_k + \mathcal{S}_k \rangle$. As in the incompressible constant property case, M_k , \mathcal{T}_k and \mathcal{S}_k represent the effects of the mappings, the turbulent transport and the pressure scrambling on the velocity component k . For the variable density case, however, all of these terms are now weighted by the density,

$$\begin{aligned} \langle \rho \rangle \frac{\widetilde{D}\widetilde{u}_k}{\widetilde{D}t} = & \left[- \frac{\partial \left(\langle \rho \rangle \widetilde{u_k'' u_1''} \right)}{\partial x} \right]_{S-ODT} + \langle M_k + \mathcal{T}_k + \mathcal{S}_k \rangle - \frac{\partial \bar{p}}{\partial x} \delta_{1k} \\ & + \frac{\partial}{\partial y} \left(\langle \mu \rangle \frac{\partial \widetilde{u}_k}{\partial y} + \langle \mu \rangle \frac{\partial \langle u_k'' \rangle}{\partial y} \right). \end{aligned} \quad (\text{F.50})$$

The same considerations for neglecting the correlation between the dynamic viscosity fluctuations and other fluctuating quantities are taken here. Also, the gravity and EHD body force terms are omitted on the assumption that they are just part of an irrotational contribution which is assumed as part of a modified pressure gradient term¹. Nonetheless, there are no buoyant EHD-enhanced channel flows evaluated in this

¹ This is the case of a buoyant horizontal channel. In a vertical channel, the gravity term would just be implemented as part of the deterministic catchup in ODT in the streamwise velocity component.

thesis. This is just written here for the sake of completion. Specifically for this case,

$$\langle M_k + \mathcal{T}_k \rangle = -\frac{\partial \left(\langle \rho \rangle \widetilde{u_k'' v_\psi''} \right)}{\partial y} = \frac{\partial \left(\langle \rho \rangle \mathcal{R}_k \right)}{\partial y}. \quad (\text{F.51})$$

In this case, $\langle M_k + \mathcal{T}_k + \mathcal{S}_k \rangle$ is the average change of the momentum component ρu_k due to eddies. The two kernel functions K_{ODT} and J_{ODT} enforce the condition $\int \mathcal{T}_k + \mathcal{S}_k dy = 0$. Given that the transport contribution should intuitively integrate to zero, \mathcal{S}_k is again arbitrarily defined, as in the incompressible constant property case, as $\mathcal{S}_k = 0$. See [72] for details regarding the calculation of \mathcal{R}_k . As before, the definition of the average material derivative in ODT needs to be interpreted according to the type of formulation, as detailed in chapter 3, resulting in the appearance of the streamwise Reynolds shear stress term. As in the constant property case, the (Favre-averaged) streamwise Reynolds shear stress is zero in fully developed hydrodynamic and thermal boundary layers (statistically streamwise homogeneous density weighted velocity profiles).

The ODT mean enthalpy equation is, correspondingly,

$$\begin{aligned} \langle \rho \rangle \frac{\widetilde{Dh}}{\widetilde{Dt}} = & \left[-\frac{\partial \left(\langle \rho \rangle \widetilde{u_1'' h''} \right)}{\partial x} \right]_{S-ODT} + \langle M_h + \mathcal{T}_h \rangle + \frac{\partial}{\partial y} \left(\langle \sigma_T \rangle \frac{\partial \langle T \rangle}{\partial y} \right) \\ & + j_2 E_2. \end{aligned} \quad (\text{F.52})$$

$\langle M_h + \mathcal{T}_h \rangle$ is the representation of the crosswise turbulent heat flux by the eddy events [72],

$$\langle M_h + \mathcal{T}_h \rangle = -\frac{\partial \left(\langle \rho \rangle \widetilde{h'' v_\psi''} \right)}{\partial y} = \frac{\partial \left(\langle \rho \rangle \mathcal{R}_h \right)}{\partial y}. \quad (\text{F.53})$$

It is possible to evaluate the turbulent heat flux directly by means of the change in the enthalpy profiles due to eddy events, see [72] for details.

The derivation of the ODT TKE equation is very similar to the incompressible constant property case derivation,

$$\begin{aligned}
\langle \rho \rangle \frac{\widetilde{D}k}{\widetilde{D}t} &= \frac{\partial}{\partial y} \left[\sum_{k=1}^3 \left(\langle \mu \rangle \left\langle \frac{\partial u_k''}{\partial y} u_k'' \right\rangle \right) \right] \\
&+ \left\{ \left[-\frac{1}{2} \frac{\partial}{\partial x} \left(\langle \rho \rangle \sum_{k=1}^3 \widetilde{u_1'' u_k'' u_k''} \right) \right]_{S-ODT} \right. \\
&+ \sum_{k=1}^3 \left[\frac{\partial}{\partial y} \left(\frac{\langle \rho \rangle \mathcal{R}_{kk}}{2} - \langle \rho \rangle \widetilde{u_k} \mathcal{R}_k \right) + \frac{\langle \mathcal{S}_{kk} \rangle}{2} \right] \left. \right\} \quad (\text{F.54}) \\
&+ \left[-\langle u_1'' \rangle \frac{\partial \bar{p}}{\partial x} + \sum_{k=1}^3 \langle u_k'' \rangle \frac{\partial}{\partial y} \left(\langle \mu \rangle \frac{\partial \widetilde{u}_k}{\partial y} \right) \right] \\
&+ \mathcal{P}_{TKE,ODT} - \epsilon_{TKE,ODT}.
\end{aligned}$$

Here, \mathcal{R}_{kk} is the bulk effect of the turbulent transport due to stochastic eddies, i.e.,

$$\langle M_{kk} + \mathcal{T}_{kk} \rangle = \frac{\partial (\langle \rho \rangle \mathcal{R}_{kk})}{\partial y}. \quad (\text{F.55})$$

As before, \mathcal{S}_{kk} can not be evaluated directly. The definition of the ODT TKE production and dissipation terms, $\mathcal{P}_{TKE,ODT}$ and $\epsilon_{TKE,ODT}$, in Eq. (F.54), can be found in appendix G.

F.4.2 Cylindrical ODT mean flow and TKE equations

As in the incompressible constant property case, the explicit representation of the mean flow in cylindrical coordinates, Eq. (F.35), is different for the streamwise momentum component in comparison to the radial and circumferential component, see [127]. Assuming now that gravity acts in streamwise direction, the streamwise, radial and circumferential mean momentum components are, respectively,

$$\begin{aligned}
\langle \rho \rangle \frac{\widetilde{D}\widetilde{u}}{\widetilde{D}t} &= - \left[\frac{\partial (\langle \rho \rangle \widetilde{u'' u''})}{\partial z} + \frac{1}{r} \frac{\partial (r \langle \rho \rangle \widetilde{u'' v''})}{\partial r} + \frac{1}{r} \frac{\partial (\langle \rho \rangle \widetilde{u'' w''})}{\partial \theta} \right] \\
&- \frac{\partial \langle p \rangle}{\partial z} + \left[\frac{\partial \widetilde{\tau}_{zz}}{\partial z} + \frac{1}{r} \frac{\partial (r \widetilde{\tau}_{rz})}{\partial r} + \frac{1}{r} \frac{\partial \widetilde{\tau}_{\theta z}}{\partial \theta} \right] \\
&+ \left[\frac{\partial \langle \tau''_{zz} \rangle}{\partial z} + \frac{1}{r} \frac{\partial (r \langle \tau''_{rz} \rangle)}{\partial r} + \frac{1}{r} \frac{\partial \langle \tau''_{\theta z} \rangle}{\partial \theta} \right] - \langle \rho \rangle g + \frac{j_1}{\beta}, \quad (\text{F.56})
\end{aligned}$$

$$\begin{aligned}
\langle \rho \rangle \frac{\widetilde{D}\widetilde{v}}{\widetilde{D}t} = & - \left[\frac{\partial \left(\langle \rho \rangle \widetilde{v''u''} \right)}{\partial z} + \frac{1}{r} \frac{\partial \left(r \langle \rho \rangle \widetilde{v''v''} \right)}{\partial r} + \frac{1}{r} \frac{\partial \left(\langle \rho \rangle \widetilde{v''w''} \right)}{\partial \theta} \right. \\
& \left. - \frac{\langle \rho \rangle \widetilde{w''w''}}{r} \right] - \frac{\partial \langle p \rangle}{\partial r} + \left[\frac{\partial \widetilde{\tau}_{rz}}{\partial z} + \frac{1}{r} \frac{\partial \left(r \widetilde{\tau}_{rr} \right)}{\partial r} + \frac{1}{r} \frac{\partial \widetilde{\tau}_{r\theta}}{\partial \theta} - \frac{\widetilde{\tau}_{\theta\theta}}{r} \right] \\
& + \left[\frac{\partial \langle \tau''_{rz} \rangle}{\partial z} + \frac{1}{r} \frac{\partial \left(r \langle \tau''_{rr} \rangle \right)}{\partial r} + \frac{1}{r} \frac{\partial \langle \tau''_{r\theta} \rangle}{\partial \theta} - \frac{\langle \tau''_{\theta\theta} \rangle}{r} \right] + \frac{j_2}{\beta'},
\end{aligned} \tag{F.57}$$

$$\begin{aligned}
\langle \rho \rangle \frac{\widetilde{D}\widetilde{w}}{\widetilde{D}t} = & - \left[\frac{\partial \left(\langle \rho \rangle \widetilde{w''u''} \right)}{\partial z} + \frac{1}{r} \frac{\partial \left(r \langle \rho \rangle \widetilde{w''v''} \right)}{\partial r} + \frac{1}{r} \frac{\partial \left(\langle \rho \rangle \widetilde{w''w''} \right)}{\partial \theta} \right. \\
& \left. + \frac{\langle \rho \rangle \widetilde{v''w''}}{r} \right] - \frac{1}{r} \frac{\partial \langle p \rangle}{\partial \theta} + \left[\frac{\partial \widetilde{\tau}_{\theta z}}{\partial z} + \frac{1}{r} \frac{\partial \left(r \widetilde{\tau}_{r\theta} \right)}{\partial r} + \frac{1}{r} \frac{\partial \widetilde{\tau}_{\theta\theta}}{\partial \theta} + \frac{\widetilde{\tau}_{r\theta}}{r} \right] \\
& + \left[\frac{\partial \langle \tau''_{\theta z} \rangle}{\partial z} + \frac{1}{r} \frac{\partial \left(r \langle \tau''_{r\theta} \rangle \right)}{\partial r} + \frac{1}{r} \frac{\partial \langle \tau''_{\theta\theta} \rangle}{\partial \theta} + \frac{\langle \tau''_{r\theta} \rangle}{r} \right] + \frac{j_3}{\beta'}.
\end{aligned} \tag{F.58}$$

As a reference, the explicit representation of the shear stress tensor components τ_{zz} , τ_{zr} , $\tau_{z\theta}$, τ_{rr} , $\tau_{r\theta}$ and $\tau_{\theta\theta}$ can be found in the Appendix B of Bird et al. [59], i.e.,

$$\begin{aligned}
\tau_{zz} &= 2\mu \frac{\partial u}{\partial z} - \frac{2}{3}\mu \left(\frac{\partial u}{\partial z} + \frac{1}{r} \frac{\partial (rv)}{\partial r} + \frac{1}{r} \frac{\partial w}{\partial \theta} \right), \\
\tau_{rr} &= 2\mu \frac{\partial v}{\partial r} - \frac{2}{3}\mu \left(\frac{\partial u}{\partial z} + \frac{1}{r} \frac{\partial (rv)}{\partial r} + \frac{1}{r} \frac{\partial w}{\partial \theta} \right), \\
\tau_{\theta\theta} &= 2\mu \left(\frac{1}{r} \frac{\partial w}{\partial \theta} + \frac{v}{r} \right) - \frac{2}{3}\mu \left(\frac{\partial u}{\partial z} + \frac{1}{r} \frac{\partial (rv)}{\partial r} + \frac{1}{r} \frac{\partial w}{\partial \theta} \right), \\
\tau_{zr} &= \tau_{rz} = \mu \left(\frac{\partial v}{\partial z} + \frac{\partial u}{\partial r} \right), \\
\tau_{r\theta} &= \tau_{\theta r} = \mu \left(\frac{\partial w}{\partial r} + \frac{1}{r} \frac{\partial v}{\partial \theta} - \frac{w}{r} \right), \\
\tau_{z\theta} &= \tau_{\theta z} = \mu \left(\frac{1}{r} \frac{\partial u}{\partial \theta} + \frac{\partial w}{\partial z} \right).
\end{aligned} \tag{F.59}$$

The explicit representation of the mean enthalpy equation, Eq. (F.38), is,

$$\begin{aligned} \langle \rho \rangle \frac{\widetilde{D}\widetilde{h}}{\widetilde{D}t} = & - \left[\frac{\partial \left(\langle \rho \rangle \widetilde{h''u''} \right)}{\partial z} + \frac{1}{r} \frac{\partial \left(r \langle \rho \rangle \widetilde{h''v''} \right)}{\partial r} + \frac{1}{r} \frac{\partial \left(\langle \rho \rangle \widetilde{h''w''} \right)}{\partial \theta} \right] \\ & + \left[\frac{\partial}{\partial z} \left(\langle \sigma_T \rangle \frac{\partial \langle T \rangle}{\partial z} \right) + \frac{1}{r} \frac{\partial}{\partial r} \left(r \langle \sigma_T \rangle \frac{\partial \langle T \rangle}{\partial r} \right) \right. \\ & \left. + \frac{1}{r} \frac{\partial}{\partial \theta} \left(\langle \sigma_T \rangle \frac{1}{r} \frac{\partial \langle T \rangle}{\partial \theta} \right) \right] + \sum_{k=1}^3 j_k E_k. \end{aligned} \quad (\text{F.60})$$

The explicit representation of the TKE in cylindrical coordinates, Eq. (F.43), is,

$$\begin{aligned} \langle \rho \rangle \frac{\widetilde{D}k}{\widetilde{D}t} = & \left[\frac{\partial}{\partial z} \left(\sum_{k=1}^3 \langle \tau''_{kz} u''_k \rangle \right) + \frac{1}{r} \frac{\partial}{\partial r} \left(r \sum_{k=1}^3 \langle \tau''_{kr} u''_k \rangle \right) + \frac{1}{r} \frac{\partial}{\partial \theta} \left(\sum_{k=1}^3 \langle \tau''_{k\theta} u''_k \rangle \right) \right] \\ & - \left\{ \frac{\partial}{\partial z} \left(\frac{\langle \rho \rangle}{2} \sum_{k=1}^3 \widetilde{u''_1 u''_k u''_k} + \langle p' u''_1 \rangle \right) \right. \\ & + \frac{1}{r} \frac{\partial}{\partial r} \left[r \left(\frac{\langle \rho \rangle}{2} \sum_{k=1}^3 \widetilde{u''_2 u''_k u''_k} + \langle p' u''_2 \rangle \right) \right] \\ & \left. + \frac{1}{r} \frac{\partial}{\partial \theta} \left(\frac{\langle \rho \rangle}{2} \sum_{k=1}^3 \widetilde{u''_3 u''_k u''_k} + \langle p' u''_3 \rangle \right) \right\} \\ & + \langle p' \left[\frac{\partial u''_1}{\partial z} + \frac{1}{r} \frac{\partial (r u''_2)}{\partial r} + \frac{1}{r} \frac{\partial u''_3}{\partial \theta} \right] \rangle \\ & + \left\{ - \langle u''_1 \rangle \frac{\partial \langle p \rangle}{\partial z} - \langle u''_2 \rangle \frac{\partial \langle p \rangle}{\partial r} - \langle u''_3 \rangle \frac{1}{r} \frac{\partial \langle p \rangle}{\partial \theta} \right. \\ & + \langle u''_1 \rangle \left[\frac{\partial \widetilde{\tau''_{zz}}}{\partial z} + \frac{1}{r} \frac{\partial (r \widetilde{\tau''_{rz}})}{\partial r} + \frac{1}{r} \frac{\partial \widetilde{\tau''_{\theta z}}}{\partial \theta} \right] \\ & + \langle u''_2 \rangle \left[\frac{\partial \widetilde{\tau''_{rz}}}{\partial z} + \frac{1}{r} \frac{\partial (r \widetilde{\tau''_{rr}})}{\partial r} + \frac{1}{r} \frac{\partial \widetilde{\tau''_{r\theta}}}{\partial \theta} - \frac{\widetilde{\tau''_{\theta\theta}}}{r} \right] \\ & \left. + \langle u''_3 \rangle \left[\frac{\partial \widetilde{\tau''_{\theta z}}}{\partial z} + \frac{1}{r} \frac{\partial (r \widetilde{\tau''_{r\theta}})}{\partial r} + \frac{1}{r} \frac{\partial \widetilde{\tau''_{\theta\theta}}}{\partial \theta} + \frac{\widetilde{\tau''_{r\theta}}}{r} \right] \right\} \\ & + \mathcal{P}_{TKE} - \epsilon_{TKE}. \end{aligned} \quad (\text{F.61})$$

The cylindrical representation for \mathcal{P}_{TKE} and ϵ_{TKE} can be found in appendix G.

The derivation of the average ODT cylindrical momentum equation is obtained following the same method as before. This derivation can be found in [72],

$$\begin{aligned} \langle \rho \rangle \frac{\widetilde{D}\widetilde{u}}{\widetilde{D}t} = & \left[-\frac{\partial \left(\langle \rho \rangle \widetilde{u''u''} \right)}{\partial z} \right]_{S-ODT} + \langle M_1 + \mathcal{T}_1 + \mathcal{S}_1 \rangle - \frac{\partial \bar{p}}{\partial z} \\ & + \frac{1}{r} \frac{\partial}{\partial r} \left(r \langle \mu \rangle \frac{\partial \widetilde{u}}{\partial r} \right) + \frac{1}{r} \frac{\partial}{\partial r} \left(r \langle \mu \rangle \frac{\partial \langle u'' \rangle}{\partial r} \right) - \langle \rho \rangle g, \end{aligned} \quad (\text{F.62})$$

$$\begin{aligned} \langle \rho \rangle \frac{\widetilde{D}\widetilde{v}}{\widetilde{D}t} = & \left[-\frac{\partial \left(\langle \rho \rangle \widetilde{v''u''} \right)}{\partial z} \right]_{S-ODT} + \langle M_2 + \mathcal{T}_2 + \mathcal{S}_2 \rangle \\ & + \left[\frac{1}{r} \frac{\partial}{\partial r} \left(r \langle \mu \rangle \frac{\partial \widetilde{v}}{\partial r} \right) - \frac{1}{r} \frac{\partial}{\partial r} \left(r \langle \mu \rangle \frac{\widetilde{v}}{r} \right) + \langle \mu \rangle \frac{\partial}{\partial r} \left(\frac{\widetilde{v}}{r} \right) \right] \\ & + \left[\frac{1}{r} \frac{\partial}{\partial r} \left(r \langle \mu \rangle \frac{\partial \langle v'' \rangle}{\partial r} \right) - \frac{1}{r} \frac{\partial}{\partial r} \left(r \langle \mu \rangle \frac{\langle v'' \rangle}{r} \right) \right. \\ & \left. + \langle \mu \rangle \frac{\partial}{\partial r} \left(\frac{\langle v'' \rangle}{r} \right) \right], \end{aligned} \quad (\text{F.63})$$

$$\begin{aligned} \langle \rho \rangle \frac{\widetilde{D}\widetilde{w}}{\widetilde{D}t} = & \left[-\frac{\partial \left(\langle \rho \rangle \widetilde{w''u''} \right)}{\partial z} \right]_{S-ODT} + \langle M_3 + \mathcal{T}_3 + \mathcal{S}_3 \rangle \\ & + \left[\frac{1}{r} \frac{\partial}{\partial r} \left(r \langle \mu \rangle \frac{\partial \widetilde{w}}{\partial r} \right) - \frac{1}{r} \frac{\partial}{\partial r} \left(r \langle \mu \rangle \frac{\widetilde{w}}{r} \right) + \langle \mu \rangle \frac{\partial}{\partial r} \left(\frac{\widetilde{w}}{r} \right) \right] \\ & + \left[\frac{1}{r} \frac{\partial}{\partial r} \left(r \langle \mu \rangle \frac{\partial \langle w'' \rangle}{\partial r} \right) - \frac{1}{r} \frac{\partial}{\partial r} \left(r \langle \mu \rangle \frac{\langle w'' \rangle}{r} \right) \right. \\ & \left. + \langle \mu \rangle \frac{\partial}{\partial r} \left(\frac{\langle w'' \rangle}{r} \right) \right]. \end{aligned} \quad (\text{F.64})$$

As before, $\mathcal{S}_k = 0$. The gradient of the Reynolds shear stresses is in this case,

$$\langle M_k + \mathcal{T}_k \rangle = -\frac{1}{r} \frac{\partial \left(r \langle \rho \rangle u''_k \widetilde{v''_k} \right)}{\partial r} = \frac{1}{r} \frac{\partial \left(r \langle \rho \rangle \mathcal{R}_k \right)}{\partial r}. \quad (\text{F.65})$$

The corresponding ODT cylindrical mean enthalpy equation is,

$$\begin{aligned} \langle \rho \rangle \frac{\widetilde{D}\widetilde{h}}{\widetilde{D}t} = & - \left[\frac{\partial \left(\langle \rho \rangle \widetilde{h''u''} \right)}{\partial z} \right]_{S-ODT} + \langle M_h + \mathcal{T}_h \rangle \\ & + \left[\frac{1}{r} \frac{\partial}{\partial r} \left(r \langle \sigma_T \rangle \frac{\partial \langle T \rangle}{\partial r} \right) \right] + j_2 E_2. \end{aligned} \quad (\text{F.66})$$

The radial turbulent heat flux is, thus, defined as,

$$\langle M_h + \mathcal{T}_h \rangle = -\frac{1}{r} \frac{\partial}{\partial r} \left(r \langle \rho \rangle \widetilde{h'' v''} \right) = \frac{1}{r} \frac{\partial}{\partial r} (r \langle \rho \rangle \mathcal{R}_h). \quad (\text{F.67})$$

In order to derive the ODT TKE equation, the procedure is the same as in the planar case,

$$\begin{aligned} \langle \rho \rangle \frac{\widetilde{D}k}{\widetilde{D}t} &= \frac{1}{r} \frac{\partial}{\partial r} \left[r \langle \mu \rangle \left(\sum_{k=1}^3 \left\langle \frac{\partial u_k''}{\partial r} u_k'' \right\rangle - \frac{\langle u_2'' u_2'' \rangle}{r} - \frac{\langle u_3'' u_3'' \rangle}{r} \right) \right] \\ &\quad \left\{ \left[-\frac{1}{2} \frac{\partial}{\partial z} \left(\langle \rho \rangle \sum_{k=1}^3 \widetilde{u_1'' u_k'' u_k''} \right) \right]_{S\text{-}ODT} \right. \\ &\quad \left. + \sum_{k=1}^3 \left\{ \frac{1}{r} \frac{\partial}{\partial r} \left[r \left(\frac{\langle \rho \rangle \mathcal{R}_{kk}}{2} - \langle \rho \rangle \widetilde{u}_k \mathcal{R}_k \right) \right] + \frac{\langle S_{kk} \rangle}{2} \right\} \right\} \quad (\text{F.68}) \\ &\quad + \left\{ -\langle u_1'' \rangle \frac{\partial \bar{p}}{\partial z} + \sum_{k=1, l=2}^3 \left[\frac{\langle u_k'' \rangle}{r} \frac{\partial}{\partial r} \left(r \langle \mu \rangle \frac{\partial \widetilde{u}_k}{\partial r} \right) \right. \right. \\ &\quad \left. \left. - \frac{\langle u_l'' \rangle}{r} \frac{\partial}{\partial r} \left(r \langle \mu \rangle \frac{\widetilde{u}_l}{r} \right) + \langle u_l'' \rangle \langle \mu \rangle \frac{\partial}{\partial r} \left(\frac{\widetilde{u}_l}{r} \right) \right] \right\} \\ &\quad + \mathcal{P}_{TKE,ODT} - \epsilon_{TKE,ODT}. \end{aligned}$$

As before,

$$\langle M_{kk} + \mathcal{T}_{kk} \rangle = \frac{1}{r} \frac{\partial}{\partial r} (r \langle \rho \rangle \mathcal{R}_{kk}). \quad (\text{F.69})$$

The definition of the ODT TKE production and dissipation terms, $\mathcal{P}_{TKE,ODT}$ and $\epsilon_{TKE,ODT}$, can be found in appendix G.

SCALING IN WALL UNITS

G.1 INCOMPRESSIBLE CONSTANT PROPERTY FLOW

The nondimensional + units are quantities normalized by the corresponding viscous scale. The friction quantities and the most used nondimensional quantities for incompressible constant property flow are summarized next:

- **Friction Reynolds number** Recall Eq. (1.6) where H is the width or height of the channel (distance between walls) and R_H is the (hydraulic) radius of the pipe,

$$Re_\tau = \frac{\langle \rho_w \rangle u_\tau H}{2\langle \mu_w \rangle} \text{ (Planar)}, \quad Re_\tau = \frac{\langle \rho_w \rangle u_\tau R_H}{\langle \mu_w \rangle} \text{ (Cylindrical)}. \quad (1.6)$$

- **Wall shear stress**

$$\tau_w \approx \langle \mu_w \rangle \left. \frac{\partial \langle u \rangle}{\partial y} \right|_w \text{ (Planar)}, \quad \tau_w \approx \langle \mu_w \rangle \left. \frac{\partial \langle u \rangle}{\partial r} \right|_w \text{ (Cylindrical)}. \quad (G.1)$$

- **Friction velocity:** Recall Eq. (1.7)

$$u_\tau = \sqrt{\frac{\tau_w}{\langle \rho_w \rangle}}. \quad (1.7)$$

- **Friction length scale**

$$L_\tau = \frac{\langle \mu_w \rangle}{\langle \rho_w \rangle u_\tau}. \quad (G.2)$$

- **Nondimensional distance from the wall**

$$y^+ = \frac{y}{L_\tau} \text{ (Planar)}, \quad (1-r)^+ = \frac{R-r}{L_\tau} \text{ (Cylindrical)}. \quad (G.3)$$

- **Inner scaled nondimensional velocity**

$$u_k^+ = \frac{u_k}{u_\tau}, \quad k \in \{1, 2, 3\}. \quad (G.4)$$

- **Inner scaled nondimensional RMS velocity**

$$u_{k,RMS} = \sqrt{\langle u_k^2 \rangle - \langle u_k \rangle^2}, \quad u_{k,RMS}^+ = \frac{u_{k,RMS}}{u_\tau}. \quad (G.5)$$

- **Generalized inner scaled incompressible Reynolds shear stresses**

$$\langle u'_i u'_j \rangle^+ = \frac{\langle u'_i u'_j \rangle}{u_\tau^2}, \quad i, j \in \{1, 2, 3\}. \quad (\text{G.6})$$

- **ODT inner scaled incompressible Reynolds shear stress**

$$\langle u'_1 u'_2 \rangle^+ = \langle u' v' \rangle^+ = \frac{\langle u'_1 u'_2 \rangle}{u_\tau^2}. \quad (\text{G.7})$$

- **Incompressible TKE**

$$k = \frac{1}{2} \sum_{k=1}^3 u_{k,RMS}^2 = \frac{1}{2} \sum_{k=1}^3 (\langle u_k^2 \rangle - \langle u_k \rangle^2), \quad k^+ = \frac{k}{u_\tau^2}. \quad (\text{G.8})$$

- **Generalized incompressible TKE production: Normalization in + units by $\rho u_\tau^4 / \nu$.**

$$\begin{aligned} \mathcal{P}_{TKE} &= -\rho \sum_{i=1}^3 \sum_{j=1}^3 \langle u'_i u'_j \rangle \frac{\partial \langle u_i \rangle}{\partial x_j} \quad (\text{Planar}), \\ \mathcal{P}_{TKE} &= -\rho \left[\langle u' u' \rangle \frac{\partial \langle u \rangle}{\partial z} + \langle u' v' \rangle \left(\frac{\partial \langle v \rangle}{\partial z} + \frac{\partial \langle u \rangle}{\partial r} \right) \right. \\ &\quad + \langle u' w' \rangle \left(\frac{\partial \langle w \rangle}{\partial z} + \frac{1}{r} \frac{\partial \langle u \rangle}{\partial \theta} \right) + \langle v' v' \rangle \frac{\partial \langle v \rangle}{\partial r} \\ &\quad + \langle w' v' \rangle \left(\frac{\partial \langle w \rangle}{\partial r} + \frac{1}{r} \frac{\partial \langle v \rangle}{\partial \theta} - \frac{\langle w \rangle}{r} \right) \\ &\quad \left. + \langle w' w' \rangle \left(\frac{1}{r} \frac{\partial \langle w \rangle}{\partial \theta} + \frac{\langle v \rangle}{r} \right) \right] \quad (\text{Cylindrical}). \end{aligned} \quad (\text{G.9})$$

- **ODT incompressible TKE production: Normalization in + units by $\rho u_\tau^4 / \nu$.**

$$\begin{aligned} \mathcal{P}_{TKE,ODT} &= -\rho \sum_{k=1}^3 \langle u'_k v'_\psi \rangle \frac{\partial \langle u_k \rangle}{\partial y} - \rho \left[\sum_{k=1}^3 \langle u'_k u'_1 \rangle \frac{\partial \langle u_k \rangle}{\partial x} \right]_{S-ODT} \quad (\text{Planar}), \\ \mathcal{P}_{TKE,ODT} &= -\rho \sum_{k=1}^3 \langle u'_k v'_\psi \rangle \frac{\partial \langle u_k \rangle}{\partial r} - \rho \left[\sum_{k=1}^3 \langle u'_k u'_1 \rangle \frac{\partial \langle u_k \rangle}{\partial z} \right]_{S-ODT} \quad (\text{Cyl.}) \end{aligned} \quad (\text{G.10})$$

- **Generalized incompressible TKE dissipation:** Normalization in + units by $\rho u_\tau^4/\nu$.

$$\begin{aligned}\epsilon_{TKE} &= \mu \sum_{i=1}^3 \sum_{j=1}^3 \left\langle \frac{\partial u'_i}{\partial x_j} \frac{\partial u'_i}{\partial x_j} \right\rangle \text{ (Planar),} \\ \epsilon_{TKE} &= \mu \left\{ \sum_{k=1}^3 \left\langle \frac{\partial u'_k}{\partial z} \frac{\partial u'_k}{\partial z} \right\rangle + \sum_{k=1}^3 \left\langle \frac{\partial u'_k}{\partial r} \frac{\partial u'_k}{\partial r} \right\rangle + \frac{1}{r^2} \sum_{k=1}^3 \left\langle \frac{\partial u'_k}{\partial \theta} \frac{\partial u'_k}{\partial \theta} \right\rangle \right. \\ &\quad \left. - \frac{2}{r^2} \langle u'_3 \frac{\partial u'_2}{\partial \theta} \rangle + \frac{2}{r^2} \langle u'_2 \frac{\partial u'_3}{\partial \theta} \rangle + \frac{\langle u'_3 u'_3 \rangle}{r^2} + \frac{\langle u'_2 u'_2 \rangle}{r^2} \right\} \text{ (Cylindrical).}\end{aligned}\tag{G.11}$$

- **ODT incompressible TKE dissipation:** Normalization in + units by $\rho u_\tau^4/\nu$.

$$\begin{aligned}\epsilon_{TKE,ODT} &= \mu \sum_{k=1}^3 \left\langle \frac{\partial u'_k}{\partial y} \frac{\partial u'_k}{\partial y} \right\rangle \text{ (Planar),} \\ \epsilon_{TKE,ODT} &= \mu \left(\sum_{k=1}^3 \left\langle \frac{\partial u'_k}{\partial r} \frac{\partial u'_k}{\partial r} \right\rangle + \frac{\langle u'_2 u'_2 \rangle}{r^2} + \frac{\langle u'_3 u'_3 \rangle}{r^2} \right) \text{ (Cylindrical).}\end{aligned}\tag{G.12}$$

G.2 VARIABLE DENSITY FLOW

Similar to the incompressible constant property flow case, the superscript + is used to indicate the scaling of quantities in nondimensional viscous or wall units. The same relations of incompressible constant property flow for the definition of friction Reynolds number, wall shear stress, friction velocity, friction length scale and the nondimensional distance from the wall in viscous units, Eqs. (1.6), (1.7), (G.1)-(G.3) remain unchanged.

- **Wall heat flux:**

$$q_w \approx \langle \sigma_{T,w} \rangle \frac{\partial \langle T \rangle}{\partial y} \Big|_w \text{ (Planar),} \quad q_w \approx \langle \sigma_{T,w} \rangle \frac{\partial \langle T \rangle}{\partial r} \Big|_w \text{ (Cylindrical).}\tag{G.13}$$

- **Friction temperature**

$$T_\tau = \frac{q_w}{\langle \rho_w \rangle \langle c_{p,w} \rangle u_\tau}.\tag{G.14}$$

- **Inner scaled nondimensional temperature**

$$T^+ = \frac{\langle T_w \rangle - \langle T \rangle}{T_\tau}\tag{G.15}$$

- **Van Driest velocity transformation:** Used for the streamwise velocity component. Defined in [128] as,

$$u_{VD} = \int_{\psi=0}^{\psi=\langle u \rangle} \left(\frac{\langle \rho \rangle}{\langle \rho_w \rangle} \right)^{\frac{1}{2}} d\psi. \quad (\text{G.16})$$

- **Inner scaled van Driest velocity**

$$u_{VD}^+ = \frac{u_{VD}}{u_\tau}. \quad (\text{G.17})$$

- **Variable density TKE**

$$k = \frac{1}{2} \sum_{k=1}^3 u_{k,RMS}^2 = \frac{1}{2} \sum_{k=1}^3 \left(\tilde{u}_k^2 - \tilde{u}_k'^2 \right), \quad k^+ = \frac{k}{u_\tau^2}. \quad (\text{G.18})$$

- **Generalized TKE production**

$$\begin{aligned} \mathcal{P}_{TKE} &= - \sum_{i=1}^3 \sum_{j=1}^3 \langle \rho \rangle \widetilde{u_i'' u_j''} \frac{\partial \tilde{u}_i}{\partial x_j} \quad (\text{Planar}), \\ \mathcal{P}_{TKE} &= - \langle \rho \rangle \left[\widetilde{u'' u''} \frac{\partial \tilde{u}}{\partial z} + \widetilde{u'' v''} \left(\frac{\partial \tilde{v}}{\partial z} + \frac{\partial \tilde{u}}{\partial r} \right) \right. \\ &\quad + \widetilde{u'' w''} \left(\frac{\partial \tilde{w}}{\partial z} + \frac{1}{r} \frac{\partial \tilde{u}}{\partial \theta} \right) + \widetilde{v'' v''} \frac{\partial \tilde{v}}{\partial r} \\ &\quad + \widetilde{w'' v''} \left(\frac{\partial \tilde{w}}{\partial r} + \frac{1}{r} \frac{\partial \tilde{v}}{\partial \theta} - \frac{\tilde{w}}{r} \right) \\ &\quad \left. + \widetilde{w'' w''} \left(\frac{1}{r} \frac{\partial \tilde{w}}{\partial \theta} + \frac{\tilde{v}}{r} \right) \right] \quad (\text{Cylindrical}). \end{aligned} \quad (\text{G.19})$$

- **ODT TKE production**

$$\begin{aligned} \mathcal{P}_{TKE,ODT} &= - \langle \rho \rangle \sum_{k=1}^3 \widetilde{u_k'' v_\psi''} \frac{\partial \tilde{u}_k}{\partial y} - \left[\langle \rho \rangle \sum_{k=1}^3 \widetilde{u_k'' u_1''} \frac{\partial \tilde{u}_k}{\partial x} \right]_{S-ODT} \quad (\text{Planar}), \\ \mathcal{P}_{TKE,ODT} &= - \langle \rho \rangle \sum_{k=1}^3 \widetilde{u_k'' v_\psi''} \frac{\partial \tilde{u}_k}{\partial r} - \left[\langle \rho \rangle \sum_{k=1}^3 \widetilde{u_k'' u_1''} \frac{\partial \tilde{u}_k}{\partial z} \right]_{S-ODT} \quad (\text{Cyl.}). \end{aligned} \quad (\text{G.20})$$

- **Generalized TKE dissipation**

$$\begin{aligned} \epsilon_{TKE} &= \sum_{i=1}^3 \sum_{j=1}^3 \langle \tau_{ij}'' \frac{\partial u_i''}{\partial x_j} \rangle \quad (\text{Planar}), \\ \epsilon_{TKE} &= \left\{ \sum_{k=1}^3 \left[\langle \tau_{iz}'' \frac{\partial u_i''}{\partial z} \rangle + \langle \tau_{ir}'' \frac{\partial u_i''}{\partial r} \rangle + \langle \tau_{i\theta}'' \frac{1}{r} \frac{\partial u_i''}{\partial \theta} \rangle \right] \right. \\ &\quad \left. - \langle \tau_{r\theta}'' \frac{w''}{r} \rangle + \langle \tau_{\theta\theta}'' \frac{v''}{r} \rangle \right\} \quad (\text{Cylindrical}). \end{aligned} \quad (\text{G.21})$$

• ODT TKE dissipation

$$\begin{aligned} \epsilon_{TKE,ODT} &= \langle \mu \rangle \sum_{k=1}^3 \left\langle \frac{\partial u_k''}{\partial y} \frac{\partial u_k''}{\partial y} \right\rangle \text{ (Planar),} \\ \epsilon_{TKE,ODT} &= \langle \mu \rangle \left(\sum_{k=1}^3 \left\langle \frac{\partial u_k''}{\partial r} \frac{\partial u_k''}{\partial r} \right\rangle + \frac{\langle u_2'' u_2'' \rangle}{r^2} + \frac{\langle u_3'' u_3'' \rangle}{r^2} \right. \\ &\quad \left. - \frac{2}{r} \left\langle u_2'' \frac{\partial u_2''}{\partial r} \right\rangle - \frac{2}{r} \left\langle u_3'' \frac{\partial u_3''}{\partial r} \right\rangle \right) \text{ (Cylindrical).} \end{aligned} \quad (\text{G.22})$$

CALCULATION OF ELECTROQUASISTATIC FIELDS

The algorithms used for the generation of the fixed electroquasistatic fields (electric field, electrostatic potential, electric current density and electric charge density) used in chapters 6 and 7 are detailed in this appendix. The fields generated for chapter 6 are 2-D fields in a cartesian or planar coordinate system, while the fields generated for chapter 7 are 1-D fields in a cylindrical coordinate system.

H.1 BOUNDARY CONDITIONS REQUIRED FOR THE CALCULATION OF ELECTROQUASISTATIC FIELDS

The solution of electroquasistatic fields is obtained by the system of equations formed by Eqs. (2.17), (2.11), (3.51) and the solenoidal electric current density equation, Eq. (3.64),

$$\underline{E} = -\nabla\phi, \quad (2.17)$$

$$\underline{J} = \rho_f \beta \underline{E}, \quad (2.11)$$

$$\rho_f = \epsilon_0 \nabla \cdot \underline{E}, \quad (3.51)$$

$$\nabla \cdot \underline{J} = 0. \quad (3.64)$$

For a given constant electrical mobility β , this system of equations reduces into a PDE for the electrostatic potential. That is, substitute, Eq. (2.11) into Eq. (3.64), and substitute the charge density by Eq. (3.51) and the electric field vector by Eq. (2.17),

$$\nabla \cdot [(\nabla^2\phi) \nabla\phi] = 0. \quad (H.1)$$

This is a third-order nonlinear PDE which requires three boundary conditions (BCs) for the electrostatic potential [129]. The third boundary condition is normally given either by the assumption of the form of the electric field around the electrode emitter surface, or by the assumption of the charge density at the electrode emitter [129]. The assumption on the electric field form is the so-called Kaptzov's hypothesis, which assumes that the electric field at the surface of the emitter electrode is constant and equal to its onset value. The onset

electric field value is given by Peek's formula for a given geometric configuration [130].

Another important comment regarding the BCs is that the solution to the Poisson equation for the pressure in an incompressible constant property flow problem does not result in the actual thermodynamic pressure field values. Similarly, the electrostatic potential field obtained by solving Eq. (H.1) with the corresponding BCs does not result in the correct electric current given by the actual Voltage-Current characteristic curve of the electrode. This is because the solution of Eq. (H.1) is a superposition of the solutions of the electrostatic potential in a control volume and the solutions in the control surface, e.g., the solution of a charge density field enclosed between the electrode and the grounded wall and the solution of a surface charge density at the electrode. That is, Eq. (3.51) must be satisfied in an integral way by both in its volume and surface equivalent integrals due to the divergence theorem. For the application of Eq. (3.51) in its surface integral form at the surface of the electrode, this implies that the gradient of the electrostatic potential in the normal direction to the surface of the electrode is discontinuous across the surface due to the inherent surface charge density at the electrode [57]. In addition, the equivalent version of Eq. (2.17), that is, Faraday's law, Eq. (2.16), implies that the electrostatic potential must be continuous across the the electrode surface. Both statements can not be justified without invoking information about the physical nature of the electrode [57]. Therefore, in order to solve Eq. (H.1) with the actual physical nature of the electrode (the appropriate voltage-current characteristic curve), three BCs for the electrostatic potential must be supplied, but also the corresponding value of the desired electric current must be supplied.

H.2 WIRE-PLATE ESP: 2-D PLANAR ELECTROQUASISTATIC FIELDS

The 2-D electric field generated by the periodic array of electrodes in streamwise direction is calculated following the method presented in [51] for the three-wire configuration.

The combination of Equations (2.17) and (3.51) results in a Poisson equation for the electrostatic potential. In the planar coordinate system, considering an invariant electric field in the spanwise direction of the channel, this is,

$$\frac{\partial^2 \phi}{\partial x^2} + \frac{\partial^2 \phi}{\partial y^2} = -\frac{\rho_f}{\epsilon_0}. \quad (\text{H.2})$$

Due to the periodic array of electrodes and the position of the electrodes in the (crosswise) centerline of the channel, the calculation of the electrostatic potential field obeys the following convenient symmetry considerations,

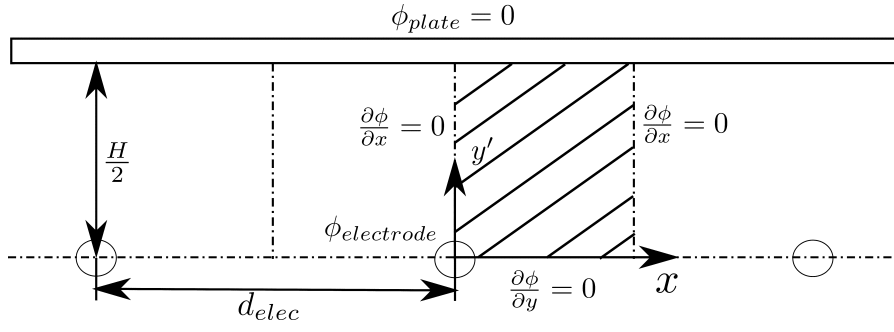


Figure H.1: Calculation region and boundary conditions for the electrostatic potential Poisson equation in the wire-plate ESP case.

- The electric field normal to the horizontal centerline symmetry line is zero, i.e., $E_2(x, y = \text{centerline}) = 0$.
- The electric field normal to the symmetry line between the streamwise electrodes is zero, i.e., $E_1(x = \text{symmetry line}, y) = 0$.
- The electric field normal to the symmetry line at the electrode position is zero, i.e., $E_1(x = \text{electrode}, y) = 0$.

Note the subscript convention used here for the electric field, according to the nomenclature section, i.e., $\underline{E} = [E_1, E_2, E_3]^T$. Additionally to these BCs, the Dirichlet BCs for the electrostatic potential at the electrode, $\phi_{\text{electrode}}$ and at the collector plate $\phi_{\text{plate}} = 0$ are used. The calculation region and BCs for the electrostatic potential are summarized in Figure H.1.

In addition to Eq. (H.2), the solenoidal electric current density vector condition must be met. Indeed, combining, Eq. (3.64) with Eqs. (2.11) and (2.17), and considering a constant ionic mobility β , results in a condition for the electric charge density field [51],

$$\nabla \rho_f \cdot \nabla \phi + \rho_f \nabla^2 \phi = 0.$$

Substituting Eq. (3.51) and (2.17), this is,

$$\rho_f^2 = \epsilon_0 \nabla \rho_f \cdot \nabla \phi. \quad (\text{H.3})$$

In planar coordinates, neglecting gradients in the spanwise direction, this leads to

$$\rho_f^2 = \epsilon_0 \left(\frac{\partial \rho_f}{\partial x} \frac{\partial \phi}{\partial x} + \frac{\partial \rho_f}{\partial y} \frac{\partial \phi}{\partial y} \right). \quad (\text{H.4})$$

It is noted that, so far neither the third boundary condition for the electrostatic potential nor the physical BC for a consistent voltage-current characteristic curve commented in the first section have been supplied or discussed. Both conditions are imposed on the problem by specifying the charge density at the electrode emitter, which will be related to the actual current value from the voltage-current characteristic curve in the solution algorithm as described next. Equations (H.2) and (H.4) are solved in an iterative way, similar to [51], as follows:

1. First, an arbitrary charge density field is assumed. An initial value for the charge density at the electrode, $\rho_{f,elec} \neq 0$ is also assumed. E.g., assume a zero charge density field and solve the Laplace equation for the electrostatic potential, Eq. (H.2). The equation is solved using a FDM in an equidistant 2-D grid,

$$\frac{\phi_{i+1,j} - 2\phi_{i,j} + \phi_{i-1,j}}{(\Delta x)^2} + \frac{\phi_{i,j+1} - 2\phi_{i,j} + \phi_{i,j-1}}{(\Delta y)^2} = -\frac{\rho_{f,i,j}}{\epsilon_0} \quad (\text{H.5})$$

Here, the subscripts i and j denote the grid cell indices in the horizontal and vertical directions, x and y . The resulting linear system of equations is solved using the linear-algebraic system interface for the algebraic multi-grid solver of the software suite Hypre [131].

2. Once the electrostatic potential field is calculated, the corresponding electric field at all grid points is calculated. The electric field at the internal mesh grid points is calculated per Eq. (2.17) using a central difference scheme and the electrostatic potential field. The electric field at the grid boundaries is either calculated with forward or backward differences using the electrostatic potential field, or given directly by the boundary conditions discussed above. It is noted that the horizontal component of the electric field at the collector is zero due to the entire collector surface being at the same electrostatic potential $\phi_{plate} = 0$.
3. The electric current density per unit length at the plate is calculated. This is the integral of the magnitude of the electric current density vector given by Eq. (2.11) with respect to x ,

$$\frac{I}{B} = 4 \int_{x=0}^{x=\frac{d_{elec}}{2}} \rho_f(x, y = \text{plate}) \beta E_2(x, y = \text{plate}) dx. \quad (\text{H.6})$$

Here, B is the depth of the channel in direction z , or the length of the electrode in the spanwise direction. d_{elec} is the distance between electrodes in streamwise direction. The factor 4 in this expression is due to the geometric consideration that only a quarter of the total plate area is being evaluated with the proposed integral. Thus, the total plate area is 4 times the integral.

4. The calculated I/B is compared to the desired electric current density per unit length value which is an input of the simulation. Depending on whether the result is smaller or larger than the desired input value of I/B , the charge density value at the electrode is adjusted arbitrarily.
5. A new charge density field is found based on the new charge density value at the electrode according to Eq. (H.4). For that, Eq. (H.4) is discretized using central difference formulas for the

electrostatic potential gradient, and backward difference formulas for the charge density gradients,

$$\begin{aligned} \rho_{f,i,j}^2 = & \epsilon_0 \left(\frac{\rho_{f,i,j} - \rho_{f,i-1,j}}{\Delta x} \frac{\phi_{i+1,j} - \phi_{i-1,j}}{2\Delta x} \right) \\ & + \epsilon_0 \left(\frac{\rho_{f,i,j} - \rho_{f,i,j-1}}{\Delta y} \frac{\phi_{i,j+1} - \phi_{i,j-1}}{2\Delta y} \right). \end{aligned} \quad (\text{H.7})$$

6. The procedure is repeated to find a new field for ϕ based on the newly calculated ρ_f field. Thereafter, steps 2. and 3. are repeated. The secant method (see [132]) is applied to find a new optimized value for the charge density at the electrode, $\rho_{f,elec}$. The procedure is then repeated until $\rho_{f,elec}$ converges within a pre-specified absolute or relative tolerance.

H.3 CYLINDRICAL ESP: 1-D CYLINDRICAL ELECTROQUASISTATIC FIELDS

Unlike in the 2-D planar case, for a concentric electrode-pipe configuration, it is possible to derive an analytical expression for the electric field and charge density field. The analytical solution is possible because a homogeneous electric field in the tangential and axial directions is physically feasible and can be assumed, thus simplifying the electroquasistatic problem into a 1-D problem. This is most readily observable in a positive corona discharge. Phenomenologically, the discharge or flow of a current in a corona is localized around the cathode (positively charged element) [133]. For a positive corona, the generation of electrons takes place within the gas, and the ionization of the air occurs in the regions of high electric field magnitude, i.e., close to the electrode. These conditions favour the formation of an electron cloud around the electrode, due to the ionization of the air, and as a consequence, a self-sustained electron avalanche from this electron cloud towards the electrode [133]. In a negative corona, the ionization of the air still occurs close to the electrode in the regions of high electric field magnitude, but now the generation of electrons takes place in the electrode itself due to the photoelectric effect. In this case, the electron cloud is formed and disrupted intermittently, given that it is being continually repelled due to its equal polarity with the electrode. Although the solenoidal current is maintained given that the asymptotic mobility ratio analysis is maintained as outlined in chapter 3, the here intermittent absence of the electron avalanche causes that the current between the anode (negative electrode) and the cathode (positively charged gas) is not uniform, e.g. $I_{cathode} \neq I_{anode}$ (in a planar context) [134]. This violates the zero divergence condition of the electric current density vector, if the latter one only has a radial component. However, the current can still be assumed to be uniform in a time-averaged context which considers an averaging

time significantly larger than the time scale of the before mentioned intermittency.

The analytical expressions for the electroquasistatic fields are summarized below and derived in [135]. A numerical method is also presented. This is because it is expected in the short future that the cylindrical ESP case is studied further with ODT in a case where the mobility ratio M_β does not approximate to 0, i.e., in a case where the electric current density vector is no longer solenoidal ($\nabla \cdot \underline{J} \neq 0$) due to the presence of temporal fluctuations of the charge density, or due to the presence of convective currents (see Eq. (3.52)).

H.3.1 Analytical solutions

For a 1-D electroquasistatic problem, the divergence condition imposed on the electric current density vector implies, as in [135],

$$rj_2 = r\rho_f\beta E_2 = \text{constant} \rightarrow I = 2\pi Br\rho_f\beta E_2 = \text{constant}. \quad (\text{H.8})$$

The electric current I is a given input to the simulations, similar to the planar case, where I/B is taken as an input (physical condition or physical BC). Here, B is the length of the electrode or length of the pipe (in the axial z direction). The radial electric field E_2 is given by the superposition of the electric fields due to the onset electric field (third BC for the electrostatic potential) and the electric field due to the ionic charge density, Eq. (3.51), see [135],

$$E_2 = \frac{1}{r\epsilon_0} \int_{r=r_{elec}}^{r=R} \rho_f r dr + E_{on,dist}. \quad (\text{H.9})$$

Here, the subindex *elec* refers to the electrode position. Eq. (H.9) refers to the same statement as that indicating that the solution of the electrostatic potential PDE, Eq. (H.1), is provided by the superposition of an homogeneous and a particular solution for ϕ [57]. The onset electric field is given by the surface integral representation of Eq. (3.51). This is the homogeneous solution for the electrostatic potential, i.e., without volumetric charge density,

$$E_{on,dist} S = q_{elec} \rightarrow E_{on,dist} = \frac{C}{r}. \quad (\text{H.10})$$

C is a constant. However, due to Eq. (2.17),

$$\phi_{on,dist} = \int_{r=r_{elec}}^{r=R} E_{on,dist} dr \rightarrow \phi_{on,dist} = C \ln \left| \frac{R}{r_{elec}} \right|. \quad (\text{H.11})$$

Therefore, the onset voltage is given by,

$$\phi_{on} = E_{on} r_{elec} \ln \left| \frac{R}{r_{elec}} \right|, \quad (\text{H.12})$$

while the onset electric field E_{on} is given by Peek's formula for air discharge in a concentric wire-cylinder configuration [130],

$$E_{on} = C_{1,Peek} \frac{N}{N_0} \left[1 + C_{2,Peek} \left(\frac{N}{N_0} r_{elec} \right)^{-\frac{1}{2}} \right]. \quad (\text{H.13})$$

Peek's formula constants $C_{1,Peek}$ and $C_{2,Peek}$ are 31×10^5 V/m and $0.0308 \text{ m}^{\frac{1}{2}}$, respectively. N/N_0 is the air relative density, with N_0 given by the air number density at standard conditions, $N_0 = 2.5 \times 10^{25} \text{ m}^{-3}$. In general, N is given by,

$$N = \frac{PC_{Av}}{R_u T}. \quad (\text{H.14})$$

R_u is the universal gas constant and C_{Av} is the Avogadro constant. Based on Eqs. (H.10) and (H.11), the appropriate representation for the electric field, due to the onset electrostatic potential is

$$E_{on,dist} = \frac{\phi_{on}}{r \ln \left| \frac{R}{r_{elec}} \right|}. \quad (\text{H.15})$$

With the obtained representation of the electric field by Eq. (H.9), it is now possible to solve for the charge density in Eq. (H.8) such that,

$$I = 2\pi B r \rho_f \beta \left(\frac{1}{r \epsilon_0} \int_{r=r_{elec}}^{r=R} \rho_f r dr + \frac{\phi_{on}}{r \ln \left| \frac{R}{r_{elec}} \right|} \right). \quad (\text{H.16})$$

Dividing this expression with respect to r results in an ODE for ρ_f (in r). This can be solved analytically, in order to arrive at the analytical solution for the charge density field [135],

$$\rho_f = \sqrt{\frac{1}{\frac{2\pi B \beta}{\epsilon_0 I} (r^2 - r_{elec}^2) + \left(\frac{2\pi B \beta \phi_{on}}{I \ln \left| \frac{R}{r_{elec}} \right|} \right)^2}}. \quad (\text{H.17})$$

The electric field can then be found by Eq. (H.9), see [135],

$$E_2 = \frac{1}{r} \sqrt{\frac{I}{2\pi B \beta \epsilon_0} (r^2 - r_{elec}^2) + \left(\frac{\phi_{on}}{\ln \left| \frac{R}{r_{elec}} \right|} \right)^2}. \quad (\text{H.18})$$

Finally, the electrostatic potential is found by integration of Eq. (H.18) with respect to r ,

$$\begin{aligned}
\phi = & \phi_{elec} - \sqrt{C_I (r^2 - r_{elec}^2) + C^2} \\
& + \sqrt{C^2 - C_I r_{elec}^2} \ln \left| \sqrt{C^2 - C_I r_{elec}^2} \sqrt{C_I (r^2 - r_{elec}^2) + C^2} + C^2 - C_I r_{elec}^2 \right| \\
& - \ln |r| \sqrt{C^2 - C_I r_{elec}^2} + C \\
& - \sqrt{C^2 - C_I r_{elec}^2} \ln \left| C \sqrt{C^2 - C_I r_{elec}^2} + C^2 - C_I r_{elec}^2 \right| \\
& + \ln |r_{elec}| \sqrt{C^2 - C_I r_{elec}^2}.
\end{aligned} \tag{H.19}$$

Note that $\phi_{elec} \neq \phi_{on}$. ϕ_{elec} can be obtained when $\phi_{plate} = 0$ and $r = R$ are substituted in Eq. (H.19). Here, ϕ_{elec} corresponds to the voltage of the characteristic voltage-current curve at the specified I . In Eq. (H.19), C and C_I are given by,

$$C = \frac{\phi_{on}}{\ln \left| \frac{R}{r_{elec}} \right|}, \quad C_I = \frac{I}{2\pi B \beta \epsilon_0}. \tag{H.20}$$

H.3.2 Numerical solution method

Two numerical solution methods are presented here. Both of these methods are best applicable, but not restricted, to positive corona discharge cases as in the analytical solution. This is again because of the characteristics of a positive corona discharge, which are used in the numerical method in order to determine the nature of the BCs which need to be used for both the electric field and the charge density field. As presented by [129], the solution of the Maxwell equations require, either an assumption on the magnitude of the electric field at the discharge electrode, or an assumption on the electric current value (plus the Dirichlet BCs for the electrostatic potential). Both assumptions are equivalent.

The first method, which is termed here *onset consistent method*, solves all of the Maxwell equations with the suggested BCs plus the assumption of the Kaptzov's hypothesis, and calculates the electric current in the system as a function of the electrostatic potential difference. The second method, which is called here *experimentally consistent*, uses the current and electrostatic potential difference measured in the experiments, in order to calculate the onset electric field at the electrode. In this thesis, the *experimentally consistent method* was used with a slight variation, so that the onset electric field is not iterated; rather, it was calculated directly by Peek's formula, Eq. (H.13). From the point of view of the solutions to the Maxwell equations, this is not consistent, given that the system is over-constrained. However, since the objective of this thesis is actually to measure the influences in the flow of a

given EHD body force by means of the change in the electroquasistatic potential energy, strict enforcement of the Maxwell equations was not given critical importance. Hence, the electric field and charge density fields are not required to be exact, given that for the evaluation of the electroquasistatic potential energy, only the electrostatic potential and a charge density difference are required instead.

In any case, the electrostatic potential difference and the electric current measured at the experiment are simply assumed as some external boundary condition. This would correspond, e.g., to an assumed electrical resistance of the electrode wire, which is independent of the flow dynamics. That is, the electrical resistance of the wire is given by some provided characteristic current-voltage curve, which is given only by the properties of the electrode material, and is not affected by the flow.

H.3.2.1 Method 1: Onset consistent numerical method

1. The numerical method begins by assuming a uniform zero charge density field $\rho_f(r)$. The onset electric field BC, E_{on} , is calculated by Eq. (H.13) and the Kaptzov's hypothesis is assumed [129].
2. Gauss's law, Eq. (3.51), is then discretized and solved using a FDM, considering the following BCs for the electric field: E_{on} is assumed at the emitter, i.e., at $r = r_{elec}$ while a zero gradient condition for the electric field is assumed at the pipe wall (grounded plate). The latter BC is derived from the application of the surface integral form of Gauss's law at an infinitesimal control volume which crosses the grounded plate (the divergence of the 1-D electric field, or the radially weighted radial derivative, is zero in the absence of a surface charge density at the grounded plate). Eq. (3.51) is discretized as,

$$\frac{1}{2r_i \Delta r} (r_{i+1} E_{2,i+1} - r_{i-1} E_{2,i-1}) = \frac{\rho_{f,i}}{\epsilon_0}. \quad (\text{H.21})$$

Here, the subindex i refers to the grid point index in an equidistant radial grid. The resulting tridiagonal linear system of equations is solved using a Tridiagonal Matrix Algorithm (Thomas algorithm) (TDMA) [136].

3. The electrostatic potential difference corresponding to the previously calculated electric field is determined. This was done by the calculation of the integral,

$$\Delta\phi = - \int_{r=0}^{r=R} E_2 dr = - \sum_i E_{2,i+\frac{1}{2}} \Delta r_i. \quad (\text{H.22})$$

Here, i refers to the grid point index and $i + 1/2$ is an intermediate point between grid points, or the center of a cell defined

between two grid points. The calculated $\Delta\phi$ is most likely not in agreement with the BCs of the electrostatic potential. Therefore, the charge density at the electrode is modified by assuming now a very small value.

4. The electric current I is determined with the new value of charge density at the electrode, plus the electric field BC (Kaptzov's hypothesis) and the given positive ionic mobility, i.e.,

$$I = \rho_{f,elec}\beta E_{on}(2\pi r_{elec}B). \quad (\text{H.23})$$

5. A new charge density field is evaluated from the obtained electric field and the charge continuity equation, Eq. (3.64), as in Eq. (H.8). That is,

$$\rho_{f,i} = \frac{I}{2\pi B\beta r_i E_{2,i}}. \quad (\text{H.24})$$

6. The process is repeated from step 2. with the new assumed charge density field. After obtaining the new electric field, the value of the charge density at the electrode is now calculated based on the secant method, in order to minimize the residual between the obtained electrostatic potential difference between pipe wall and electrode and the imposed BCs for ϕ . That is, the before mentioned residual is calculated as,

$$f_{res} = \left| (\phi_{BC,r=r_{elec}} - \phi_{BC,r=R}) - \sum_i E_{2,i+\frac{1}{2}}\Delta r_i \right|. \quad (\text{H.25})$$

And the new charge density at the electrode is calculated using the secant method as,

$$\rho_{f,elec}^{n+1} = \rho_{f,elec}^n - \frac{f_{res}^n (\rho_{f,elec}^{n-1} - \rho_{f,elec}^n)}{f_{res}^{n-1} - f_{res}^n}. \quad (\text{H.26})$$

Here, $n-1$, n and $n+1$ refer to the values of the charge density at the electrode in the previous, current and next iteration. This process is repeated until the residual function given by Eq. (H.25) converges within a pre-specified absolute or relative tolerance. The process finishes with the final radial profiles for the electric field and the charge density.

7. The final radial profile for the electrostatic potential is calculated with the converged charge density field using Gauss's law, i.e., $\nabla^2\phi = -\rho_f/\epsilon_0$. Gauss's law is discretized in this case as,

$$\frac{1}{r_i} \frac{\phi_{i+1} - \phi_{i-1}}{2\Delta r} + \frac{\phi_{i+1} - 2\phi_i + \phi_{i-1}}{\Delta r^2} = -\frac{\rho_{f,i}}{\epsilon_0}. \quad (\text{H.27})$$

The Dirichlet BCs for the electrostatic potential at the emitter electrode ϕ_{elec} and $\phi_{plate} = 0$ are used in order to solve the resulting tridiagonal linear system of equations with a TDMA [136].

H.3.2.2 Method 2: Experimentally consistent numerical method

1. The numerical method begins by assuming an arbitrary nonzero uniform charge density field $\rho_f(r)$. The onset electric field BC, E_{on} , is calculated by Eq. (H.13) and the Kaptzov's hypothesis is assumed [129].
2. Gauss's law, Eq. (3.51), is then discretized and solved using a FDM considering the following BCs for the electric field: E_{on} is assumed at the emitter, i.e., at $r = r_{elec}$, while a zero gradient condition for the electric field is assumed at the pipe wall (grounded plate). Eq. (3.51) is discretized as Eq. (H.21), and solved correspondingly, as in the *onset consistent method*.
3. In comparison with the *onset consistent method*, the electric current I is taken directly from the experimental measurements. The iteration process must proceed nevertheless in order to fit the electric field. A new charge density field is evaluated from the obtained electric field and the charge continuity equation, Eq. (H.24).
4. It is clear that this charge density field is most likely different to the one assumed at the beginning of the procedure. Therefore, a new onset value for the electric field, E_{on} is assigned. In practice, a 2% increase is used in this thesis. With this new value of E_{on} and the new charge density field, a new electric field is calculated, according to Eq. (H.21). The electrostatic potential difference corresponding to such field is then determined and the new value of the onset electric field E_{on} is now calculated based on the secant method in order to minimize the residual between the obtained electrostatic potential difference between the pipe wall and the electrode, and the imposed BCs for ϕ . The residual is calculated per Eq. (H.25). The new onset electric field value is calculated by the secant method as,

$$E_{on}^{n+1} = E_{on}^n - \frac{f_{res}^n (E_{on}^{n-1} - E_{on}^n)}{f_{res}^{n-1} - f_{res}^n}. \quad (\text{H.28})$$

Here, $n - 1$, n and $n + 1$ refer to the values of the onset electric field in the previous, current and next iteration. This process is repeated until the residual function given by Eq. (H.25) converges within a pre-specified absolute or relative tolerance. The process finishes with the final radial profiles for the electric field and the charge density.

5. The final radial profile for the electrostatic potential is calculated with the converged charge density field using Gauss's law, i.e., $\nabla^2\phi = -\rho_f/\epsilon_0$. Gauss's law is discretized as in Eq. (H.27). The

Dirichlet BCs for the electrostatic potential at the emitter electrode ϕ_{elec} and $\phi_{plate} = 0$ are used in order to solve the resulting tridiagonal linear system of equations with a TDMA [136].

H.3.2.3 *Modified experimentally consistent method used in this thesis (modified method 2)*

As already discussed, a variation of the previously explained method 2 is used in this thesis.

1. Same as in method 2. The numerical method begins by assuming an arbitrary nonzero uniform charge density field $\rho_f(r)$. The onset electric field BC, E_{on} , is calculated by Eq. (H.13) and the Kaptzov's hypothesis is assumed [129].
2. Same as in method 2. Gauss's law, Eq. (3.51), is then discretized and solved using a FDM considering the following BCs for the electric field: E_{on} is assumed at the emitter, i.e., at $r = r_{elec}$, while a zero gradient condition for the electric field is assumed at the pipe wall (grounded plate).
3. Same as in method 2. The electric current I is taken directly from the experimental measurements. The iteration process must proceed in order to fit the electric field. A new charge density field is evaluated from the obtained electric field and the charge continuity equation, Eq. (H.24).
4. The process is repeated from step 2. with the new assumed charge density field (fixed point iteration). This process is repeated until the maximum norm of the difference between the assumed and the recalculated charge density field (maximum difference in the radial grid) converges within a pre-specified absolute or relative tolerance. The process finishes with the final radial profiles for the electric field and the charge density, respectively.
5. The final radial profile for the electrostatic potential is calculated with the converged charge density field using Gauss's law, i.e., $\nabla^2\phi = -\rho_f/\epsilon_0$. Gauss's law is discretized as in Eq. (H.27). The Dirichlet BCs for the electrostatic potential at the emitter electrode ϕ_{elec} and $\phi_{plate} = 0$ are used in order to solve the resulting tridiagonal linear system of equations with a TDMA [136].

BIBLIOGRAPHY

- [1] D. Bernoulli. *Hydrodynamica: sive de viribus et motibus fluidorum commentarii*. Johannis Reinholdi Dulseckeri, 1738.
- [2] G.K. Mikhailov. "Chapter 9 - Daniel Bernoulli, *Hydrodynamica* (1738)." In: *Landmark Writings in Western Mathematics 1640-1940*. Ed. by I. Grattan-Guinness, Roger Cooke, Leo Corry, Pierre Crépel, and Niccolo Guicciardini. Amsterdam: Elsevier Science, 2005, pp. 131–142. ISBN: 978-0-444-50871-3. DOI: <https://doi.org/10.1016/B978-044450871-3/50090-5>.
- [3] J. C. Maxwell. "V. Illustrations of the dynamical theory of gases.—Part I. On the motions and collisions of perfectly elastic spheres." In: *The London, Edinburgh, and Dublin Philosophical Magazine and Journal of Science* 19.124 (1860), pp. 19–32.
- [4] J. C. Maxwell. *A treatise on electricity and magnetism*. Vol. 1. Clarendon press, 1873.
- [5] O. Reynolds. "III. An experimental investigation of the circumstances which determine whether the motion of water shall be direct or sinuous, and of the law of resistance in parallel channels." In: *Proc. R. Soc. Lond.* 35.224-226 (1883), pp. 84–99. DOI: [10.1098/rspl.1883.0018](https://doi.org/10.1098/rspl.1883.0018).
- [6] C. L. Navier. "Sur les Lois des Mouvement des Fluides, en Ayant Egard a L'adhesion des Molecules." In: *Annales de Chimie et de Physique* 19 (1821), pp. 244–260.
- [7] J. Bertrand. "Sur l'homogénéité dans les formules de physique." In: *Cahiers de recherche de l'Academie de Sciences* 86 (1878), pp. 916–920.
- [8] K. Avila, D. Moxey, A. Lozar, M. Avila, D. Barkley, and B. Hof. "The Onset of Turbulence in Pipe Flow." In: *Science* 333 (2011), pp. 192–196. DOI: [10.1126/science.1203223](https://doi.org/10.1126/science.1203223).
- [9] Y. Çengel and J. Cimbala. *Fluid mechanics: Fundamentals and applications*. McGraw-Hill, 2006.
- [10] W. Gilbert. *De Magnete*. Translation: Chiswick Press, London, 1901. 1600.
- [11] K. Adamiak. "Numerical models in simulating wire-plate electrostatic precipitators: A review." In: *J. Electrostat.* 71.4 (2013), pp. 673–680. DOI: [10.1016/j.elstat.2013.03.001](https://doi.org/10.1016/j.elstat.2013.03.001).
- [12] M. Bazant. *10.626 Electrochemical Energy Systems*. Massachusetts Institute of Technology: MIT OpenCourseWare. License: Creative Commons BY-NC-SA. 2014. URL: <https://ocw.mit.edu>.

- [13] M. Robinson. "Movement of air in the electric wind of the corona discharge." In: *Trans. Am. Inst. Electr. Eng., Part 1* 80.2 (1961), pp. 143–150. DOI: [10.1109/TCE.1961.6373091](https://doi.org/10.1109/TCE.1961.6373091).
- [14] F. Hauksbee. *Physico-Mechanical Experiments On Various Subjects*. London: R. Brugis, 1709.
- [15] C. J. C. Biscombe. "The Discovery of Electrokinetic Phenomena: Setting the Record Straight." In: *Angew. Chem., Int. Ed.* 56.29 (2017), pp. 8338–8340. DOI: [10.1002/anie.201608536](https://doi.org/10.1002/anie.201608536).
- [16] N. Gautherot. "Mémoire sur le galvanisme." In: *Annales de Chimie ou Recueil* 1.39 (1801), pp. 203–210.
- [17] F. F. Reuss. "Sur un nouvel effet de l'électricité galvanique." In: *Mem. Soc. Imp. Natur. Moscou* 2 (1809), pp. 327–337.
- [18] *Millenium Problems: Navier-Stokes Equation*. Accessed: 2019-11-03. URL: <https://www.claymath.org/millennium-problems/navier%E2%80%93stokes-equation>.
- [19] L. F. Richardson. *Weather prediction by numerical process*. Cambridge university press, 1922.
- [20] L. F. Richardson. "The supply of energy from and to atmospheric eddies." In: *Proc. R. Soc. London, Ser. A* 97.686 (1920), pp. 354–373. DOI: [10.1098/rspa.1920.0039](https://doi.org/10.1098/rspa.1920.0039).
- [21] A. N. Kolmogorov. "The local structure of turbulence in incompressible viscous fluid for very large Reynolds numbers." In: *Proc. R. Soc. London, Ser. A* 434.1890 (1991), pp. 9–13. DOI: [10.1098/rspa.1991.0075](https://doi.org/10.1098/rspa.1991.0075).
- [22] R. Lewandowski and B. Pinier. "The Kolmogorov Law of Turbulence What Can Rigorously Be Proved? Part II." In: *The Foundations of Chaos Revisited: From Poincaré to Recent Advancements*. Ed. by Christos Skiadas. Cham: Springer International Publishing, 2016, pp. 71–89. DOI: [10.1007/978-3-319-29701-9_5](https://doi.org/10.1007/978-3-319-29701-9_5).
- [23] J. Jiménez. "The physics of wall turbulence." In: *Phys. A (Amsterdam, Neth.)* 263.1 (1999). Proceedings of the 20th IUPAP International Conference on Statistical Physics, pp. 252–262. ISSN: 0378-4371. DOI: [https://doi.org/10.1016/S0378-4371\(98\)00507-X](https://doi.org/10.1016/S0378-4371(98)00507-X).
- [24] I. Marusic, B. J. McKeon, P. A. Monkewitz, H. M. Nagib, A. J. Smits, and K. R. Sreenivasan. "Wall-bounded turbulent flows at high Reynolds numbers: recent advances and key issues." In: *Phys. Fluids* 22.6 (2010), p. 065103. DOI: [10.1063/1.3453711](https://doi.org/10.1063/1.3453711).
- [25] M. Hultmark, M. Vallikivi, S. C. C. Bailey, and A. J. Smits. "Turbulent pipe flow at extreme Reynolds numbers." In: *Phys. Rev. Lett.* 108.9 (2012), p. 094501. DOI: [10.1103/PhysRevLett.108.094501](https://doi.org/10.1103/PhysRevLett.108.094501).

- [26] J. Kim, P. Moin, and R. Moser. "Turbulence Statistics in fully developed channel flow at low Reynolds number." In: *J. Fluid Mech.* 177 (1987), pp. 133–166. DOI: [10.1017/S0022112087000892](https://doi.org/10.1017/S0022112087000892).
- [27] R. Moser, J. Kim, and N. Mansour. "Direct Numerical Simulation of turbulent channel flow up to $Re_\tau = 590$." In: *Phys. Fluids* 11.4 (1999), pp. 943–945. DOI: [10.1063/1.869966](https://doi.org/10.1063/1.869966).
- [28] H. Abe, H. Kawamura, and Y. Matsuo. "Direct Numerical Simulation of a Fully Developed Turbulent Channel Flow With Respect to the Reynolds Number Dependence." In: *J. Fluids Eng* 123.2 (2001).
- [29] J. C. Del Álamo, J. Jiménez, P. Zandonade, and R. Moser. "Scaling of the energy spectra of turbulent channels." In: *J. Fluid Mech.* 500 (2004), pp. 135–144. DOI: [10.1017/S002211200300733X](https://doi.org/10.1017/S002211200300733X).
- [30] S. Hoyas and J. Jimenez. "Scaling of the velocity fluctuations in turbulent channels up to $Re_\tau = 2003$." In: *Phys. Fluids* 18.011702 (2006). DOI: [10.1063/1.2162185](https://doi.org/10.1063/1.2162185).
- [31] M. Lee and R. Moser. "Direct Numerical Simulation of turbulent channel flow up to $Re_\tau = 5200$." In: *J. Fluid Mech.* 774 (2015), pp. 395–415. DOI: [10.1017/jfm.2015.268](https://doi.org/10.1017/jfm.2015.268).
- [32] S. B. Pope. *Turbulent flows*. IOP Publishing, 2001.
- [33] M. Everts and J. P. Meyer. "Heat transfer of developing and fully developed flow in smooth horizontal tubes in the transitional flow regime." In: *Int. J. Heat Mass Transfer* 117 (2018), pp. 1331–1351. DOI: [10.1016/j.ijheatmasstransfer.2017.10.071](https://doi.org/10.1016/j.ijheatmasstransfer.2017.10.071).
- [34] M. Everts and J. P. Meyer. "Relationship between pressure drop and heat transfer of developing and fully developed flow in smooth horizontal circular tubes in the laminar, transitional, quasi-turbulent and turbulent flow regimes." In: *Int. J. Heat Mass Transfer* 117 (2018), pp. 1231–1250. DOI: <https://doi.org/10.1016/j.ijheatmasstransfer.2017.10.072>.
- [35] M. Everts and J. P. Meyer. "Single-phase mixed convection of developing and fully developed flow in smooth horizontal circular tubes in the laminar and transitional flow regimes." In: *Int. J. Heat Mass Transfer* 117 (2018), pp. 1251–1273. DOI: [10.1016/j.ijheatmasstransfer.2017.10.070](https://doi.org/10.1016/j.ijheatmasstransfer.2017.10.070).
- [36] M. Everts and J. P. Meyer. "Flow regime maps for smooth horizontal tubes at a constant heat flux." In: *Int. J. Heat Mass Transfer* 117 (2018), pp. 1274–1290. DOI: [10.1016/j.ijheatmasstransfer.2017.10.073](https://doi.org/10.1016/j.ijheatmasstransfer.2017.10.073).
- [37] V. Gnielinski. "On heat transfer in tubes." In: *Int. J. Heat Mass Transfer* 63 (2013), pp. 134–140. DOI: <https://doi.org/10.1016/j.ijheatmasstransfer.2013.04.015>.

- [38] D. M. McEligot, C. W. Coon, and H. C. Perkins. "Relaminarization in tubes." In: *Int. J. Heat Mass Transfer* 13.2 (1970), pp. 431–433. DOI: [10.1016/0017-9310\(70\)90118-3](https://doi.org/10.1016/0017-9310(70)90118-3).
- [39] S. Satake, T. Kunugi, and R. Himeno. "High Reynolds number computation for turbulent heat transfer in a pipe flow." In: *International Symposium on High Performance Computing*. Springer, 2000, pp. 514–523. DOI: [10.1007/3-540-39999-2_49](https://doi.org/10.1007/3-540-39999-2_49).
- [40] X. Wu and P. Moin. "A direct numerical simulation study on the mean velocity characteristics in turbulent pipe flow." In: *J. Fluid Mech.* 608 (2008), pp. 81–112. DOI: [10.1017/S0022112008002085](https://doi.org/10.1017/S0022112008002085).
- [41] C. Chin, J. P. Monty, and A. Ooi. "Reynolds number effects in DNS of pipe flow and comparison with channels and boundary layers." In: *Int. J. Heat Fluid Flow* 45 (2014), pp. 33–40. DOI: [10.1016/j.ijheatfluidflow.2013.11.007](https://doi.org/10.1016/j.ijheatfluidflow.2013.11.007).
- [42] J. Ahn, J. H. Lee, J. Lee, J.-H. Kang, and H. J. Sung. "Direct numerical simulation of a 30R long turbulent pipe flow at $Re = 3008$." In: *Phys. Fluids* 27.6 (2015), p. 065110. DOI: [10.1063/1.4922612](https://doi.org/10.1063/1.4922612).
- [43] F. C. Nicoud. *Numerical study of a channel flow with variable properties*. CTR Annual Research Briefs 1998. 1998.
- [44] S. Ghosh, H. Foysi, and R. Friedrich. "Compressible turbulent channel and pipe flow: similarities and differences." In: *J. Fluid Mech.* 648 (2010), pp. 155–181. DOI: [10.1017/S0022112009993004](https://doi.org/10.1017/S0022112009993004).
- [45] X. Xu, J. S. Lee, and R. Pletcher. "A compressible finite volume formulation for large eddy simulation of turbulent pipe flows at low Mach number in Cartesian coordinates." In: *J. Comput. Phys.* 203 (2005), pp. 22–48. DOI: [10.1016/j.jcp.2004.08.005](https://doi.org/10.1016/j.jcp.2004.08.005).
- [46] J. H. Bae, J. Y. Yoo, H. Choi, and D. M. McEligot. "Effects of large density variation on strongly heated internal air flows." In: *Phys. Fluids* 18.7 (2006), p. 075102. DOI: [10.1063/1.2216988](https://doi.org/10.1063/1.2216988).
- [47] D. Modesti and S. Pirozzoli. "Direct numerical simulation of supersonic pipe flow at moderate Reynolds number." In: *Int. J. Heat Fluid Flow* 76 (2019), pp. 100–112. DOI: <https://doi.org/10.1016/j.ijheatfluidflow.2019.02.001>.
- [48] M. S. Cha, S. M. Lee, K. T. Kim, and S. H. Chung. "Soot suppression by nonthermal plasma in coflow jet diffusion flames using a dielectric barrier discharge." In: *Combust. Flame* 141.4 (2005), pp. 438–447. DOI: [10.1016/j.combustflame.2005.02.002](https://doi.org/10.1016/j.combustflame.2005.02.002).
- [49] M. M. Ohadi, D. A. Nelson, and S. Zia. "Heat transfer enhancement of laminar and turbulent pipe flow via corona discharge." In: *Int. J. Heat Mass Transfer* 34.4 (1991), pp. 1175–1187. ISSN: 0017-9310. DOI: [https://doi.org/10.1016/0017-9310\(91\)90026-B](https://doi.org/10.1016/0017-9310(91)90026-B).

- [50] D. A. Nelson, S. Zia, R. L. Whipple, and M. M. Ohadi. "Corona discharge effects on heat transfer and pressure drop in tube flows." In: *J. Enh. Heat Transfer* 7.2 (2000). DOI: [10.1615/JEnhHeatTransf.v7.i2.20](https://doi.org/10.1615/JEnhHeatTransf.v7.i2.20).
- [51] T. Yamamoto. "Electrohydrodynamic secondary flow interaction in an electrostatic precipitator." PhD thesis. The Ohio State University, 1979. URL: http://rave.ohiolink.edu/etdc/view?acc_num=osu1487089582132054.
- [52] W. Zhao and G. Wang. "Scaling of velocity and scalar structure functions in ac electrokinetic turbulence." In: *Phys. Rev. E* 95.2 (2017), p. 023111. DOI: [10.1103/PhysRevE.95.023111](https://doi.org/10.1103/PhysRevE.95.023111).
- [53] A. Soldati and S. Banerjee. "Turbulence modification by large-scale organized electrohydrodynamic flows." In: *Phys. Fluids* 10.7 (1998), pp. 1742–1756. DOI: [10.1063/1.869691](https://doi.org/10.1063/1.869691).
- [54] IEEE-DEIS-EHD Technical Committee. "Recommended international standard for dimensionless parameters used in electrohydrodynamics." In: *IEEE Trans. DEI* 10.1 (2003), pp. 3–6. DOI: [10.1109/TDEI.2003.1176545](https://doi.org/10.1109/TDEI.2003.1176545).
- [55] W. K. H. Panofsky and M. Phillips. *Classical electricity and magnetism*. Vol. 2. Addison-Wesley Publishing Company, Inc., 1962.
- [56] J. R. Melcher. *Continuum electromechanics*. Vol. 2. MIT press Cambridge, 1981.
- [57] H. A. Haus and J. R. Melcher. *Electromagnetic fields and energy*. Accessed on 28.12.2019. Also available from Prentice-Hall: Englewood Cliffs, NJ, 1989. ISBN: 9780132490207. License: Creative Commons Attribution-Noncommercial-Share Alike. URL: <https://ocw.mit.edu/resources/res-6-001-electromagnetic-fields-and-energy-spring-2008>.
- [58] S. Kumar and D. Ramkrishna. "On the solution of population balance equations by discretization—I. A fixed pivot technique." In: *Chem. Eng. Sci.* 51.8 (1996), pp. 1311–1332. DOI: [10.1016/0009-2509\(96\)88489-2](https://doi.org/10.1016/0009-2509(96)88489-2).
- [59] R. B. Bird, W. E. Stewart, and E. N. Lightfoot. *Transport phenomena*. John Wiley & Sons, 2007.
- [60] C. G. Speziale. "Turbulence modeling for time-dependent RANS and VLES: a review." In: *AIAA Journal* 36.2 (1998), pp. 173–184. DOI: [10.2514/2.7499](https://doi.org/10.2514/2.7499).
- [61] B. Chaouat. "The state of the art of hybrid RANS/LES modeling for the simulation of turbulent flows." In: *Flow, Turbul. Combust.* 99.2 (2017), pp. 279–327. DOI: [10.1007/s10494-017-9828-8](https://doi.org/10.1007/s10494-017-9828-8).

- [62] A. R. Kerstein. "One-dimensional turbulence: model formulation and application to homogeneous turbulence, shear flows, and buoyant stratified flows." In: *J. Fluid Mech.* 392 (1999), pp. 277–334. DOI: [10.1017/S0022112099005376](https://doi.org/10.1017/S0022112099005376).
- [63] A. R. Kerstein. "Linear-eddy modelling of turbulent transport. Part 6. Microstructure of diffusive scalar mixing fields." In: *J. Fluid Mech.* 231 (1991), pp. 361–394. DOI: <https://doi.org/10.1017/S0022112091003439>.
- [64] D. Lignell, A. R. Kerstein, G. Sun, and E. Monson. "Mesh adaptation for efficient multiscale implementation of One-Dimensional Turbulence." In: *Theor. Comput. Fluid Dyn.* 27.3-4 (2013), pp. 273–295. DOI: [10.1007/s00162-012-0267-9](https://doi.org/10.1007/s00162-012-0267-9).
- [65] L. Prandtl. "7. Bericht über Untersuchungen zur ausgebildeten Turbulenz." In: *Z. Angew. Math. Mech.* 5.2 (1925), pp. 136–139. DOI: [10.1002/zamm.19250050212](https://doi.org/10.1002/zamm.19250050212).
- [66] D. Lignell, V. B. Lansinger, J. A. Medina Méndez, M. Klein, A. R. Kerstein, H. Schmidt, M. Fistler, and M. Oevermann. "One-dimensional turbulence modeling for cylindrical and spherical flows: model formulation and application." In: *Theor. Comput. Fluid Dyn.* 32.4 (2018), pp. 495–520. DOI: [10.1007/s00162-018-0465-1](https://doi.org/10.1007/s00162-018-0465-1).
- [67] P. A. W. Lewis and G. S. Shedler. "Simulation of nonhomogeneous poisson processes by thinning." In: *Naval Res. Logistics Quart.* 26.3 (1979), pp. 403–413. DOI: [10.1002/nav.3800260304](https://doi.org/10.1002/nav.3800260304).
- [68] R. McDermott. "Towards One-Dimensional Turbulence Subgrid Closure for Large-Eddy Simulation." PhD thesis. University of Utah, 2005.
- [69] W. T. Ashurst and A. R. Kerstein. "One-dimensional turbulence: Variable-density formulation and application to mixing layers." In: *Phys. Fluids* 17.2 (2005), p. 025107. DOI: [10.1063/1.1847413](https://doi.org/10.1063/1.1847413).
- [70] W. T. Ashurst and A. R. Kerstein. "Erratum: "One-dimensional turbulence: Variable-density formulation and application to mixing layers"." In: *Phys. Fluids* 21.11 (2009), p. 119901. DOI: [10.1063/1.3266876](https://doi.org/10.1063/1.3266876).
- [71] J. Sutherland, N. Punati, and A. R. Kerstein. *A Unified Approach to the Various Formulations of the One-Dimensional-Turbulence Model*. Tech. rep. 100101. Institute for Clean and Secure Energy (ICSE), 2010. URL: www.researchgate.net/profile/Alan_Kerstein/publication/266471770_A_Unified_Approach_to_the_Various_Formulations_of_the_One-Dimensional-Turbulence_Model.

- [72] J. A. Medina Méndez, M. Klein, and H. Schmidt. “One-Dimensional Turbulence investigation of variable density effects due to heat transfer in a low Mach number internal air flow.” In: *Int. J. Heat Fluid Flow* 80.108481 (2019). DOI: [10.1016/j.ijheatfluidflow.2019.108481](https://doi.org/10.1016/j.ijheatfluidflow.2019.108481).
- [73] Z. Jozefik, A. R. Kerstein, H. Schmidt, S. Lyra, H. Kolla, and J. Chen. “One-dimensional turbulence modeling of a turbulent counterflow flame with comparison to DNS.” In: *Combust. Flame* 162 (2015), pp. 2999–3015. DOI: [10.1016/j.combustflame.2015.05.010](https://doi.org/10.1016/j.combustflame.2015.05.010).
- [74] J. A. Medina Méndez, H. Schmidt, F. Mauss, and Z. Jozefik. “Constant volume n-Heptane autoignition using One-Dimensional Turbulence.” In: *Combust. Flame* 190 (2018), pp. 388–401. DOI: [10.1016/j.combustflame.2017.12.015](https://doi.org/10.1016/j.combustflame.2017.12.015).
- [75] A. R. Kerstein, W. T. Ashurst, S. Wunsch, and V. Nilsen. “One-dimensional turbulence: Vector formulation and application to free-shear flows.” In: *J. Fluid Mech.* 447 (2001), pp. 85–109. DOI: [10.1017/S0022112001005778](https://doi.org/10.1017/S0022112001005778).
- [76] J. H. Davidson and E. J. Shaughnessy. “Turbulence generation by electric body forces.” In: *Exp. Fluids* 4.1 (1986), pp. 17–26. DOI: [10.1007/BF00316781](https://doi.org/10.1007/BF00316781).
- [77] J. C. R. Hunt. “Effects of Body Forces on Turbulence.” In: *Advances in Turbulence V*. Ed. by Roberto Benzi. Dordrecht: Springer Netherlands, 1995, pp. 229–235. ISBN: 978-94-011-0457-9.
- [78] Z. Jozefik, A. R. Kerstein, and H. Schmidt. “Towards a Compressible Reactive Multiscale Approach Based on One-Dimensional Turbulence.” In: *Active Flow and Combustion Control*. Springer, 2014, pp. 197–211. DOI: [10.1007/978-3-319-11967-0](https://doi.org/10.1007/978-3-319-11967-0).
- [79] S. Wunsch and A. R. Kerstein. “A model for layer formation in stably stratified turbulence.” In: *Phys. Fluids* 13.3 (2001), pp. 702–712. DOI: [10.1063/1.1344182](https://doi.org/10.1063/1.1344182).
- [80] E. D. Gonzalez-Juez, A. R. Kerstein, and D. Lignell. “Reactive Rayleigh–Taylor turbulent mixing: a one-dimensional-turbulence study.” In: *Geophys. Astrophys. Fluid Dyn.* 107.5 (2013), pp. 506–525. DOI: [10.1080/03091929.2012.736504](https://doi.org/10.1080/03091929.2012.736504).
- [81] F. Meiselbach. “Application of ODT to turbulent flow problems.” PhD thesis. Brandenburgische Technische Universität Cottbus-Senftenberg, 2015.
- [82] M. Klein. *Buoyant ODT in Planar, Cylindrical and Spherical Geometry with Position-Dependent Gravity*. Private communication. 2018.

- [83] A. Abdelsamie, G. Fru, T. Oster, F. Dietzsch, G. Janiga, and D. Thévenin. "Towards direct numerical simulations of low-Mach number turbulent reacting and two-phase flows using immersed boundaries." In: *Comput. Fluids* 131 (2016), pp. 123–141. DOI: [10.1016/j.compfluid.2016.03.017](https://doi.org/10.1016/j.compfluid.2016.03.017).
- [84] B. Savard and G. Blanquart. "Broken reaction zone and differential diffusion effects in high Karlovitz n-C₇H₁₆ premixed turbulent flames." In: *Combust. Flame* 162.5 (2015), pp. 2020–2033. DOI: <https://doi.org/10.1016/j.combustflame.2014.12.020>.
- [85] R. Yu, J. Yu, and X.-S. Bai. "An improved high-order scheme for DNS of low Mach number turbulent reacting flows based on stiff chemistry solver." In: *J. Comput. Phys.* 231.16 (2012), pp. 5504–5521. DOI: <https://doi.org/10.1016/j.jcp.2012.05.006>.
- [86] W. E. Pazner, A. Nonaka, J. B. Bell, M. S. Day, and M. L. Minion. "A high-order spectral deferred correction strategy for low Mach number flow with complex chemistry." In: *Combust. Theory Modell.* 20.3 (2016), pp. 521–547. DOI: [10.1080/13647830.2016.1150519](https://doi.org/10.1080/13647830.2016.1150519).
- [87] E. Motheau and J. Abraham. "A high-order numerical algorithm for DNS of low-Mach-number reactive flows with detailed chemistry and quasi-spectral accuracy." In: *J. Comput. Phys.* 313 (2016), pp. 430–454. ISSN: 0021-9991. DOI: <https://doi.org/10.1016/j.jcp.2016.02.059>.
- [88] P. Atten, F. M. J. McCluskey, and A. C. Lahjomri. "The Electrohydrodynamic Origin of Turbulence in Electrostatic Precipitators." In: *IEEE Trans. Ind. Appl.* IA-23.4 (1987), pp. 705–711. DOI: [10.1109/TIA.1987.4504969](https://doi.org/10.1109/TIA.1987.4504969).
- [89] J. Principe and R. Codina. "Mathematical models for thermally coupled low speed flows." In: *Adv. Theor. Appl. Mech.* 2.2 (2009), pp. 93–112.
- [90] B. Müller. "Low-Mach-Number Asymptotics of the Navier-Stokes Equations." In: *J. Eng. Math.* 34.1 (1998), pp. 97–109. DOI: [10.1023/A:1004349817404](https://doi.org/10.1023/A:1004349817404).
- [91] J. A. Medina M., H. Schmidt, and D. Lignell. *Application of the One-Dimensional Turbulence model to incompressible channel and pipe flow*. Unpublished results. Article submitted to *Z. Angew. Math. Mech.* 2019. URL: https://ignite.byu.edu/public/Medina_2019.pdf.
- [92] G. I. Taylor. "The spectrum of turbulence." In: *Proc. R. Soc. London, Ser. A* 164.919 (1938), pp. 476–490. DOI: [10.1098/rspa.1938.0032](https://doi.org/10.1098/rspa.1938.0032).

- [93] N. Krishnamoorthy. "Reaction Models and Reaction State Parametrization for Turbulent Non-Premixed Combustion." PhD thesis. University of Utah, 2008.
- [94] G. K. El Khoury, P. Schlatter, A. Noorani, P. F. Fischer, G. Brethouwer, and A. V. Johansson. "Direct Numerical Simulation of Turbulent Pipe Flow at Moderately High Reynolds Numbers." In: *Flow, Turbul. Comb.* 91.3 (2013), pp. 475–495. DOI: [10.1007/s10494-013-9482-8](https://doi.org/10.1007/s10494-013-9482-8).
- [95] M. Fagner and H. Schmidt. "Investigating asymptotic suction boundary layers using a one-dimensional stochastic turbulence model." In: *J. Turbul.* 18.10 (2017). DOI: [10.1080/14685248.2017.1335869](https://doi.org/10.1080/14685248.2017.1335869).
- [96] R. C. Schmidt, A. R. Kerstein, S. Wunsch, and V. Nilsen. "Near-wall LES closure based on one-dimensional turbulence modeling." In: *J. Comput. Phys.* 186 (2003), pp. 317–355. DOI: [10.1016/S0021-9991\(03\)00071-8](https://doi.org/10.1016/S0021-9991(03)00071-8).
- [97] J. Jiménez, S. Hoyas, M. Simens, and Y. Mizuno. "Turbulent boundary layers and channels at moderate Reynolds numbers." In: *J. Fluid Mech.* 657 (2010), pp. 335–360. DOI: [10.1017/S0022112010001370](https://doi.org/10.1017/S0022112010001370).
- [98] F. T. Schulz, C. Glawe, H. Schmidt, and A. R. Kerstein. "Toward modeling of CO₂ multi-phase flow patterns using a stochastic multi-scale approach." In: *Environ. Earth Sci.* 70.8 (2013), pp. 3739–3748. DOI: [10.1007/s12665-013-2461-5](https://doi.org/10.1007/s12665-013-2461-5).
- [99] D. G. Goodwin, R. L. Speth, H. K. Moffat, and B. W. Weber. *Cantera: An Object-oriented Software Toolkit for Chemical Kinetics, Thermodynamics, and Transport Processes*. Version 2.4.0. 2018. DOI: [10.5281/zenodo.1174508](https://doi.org/10.5281/zenodo.1174508).
- [100] J. A. Medina Méndez and H. Schmidt. "One-dimensional turbulence investigation of incompressible and low Mach number variable density pipe-flow." In: *Proc. Appl. Math. Mech.* 18.1 (2018), e201800090. DOI: [10.1002/pamm.201800090](https://doi.org/10.1002/pamm.201800090).
- [101] T. Echekki, A. R. Kerstein, and T. Dreeben. "One-Dimensional Turbulence Simulation of Turbulent Jet Diffusion Flames: Model Formulation and Illustrative Applications." In: *Combust. Flame* 125 (2001), pp. 1083–1105. DOI: [10.1016/S0010-2180\(01\)00228-0](https://doi.org/10.1016/S0010-2180(01)00228-0).
- [102] H. Shih and P. E. DesJardin. "Near-wall modeling of an isothermal vertical wall using one-dimensional turbulence." In: *Int. J. Heat Mass Transfer* 50.7-8 (2007), pp. 1314–1327. DOI: [10.1016/j.ijheatmasstransfer.2006.09.005](https://doi.org/10.1016/j.ijheatmasstransfer.2006.09.005).
- [103] E. R. Van Driest. "On Turbulent Flow Near a Wall." In: *Journal of the Aeronautical Sciences* 23.11 (1956), pp. 1007–1011. DOI: [10.2514/8.3713](https://doi.org/10.2514/8.3713).

- [104] M. Klein and H. Schmidt. "Investigating the Reynolds number dependency of the scalar transfer to a wall using a stochastic turbulence model." In: *Proc. Appl. Math. Mech.* 18.1 (2018), pp. 1–2. DOI: [10.1002/pamm.201800238](https://doi.org/10.1002/pamm.201800238).
- [105] J. H. Bae, J. Y. Yoo, and H. Choi. "Direct numerical simulation of turbulent supercritical flows with heat transfer." In: *Phys. Fluids* 17.10 (2005), p. 105104. DOI: [10.1063/1.2047588](https://doi.org/10.1063/1.2047588).
- [106] H. Tanaka, S. Maruyama, and S. Hatano. "Combined forced and natural convection heat transfer for upward flow in a uniformly heated, vertical pipe." In: *Int. J. Heat Mass Transfer* 30.1 (1987), pp. 165–174. ISSN: 0017-9310. DOI: [https://doi.org/10.1016/0017-9310\(87\)90069-X](https://doi.org/10.1016/0017-9310(87)90069-X).
- [107] H. Kawamura. "Analysis of transient turbulent flow using a phenomenological model of turbulence." In: *Proc. 21st National Heat Transfer Symposium.* 1984, pp. 40–42.
- [108] W. P. Jones and B. E. Launder. "The calculation of low-Reynolds-number phenomena with a two-equation model of turbulence." In: *Int. J. Heat Mass Transfer* 16.6 (1973), pp. 1119–1130. ISSN: 0017-9310. DOI: [https://doi.org/10.1016/0017-9310\(73\)90125-7](https://doi.org/10.1016/0017-9310(73)90125-7).
- [109] H. Tanaka, A. Tsuge, M. Hirata, and N. Nishiwaki. "Effects of buoyancy and of acceleration owing to thermal expansion on forced turbulent convection in vertical circular tubes—criteria of the effects, velocity and temperature profiles, and reverse transition from turbulent to laminar flow." In: *Int. J. Heat Mass Transfer* 16.6 (1973), pp. 1267–1288. ISSN: 0017-9310. DOI: [https://doi.org/10.1016/0017-9310\(73\)90135-X](https://doi.org/10.1016/0017-9310(73)90135-X).
- [110] H. Tanaka and T. Noto. "Effect of natural convection on turbulent forced convection heat transfer in a vertical tube." In: *Proc. 10th National Heat Transfer Symposium.* 1973, pp. 225–228.
- [111] F. P. Incropera, A. S. Lavine, T. L. Bergman, and D. P. DeWitt. *Fundamentals of heat and mass transfer.* Wiley, 2007.
- [112] J. A. Medina Méndez, H. Schmidt, and U. Riebel. "Towards a One-Dimensional Turbulence Approach for Electrohydrodynamic Flows." In: *Proc. 11th Int. Symp. Turb. Shear Flow Phen. (TSFP11).* Begel House Inc., 2019. URL: <http://www.tsfp-conference.org/proceedings/2019/265.pdf>.
- [113] T. Yamamoto and H. R. Velkoff. "Electrohydrodynamics in an electrostatic precipitator." In: *J. Fluid Mech.* 108 (1981), pp. 1–18. DOI: [10.1017/S002211208100195X](https://doi.org/10.1017/S002211208100195X).
- [114] A. V. Hershey. *The Helmholtz Theorem.* Tech. rep. Naval Postgraduate School Monterey CA., 1986. URL: <https://core.ac.uk/download/pdf/36725298.pdf>.

- [115] H.-S. Dou. "Mechanism of flow instability and transition to turbulence." In: *International Journal of Non-Linear Mechanics* 41.4 (2006), pp. 512–517. DOI: <https://doi.org/10.1016/j.ijnonlinmec.2005.12.002>.
- [116] C. Bacher and U. Riebel. "Electrohydrodynamically enhanced mass and heat transfer in wire-tube electrostatic precipitators." In: *Proceedings of ICESP*. Vol. 2018. ICESP2018. Charlotte, USA, 2018.
- [117] H. R. Hassé M. A. D.Sc. "X. Langevin's theory of ionic mobility." In: *The London, Edinburgh, and Dublin Philosophical Magazine and Journal of Science* 1.1 (1926), pp. 139–160. DOI: [10.1080/14786442608633618](https://doi.org/10.1080/14786442608633618).
- [118] J. P. Abraham, E. M. Sparrow, and W. J. Minkowycz. "Internal-flow Nusselt numbers for the low-Reynolds-number end of the laminar-to-turbulent transition regime." In: *Int. J. Heat Mass Transfer* 54.1 (2011), pp. 584–588. ISSN: 0017-9310. DOI: <https://doi.org/10.1016/j.ijheatmasstransfer.2010.09.012>.
- [119] V. Gnielinski, S. Kabelac, M. Kind, H. Martin, D. Mewes, K. Schaber, and P. Stephan. *VDI-Wärmeatlas*. Vol. 10. Springer, 2006.
- [120] J. P. Abraham, E. M. Sparrow, and J. C. K. Tong. "Heat transfer in all pipe flow regimes: laminar, transitional/intermittent, and turbulent." In: *Int. J. Heat Mass Transfer* 52.3 (2009), pp. 557–563. ISSN: 0017-9310. DOI: <https://doi.org/10.1016/j.ijheatmasstransfer.2008.07.009>.
- [121] J. S. Chang and K. Urashima. "Electrohydrodynamic Gas Flow Regime Map in a Wire-Plate Type Electrostatic Precipitator." In: *Int. J. Plasma Environ. Sci. Technol.* 3.2 (2009), pp. 138–141. URL: <http://ijpest.com/Contents/03/2/PDF/03-02-138.pdf>.
- [122] J. H. Ferziger and M. Perić. *Computational methods for fluid dynamics*. Vol. 3. Springer, 2002.
- [123] F. Moukalled, L. Mangani, and M. Darwish. *The finite volume method in computational fluid dynamics*. Vol. 1. Springer, 2016.
- [124] Y. Çengel. *Heat and mass transfer: a practical approach*. McGraw-Hill, 2006.
- [125] D. Fowler and E. Robson. "Square Root Approximations in Old Babylonian Mathematics: YBC 7289 in Context." In: *Historia Mathematica* 25.HM982209 (1998), pp. 366–378.
- [126] W. W. Liou and T.-H. Shih. *On the Basic Equations for the Second-Order Modeling of Compressible Turbulence*. Tech. rep. 105277. Cleveland, OH, USA: NASA, 1991. URL: <https://ntrs.nasa.gov/archive/nasa/casi.ntrs.nasa.gov/19920002084.pdf>.

- [127] *Del in cylindrical and spherical coordinates*. Accessed: 2019-12-18. URL: https://en.wikipedia.org/wiki/Del_in_cylindrical_and_spherical_coordinates.
- [128] J. P. Dussauge and J. Gaviglio. "The rapid expansion of a supersonic turbulent flow: role of bulk dilatation." In: *J. Fluid Mech.* 174 (1987), pp. 81–112. DOI: [10.1017/S0022112087000053](https://doi.org/10.1017/S0022112087000053).
- [129] S. Cristina, G. Dinelli, and M. Feliziani. "Numerical computation of corona space charge and V-I characteristic in DC electrostatic precipitators." In: *IEEE Trans. Ind. Appl.* 27.1 (1991), pp. 147–153. DOI: [10.1109/28.67546](https://doi.org/10.1109/28.67546).
- [130] F. W. Peek. *Dielectric phenomena in high voltage engineering*. Vol. 1. McGraw-Hill Book Company, Inc., 1915.
- [131] Lawrence Livermore National Laboratory Center for Applied Scientific Computing. *User's Manual: hypre, high performance preconditioners*. Version 2.11.2. 2017.
- [132] S. C. Chapra and R. P. Canale. *Numerical methods for engineers*. Vol. 2. McGraw-Hill New York, 1998.
- [133] C. F. Gallo. "Corona-A Brief Status Report." In: *IEEE Trans. Ind. Appl.* IA-13.6 (1977), pp. 550–557. DOI: [10.1109/TIA.1977.4503458](https://doi.org/10.1109/TIA.1977.4503458).
- [134] D. B. Go. *Gaseous ionization and ion transport: An introduction to gas discharges*. Class notes AME 60637 Ionization and Ion Transport. 2012. URL: https://www3.nd.edu/~sst/teaching/AME60637/notes/Go_ions_v4_031912.pdf.
- [135] C. Lübbert. "Zur Charakterisierung des gequenchten Zustandes im Elektroabscheider." PhD thesis. Brandenburgische Technische Universität Cottbus, 2011.
- [136] G. E. Karniadakis and R. M. Kirby II. *Parallel Scientific Computing in C++ and MPI: A Seamless Approach to Parallel Algorithms and their Implementation*. Cambridge University Press, 2003. DOI: [10.1017/CB09780511812583](https://doi.org/10.1017/CB09780511812583).

COLOPHON

This document was typeset using the typographical look-and-feel `classicthesis` developed by André Miede and Ivo Pletikosić. The style was inspired by Robert Bringhurst's seminal book on typography "*The Elements of Typographic Style*". `classicthesis` is available for both \LaTeX and \LyX :

<https://bitbucket.org/amiede/classicthesis/>

Happy users of `classicthesis` usually send a real postcard to the author, a collection of postcards received so far is featured here:

<http://postcards.miede.de/>

Thank you very much for your feedback and contribution.